(Co)-Doping of Lead-Free Piezoceramics

TECHNISCHE
UNIVERSITÄT
DARMSTADT

Material- und Geowissenschaften

Nichtmetallisch-Anorganische Werkstoffe
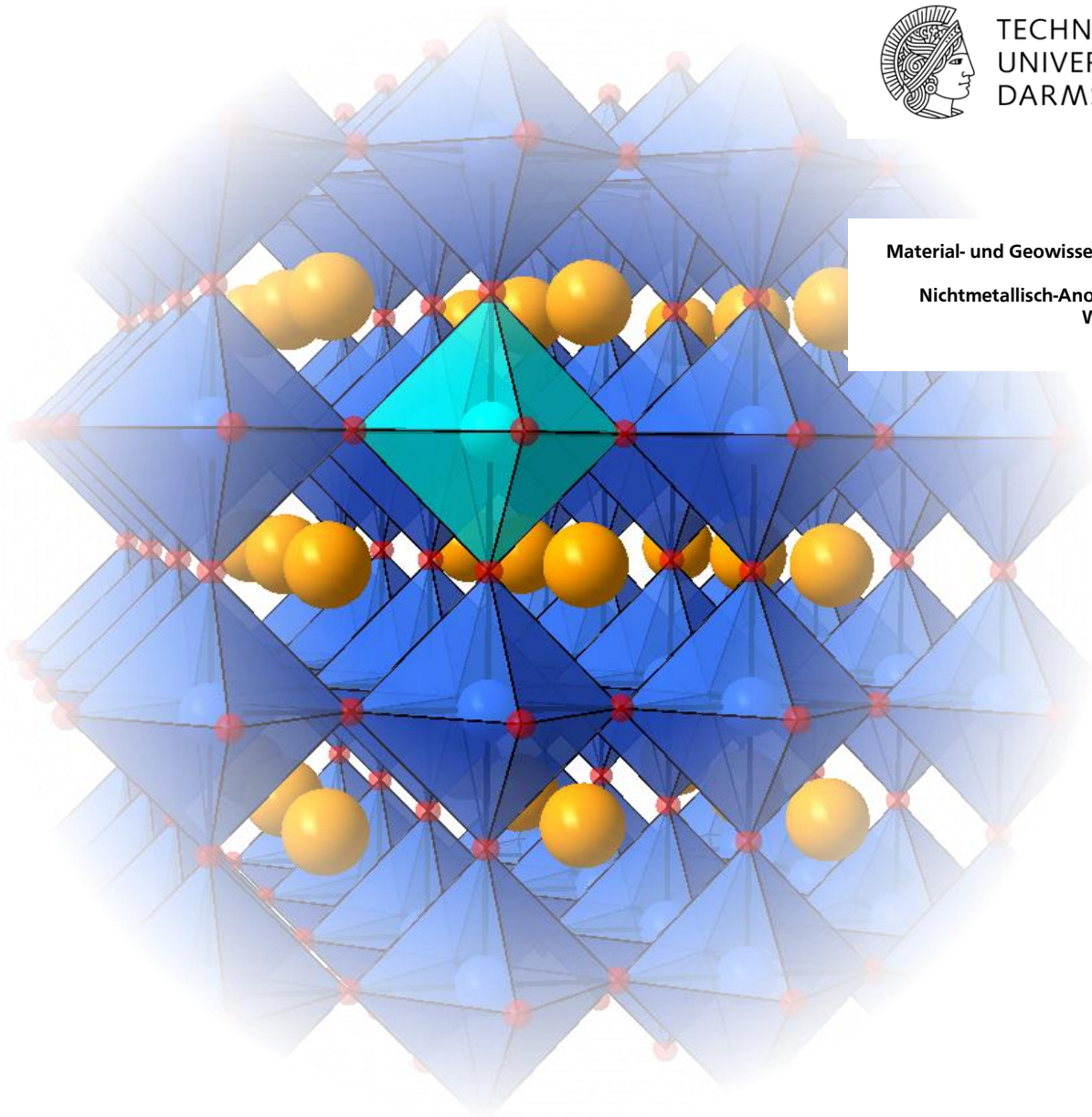
(Co)-Doping of Lead-Free Piezoceramics

Dem Fachbereich der Material- und Geowissenschaften der Technischen Universität Darmstadt zur Erlangung des akademischen Grades

Doktor *rerum naturalium*

genehmigte, vorgelegte Dissertation von

Martin Manfred Blömker, M.Sc., geboren am 14.05.1984 in Münster (Westfalen).

1. Gutachten: Prof. Dr. Jürgen Rödel

2. Gutachten: Prof. Dr. Andreas Klein

Tag der Einreichung: 09. November 2015

Tag der Verteidigung: 29. Januar 2016

Darmstadt, 2016 – D17

To Leonore, Manfred and Ingo.

Acknowledgements

Abstract

This work encompassed an in depth investigation of the defect chemistry and piezoelectric properties of $Bi_{0.5}(Na_{(1-w)}K_w)_{0.5}Ti_{(1-x-y)}Cu_xV_yO_3$ with w = 0.1, 0.2 and 0.3 and x and y < 0.01, synthesized by a solid state process. A pseudocubic perovskite phase with no detectable impurities was verified by X-ray diffraction, while doping tended to reduce the rhombohedral character of $Bi_{0.5}(Na_{0.9}K_{0.1})_{0.5}TiO_3$ (BNKT10) ceramics. Doping BNKT10 was shown to result in more homogenous grain size distributions, elucidated by analyzing scanning electron microscopy images. Small and large signal piezoelectric measurements also revealed that the tetragonal phase of $Bi_{0.5}(Na_{0.7}K_{0.3})_{0.5}TiO_3$ is disproportionally affected by doping. The transition temperature from ferroelectric to relaxor phase (T_{f-r}), the coercive field, and the remanent polarization drop for compositions with high K-content, while the maximum strain is mostly increased. The general trend of decreasing T_{f-r} in these high K tetragonal materials can be rationalized by A-site defects and the resulting increased distribution of random fields. Impedance spectroscopy at resonance indicates a high electromechanical coupling factor of planar samples in thickness mode (k_t up to 0.56), which is useful for sensing applications in combination with the observed low mechanical quality factor (Q_M) of 9 in thickness direction. Impedance spectroscopy at elevated temperatures revealed that doping resulted in a decrease in the activation energy (E_A) of 110±10 meV from 1.37 eV of undoped $Bi_{0.5}(Na_{0.9}K_{0.1})_{0.5}TiO_3$ for both single element doping with Cu or V, as well as simultaneous doping with both Cu and V. Furthermore, the resistivities of doped BNKT10 ceramics (3.3×10^3 Ωm to 1.3×10^7 Ωm) were consistently lower than those of the undoped BNKT10 ceramics (1.6×10^5 Ωm to 2.0×10^8 Ωm). The variation of the oxygen partial pressure from 0.21 bar (synthesis condition) to 1 bar, 2.1×10^{-6} bar and < 10^{-18} bar likewise lead to consistently decreased E_A and resistivities with values as low as 0.23 eV and 1.9×10^0 Ωm to 2.7×10^3 Ωm, respectively. Electron paramagnetic resonance spectroscopy (EPR) and X-ray photoelectron spectroscopy (XPS) indicated the presence of Cu^{2+}, V^{4+} and V^{5+} in the doped ceramics, while lower oxidation states of Cu and V could be excluded. EPR spectroscopy indicated Cu^{2+} and V^{4+} in a rhombic environment with major distortion in one direction and minor distortion in the other directions. While V^{4+} is introduced into the B-site of the bulk, Cu^{2+} was shown to dominantly segregate from the bulk, most likely at the grain boundary due to the creation of a liquid phase during sintering. This correlates with the increasing density with increasing Cu content and the observed trend of a lowered Q_M with increasing Cu content, presumably due to leakage. The solubility limit of Cu in the bulk was found to be < 0.05 at.%. All doped BNKT10 ceramics, containing Cu, were shown to possess Cu in two different rhombic electronic environments, namely CuO_6 and CuO_4. For V doping, a discernable, albeit, small (<400 meV) increase in Fermi level was determined by XPS, suggesting a donor doping effect corroborated by the lower resistivities and E_A of these samples likely due to charge compensation induced electrons. The overall defect chemistry of the Cu and V doped ceramics was revealed

to be influenced by (I) bismuth, sodium and potassium acceptor vacancies, resulting from the host material, (II) additional n-type doping induced electrons, (III) few bulk Cu^{2+} acceptor centers, resulting from Cu doping, (IV) V^{5+} donor states, introduced through V doping, and (V) in all cases the concentration and mobility of oxygen vacancies.

Table of Content

List of Symbols and Abbreviations

A	hyperfine coupling constant, SI-unit: MHz
AC	alternating current
AT	cutting direction 35° 25' to the Z crystal axis of quartz
A_{xx}	hyperfine coupling constant in direction of principal x-axis, SI-unit: MHz
A_{yy}	hyperfine coupling constant in direction of principal y-axis, SI-unit: MHz
A_{zz}	hyperfine coupling constant in direction of principal z-axis, SI-unit: MHz
BA	$BiAlO_3$
BCT-BZT	$BaCa_{(1-x)}Ti_xO_3 - BaZr_{(1-y)}Ti_yO_3$
BE	binding energy
BKT	$Bi_{0.5}K_{0.5}TiO_3$
BLSF	bismuth layer-structured ferroelectric
BLT	$Bi_{0.5}Li_{0.5}TiO_3$
BNKT	$Bi_{0.5}(Na,K)_{0.5}TiO_3$
BNKLT	$Bi_{0.5}(Na,K,Li)_{0.5}TiO_3$
BNT	$Bi_{0.5}Na_{0.5}TiO_3$
BSE	backscattered electron
BST	$Ba_{(1-x)}Sr_xTiO_3$
BT	$BaTiO_3$
BZnT	$Bi_{1/2}Zn_{1/2}TiO_3$
BZT	$BaZr_{(1-x)}Ti_xO_3$
c/a ratio	ratio of principal c-axis to principal a-axis of a given unit cell
CPE	constant phase element
C_0	shunt capacitance of equivalent electrical circuit, SI-unit: F
DAISY-BAT	Darmstadt Integrated System for Battery Research
DC	direct current
d_{33}	piezoelectric constant in parallel to the poling direction, SI-unit: pm/V

d_{33}^*	maximum obtainable strain to electric field ratio, SI-unit: pm/V
EPR	electron paramagnetic resonance spectroscopy
ESR	electron spin resonance (see EPR)
E_A	activation energy, SI-unit: eV
E_c	coercive electric field, SI-unit: kV/mm
E_i	internal bias field, SI-unit: kV/mm
E_{max}	maximum electric field, SI-unit: kV/mm
E_{pass}	pass energy, SI-unit: eV
E_{pol}	electric poling field, SI-unit: kV/mm
ε	dielectric permittivity, SI-unit: F/m
ε_0	dielectric permittivity of vacuum, SI-unit: F/m
ε_r	relative dielectric permittivity, SI-unit: F/m
ε'	dielectric permittivity (real part), SI-unit: F/m
ε''	dielectric permittivity (imaginary part), SI-unit: F/m
f	frequency, SI-unit: Hz
F	cross-sectional area of a sample, SI-unit: m²
FE	ferroelectric
f_a	frequency at antiresonance, SI-unit: Hz
f_m	frequency of minimum impedance, SI-unit: Hz
f_n	frequency of maximum impedance, SI-unit: Hz
f_p	parallel resonance frequency at maximum resistance, SI-unit: Hz
f_r	frequency at resonance, SI-unit: Hz
f_s	motional resonance frequency at maximum conductance, SI-unit: Hz
g	g-factor (dimensionless)
$g_\perp$	perpendicular g-factor (dimensionless)
$g_\parallel$	parallel g-factor (dimensionless)
g_{iso}	isotropic g-factor (dimensionless)
g_{xx}	g-factor in direction of principal x-axis (dimensionless)

g_{yy}	g-factor in direction of principal y-axis (dimensionless)
g_{zz}	g-factor in direction of principal z-axis (dimensionless)
FOM	figure of merit
I	current, SI-unit: A
JT	Jahn-Teller
KN	$KNbO_3$
KNN	$K_{(1-x)}Na_xNbO_3$
k_B	Boltzmann constant (8.6173324×10^{-5}), SI-unit: eV K^{-1}
k_p	resonance mode in plane of a cylindrical sample
k_t	resonance mode in thickness direction of a cylindrical sample
L	length of sample (thickness), SI-unit: m
LN	$LiNbO_3$
MLA	multilayer actuator
MLCC	multilayer ceramic capacitor
MPB	morphotropic phase boundary
NN	$NaNbO_3$
n_{range}	number of grains with a certain range of diameters
n_{total}	total number of grains in the analyzed electron microscopy images
ω	phase angle, in °
PE	paraelectric
PLZT	$Pb_{(1-x)}La_xZrO_3$- $Pb_{(1-y)}La_yTiO_3$
PMN	$PbMg_{1/3}Nb_{2/3}O_3$
PMN-PT	$PbMg_{1/3}Nb_{2/3}O_3$- $PbTiO_3$
PPT	polymorphic phase transition
PSZT	$Pb_{(1-x)}Sr_xZrO_3$- $Pb_{(1-y)}Sr_yTiO_3$
PT	$PbTiO_3$
PTCR	positive temperature coefficient resistor
PZT	$PbZrO_3$- $PbTiO_3$

PZN	$PbZn_{1/3}Nb_{2/3}O_3$
PZN-PT	$PbZn_{1/3}Nb_{2/3}O_3$- $PbTiO_3$
P-E	polarization *vs*. electric field
P_{max}	maximum polarization, SI-unit: $\mu C/cm^2$
P_{rem}	remanent polarization, SI-unit: $\mu C/cm^2$
P_{sat}	saturation polarization, SI-unit: $\mu C/cm^2$
Q_M	mechanical quality factor
$Q_{M,p}$	mechanical quality factor of the planar resonance mode
$Q_{M,t}$	mechanical quality factor of the thickness resonance mode
R	resistance, SI-unit: Ω
RPM	rotations per minute, SI-unit: Hz
RSF	relative sensitivity factor
RT	room temperature (about 20 °C to 26 °C), in °C, SI-unit: K
ρ	resistivity, SI-unit: Ωm
$\rho_{Archimedes}$	density after Archimedes, SI-unit: kg/m^3
ρ_{rel}	relative density in %
ρ_{theo}	theoretical density, calculated from the XRD pattern, SI-unit: kg/m^3
SE	secondary electron
SEM	scanning electron microscope
ST	$SrTiO_3$
S-E	strain *vs*. electric field
S_{max}	maximum strain
S_{neg}	negative strain
σ_i	ionic conductivity
σ_n	electronic conductivity
σ_p	hole conductivity
σ_{total}	overall conductivity
tanδ	loss tangent or also called dissipation factor

T_C	*Curie* temperature, in °C, SI-unit: K
T_d	depolarization temperature, in °C, SI-unit: K
T_{f-r}	transition temperature: ferroelectric to relaxor, in °C, SI-unit: K
T_{r-t}	transition temperature: rhombohedral to tetragonal, in °C, SI-unit: K
T_{sint}	sintering temperature, in °C, SI-unit: K
T_M	temperature of maximum permittivity, in °C, SI-unit: K
U	voltage, SI-unit: V
v	vacancy (*not in Kröger-Vink notation*, to not confuse it with vanadium)
V	vanadium (*standard Kröger-Vink notation*)
XPS	X-ray photoelectron spectroscopy
XRD	X-ray diffraction
Z	complex impedance , SI-unit: Ω
|Z|	absolute value of the complex impedance, SI-unit: Ω
Z'	real part of the impedance / resistance, SI-unit: Ω
Z"	imaginary part of the impedance / reactance, SI-unit: Ω
Z_m	maximum impedance at resonance

1. Introduction

Piezoelectric materials nowadays can be found in numerous diverse applications, ranging from actuators as in fuel injection devices, (nano-)positioning, vibration reduction and energy harvesting to sensing applications.[1-6] Examples are hydrophones (*e.g.* for sonar applications), ultrasonic imaging or parking assistants.

As of 2009, an overwhelming 98% of the production of piezoelectric bulk actuators was lead-containing. Lead, a known neurotoxin [7,8], is released into the environment during thermal processing of the raw materials in the form of PbO as well as during hard machining of components, furthermore requiring expensive waste disposal and recycling. Several governmental regulations worldwide were recently put into place to reduce the health risks of lead-containing materials.[9-11] This urgent need for lead-free materials gave rise to global research efforts to replace lead-containing materials such as $PbTiO_3$ (PT), $PbZrO_3$-$PbTiO_3$ (PZT), $Pb(Mg_{1/3}Nb_{2/3})O_3$ (PMN) or $PbZn_{1/3}Nb_{2/3}O_3$ (PZN) by emerging alternatives.[3,5,12-21] So far, merely few lead-free materials have been found that are able to match or surpass the properties of the lead variants.

The system $Bi_{0.5}Na_{0.5}TiO_3$-$Bi_{0.5}K_{0.5}TiO_3$ (BNT-BKT or also BNKT)[22-27], is a promising candidate, to replace lead in certain piezoelectric applications, since it is able to form solid solutions with various other elements that improve ferroelectric (FE) and piezoelectric properties such as for instance barium [28-32], niobium[33-36], lithium[37-40] or manganese[41-43] to name the most researched solid solutions. BNT-based materials are not toxic and Bi itself is even used in pharmaceutics [44,45]. Combining two or more end-members of such a solid solution can lead to improved piezoelectric properties superior to both pure end-members by mechanisms that are still not fully understood and currently debated in the literature. This is also well described for lead-based systems. Drawbacks to date are the low depolarization temperature and a high poling field compared to lead-based materials.

The underlying question of the following work is: Is it possible to improve this system and its defect chemistry in particular, by tailored co-doping and optimized processing, in such a way that it can compete with one or more of today's lead-based systems?

The aim of this research was to explore novel dopants and especially dopant combinations, which are able to be incorporated into the pure BNKT system or solid solutions thereof. Especially for electronic devices and furthermore commercially used lead-based materials, it is common practice to intentionally introduce defects, thereby influencing different material properties. Therefore, further investigation on dopant influence on piezoelectrical properties, *e.g.* the maximum strain, the depolarization temperature, the induced polarization, but also time dependent characteristics as frequency dependent permittivity as well as ageing and fatigue of the material, is required to determine optimum doping concentrations of candidate elements for specific applications.

2. Background and Literature Review

In the following section, the basics of doped piezoelectric ceramics and their defect chemistry are described. The general part of this section is mostly based on a publication of Pramanick *et al.* [46], a book of D. M. Smyth [47] as well as a book chapter of W. Cao [48].

All defects discussed in this thesis will be noted in the Kröger-Vink notation (*cf.* Kröger *et al.* [49]). One deviation from this notation is made in this work: To differentiate vanadium from a vacancy, all vacancies are indicated by a small v, while vanadium is indicated by a capital V.

Since the overwhelming majority of crystal structures discussed belongs to the family of perovskites, following short overview is given.

The family of perovskites entails compositions with the same crystal structure as the mineral perovskite $CaTiO_3$. The ideal perovskite structure is a close packed cubic structure, with a general formula ABO_3 with the A-ion roughly being twice the size as the B-ion. The A-site ions are sitting in a 12-fold coordinated environment with oxygen as partner (*cf.* Figure 2.1(a)) whereas the B-ions are found on an octahedral lattice site, being coordinated with six oxygen ions, which is represented in Figure 2.1(b). Lots of materials have the perovskite structure or close relatives, since it is a favorable arrangement for anions and cations.

(a)

(b)
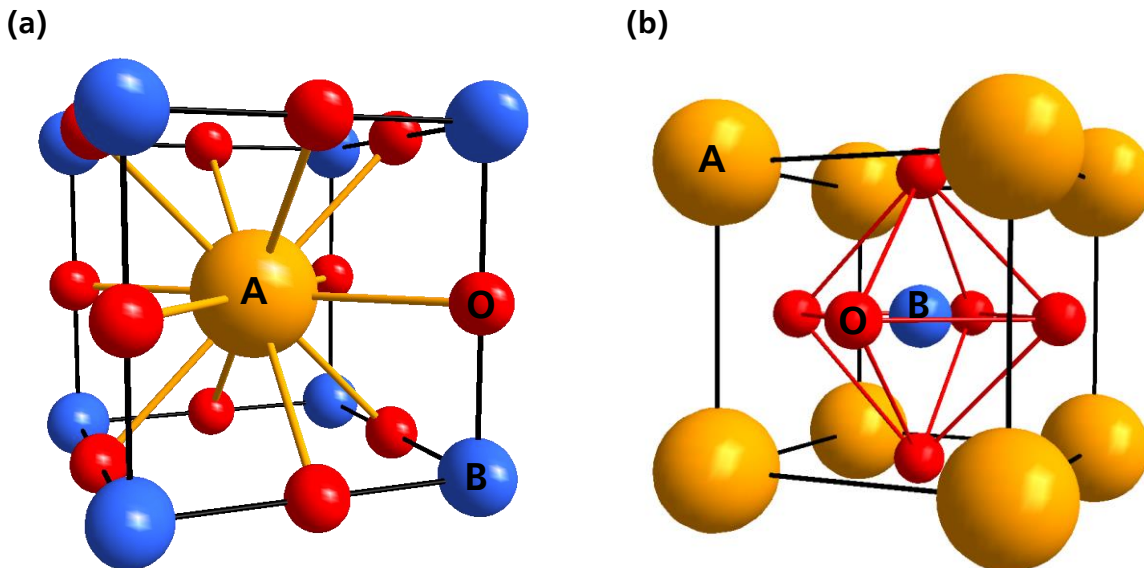
Figure 2.1   Schematic of the ABO_3 perovskite structure emphasizing (a) the dodecahedral lattice position with the A-ion – *e.g.* Ca^{2+} in the center and (b) the octahedral lattice position with the B-ion – *e.g.* Ti^{4+} in the center. Not to scale.

The fact that the original perovskite $CaTiO_3$ does not fit the description of an ideal perovskite, since it is slightly distorted due to the small A-ion Ca^{2+} that is not able to fill the A lattice site completely, already gives an idea of the opportunity to influence the crystal structure by the choice of incorporated elements.

2.1. Ferroelectric and Piezoelectric Basics
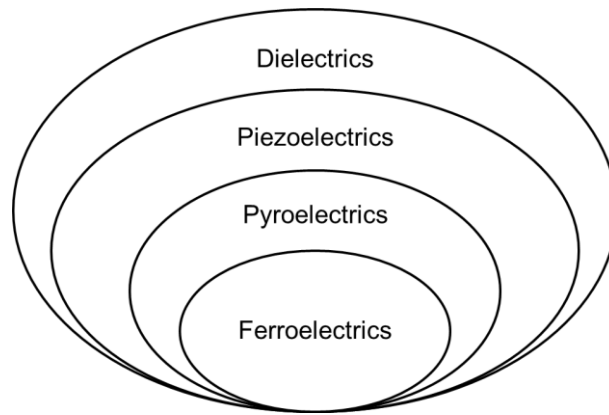
Figure 2.1.1 Schematic of sub-groups of dielectric materials.

In order to understand piezoelectric phenomena, one can first discern the basic principles underlying dielectric materials in general. Dielectrics entail different sub-groups, piezoelectrics being one of them, (*cf.* Figure 2.1.1) that will be further discussed in the following sections.

2.1.1. Dielectrics

Dielectric materials are characterized by a band gap > 2.5 eV, thus are very poor conductors, since they (in the ideal case) have no electronic carriers. This is why they react to an external applied electric field by displacement of ions and electrons, which results in the dielectric displacement D

$$D_i = \varepsilon_0 E_i + P_i \quad , \tag{2.1.1.1}$$

with ε_0 being the dielectric constant of vacuum, E_i the electric field and P_i the polarization. ε_r, the relative dielectric constant is described by

$$\varepsilon_r = \frac{\varepsilon'}{\varepsilon_0} \tag{2.1.1.2}$$

and expresses the ratio between charge stored on an electroded material divided by the permittivity of vacuum at the same electric field. Usually ε_r ranges around five for organic and 20 for inorganic materials. Dielectric materials generally have a high dielectric constant up to $10^2 - 10^5$.

Upon the application of alternating current (AC) to dielectrics, one can differentiate the real (out of phase) and imaginary (in-phase) contributions to the permittivity. Reasons for that can either be resistive leakage or dielectric absorption or both. Thus the loss tangent **tanδ** is defined by

$$tan\delta = \frac{\varepsilon''}{\varepsilon'} \quad , \qquad (2.1.1.3)$$

which expresses the ratio of the imaginary out of phase component (ε'') of the complex permittivity and the real in-phase component (ε'). It is described by

$$\varepsilon = \varepsilon' - i\varepsilon'' \quad . \qquad (2.1.1.4)$$

2.1.2. Piezoelectricity

In piezoelectric materials, an applied stress σ is correlated with the creation of electric charge in combination with strain of the material. This can be described by

$$D_i = d_{ikl}\sigma_{kl} \quad . \qquad (2.1.2.1)$$

Furthermore an applied electric field E results in strain S

$$S_{ij} = d_{kij}E_k \quad . \qquad (2.1.2.2)$$

The piezoelectric constant d, having a unit of C/N is identical for both effects:

$$d = \frac{D}{\sigma} = \frac{S}{E} \qquad . \qquad (2.1.2.3)$$

As for ceramics the piezoelectric constant can vary along different axes, d is written in tensor form, where equation (2.1.2.4) describes the direct piezoelectric effect, while equation (2.1.2.5) describes the converse or indirect piezoelectric effect.

$$D_i = d_{ijk}\sigma_{jk} + \varepsilon_{ijk}^{\sigma}E_J \qquad (2.1.2.4)$$

$$S = s_{ijk}^{E}\sigma_{jk} + d_{ijk}E_j \qquad (2.1.2.5)$$

Here the stress σ and strain **S** are related to the electric field and the displacement.

$$k^2 = \frac{E_{el/mech}}{E_{total}} \quad (2.1.2.6)$$

$$k^2 = \frac{E_{mech/el}}{E_{total}} \quad (2.1.2.7)$$

The electromechanical coupling factor k is correlated to the strength of the piezoelectric effect and compares the quantity of electrical energy converted to mechanical energy $E_{el/mech}$ with respect to the total energy input (E_{total}) into the system (*cf.* Equation 2.1.2.6) or conversely the mechanical energy converted to electrical energy $E_{mech/el}$ with respect to the total mechanical energy input into the system (*cf.* Equation 2.1.2.7), providing a means of judging the efficiency of conversion. The coupling factor scales with the degree of poling of a given sample.

High coupling efficiency is important for transducer and sensor applications. For instance in surface acoustic wave sensors, a higher k allows for a higher measurable voltage oscillation upon mechanical vibration (acoustic waves). In case of transducers, materials with a higher k, require a lower driving voltage for the generation of acoustic waves, under otherwise similar conditions.

Often-times $\boldsymbol{d_{33}^*}$ is used to describe actuator characteristics. It can be calculated in the following way

$$\boldsymbol{d_{33}^*} = \frac{S_{max}}{E_{max}} \quad (2.1.2.8)$$

using the maximum attainable strain S_{max} and the maximum applied electric field E_{max}.

2.1.3. Ferroelectricity

Ferroelectricity implies the reversibility of the orientation of the electric dipole in a crystal by means of an electric field. The difference to pyroelectricity is that the applied electric field needed for reversal is smaller than the electric breakdown field or the field required for irreversible arrangement of atoms. Ferroelectric materials display a spontaneous electric polarization below the Curie temperature (T_c), depolarization temperature (T_d) or transition temperature from ferroelectric to relaxor state (T_{f-r}).

2.1.4. Phase Transitions

Lots of piezoelectric materials are a mixture of two (or more) constituents, *e.g.* PZT is a solid solution of PT and $PbZrO_3$ (PZ). As the combined pure individual members may have different phases (*e.g.* pure PT is tetragonal and pure PZ is rhombohedral), there must in every case be a confined boundary between the constituents, or, as it is the case for a lot of lead-free solid solutions, a broader region with phase coexistence. As direct transitions from tetragonal to rhombohedral phases are not allowed by symmetry, a bridging monoclinic symmetry serves as an explanation for their coexistence.[50]

Strictly speaking, the term morphotropic refers to phase transitions induced by composition only.[51] Thus, due to the additional temperature dependence (and not solely concentration dependence) of the phase transitions, it is defined as polymorphic phase transition (PPT) in lead-free materials, however, as it is common nomenclature with respect to ferroelectric materials, the boundary between rhombohedral and tetragonal phases will be addressed as MPB hereinafter.

The material properties close to the MPB may deviate substantially from the phase pure constituents (*cf.* Figure 2.1.4.1). At or in vicinity of the MPB, dielectric and piezoelectric properties of the materials exhibit maxima, which is why it is of importance to investigate material behavior at the MPB.
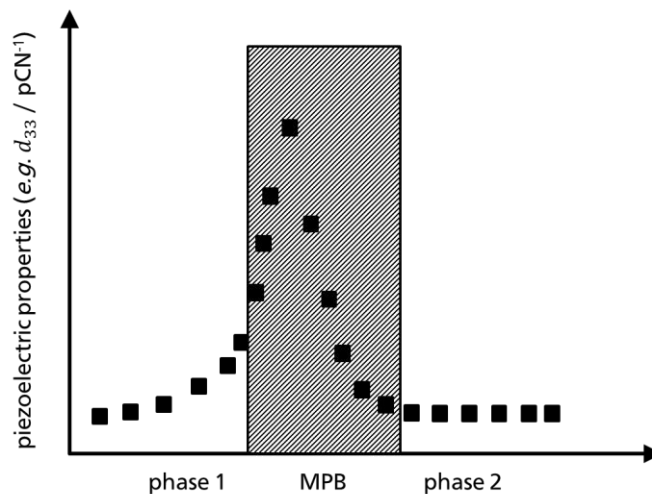
Figure 2.1.4.1   Schematic of the maximized piezoelectric properties at a MPB between two distinct phases.

2.1.5. Relaxor Piezoelectrics

Relaxors are generally characterized by atomic disorder and resulting field disorder.[16] Well-ordered systems in contrary lead to the stabilization of domains, which are essentially a long range alignment of the polarization vectors. In relaxor materials this

long range order is interrupted by disorder in the material. As piezoelectric material systems can be complex, in particular charge disorder, size disorder, the presence or absence of lone electron pairs of atoms without particular order, all can contribute to the local disorder of the material. This can be described by the concept of so called random fields. Random fields reduce the correlation length of polarized units, which means the stabilized domains are smaller than without disorder.

Upon the application of an electric field, so called *ergodic relaxor* materials display a pronounced strain of the material, accompanied by polarization vector ordering. Both, however, revert to a random, disordered state, once the electric field is removed. *Ergodic* relaxors display no measurable remanent polarization after such treatment. For *non-ergodic* relaxors, the FE order is retained beyond removal of the applied electric field. In general a pronounced frequency dispersion of the permittivity is characteristic of relaxor materials.

2.2. Measurement Theory and Basics

2.2.1. Electron Paramagnetic Resonance Spectroscopy

Electron paramagnetic resonance spectroscopy (EPR) detects unpaired electrons. It is therefore insensitive to Na^+ with $3s^0$, K^+ with $4s^0$, Ti^{4+} $3d^0$ and Bi^{3+} with $6p^0$ electronic configuration, allowing for excellent distinction between BNKT base composition and added dopants. Doping with Cu^{2+} and V^{4+}, which possess $3d^9$ and $3d^1$ electronic configuration, respectively (*cf.* Figure 2.2.1.1), allows for detection and distinction of those EPR-active centers. Strong Jahn-Teller-splitting (JT-splitting) is to be expected for Cu^{2+}, while V^{4+} is expected to exhibit minor JT-splitting, corresponding with a stronger and minor local oxygen octahedra distortion, respectively.

The Spin Hamiltonian for a single unpaired electron with a spin **S** of $\frac{1}{2}$ can be described by

$$\hat{H} = \beta_e \boldsymbol{B_0} \cdot \boldsymbol{g} \cdot \boldsymbol{S} - \beta_n \boldsymbol{B_0} \cdot \boldsymbol{g_n} \cdot \boldsymbol{I} + \boldsymbol{S} \cdot \boldsymbol{A} \cdot \boldsymbol{I} \quad , \qquad (2.2.1.1)$$

where β_e represents the respective Bohr magneton and β_n is the respective nuclear magneton, while $\boldsymbol{g_n}$ corresponds to the nuclear g-factor. The first term of Equation 2.2.1.1 represents the respective electronic and nuclear Zeeman interactions, with $\boldsymbol{B_0}$ being the applied external magnetic field with respect to the **g**-matrix. This equation omits theoretically possible quadrupole interactions.
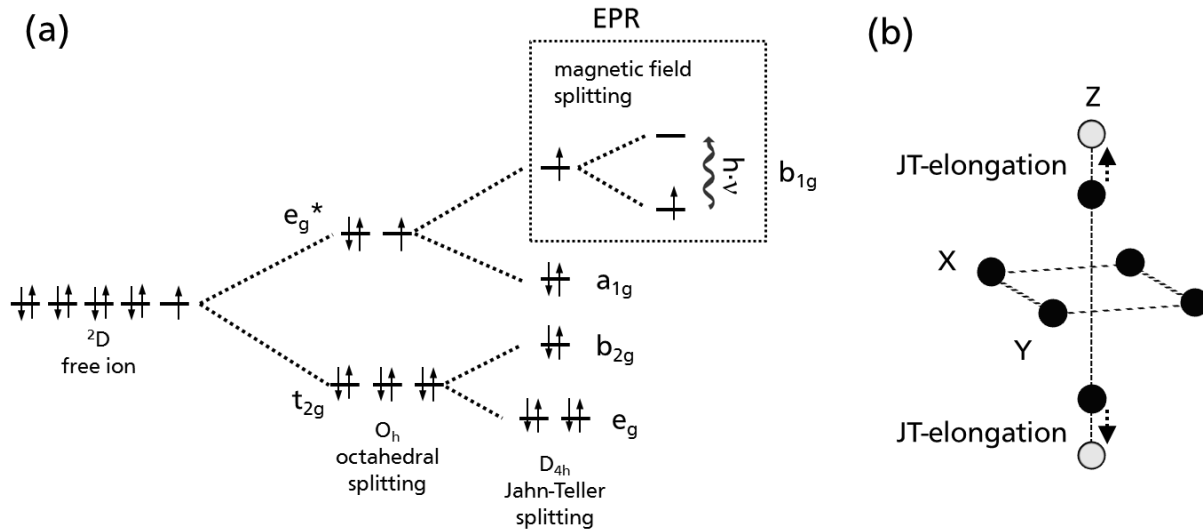
Figure 2.2.1.1   Schematic (a) of octahedral splitting and additional JT-splitting, with the electron configuration exemplarily chosen for Cu^{2+}. Indicated in detail is the EPR transition of electrons in b_{1g} orbitals oriented parallel to the magnetic field to an energetically higher state in which the electrons assume an antiparallel configuration with respect to the applied external magnetic field. In (b) the distortion of an octahedron, resulting from JT-splitting is depicted.

The **g**-matrix is a symmetric 3x3 matrix, reflecting the fact that the Zeeman interaction can be dependent on the observed direction *i.e.* the system may display anisotropy depending on the site symmetry of the respective paramagnetic center. Rhombic, axial and isotropic or spherical electronic symmetry are distinguished. The g-matrix in the rhombic case is described by

$$\boldsymbol{g} = \begin{bmatrix} \boldsymbol{g}_{xx} & 0 & 0 \\ 0 & \boldsymbol{g}_{yy} & 0 \\ 0 & 0 & \boldsymbol{g}_{zz} \end{bmatrix} . \qquad (2.2.1.2)$$

For isotropic interactions

$$\boldsymbol{g}_{iso} = \boldsymbol{g}_{xx} = \boldsymbol{g}_{yy} = \boldsymbol{g}_{zz} , \qquad (2.2.1.3)$$

holds true, since regardless of observing direction the electronic interactions are the same. Axial electronic environment with unidirectional distortion (in direction of principal z axis) is furthermore characterized by

$$(\boldsymbol{g}_{\perp} = \boldsymbol{g}_{xx} = \boldsymbol{g}_{yy}) \neq (\boldsymbol{g}_{\parallel} = \boldsymbol{g}_{zz}) . \qquad (2.2.1.4)$$

In analogy the hyperfine splitting constant **A**, which describes the interaction between electron spin and nuclear spin of an atom, can be described by a symmetric 3x3 matrix, exemplarily indicated for the rhombic case:

$$A = \begin{bmatrix} A_{xx} & 0 & 0 \\ 0 & A_{yy} & 0 \\ 0 & 0 & A_{zz} \end{bmatrix} \; . \qquad (2.2.1.5)$$

Since both Cu^{2+} and V^{4+} have a spin of $\frac{1}{2}$, equation 2.2.1.1 was used in either case to simulate the EPR spectra. Hyperfine interaction (**A**) was also taken into account *via* this equation. The copper hyperfine interaction was in particular implemented by the second term of the equation, with $\mathbf{I}^{Cu} = \frac{3}{2}$ and in the other case $\mathbf{I}^{Va} = \frac{5}{2}$. For Cu^{2+} hyperfine interaction it was taken into account that two individual stable naturally occurring copper isotopes with abundances of ^{63}Cu: 69.09% and ^{65}Cu: 30.91% exist. The vanadium hyperfine interaction was solely simulated for the stable ^{51}V isotope, which has a close to exclusive abundance of 99.75%.

2.2.2. Electrical Measurements

Electrical impedance is a measure of the complex ratio of the voltage to the current in an AC circuit:

$$Z(t) = \frac{U(t)}{I(t)} \; , \qquad (2.2.2.1)$$

where I is the current through the conductor and U is the potential difference across the conductor. It describes how strongly a material opposes the flow of electric current in an AC circuit, where Z is depending on time (or frequency). In case of direct current (DC), the impedance is equal to the resistance of a given circuit.

Ceramics never purely behave in an ideal Debye-like manner, which can be described by

$$Z^{-1} = R^{-1} + j\omega C \; , \qquad (2.2.2.2)$$

where the equivalent circuit is a single parallel resistance-capacitor element with R being the resistance, $j = \sqrt{-1}$, ω is the phase angle, C the capacitance and Z the corresponding complex impedance.

The deviation from Debye behavior can have several causes, for instance the grain size distribution being inhomogeneous. Constant phase elements (CPE) are therefore commonly used to represent the deviation from this ideal behavior. The impedance of a CPE is given by

$$Z^{-1} = Q(j\omega)^{\alpha} \; , \qquad (2.2.2.3)$$

where Q and α are constants ($0 < \alpha < 1$). When $\alpha = 1$, the CPE describes capacitive behavior. In case of $\alpha = 0$ it resembles an ohmic resistance. Hence, it helps to evaluate non-ideal capacitive or resistive behavior.

In contrast to (ideal) single crystals, ceramic materials can be electrically inhomogeneous and electrical responses may overlap. In this case equivalent circuits allow for the deconvolution of different regions (*e.g.* grain boundary and bulk) in the material.[52-54]

Equivalent circuits are used to represent an electrical model of the electro-mechanical processes, for instance the oscillations at resonance (*cf*. Figure 2.2.2.1), occurring in a material. They are, thus, allowing to understand electric properties and, beyond that, the extraction of materials parameters such as capacitances or resistances to correlate them with the electro-mechanical behavior.
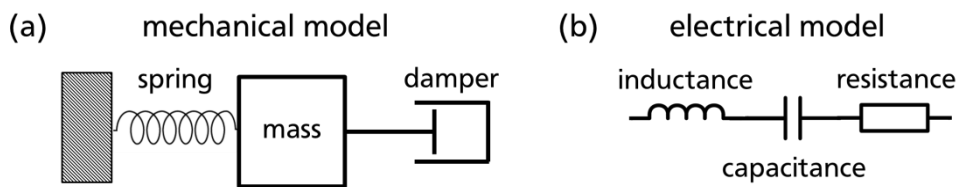
Figure 2.2.2.1 Simple schematics of analogous mechanical (a) and electrical (b) oscillation processes in piezoelectric materials. The capacitor, inductor and resistor of the electrical model are analogous to spring, mass and damper of the mechanical model, respectively.

In the models, the inductance correlates with a spring, which mainly describes the material stiffness. The stiffness of the material is in turn determined by the Young's modulus and the dimensions of the material and depends on the load resistance and working frequency. As an important factor, the capacitance (electrical model) or mass (mechanical model) predominantly influences the resonance frequency. Energy dissipation is implemented in the models by the resistor (electrical model) or damper (mechanical model). It is a function of the used working frequency, the piezoelectric properties of the material and the amplitude of the applied force (mechanical model) or applied field (electrical model). The energy can dissipate in the form of heat.

In order to determine activation energies of a material, the resistances of a sample at different elevated temperatures can be used to calculate the resistivity ρ according to

$$\rho = \frac{R \cdot F}{L} \quad , \tag{2.2.2.4}$$

with R being the respective resistance, F the cross-sectional area (electrode area of one face) of the sample and L the length (in case of this work the thickness) of the sample. With the obtained resistivity it is possible to approximate the

activation energy E_A of each electrical process by using following Arrhenius-type equation

$$\rho = \rho_0 e^{\frac{-E_a}{k_B T}} \quad , \tag{2.2.2.5}$$

with ρ_0 being a pre-factor and k_B being the Boltzmann constant, from which one can obtain E_a:

$$E_a = -k_B \left[\frac{\partial \ln \rho}{\partial \frac{1}{T}} \right] . \tag{2.2.2.6}$$

Commonly, an Arrhenius plot (*cf*. Figure 2.2.2.2) is chosen to visualize the data obtained from impedance measurements at different temperatures, in which E_a correlates with the slope of the plot multiplied by k_B. The experimental data should in the ideal case yield a straight line if it follows Arrhenius-type behavior.
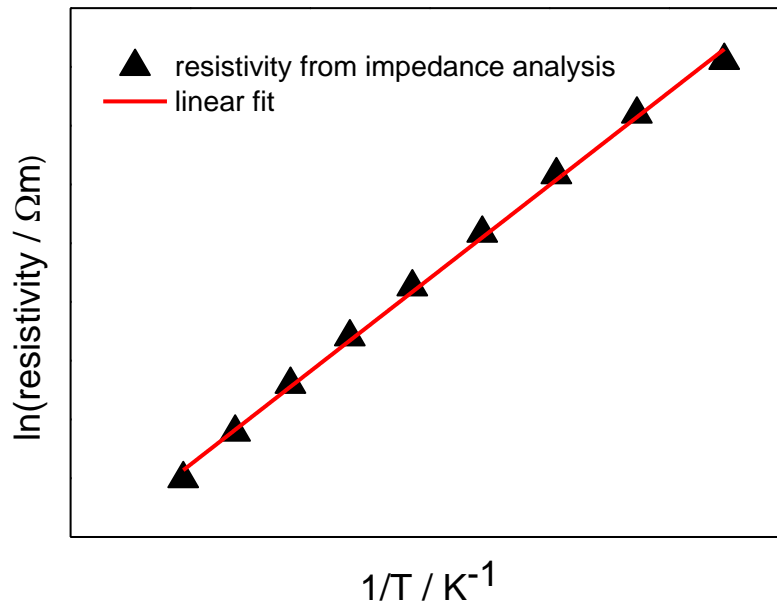
Figure 2.2.2.2   Exemplary Arrhenius plot, displaying the natural logarithm of the resistivity *vs*. the inverse temperature with indicated linear fit.

2.3. Lead-Free Piezoceramics

In this section promising lead-free piezoelectric ceramic materials are presented. Lead-free piezoelectrics are mandatory to make the processing, usage and disposal of the piezoelectric materials safer by eliminating the dangerous exposure to highly toxic lead right at the source. Beyond the scope of toxicity, lead-free materials were

additionally demonstrated to outperform lead-based materials in specific applications and are therefore viable candidates to be investigated in depth.

There are several variants of piezoelectric materials that do not contain lead. However, most of them, like for instance Rochelle salt, quartz or KH_2PO_4 play a merely historical or niche role and are furthermore not able to provide very high polarization or strain by their piezoelectrical response.

Layered structures [55-58], primarily being in commercial use for high temperature applications, represent more of a niche product. An example for that would be bismuth layer-structured ferroelectrics (BLSFs) with a very high $T_c > 800$ °C, putting BLSF type systems in a unique position for high temperature piezoelectric applications [59-62].

The long-known pure BT as well as BT-based systems all possess a high electromechanical coupling factor[59], *e.g.* in combination with calcium and zirconium in the system $BaCa_{(1-x)}Ti_xO_3 - BaZr_{(1-y)}Ti_yO_3$ (BCT-BZT)[63,64]. BT-based systems have been used as piezoceramic material before the discovery of PZT *e.g.* in sonar or hydrophone applications. However, the main use today is as MLCC followed by use as PCTR. This recess of commercial use can be seen as rooted in the major drawback of BT: a T_c of about 120°C, which is significantly lower than that of PZT and renders it inferior to PZT with respect to usable temperature range and additionally with respect to temperature stability.

The two most researched lead-free material classes to date are the alkali-niobate-based and sodium bismuth titanate-based systems, which are detailed in the following sub-sections. For further reading and minute details, several reviews, books and specific papers exist that describe lead-free piezoceramics [3,13,15-21,62,65].

Due to the manifold piezoelectric applications with different specific requirements and figure of merit (FOM), several lead-free alternatives are pursued in research. All those variants have certain advantages and disadvantages, such as operating temperature restrictions due to the material. This renders some materials useful in one application, whereas in other temperature regimes, different materials may excel. Table 2.3.1 gives an idea about the underlying key FOM that highlight the most important materials parameters with respect to certain applications and their operating temperature range.

Table 2.3.1 | Available Lead-Free Materials, Their Applications and FOM (following [5])

material	application(s)	approx. range of operation	FOM	ref.
layered (textured) BLSF and other layered structures	aerospace, aircraft, nuclear sensors	500 °C - 1500 °C	d_{33}, $k^2 \cdot Q_M$, $d \cdot g$	58,66-68
AT cut quartz	resonator	RT - 580 °C	Q_M, F_r- TC	5
KNN-based	ultrasonic/automotive/SMD sensor, fuel injection actuator, ultrasonic motor	RT -300 °C	$k^2 \cdot Q_M$	69
KNN-based	ultrasonic sensor, ultrasonic cleaner, transformer, motor	RT - 250°C	$k^2 \cdot Q_M$, v_{max}	69,70
KNN-based	microphone, buzzer, actuator	RT - 250°C	d_{33}, S_{max}/E_{max}, $d \cdot g$	71
BNT-based	ultrasonic sensor, ultrasonic cleaner, transformer, motor	RT - 200°C	$k^2 \cdot Q_M$, v_{max}	72,73
BNT-based	actuator	RT - 100°C	d_{33}, S_{max}/E_{max}	74-76
PVDF (polymer)	microphone, buzzer, actuator	RT - 170°C	d_{33}, S_{max}/E_{max}, $d \cdot g$	5
BT-based (BCT-BZT)	sensor / actuator	RT - 100°C	d_{33}, S_{max}/E_{max}	77,78

2.3.1. Alkali-Niobate-Based Ceramics

The system KNN and solid solutions thereof are a widely studied lead-free system that especially received strong attention after an investigation published by Saito et al. [3]. The publication created high interest in the material system and lead to extensive follow-up research, though the system itself has been known for about 50 years [79-81]. One reason that the material was not thoroughly investigated in the early years after the discovery is the complicated processing due to difficult sintering in a narrow window, making alkali-niobate systems harder to process than for instance BT [82]. But also the finding of PZT as a material, which is easier to process, can be seen as reason for the long delay of research interest in the material.

Forming solid solutions with other end-members, *e.g.* lithium niobate, enables easier processing, since lithium oxide is able to act as a sintering aid, creating a liquid phase during sintering. Figure 2.3.1.1 gives an idea about the range of compositions in the $KNbO_3$-$NaNbO_3$-$LiNbO_3$ (KN-NN-LN)-system, schematically sketched in grey, which could to date be obtained with reasonable densities and the piezoelectric properties could be assessed (in the other cases, the samples presumably will have been leaky).
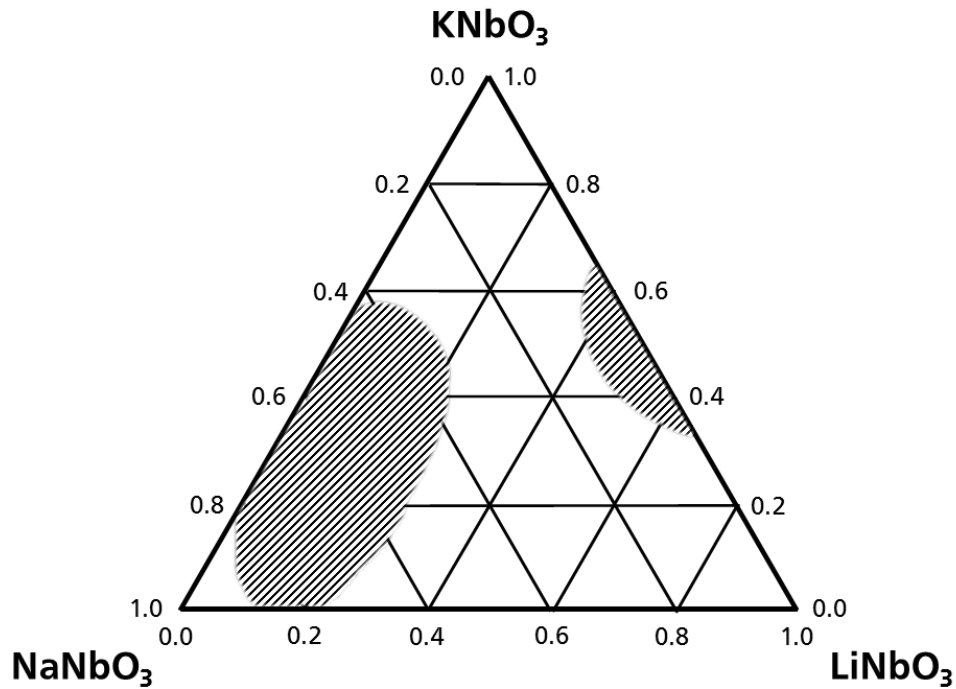
Figure 2.3.1.1   Compositions in the KN-NN-LN ternary system that were successfully sintered and it was possible to perform electrical measurements (the hatched areas represent the approximate regions, entailing reported compositions, detailed by S. Priya (ed.)[65]).
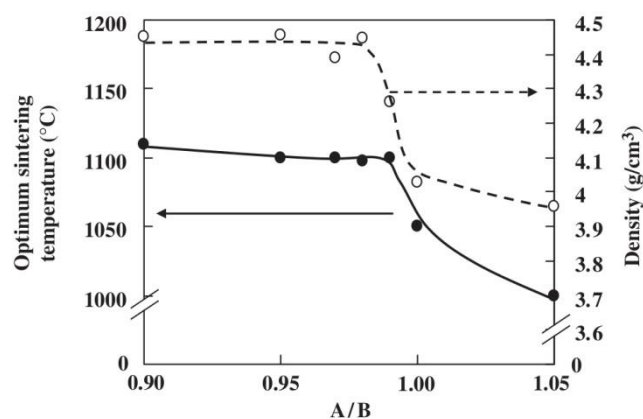
Figure 2.3.1.2   Influence of the A / B (K / Nb) ratio on absolute density and sintering temperature of the compositions (adapted from Matsubara *et al.* [70] and reprinted with permission, copyright © 2005, John Wiley and Sons, Inc.).

As Figure 2.3.1.2 illustrates: in addition to the narrow compositional ranges that are possible to process with moderate efforts, another factor that complicates the synthesis of ceramics in the KNN-system is that the A- and B-site ratio highly influences different sintering properties such as density and optimum sintering temperature. For increased A-site excess atoms, as well as for the stoichiometric composition, a drop in sintering temperature and density can be observed. In addition, the evaporation of alkali oxides and phase stability at high temperatures pose further challenges. The density was reported highest for B-site excess stoichiometry with a plateau for the observed compositional ratios at about 4.4 g/cm³.

If no countermeasures are employed, the difficulties in processing can lead to reduced density of the ceramics, thus weakened piezoelectrical properties. To prevent these phenomena, there are different means to control the sintering process. Firstly, it is possible to use methods such as hot(-isostatic) pressing [83], pulsed laser deposition [84] or spark plasma sintering [85-87] to compact the material. The overall achievable densification by hot pressing results in improved ceramics with 99.0 - 99.8 % relative density, exhibiting a coupling coefficient of 0.48 [88]. Those methods, however, are expensive and thus not suitable for a cost-efficient large scale production of alkali-niobate-based piezoelectric ceramics. Owing to this, secondary options to deal with those difficulties, namely sintering additives and off-stoichiometry-sintering (as Figure 2.3.1.2 already suggests), are being investigated, with a focus on the industrial applicability of these processes. Sintering aids have been used in the form of simple oxides *e.g.* CuO [89-92], Bi_2O_3 [93] or complex additives like $K_4Cu(Nb/Ta)_8O_{23}$ [70,94] and enable dense sintering without the need for hot pressing methods.

Another researched approach to alter the piezoelectric properties of KNN-based materials is to lower the orthorhombic to tetragonal phase transition, which occurs at about 200°C in pure KNN [95] close to room temperature. This has been achieved by introducing other elements into the system that lead to improved electromechanical response. However, this is obviously at the expense of a lower depolarization temperature, in addition accompanied by a strong dependency of piezoelectrical properties on the temperature. To avoid temperature dependent properties, it is possible to lower the transition temperature well below RT, for instance by adding calcium [96] or lithium and antimony [97,98] to the system. This ensures that there is no phase transition in the operational range of the piezoceramic element. Since key piezoelectric properties, such as d_{33} and $d_{33}*$, are decreased upon lowering of the phase transition below RT, this can be seen as a hardly avoidable trade-off between temperature stability and piezoelectric performance.

With respect to mechanical strength and fracture toughness, there are fewer studies. Those indicate mechanical strength and fracture toughness of alkali-niobate-based ceramic materials that are comparable to that of PZT ceramics [59,98].

2.3.2. Bismuth Sodium Titanate-Based Ceramics

In contrast to section 2.6.1, with a focus on the defect chemistry of BNT-based materials, this section is more focused on general piezoelectric features and mechanisms.

Bismuth sodium titanate (BNT) is a material, already known since 1960, after being discovered by Smolenskii *et al.* [99]. It has a perovskite structure with rhombohedral symmetry. BNT displays multiple phase transitions that are not clearly defined for the pure material. The phase transitions from rhombohedral to tetragonal T_{R-T} and subsequently to cubic T_{T-C} are approximately at 300°C and 540°C, respectively, for BNT single crystals [100]. Due to the breakdown of the ferroelectric order below T_c, leading to polarization loss way before T_c, the FOM for the very upper limit of the usable temperature range is the so called T_{f-r}. It indicates the transition from ferroelectric to relaxor state which does not coincide with T_c. For BNT solid solutions, a relationship between T_{R-T} and ionic radius was reported by Hiruma *et al.* [101]. They found, that the T_{R-T} decreases upon addition of all investigated A-site dopants but Pb^{2+}.

Due to a high coercive field (E_C) of approximately 7 kV/mm, a high field is required to pole the pure material without causing an electric breakdown, making investigations on pure BNT difficult. The high poling field can be circumvented by forming solid solutions with other end-members that change the piezoceramic properties and reduce the necessary poling field. Henceforth, binary systems as BNT-BT, BKT-BT, $Bi_{0.5}Na_{0.5}TiO_3$ -$SrTiO_3$ (BNT-ST) or BNKT or ternary systems as BNKT-BT, BNKT-KNN, BNKT-BZT or $Bi_{0.5}Na_{0.5}TiO_3$-$Bi_{0.5}Li_{0.5}TiO_3$-$Bi_{0.5}Li_{0.5}TiO_3$ (BNT-BLT-BKT) prevail current research and not pure BNT.
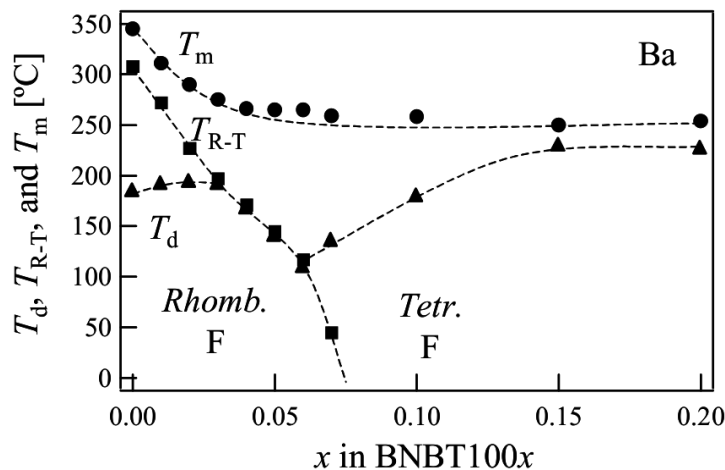
Figure 2.3.2.1   Phase diagram of BNT-BT close to the proposed MPB (adapted from Hiruma *et al.* [101] and reprinted with permission, copyright © 2007 Trans Tech Publications, Switzerland).

In the BNT-BT system, BNT-6BT is the most researched composition and displays an MPB between the rhombohedral phase at high BNT contents and the tetragonal phase at high BT contents, which entails BNT-6BT (*cf*. Figure 2.3.2.1). Above T_{f-r} a relaxor phase exists.

The poling history of BNT-based materials plays a non-negligible role, as can be seen in Figure 2.3.2.2. Transitions from relaxor to FE behavior are possible and were characterized as irreversible at high electric fields, for instance at BT concentrations of seven mol.% by Ma *et al.*[102]. This is accompanied by the evidence of monoclinic phases under field [103] above T_{f-r}.

Properties that can be obtained at the MPB are 125 pC/N, k_{33} =0.55 and a tanδ of 1.3 % as reported by Takenaka *et al.*[104]. This increase in aforementioned piezoelectric key figures is, however, at the expense of T_{f-r}, which is being reduced, and furthermore accompanied by a strongly curved MPB, which translates to high dependence of material properties on temperature. Processing-wise BNT-BT can be sintered at lower temperatures (1100-1200°C) than pure BNT, which adds the benefit of reduced evaporation of components during sintering. Compared to that, the far less investigated BKT-BT system exhibits inferior piezoelectric properties of d_{33} = 60 pC/N and k_{33} = 0.37, while the T_C of 290°C is in close proximity of the T_C of BNT-BT as reported by Hiruma *et al.* [105].

BNT-ST, first reported by Sakata *et al.* [106], allows for strains of 0.28 at 0.1 Hz, 6 kV/cm and a composition of BNT-28ST. At compositions below 26% ST, a rhombohedral perovskite structure was confirmed by X-ray diffraction (XRD); for ST-contents higher than 28%, the system was characterized as metrically cubic. BNT-ST was reported to reach a maximum d_{33} value of 127 pC/N at 24% ST, while above 28% ST no piezoelectric response was found.
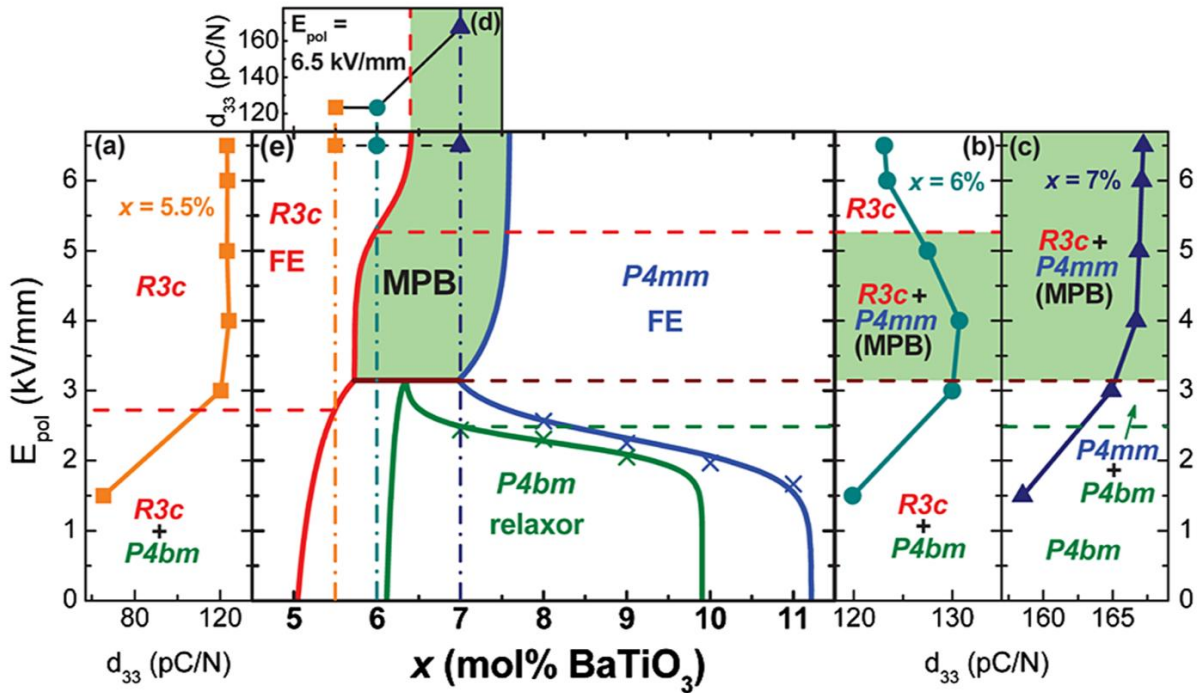
Figure 2.3.2.2 Multifigure with d_{33} at different E_{pol} for (a) x = 5.5%, (b) x = 6% and (c) x = 7% BT content. (d) displays the d_{33} as function of composition at E_{pol} = 6.5 kV/mm. (e) is the proposed phase diagram for (1-x)BNT-xBT (adapted from Ma *et al.*[102] and reprinted with permission, copyright © 2012 American Physical Society).

The system BNKT features a MPB with maximum d_{33} around BNT-20BKT (*cf.* Figure 2.3.2.3), as reported by several authors [23,27,107,108], which is widely investigated also in the single crystal state. Compared to KNN-based systems, the sintering process is rather well controlled and understood. On the one hand there is the classical oxide route, comprising oxide or carbonate starting materials, with sintering taking place at about 1100°C to 1200°C, leading to dense ceramics. Properties that can be realized by this synthesis are a d_{33} of 140 – 190 pC/N at a k_p of 0.27 to 0.35 in combination with a lowered T_d of 130-170°C, as for instance reported by Sasaki *et al.* [109] as well as other researchers [22,24,25,108,110]. On the other hand, different synthesis methods in order to produce bulk ceramics, single crystals, thin films and thick films and especially textured ceramics and films, have been investigated so far.

Single crystals were for instance produced by the flux method [111-114] or the top seed solution grown method [115-117] and yielded different properties, depending on composition as well as growing method. Pure BNKT single crystals were reported to exhibit d_{33} of 120 to 170 pC/N and a maximum strain of about 0.25% at a field of 8 kV/mm.
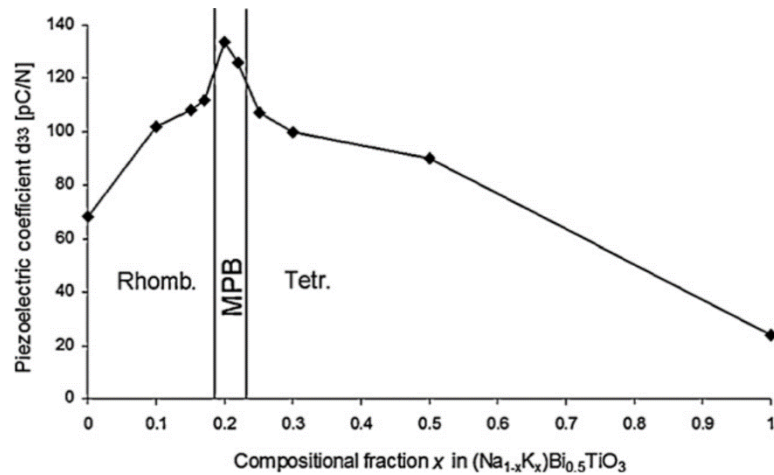
Figure 2.3.2.3 The MPB of BNKT illustrated with the example of piezoelectric constant d_{33} at RT *vs*. BNKT composition (adapted from Otoničar *et al.*[23] and reprinted with permission, copyright © 2009 Elsevier Ltd. All rights reserved).

For BNT > 0.8, BNKT compositions were found to exhibit rhombohedral symmetry and in addition display pseudo-rhombohedral octahedral distortions due to rotations and ion displacement. In the tetrahedral region with BNT < 0.8, only in-phase rotations are said to be present, however, as reported by Levin *et al.*, limited to the nano-scale.[26] Further it was concluded that no miniaturization of FE non-180° domains is present near the MPB.
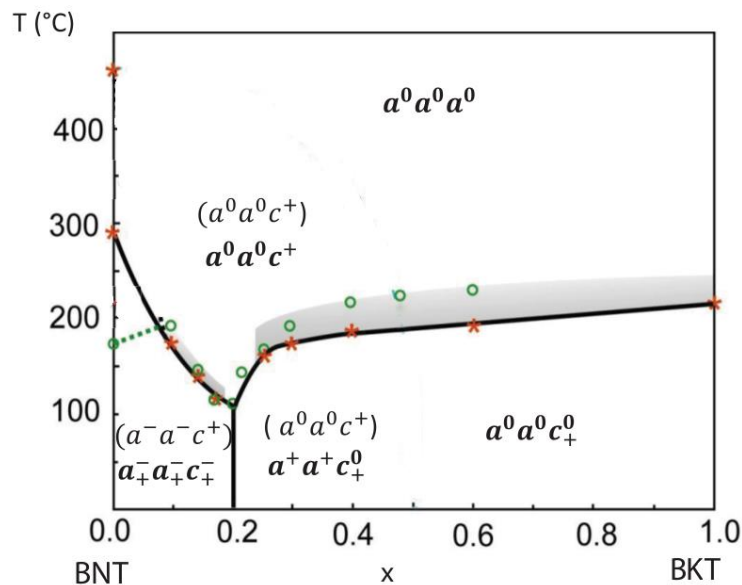
Figure 2.3.2.4 Phase diagram of the (1-x)BNT-xBKT system determined from XRD, TEM and dielectric measurements. Open green circles represent the temperatures of the FE anomaly derived from dielectric data, the solid black line corresponds to the transition data as seen in XRD data. Light grey areas display the transition width and the green dashed line indicates the FE transition below tilting. The tilting is indicated to a notation according to Stokes *et al*. [118] (adapted from Levin *et al*. [26] and reprinted with permission, copyright ©2013 American Physical Society).

For single crystals, piezoelectric properties can be dramatically improved by the introduction of BT. While in the ceramic material, one is able to obtain moderate strain increases by the addition of BT to the system, BNKT-BT single crystals feature very high strains of 0.87 and in addition were reported to feature a 0.7% jump in strain at a threshold of approximately 2 kV/mm [114].

It is possible to introduce relaxor-type behavior to BNKT at the MPB, by for instance adding $Bi_{1/2}Zn_{1/2}TiO_3$ (BZnT), which in this particular case induces relaxor behavior between 2 and 4 % BZnT content, as reported by Dittmer et $al.$ [119]. The relaxor behavior was reported to lead to an increased S_{max}/E_{max} of over 500 pm/V, which was attributed to the loss of remanent strain. Flattened permittivity curves in combination with a lower dielectric loss were found in the system. The authors see those effects as a result of mixed B-site occupancy through the introduction of Zn^{2+} rather than the influence of the end-member BZnT.

Patterson et $al.$ [120], working in the same ternary system but in the tetragonal region of the BNKT system at 40% BKT content, observed a secondary phase transition at lower concentrations (2.5%) of BZnT. This was said to be comparable to the transition occurring at the MPB of the pure BNKT system. Upon further addition of BZnT, flattening of the permittivity curves, maximum strain values of 0.33 and a S_{max}/E_{max} of 547 pm/V was reported. The evolving relaxor behavior upon addition of BZnT is comparable to the results presented by Dittmer et $al.$ at MPB-composition.

By employing B-site additives ($(Zr,Fe)_{1/2}Nb_{1/2}$, $Zn_{1/3}Nb_{2/3}$ and $Mg_{1/3}Nb_{2/3}$), containing Zn^{2+} and Mn^{2+}, which are also known to introduce relaxor-type behavior in PZT-based materials, Yamada et $al.$ found flattened permittivity behavior and decreased Curie temperatures for those materials. Those findings hint at the possibility of a phase transition shift towards lower temperatures, comparable to the findings of Dittmer et $al.$ and Patterson et $al.$. However, since they did not conduct piezoelectric measurements, no definite statement about these properties can be made.

Another widely researched ternary system is BNKT with the addition of niobium by means of the formal end-members KN [33] or KNN (of which the BNT-rich end is detailed in Figure 2.6.2.5).
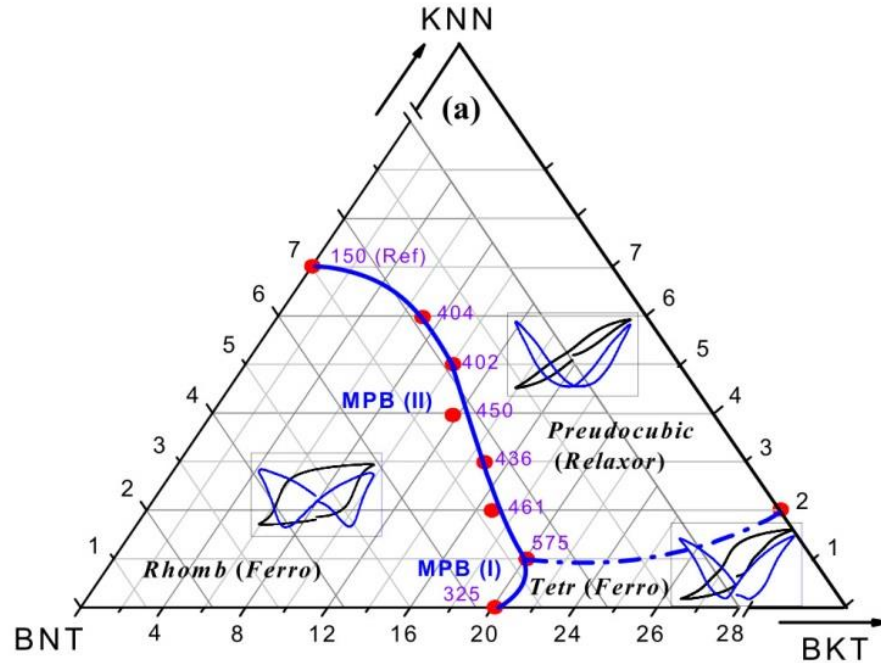
Figure 2.3.2.5 Phase diagram of BNKT-KNN, focusing on the MPB-region, which consists of pseudocubic relaxor phase, rhombohedral ferroelectric phase and tetragonal ferroelectric phase. The magnitude of the d_{33}* is displayed in purple at the respective composition, indicated by a red dot. (adapted from Hao *et al.* [121] and reprinted with permission, copyright ©2013 AIP Publishing LLC).

With respect to the temperature evolution of the piezoelectric properties, Seifert *et al.* [35], working in the same system, found a temperature insensitive behavior at sufficiently high KNN concentrations. They attributed this to the disrupted ferroelectric order and thereby introduced relaxor behavior of the material. This proposed mechanism is confirmed by work of Hao *et al.*[121], who performed *in-situ* high energy X-ray scattering experiments under external electric field and found a distortion from the pseudocubic structure at applied fields. The temperature insensitive behavior can already be found at addition of minor amounts of KNN to the BNKT system (*cf.* Figure 2.3.2.6), inducing a phase transition shift below room temperature. Textured ceramics of this type can be synthesized as demonstrated by for instance Gao *et al.* [122]
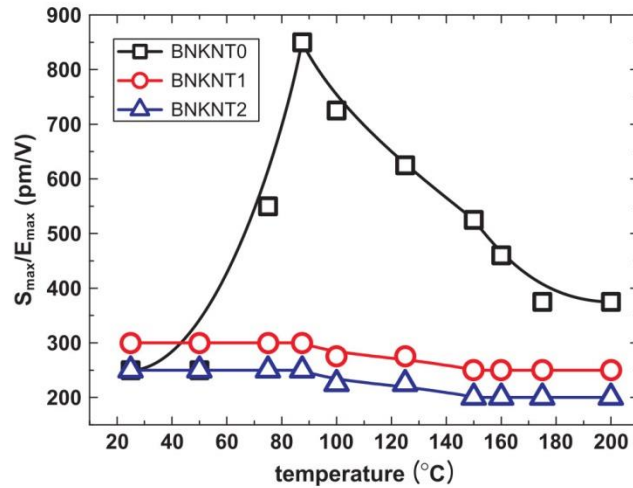
Figure 2.3.2.6 Dependence of S_{max}/E_{max} on the temperature for different BNKNT compositions of (1–x) (0.8BNT–0.2BKT)–x (0.97KNN–0.03BKT) (x= 0.01, 0.02 in mol%), exhibiting a strong correlation for BNKNT0 and temperature insensitive strain *vs.* temperature behavior for BNKNT1 and-2. (adapted from Seifert *et al.* [35] and reprinted with permission, copyright © 2010 The American Ceramic Society).

The introduction of lithium into the BNKT system, which was found to reduce the sintering temperature [39] and increase the planar mode electromechanical coupling factor up to 0.38 [123], influences the depolarization temperature. This in turn was found to exhibit a microstructural dependence on the employed lithium source, according to Lei *et al.* [124,125]. In contrast to most other end-members or additives, including BLT, higher T_c and T_{f-r} were found for excess doping of the BNKT system with Li_2CO_3 [40], while electric properties improved at the same time.

Manganese is mostly introduced to the BNKT system by excess doping and was found to decrease the final grain size of the ceramic through inhibited grain growth during sintering [126,127]. In addition a lowering of the leakage current upon manganese excess doping was studied by Wu *et al.* [128], which is also reported for the system BNKT-BT with manganese doping [42]. The increase in piezoelectrical properties in the reported cases is at the expense of T_{f-r}.

In the literature, several ways to introduce lanthanum into the BNKT system, such as the replacement of bismuth with lanthanum [129] or the excess doping of BNKT at the MPB [130] or close to the MPB in addition with strontium [131] as well as in the tetragonal region [132] are described. The obtainable d_{33} range from 153 to 215 pC/N. While this goes hand in hand with a significant decrease in T_{f-r} for most of the studied systems, the tetragonal BNKT starting composition with lanthanum excess doping was reported to exhibit a fairly high T_{f-r} of 219°C. The high T_{f-r} was attributed to a decrease in oxygen vacancies which also resulted in lower breakdown strength according to Yoshii *et al.* [132].

Ullah *et al.* [133-137] investigated several aspects of BiAlO$_3$ (BA) incorporation into the BNKT system. The generally observed effect that BA-addition leads to relaxor properties, finally resulting in a relaxor material at the MPB, as well as on both sides of the MPB, was attributed to the reduction of the ferroelectric order through cation disordering [138,139]. Since BNKT-BA possesses a low E$_c$, Su *et al.* [140] employed it as matrix material in combination with BNT seeds in order to improve the obtained strain to about 0.4 % by means of a composite approach.

For further details on particular dopants and additives to the BNKT system, tables 8.1 and 8.2 located in the appendix and the references contained therein can be consulted.

In conclusion, it can be said that there is a wide range of investigated end-members and combinations thereof as well as specific dopants for all lead-free systems.

For room temperature applications with low thermal fluctuations, BCT-BZT appears to be a promising member with excellent piezoelectric properties that can replace existing lead-based materials.

Offering higher operating temperatures, the alkali-niobate-based materials comprise low density, fairly high mechanical strength and high piezoelectric response. They, however, still lack a robust and reproducible synthesis process. One additional drawback from an economic standpoint is that the raw materials Nb$_2$O$_5$ and Ta$_2$O$_5$ are inflating the price of the ceramic products. Latest research suggests that for multilayer actuators (MLAs), the employed electrode can be nickel, allowing cutting costs versus silver palladium or platinum electrodes [141,142].

Bismuth sodium titanate-based ceramics in turn offer easier processing conditions and a wider operating range with respect to temperature, however, with to date lower obtainable d$_{33}$ than BCT-BZT systems or KNN-based systems. The additional T$_{f-r}$, which limits the operating temperature below T$_c$, still allows for higher operating temperatures than for instance BCT-BZT, but is not able to match the temperature range of KNN-based materials.

As a concluding remark, it can be said, that some of the above mentioned lead-free materials are already used in applications. However, the general trend for replacing lead-based materials is, that most probably more than one of the lead-free system presented in this section and possible even novel materials are needed for the varying application demands, as for instance temperature ranges or other FOM of piezoelectric materials.[5]

2.4. Defect Chemistry of Piezoelectric Materials

Co-doping in general can be described as the doping of materials with more than one foreign element. Using co-doping, one is able to influence mainly the defect chemistry of functional materials, which in turn governs mechanisms that can influence processing properties or parameters as well as characteristics of the final material. Doping of materials enables influencing defect complexes, complex associates, ionic transport, extrinsic electronic disorder, grain boundaries as well as extrinsic ionic disorder by introducing extrinsic nonstoichiometry into the material [143].

Dopant ions usually replace normal ions of the host compound lattice - a state which can be described as a solid solution. Interstitial dopants, situated in-between sites of normal ions of the host compound lattice, are known but uncommon for piezoceramics. In the field of piezoelectric ceramics, most of the doping takes place on the cationic lattice. However, few anionic replacements for oxygen with fluorine or nitrogen are reported in literature [144-151].
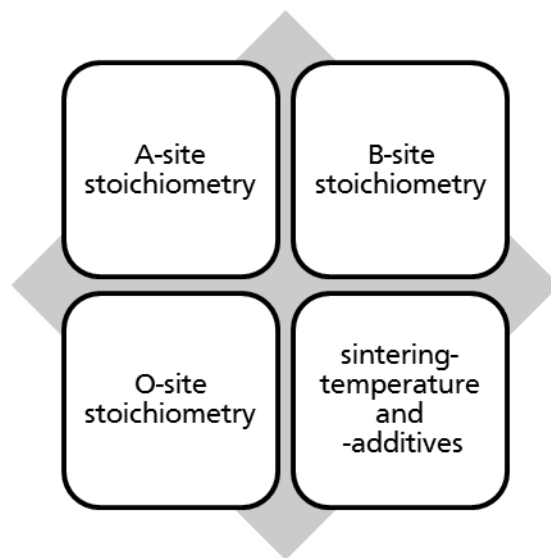
Figure 2.4.1 Schematic of key parameters influencing the defect chemistry of ABO_3-type perovskite materials.

Two types of strategies are commonly employed in chemical substitution doping of piezoceramics, one being the replacement of lattice site ions with other isovalent atoms, possessing a different effective ionic radius. The radial difference leads to a distorted environment near the doping site, which can make the structure less stable and improve the material's response to mechanical forces. This can for example be achieved by replacing Ba^{2+} with Sr^{2+} or Ti^{4+} with Zr^{4+}.

The second possibility is to replace normal lattice site ions with aliovalent ions, which have an ionic charge, different from the normal ion charge (see also Figure 2.4.1). This has a more pronounced effect on the defect chemistry of the material, due to

direct influence on electric charges in the material. The ionic charge of the foreign ion that replaces the ion of the normal lattice can be either higher than the charge of the latter one, which is then called donor doping or lower, resulting in so called acceptor doping. Examples are the replacement of Ti^{4+} with Fe^{3+} (acceptor doping) or replacing Ti^{4+} with Nb^{5+} (donor doping). This disturbance of the local charge balance leads to the creation of vacancies to restore the global electrical equilibrium. Aliovalent dopants and vacancies may form defect dipoles in the lattice, which is schematically represented in Figure 2.4.2.
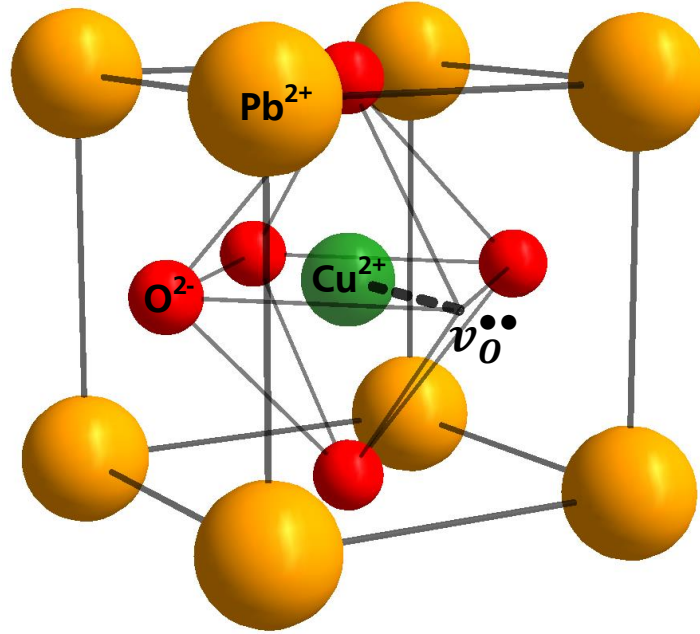
Figure 2.4.2 Schematic of a defect complex in the PbTiO$_3$ structure: Pb ions are situated on the perovskite A-site, Cu^{2+} replaces Ti^{4+} on the B-site. The dashed line represents the electrostatic force between the acceptor Cu^{2+} and an oxygen vacancy ($v_O^{\bullet\bullet}$). Not to scale.

BaTiO$_3$ (BT) allows for the whole spectrum of possibilities to influence piezoelectric properties. This is why hereinafter it is taken as exemplary piezoceramic material to discuss the interaction of defect chemistry with materials properties in detail.

Besides the oxygen vacancies $v_O^{\bullet\bullet}$ introduced by an environment with low oxygen activity

$$O_O^X \leftrightarrow \frac{1}{2} O_2 + v_O^{\bullet\bullet} + 2e'$$ (2.4.1)

and cation vacancies that may occur on the Ti-site of the system through BaO excess

$$BaO \rightarrow Ba_{Ba}^X + v_{Ti}'''' + O_O^X + 2v_O^{\bullet\bullet}$$ (2.4.2)
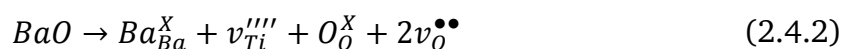
or on the Ba-site, caused by Ti excess

$$TiO_2 \rightarrow V''_{Ba} + Ti^X_{Ti} + 2O^X_O + v^{\bullet\bullet}_O \quad , \tag{2.4.3}$$
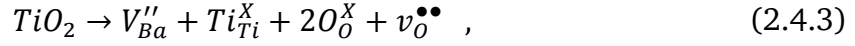
acceptor doping with for instance Fe_2O_3 creates both iron on titanium places and oxygen vacancies

$$2BaO + Fe_2O_3 \rightarrow 2Ba^X_{Ba} + 2Fe'_{Ti} + 5O^X_O + v^{\bullet\bullet}_O \quad , \tag{2.4.4}$$
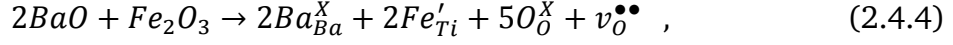
which form upon incorporation into the lattice. Acceptor doping in the case of $BaTiO_3$ is possible with A-site ions that have a lower ionic charge of $+1$ like *e.g.* K^+ and Na^+, B-ions that have an ionic charge lower than that of Ti, such as Fe^{3+} or Al^{3+} or by introducing N^{3-} into the oxygen site [152].

Acceptor dopants and oxygen vacancies can form so called defect dipoles, which are indicated in brackets with the overall charge indicated (*e.g.* $(Ti^{3+\prime} - v^{\bullet\bullet}_O)^\bullet$). Those defect dipoles influence the conduction properties by resulting in different charge compensation: for Ba/Ti = 0.99, this is mainly by electrons and for Ba/Ti = 1.01, it is dominated by titanium vacancies [48]. The electron charge compensation mechanism in BT-based materials is in contrast to for instance PZT-based materials or other lead-free materials, where (A-site) vacancy charge compensation predominates.

In turn, donor doping of $BaTiO_3$ can be achieved by introducing A-site ions with a higher ionic charge ($>+2$) as for instance La^{3+}, B-ions with an ionic charge higher than $+4$,*e.g.* Nb^{5+}, or doping with fluorine, leading to F^- ions on the oxygen site.

Interstitial doping is uncommon for ferroelectric perovskite materials with B_2O_3 doping of $BaTiO_3$ being an exception, which creates the following defect chemistry:

$$B_2O_3 \rightarrow 2B^{\bullet\bullet\bullet}_i + 3O^X_O + 3v''_{Ba} \quad , \tag{2.4.5}$$
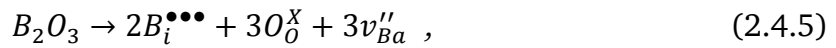
where interstitial boron ($B^{\bullet\bullet\bullet}_i$) leads to an expansion of the crystal lattice. Since interstitial doping is mostly restricted to boron in perovskite piezoceramics, it will not be considered in the following sections.

Through those doping strategies, grain boundaries of the ceramics can be influenced. An example is donor doping of $BaTiO_3$ with large amounts of Nb under specific synthesis conditions. In this case, Nb will predominantly reside in the grains and not the grain boundary: the grain boundaries possess relatively more acceptor states. This leads to a pair of symmetric Schottky barriers (*cf.* Figure 2.4.3), creating an energy barrier along grain boundaries, which in turn may cause a very high electrical resistivity with pronounced temperature dependency, depending on how many acceptor states are introduced into the grain boundary.[153] The resulting positive

temperature coefficient resistance (PTCR) effect exists because the concentration of Schottky defects itself has a strong temperature dependency.
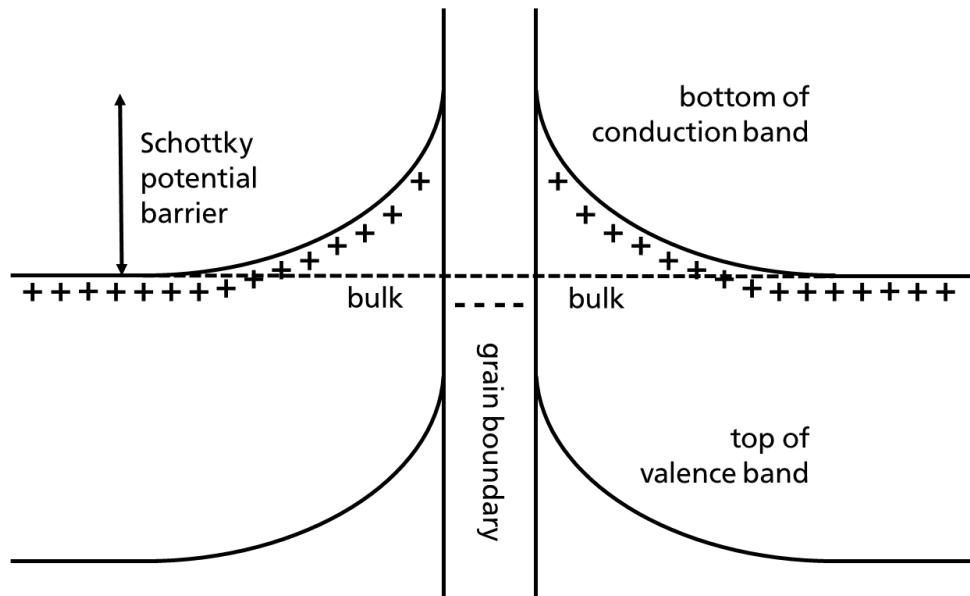
Figure 2.4.3 Schematic of double Schottky barrier: left and right hand side: grains, creating the barrier and increasing the resistance of the overall material.

Another ferroelectric feature that can be influenced by doping is the domain wall. Domains themselves are regions with dipoles aligned in the same direction. The number of possible domain orientations per ideal single crystal, all having the same energy, depends on the type of crystal lattice. For $BaTiO_3$ it is six. Since in a large crystal many domains are coexisting, so called domain walls, which can be interpreted as defective structures, can be found in piezoelectric materials. These create a stress gradient that will strongly interact with other defects described in this section.[154]
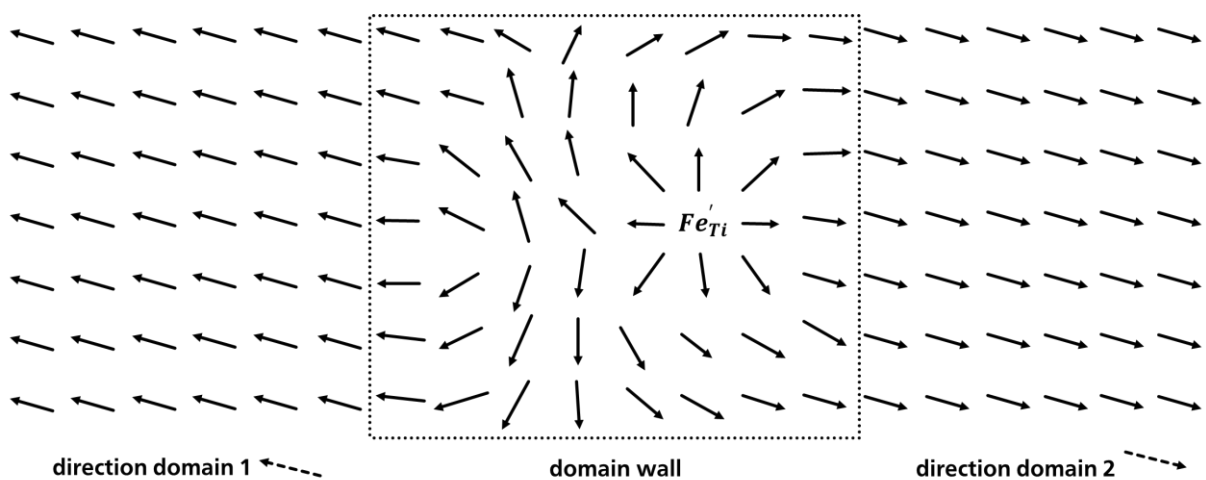
Figure 2.4.4 Simplified sketch of dipole (arrows) alignment with respect to an exemplary Fe'_{Ti} defect and the pinned surrounding domain wall, indicated by the dotted box.

Since aliovalent dopants are charged defect centers in the material, they will influence the alignment of the polarization of neighboring dipoles and thereby the location of domain walls. In addition, they reduce the mobility of domain walls (*cf*. Figure 2.4.4). In PZT and BT-based materials, this occurs to such an extent that aged samples will display a so called internal bias field (E_i).[155] This field is a result of domain pinning, which means that after a given time, the dipoles permanently align with respect to (preferentially) charged defect centers (*cf*. Figure 2.4.5).[156] This is for instance possible by means of oxygen vacancy hopping to align the dipolar moment with the internal field.
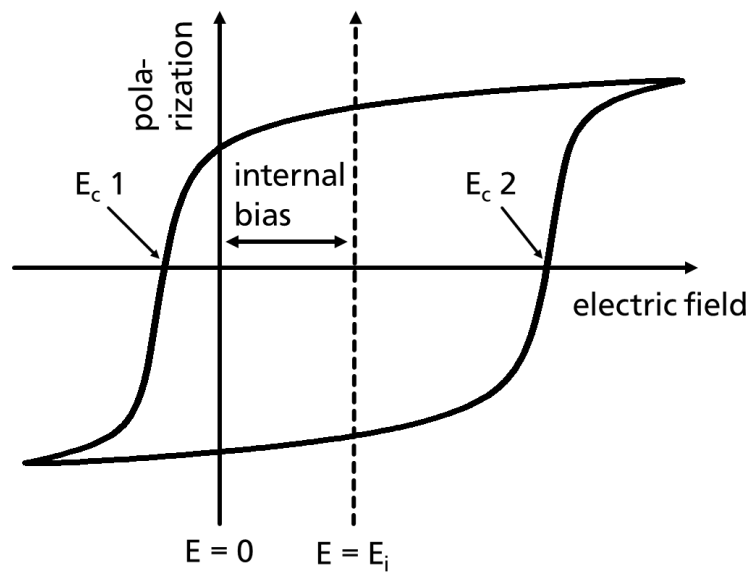
Figure 2.4.5 Schematic of FE polarization *vs*. electric field loop, displaying an internal bias field, different coercive fields (E_c 1 and E_c 2) and the characteristic offset electric field of the FE loop.

Depending on the dopants, different piezoelectric characteristics of the material can be obtained. In the case that few charged defects (vacancies or aliovalent dopants) are present in the ceramic, the domain walls can move largely uninfluenced and therefore no high energy barrier from internal fields needs to be overcome to reorient the domains.

Such materials will display low coercive fields in combination with low remanent polarization (*cf*. Figure 2.4.6(a)). Materials with these characteristics are commonly called "soft" piezoelectric. As pinning will reduce the domain wall mobility due to discussed stabilization effect, doping that creates locally charged defect species in the ceramics will lead to higher coercive fields and higher remanent polarization (*cf*. Figure 2.4.6(b)). This is commonly called "hard" piezoelectric behavior.
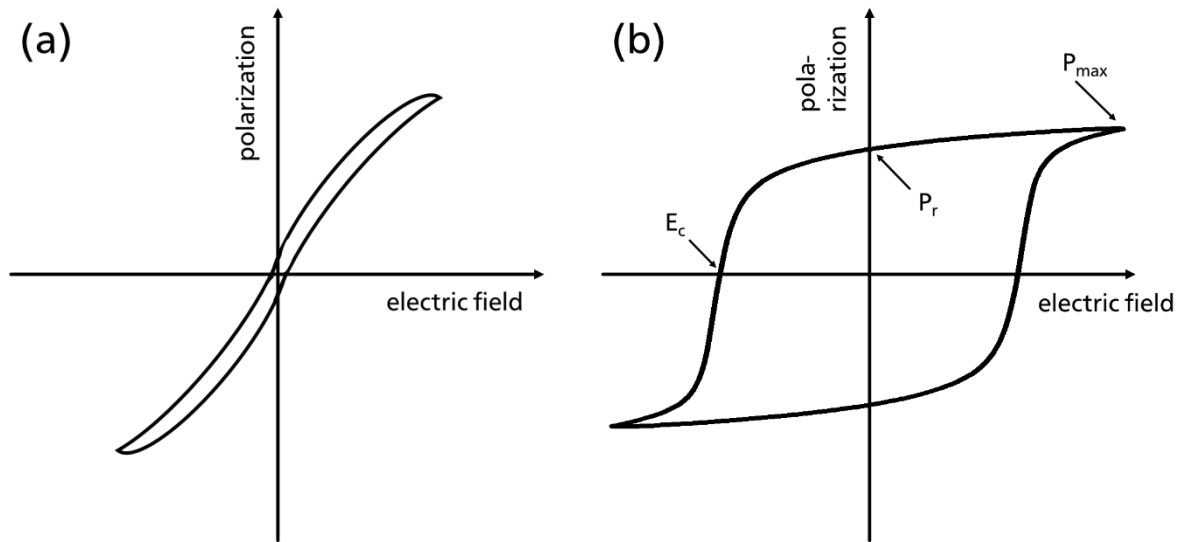
Figure 2.4.6 Schematic of FE polarization *vs*. electric field loops of (a) characteristic "soft" material with very low E_c and P_r and (b) a "hard" material with pronounced E_c and high P_r.

A very thorough study of the defect chemistry of PZT with an incorporation of 1 mole-% A-site donor dopant La^{3+} and 0.5 mole-% B-site acceptor dopant Fe^{3+} by Erdem *et al* [157], addresses the question, by which mechanism co-doping - in contrast to pure acceptor doping with Fe^{3+} - influences ageing and other ferroelectric properties of the material. Therefore, they studied co-doped PZT by means of multifrequency EPR spectroscopy, which was also employed for purely acceptor doped PZT compositions in other studies. This yielded mixed results: for Fe^{3+} doped PT and PZT compositions [158] defect dipoles could be observed by the technique, but not in the case of for instance acceptor centers as Cr^{3+} or Cu^{2+} [159,160]. Investigations on other rare earth A-site donor ions *e.g.* gadolinium [161] lead to similar results.
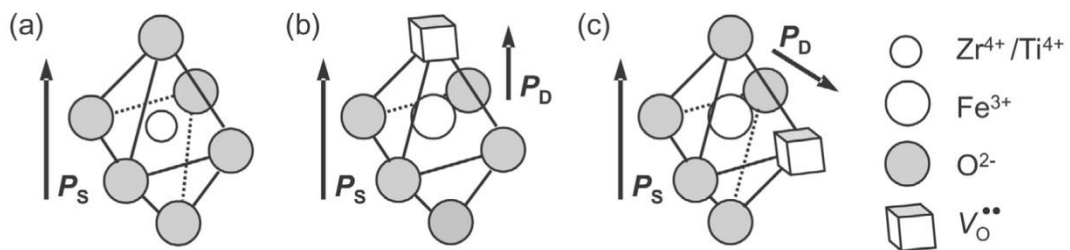
Figure 2.4.7 Schematic of defect dipole orientation for (a) pure PZT, (b) PZT with a $(Fe'_{Ti} - v_O^{\bullet\bullet})$ defect dipole oriented along the c-axis and (c) the same dipole oriented in the crystallographic a-b-plane (adapted from Erdem *et al.* [157] and reprinted with permission, copyright © 2011 IEEE).

With EPR spectroscopy they revealed, that $Fe'_{Ti,Zr}$ is displaced in opposite direction of the neighboring oxygen vacancy $v_O^{\bullet\bullet}$, whereby the defect dipole moment was measured to be increased, owing to the longer distance in-between the two defects in the dipole $(Fe'_{Ti,Zr} - v_O^{\bullet\bullet})^{\bullet}$. Furthermore, they speculate that this defect dipole is favored over a complete local charge compensation, as known for instance for co-

doping with Fe^{3+} and the A-site donor dopant La^{3+}. Figure 2.4.7 sketches the proposed model, in which a reorientation of the defect dipole is occurring upon exposure to an electric field or mechanical stress, which is believed to be realized by spontaneous diffusion of $v_O^{\bullet\bullet}$ about the center atom of the octahedron.

Generally speaking – thus moving back from the specific example of $BaTiO_3$ and PZT – the intentional introduction of defects into a normally ordered crystal structure through doping is believed to move the system further away from the energetically stable state, thereby lowering energetic barriers for the ferroelectric switching of the materials, which results in higher piezoelectric properties. This is important for applications, because it enables the tuning of characteristic features as *e.g.* the conductivity by influencing the defect chemistry of the final product, thus allowing for specific tailoring of desired properties.

In the following sub-sections, relevant commercial systems are being described with respect to how important material properties can be fine-tuned by introducing the right defect chemistry through chemical co-doping, with a specific focus on BNT-based systems in section 2.6.

2.5. Co-Doping of Lead-Based and BaTiO₃-Based Piezoceramics

As detailed in the previous section, doping can have a profound effect on the defect chemistry and thereby on piezoelectric and electric properties of ceramics. In many commercial piezoelectric ceramics (for instance PIC151 or PIC181 by PI Ceramic GmbH, Lederhose, Germany), co-doping with more than one aliovalent dopant simultaneously is employed to create defect dipoles in the material and to control domain wall mobility, Schottky barriers and influence the oxygen vacancy concentration in order to tailor piezoelectric and electric properties.

2.5.1. Co-Doping $BaTiO_3$ and $BaTiO_3$-Based Systems

$BaTiO_3$ is a material in practical use for longer than 60 years, not only because of its piezoelectric properties, but also due to applications as capacitor, utilizing the dielectric features of the material [162]. Above its Curie temperature (130°C) it forms a cubic perovskite and is paraelectric (PE). At any temperature below that, $BaTiO_3$ exhibits ferroelectric behavior. Undoped $BaTiO_3$ displays an excess of acceptor impurities, behaving like a semi-conductor with a band gap of ~3.1 eV and resistivity in the range of 10^{10} Ωcm [163]. Doped and co-doped $BaTiO_3$ ceramics are used as capacitors, piezoelectric devices, as well as semiconductors and thermistors [164], the largest market being multilayer ceramic capacitors (MLCCs) and PTCRs. Due to the

long history as well as high volume of research and publications, the functional and defect properties of $BaTiO_3$ are fairly well understood.

The intrinsic defect chemistry of pure $BaTiO_3$ is mainly dominated by the formation of full Schottky defects:

$$Ti^X_{Ti} + Ba^X_{Ba} + O^X_O \rightarrow v''_{Ba} + v''''_{Ti} + 3v^{\bullet\bullet}_O \qquad (2.5.1.1)$$
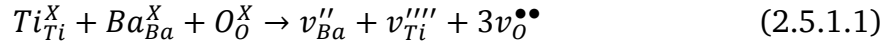
which are energetically favored over following Frenkel disorders

$$O^X_O \rightarrow O''_i + v^{\bullet\bullet}_O \qquad (2.5.1.2)$$

$$Ba^X_{Ba} \rightarrow v''_{Ba} + Ba^{\bullet\bullet}_i \qquad (2.5.1.3)$$

$$Ti^X_{Ti} \rightarrow v''''_{Ti} + Ti^{\bullet\bullet\bullet\bullet}_i \qquad (2.5.1.4)$$
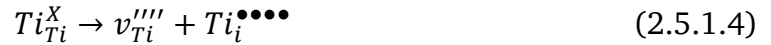
with energies being 2.29 eV per defect for the formation of a complete Schottky defect and 4.49, 5.94 and 7.57 eV per defect for the formation of an oxygen, barium and titanium Frenkel defect, respectively [165]. This correlates well with the fact that interstitial doping in $BaTiO_3$ is very uncommon.

Co-doping solely on the A-site was undertaken by for instance Wu *et al.* [166], introducing potassium and lanthanum into the perovskite crystal lattice. $K_{0.043}La_{0.007}Ba_{0.95}TiO_3$, which corresponds with an acceptor-dominant composition, exhibits a dielectric peak comparable to pure $BaTiO_3$, whereas the composition with donor-dominant behavior ($K_{0.007}La_{0.043}Ba_{0.95}TiO_3$) exhibited large broadening of the dielectric peak combined with a shift to lower temperatures (*cf.* Figure 2.5.1.1).

Structurally, an increased tetragonality was reported for an increasing K/La ratio. The highest piezoelectric d_{33} value of 160 pC/N was reported for the acceptor-dominated composition. Karaki *et al.* [167] in contrast to starting from pure $BaTiO_3$, worked on the effects of Bi_2O_3 and Li_2O as additives to already Mn-doped $BaTiO_3$ piezoelectric ceramics, finding an impact of the dopants on E_c, which rose from 120 to 500V/mm, while d_{33} decreased from 400 to 200 pC/N, maintaining a coupling factor in planar direction (k_p) of ~0.36, which was said to be beneficial for applications in ultrasonic imaging.
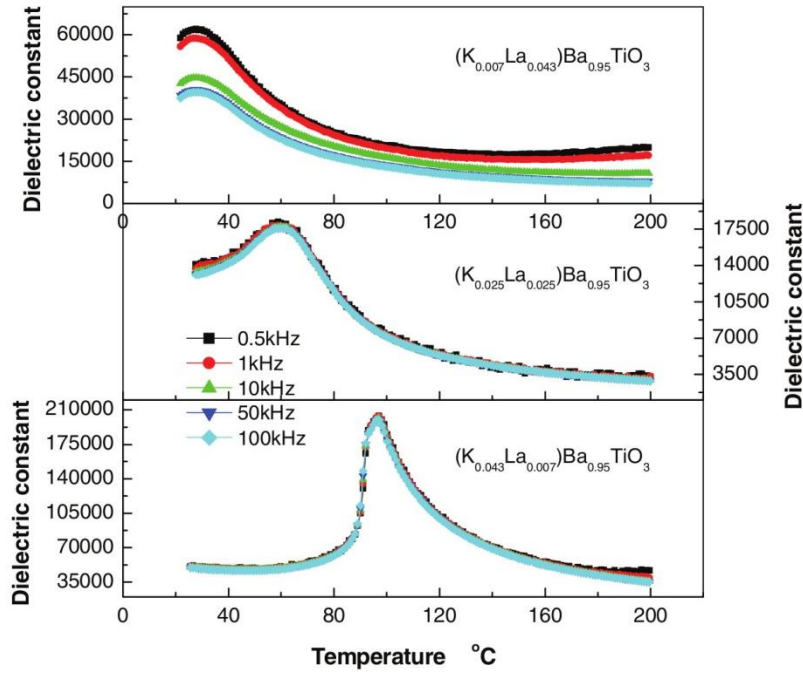
Figure 2.5.1.1   Dielectric constant *vs.* temperature for different La/K-ratios upon heating (adapted from Wu *et al.* [166] and reprinted, copyright © 2012 Taylor & Francis).

Assuming perfectly homogeneous distribution of defects throughout the material [168] does not suffice to explain the (piezo-)electrical behavior of BaTiO$_3$ grain boundaries after (co-)doping. According to Chiang *et al.* [169], acceptor segregation in company with the absence of donor segregation lead to solute segregation. They were unable to find a point of zero potential between acceptor and donor doped solid solutions, which they attributed to a marked preference of the BaTiO$_3$ grain boundary for Ti-ion adsorption. The sign of the space-charge potential of those grain boundaries was reported to be unaltered by even large amounts of solute dopants. This finding is comparable to the excessive donor doping of BaTiO$_3$, described in section 2.4, which results in PTCR behavior.

Co-doping of BaTiO$_3$ is majorly reported for two possible types of doping: firstly A-site donor- with B-site acceptor doping and secondly acceptor- in combination with donor doping both on the A-site of the lattice.

Shihua *et al.* [170] and Ting *et al.* [164] both report on the co-doping with lanthanum and manganese, both having a different perspective. Ting *et al.* went into detail on the defect chemistry of the material, measuring resistivity and complex impedance. They found that charge compensation of the dopants can be described by

$$2Mn_{Ti}'' + e' = La_{Ba}^\bullet h^\bullet. \tag{2.5.1.5}$$
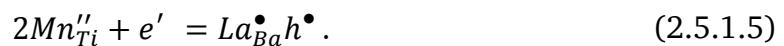
Additionally, they find an increased grain boundary resistance, that they attributed to the formation of cation vacancies, v_{Ba}'' or v_{Ti}''''. However, they did not report on the

piezoelectric behavior of the material. Shihua *et al.* generally reported decreasing piezoelectric properties upon higher lanthanum content, which they attributed to the charged defects v''_{Ba} or v''''_{Ti} that were said to give rise to random electric fields, which in turn was claimed to influence the broadening of the dielectric transition peak of the co-doped ceramics. Another study on co-doping with lanthanum as A-site donor and cerium as B-site isovalent ion was conducted by Lu *et al.* [171], indicating a solid solution and relaxor-type behavior for the incorporation of Ce^{4+} on the B-site.

Other trivalent ions such as Dy^{3+} or Y^{3+} [162,172-174] were used as A-site donor dopant in combination with B-site acceptor doping with Mn^{3+} or Mg^{2+}. For those dopant combinations in $BaTiO_3$, a core-shell structure in the grain boundary is proposed to be the origin of the influence on temperature dependent properties. They provided further insight into the co-doping mechanisms, but unfortunately no piezoelectric characterization was performed. Niobium in combination with cobalt in a BT-BNT system allows for a higher T_c and, as Hsiang *et al.* [175] point out, induces domain wall pinning in the ceramics.

2.5.2. Co-Doping of PZT and PZT-Based Systems

For PZT, several different dopants were tested and characterized. As in the case of $BaTiO_3$, the defect chemistry of PZT is rather well understood. In general, PZT-based systems, acceptor doping on the A-site (*e.g.* Li^+, K^+ or Na^+) and/or acceptor doping on the B-site (*e.g.* Al^{3+}, $Mn^{2+/3+}$, Mg^{2+}) causes a defect chemistry, being for instance

$$Al_2O_3 \rightarrow 2Al'_{Ti,Zr} + v_O^{\bullet\bullet} + 3O_O^X \qquad (2.5.2.1)$$

$$K_2O \rightarrow 2K'_{Pb} + v_O^{\bullet\bullet} + O_O^X \qquad (2.5.2.2)$$
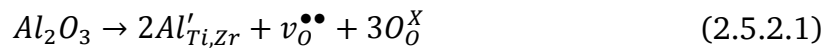
for B- and A-site substitution, respectively. This leads to an increase in oxygen vacancies in the PZT lattice. Acceptor doped PZT compositions are generally reported to exhibit pronounced ferroelectric ageing [176], since those formed oxygen vacancies may reorient by for instance hopping and thereby stabilize internal electric fields in the ceramic.

Donor doping on A-site (*e.g.* rare earth $^{3+}$) and B-site (*e.g.* Nb^{5+}, Ta^{5+}), in turn leads to cationic A-site or cationic B-site vacancies, for instance through introducing niobium or lanthanum:

$$Nb_2O_5 + PbO \rightarrow 2Nb^{\bullet}_{Ti,Zr} + v''_{Pb} + 6O_O^X \qquad (2.5.2.3)$$

$$La_2O_3 + 3TiO_2 \rightarrow 2La_{Pb}^{\bullet} + v_{Pb}'' + 3Ti_{Ti}^X + 9O_O^X \tag{2.5.2.4}$$
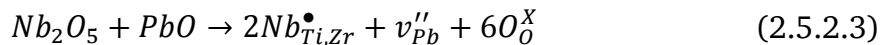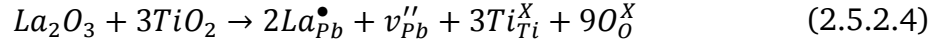
which both create lead vacancies and are reported to reduce oxygen vacancies inside the PZT crystal lattice [177]. In contrast to doped BaTiO$_3$ based materials, ionic, but not electronic charge compensation, prevails. The exact mechanism of how this induces piezoelectric softening is not fully understood to date and still being up for discussion. One explanation, supported by different publications [178,179], is that immobile defect dipoles (in the reported case: $Nb_{Ti,Zr}^{\bullet} - v_{Pb}''$) with immobility near room temperature destabilize the domain order by random fields. This in turn was found to lower the stability of the domain structure against external fields, thus causing the piezoelectric softening [177,180,181]. The beneficial effect of this is often-times improved fatigue behavior [59] with respect to ferroelectric properties such as S$_{max}$, P$_{max}$ or permittivity.

One widely used and described co-doping pair for PZT is manganese as acceptor dopant and fluorine as donor dopant. Manganese is situated on the B lattice site and is able to assume different oxidation states Mn^{2+}, Mn^{3+} or Mn^{4+}, which coexist in the PZT lattice, with $Mn^{4+} \cong Mn^{2+} \ll Mn^{3+}$, and are able to reduce the local space charges by changing the respective oxidation state [182]. Due to its acceptor nature, it introduces more oxygen vacancies to the system:

$$Mn_2O_3 \rightarrow 2Mn_{Ti,Zr}' + v_O^{\bullet\bullet} + 3O_O^X \tag{2.5.2.5}$$
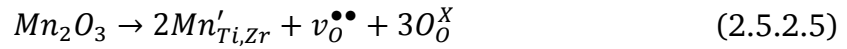
thereby pinning domain walls and leading to hard piezoelectric behavior [183]. The introduction of fluorine as a donor dopant is reported to – in contrast to donor doping on the A- or B-site – not lead to additional lead vacancies, but to compensate oxygen vacancies by introducing F$^-$ into the anion lattice

$$PbF_2 + v_O^{\bullet\bullet} \rightarrow Pb_{Pb}^X + 2F_O^{\bullet} \tag{2.5.2.6}$$

thereby not only reducing the conductivity in the case of manganese co-doped samples [184], but also possibly forming defect dipoles

$$F_O^{\bullet} + Mn_{Ti,Zr}' \rightarrow (F_O^{\bullet} + Mn_{Ti,Zr}') \tag{2.5.2.7}$$
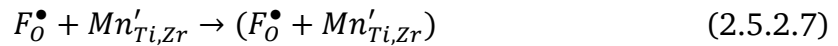
that are less mobile than the otherwise formed dipoles ($v_{Pb}'' - v_O^{\bullet\bullet}$). In a study by Guiffard et $al.$ [182] on fluorine doping in combination with various other cations, high piezoelectric properties (d$_{33}$ of >300 pC/N, Q$_m$ ~1000) and good cycling behavior [185] were reported for those compositions. Figure 2.5.2.1 exemplifies the piezoelectric response of four out of five investigated different co-doping systems.
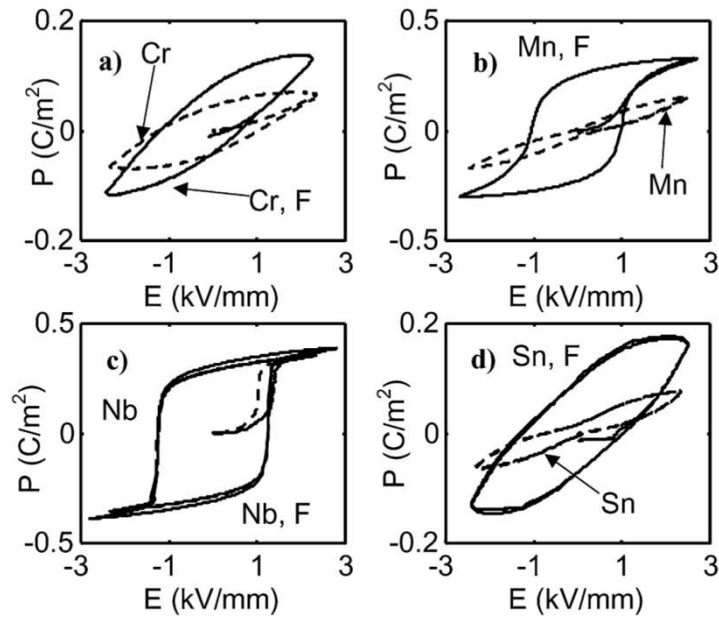
Figure 2.5.2.1 Bipolar P-E loops of aged and unpoled (a) Cr, (b) Mn, (c) Nb and (d) Sn doped PZT-based materials, single element doped (dashed lines) and co-doped with fluorine (solid lines) (reprinted from Guiffard *et al.* [182], copyright © 2012 Taylor & Francis).

They compared manganese-fluorine with magnesium-fluorine co-doping and found that the dependence of defect dipoles on the fluorine content only holds true for manganese-fluorine co-doping. For magnesium doped PZT, mentioned fluorine co-doping and in addition B-site niobium co-doping, did not influence the oxygen vacancy concentration.

Recent works by Nguyen *et al.* [186] and Detalle *et al.* [185], who focused on the system $PbTi_{(1-x)}Zr_xO_3$-$Ba_{(1-x)}Sr_xTiO_3$ (PZT-BST), suggest that this is also valid in the case where additional isovalent dopants are present in the system. They report the same hardening effect as for the addition of manganese only and also address it to the increased presence of oxygen vacancies. Upon magnesium and fluorine co-doping, it was found that above three at.% of fluorine content, the dielectric properties increased, correlating with a donor behavior below this threshold, specific to fluorine compared to other donor dopants *e.g.* niobium. For thin film applications this threshold is reported lower at about 1.5 at.% fluorine. They point out that especially with respect to long-term stability, manganese and fluorine co-doping is able to create solid solutions which allow for both hard piezoelectric responses and long-term stability. Boucher *et al.* [187] report on how to optimize the system by adjusting the Ti/Zr ratio.

Introducing B-site donors into the PZT-Mn system, different behavior than in the case of fluorine doping below mentioned threshold can be seen. Though reducing the maximum overall strain Park *et al.* [188] were able to obtain a material by niobium and manganese co-doping, that is nearly temperature-independent in a range of -30 – 50°C and reported mechanical quality factors Q_M of ~300 and ~450, while k_p remains high

with values > 0.6. Their proposed and discussed mechanism is attributed to domain pinning by manganese, which is said to compensate the Nb_2O_5 donor doping effects, such as a lowered Q_M, lowered Q_E and lower density.

Cheon *et al.*°[189] in contrast introduced two B-site acceptor dopants into a $Pb_{(1-x)}Sr_xZrO_3$-$Pb_{(1-x)}Sr_xTiO_3$ (PSZT) system at the same time, that are both known to improve the ageing behavior of PZT solid solutions. Besides manganese, chromium was taken as a second additive, however, not drastically changing the resulting material properties compared to simple chromium doping.
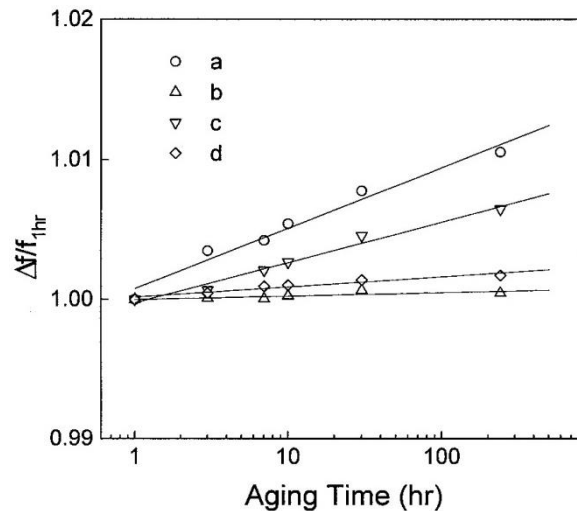
Figure 2.5.2.2   Ageing of the resonance frequency of (a) undoped, (b) Cr-doped, (c) Mn-doped and (d) Mn-Cr co-doped PSZT (adapted from C. I. Cheon *et al.* [189] and reprinted with permission, copyright © 1999, Kluwer Academic Publishers).

Concerning ageing they found that the material responds very similar to solely chromium doped PSZT with respect to the resonance frequency of the material (*cf.* Figure 2.5.2.2), the piezoelectric figures ε_r and Q_M of the co-doped material being 1004 and 505, respectively. Gao *et al.* [190] report on another pair of acceptor co-dopants: Zn^{2+} on the B-site and Li^+ on the A-site, finding high d_{33} values of 397 pC/N for 1 wt.% ZnO/Li_2O additions, but in contrast to Cheon *et al.*, they observe a significantly lower Q_m of ~150 for this composition.

Instead of using acceptor-acceptor co-doping combinations, in a more application oriented publication, Bourim *et al.* [191] employed the donor-donor co-doping pairs lanthanum and niobium as A-/B-site co-dopants in a PZT composition with excess lead. The applications they focus on are microcantilevers and microbridged actuators, which were found to benefit from the higher resistivity and fast domain switching due to easy domain reorientation of the co-doped material.

An enhancement of the fatigue properties of PZT by co-doping with manganese as acceptor and lanthanum as a donor was reported by Shi *et al.* [192]. Shi *et al.* used a metal organic deposition method to prepare thin films of the material, focusing on fatigue of the remanent and saturated polarization, which they found to be reduced

by about 18% after 10^8 cycles, less than otherwise reported in the literature at the time.
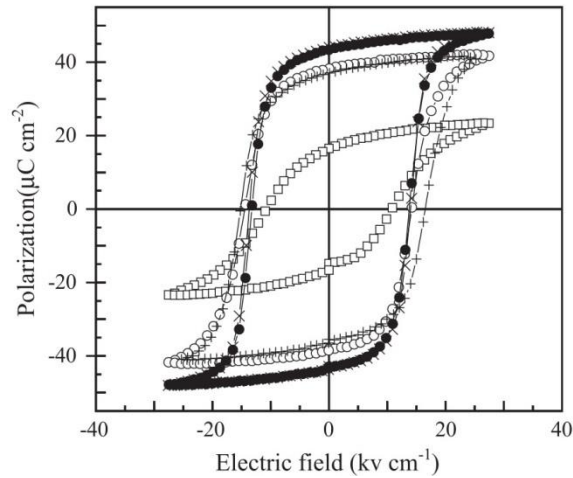
Figure 2.5.2.3 Bipolar P-E looks of PZT with □: x=0.0; ○: x=0.01; ●: x=0.015; ×: x=0.02 and +: x=0.025 (adapted from Zhang *et al.* [193] and reprinted with permission, copyright © 2003 Elsevier B.V. All rights reserved.).

Zhang *et al* [193] find an increase in the piezoelectric response for yttrium and niobium co-doped materials (*cf.* Figure 2.5.2.3), in addition with a decreased grain size of the resulting ceramic. The defect chemistry of this A-site donor, B-site acceptor material was not discussed in detail.

2.5.3. Summary of Mechanisms in Lead- and BaTiO$_3$-Based Ceramics

Co-doping is employed for all commercially relevant piezoelectric ceramics, because this approach influences material properties positively that are important in industrial applications. By co-doping it was proven possible to even enhance properties, which are considered contradictory, if solely doped with a single foreign element. The majority of co-doping pairs is an acceptor-donor combination, be it A-site-B-site, A-site-A-site or rarely B-site-B-site co-doping, though donor-donor and acceptor-acceptor combinations on different lattice sites of the perovskite system are also reported.

Important mechanisms and concepts for the understanding of co-doping in piezoelectric ceramics are: I. the increase of resistivity through Schottky barriers in grain boundaries, II. the concept of domain wall pinning/mobility and III. the concept of defect dipoles and their electrically/mechanically introduced reorientation through oxygen vacancy hopping.

Isovalent additives as Sr^{2+} or Ca^{2+}, in general have less influence on mechanisms related to the defect chemistry and are usually added in high amounts ($\gg$ 1 at.%) to form solid solutions as end-member.

2.6. Literature on (Co-)-Doping of BNT-Based Systems

2.6.1. BNT

For single dopants, such as for instance manganese [194], as reported by Eichel *et al.* [195], a detailed description of the underlying mechanisms and the chemical surrounding of the dopant also with respect to occurring oxygen vacancies and defect dipoles is provided. The general observations of the defect chemistry of the material that also holds true for the commercial piezoceramics. Namely that acceptor doping leads to an increase in oxygen vacancies, *e.g.* by

$$A_2O_3 \rightarrow 2A'_{Ti} + v_O^{\bullet\bullet} + 3O_O^X \tag{2.6.1.1}$$

$$A_2O \rightarrow 2A'_{Bi,Na} + v_O^{\bullet\bullet} + O_O^X \tag{2.6.1.2}$$

for B-site and A-site acceptor doping with a dopant "A", respectively. Donor doping with low amounts reduces oxygen vacancies and higher amounts furthermore lead to A-site or sometimes B-site vacancies,

$$4D_2O_5 + Bi_2O_3 + Na_2O \rightarrow 8D_{Ti}^{\bullet} + 2v_{Bi}''' + 2v_{Na}' + 24O_O^X \tag{2.6.1.3}$$

$$2D_2O_3 + 6TiO_2 \rightarrow 2D_{Bi}^X + 2D_{Na}^{\bullet\bullet} + v_{Bi}''' + v_{Na}' + 6Ti_{Ti}^X + 18O_O^X \tag{2.6.1.4}$$
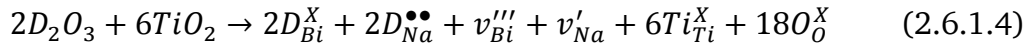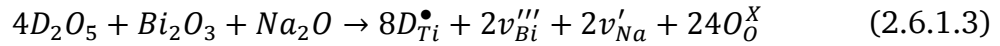
in case of B-site and A-site donor doping with a dopant "D", respectively. This is also known for single element substituted BNT-based materials. These A-site vacancies, created upon introduction of A- and B-site donor dopants [196], are reported to increase the destabilization of ferroelectric order.

The major difference in B-site doping of BNT-BT-based systems compared to PZT is the negative effect on T_d, a phenomenon not, or not as strongly, observed in PZT systems, which for instance Sung *et al.* [197,198] compared by taking a look at doping with several B-site ions (*cf.* Tables 2.6.1.1 and 2.6.1.2). The general observation, widely valid for A-site and B-site doping, as also stated by Rödel *et al.* [15], is that doping or substitution in larger amounts usually leads to improved piezoelectric properties at room temperature, however "mostly at the expense of a decrease in T_d or vice versa" [15]. Additionally, the reduced oxygen vacancy concentration caused by donor doping results in lowered electrical conductivity [199].

Table 2.6.1.1 | Effect of Different B-Site Dopants on Different Materials Properties (adapted from Sung *et al.* [197])

	isovalent (undoped BNT)	donor doping			acceptor doping	
	Ti^{4+}	Nb^{5+}	Ta^{5+}	W^{6+}	Mn^{3+}	Sc^{3+}
ionic radius / Å	0.605	0.64	0.64	0.60	0.645	0.745
phase purity / mol.%	yes	1.0	0.8	0.4	2.0	0.8
grain size / µm	~20	~2	~5	~5	>20	~15
d_{33} / pC/N	74	87	84	84	66	77
k_p	0.17	0.17	-	0.16	0.13	0.16
Q_M	320	160	202	180	369	269
ε	324	↑	-	↑	-	-
tanδ	0.02	↑	-	-	↓	↑
T_d / °C	190	129	-	-	167	-
E_c @ 60 Hz / kV/mm	~4.1	~2.4	~1.8	~2.0	-	-
P_r @60 Hz / µC/cm²	~35	-	-	~40	-	-

Table 2.6.1.2 | Comparison of the Effect of Different B-Site Dopants on Materials Properties on BNT and PZT (adapted from Sung *et al.* [197]; the PZT trends are from Jaffe *et al.* [59]).

	donor doping		acceptor doping	
	PZT	BNT	PZT	BNT
d_{33}	↑	↑	↓	↓
k_p	↑	-	↓	↓
Q_M	↓	↓	↑	↑
ε	↑	↑	↓	-
tanδ	↑	↑	↓	↓
T_c or T_d	-	↓	-	↓
E_c	↓	↓	↑	-
P_r	↓	-	↑	-

The influence of doping on d_{33}-values of BNT-ceramics was reported to be comparable to PZT, namely an increase of d_{33} through B-site donor doping in contrast to a decrease in d_{33} through acceptor B-site doping. Mechanistically, Sung *et al.* attributed

this to the ability of domain walls to move. The A-site vacancies introduced by B –site donor doping are said to have led to an improved domain alignment during poling, which explains the higher d_{33}-values. This mobility is lowered due to domain wall pinning by oxygen vacancies, which consequently results in a lower d_{33}. The oxygen vacancies are in turn introduced by B-site acceptor doping. The lower d_{33} is said to be able to overcome by forming $v_O^{\bullet\bullet}$ defect dipoles with a lower mobility.

Chen *et al.* [200] and Kim *et al.* [201] both report on the addition of lithium acceptor and niobium donor doping of BNT with different concentrations of lithium and niobium. Increasing d_{33} and decreasing T_d were found. However, the additions are in the range of mole-%, not qualifying for the range of co-doping, but rather presenting forms of novel solid solution systems such as the widely reported and investigated BNT-BT [202-205], $Bi_{0.5}Na_{0.5}TiO_3$-$K_{(1-x)}Na_xNbO_3$ BNT-KNN [35,206], BNT-BT-KNN [207-211] or BNKT systems (*cf.* section 2.6.2 for BNKT). There are plenty of other reports on the introduction of more than one element to BNT [212-220], where researchers add very high amounts of substituents, which at least can give hints at different trends of substitution effects with multiple ions.

Co-doping of pure BNT with 0 – 2.5 at.% of dopants was carried out by Danwittayakul *et al.* [221], using iron B-site doping in combination with lanthanum A-site doping, leading to increased d_{33} and higher resistivity of the material. In contrast to that, Mahboob *et al.* [222] introduced equimolar amounts of niobium and neodymium into the material, finding a different conduction mechanism, depending on the amount of dopants added. Impedance spectroscopic investigations revealed a short range translational electron hopping mechanism between Ti^{4+}-Ti^{3+} and Nb^{5+}-Nb^{3+} in the low frequency region and a high frequency reorientation mechanism through the rotation of $(Ti^{3+\prime} - v_O^{\bullet\bullet})$ or $(Nb^{3+\prime} - v_O^{\bullet\bullet})$. Singh *et al.* [223] used the BNT-KNN-system as a basis to dope it with three other ions, namely lithium, tantalum and antimony, achieving high strains of 0.4%, in combination with a T_d of 110°C.

2.6.2. BNKT-Based Systems

The system BNKT that is in focus in this work, is widely reported and described in literature concerning chemistry [224,225], microstructure [226-237], atomic-structure [238-240], electromechanical properties [23,24,107,108,241-249], the influence of temperature on those properties [22,110,250,251] and processing of the system [252,253]. Despite this high general interest, little attention has been paid to the defect chemistry that can be tailored by co-doping, as already elaborated in the case of PZT- or BT-based materials.

It has to be noted that most of the reported multi-element additions make use of isovalent additives in combination with one donor or acceptor if at all. Few publications deal with combined acceptor-donor co-doping combinations.

Three of them utilize lithium acceptor doping on the A-site [254-256] in combination with another donor element, which provides larger grains in the ceramics, an increase in T_d in one case and strain increased up to 0.45%. The enhanced properties in those materials are usually attributed to a destabilization of the ferroelectric order. The large strain of the materials is generally achieved by doping the material to such an extent that a relaxor material is created.

Do *et al.* [257] were able to reduce the sintering temperature to 975°C by introducing copper and niobium to the system. Niobium was chosen to compensate for the created oxygen vacancies of the copper excess doping. Another report on lanthanum A-site substitution in combination with aluminum substitution [258] also reports a high piezoelectrical strain of about 0.4%. However, they put no emphasis on defect chemical investigation.

General trends that can be extracted from this literature data are the mentioned tendency of the BNT system to mostly display an inverse relation between T_d and d_{33}, which holds true apart from the exceptions lithium, manganese and erbium. In addition, one can say that the achievable d_{33} or d_{33}^* -values are in the same range for the published BNKT morphotropic phase boundary (MPB) [259] compositions. Apart from those publications on MPB- materials, some reports investigate BNKT at the composition $Bi_{0.5}Na_{0.25}K_{0.25}TiO_3$, making use of the significantly higher depolarization temperature of this base composition. Tables 8.1 and 8.2 in the appendix provide detailed overview over manifold reports on single and multiple element doping/substitution in the BNKT system and their general influence on piezoelectric and thermoelectric properties, thus corroborating mentioned trends.

3. Experimental

3.1. Introduction

The following section details the experimental procedures of this work, entailing everything from the synthesis of the powders to electrical characterization, diffraction studies or complex impedance spectroscopy and EPR. Unless otherwise stated, the outlined experimental details of all employed methods and equipment apply to every produced and characterized sample.

3.2. Employed Methods and Equipment

3.2.1. Ceramic Synthesis and Further Processing of Samples

$Bi_{0.5}(Na_{0.9}K_{0.1})_{0.5}Ti_{(1-x-y)}Cu_xV_yO_3$ ceramics (hereinafter designated as BNKT10:100xCu,100yV), $Bi_{0.5}(Na_{0.8}K_{0.2})_{0.5}Ti_{(1-x-y)}Cu_xV_yO_3$ (hereinafter designated as BNKT20:100xCu,100yV) and $Bi_{0.5}(Na_{0.7}K_{0.3})_{0.5}Ti_{(1-x-y)}Cu_xV_yO_3$ (hereinafter designated as BNKT30:100xCu,100yV), all with stoichiometric V doping ($x = 0$; $y = 0.01$ and 0.005), Cu doping ($x = 0.005$, 0.0005 and 0.0001; $y = 0$) as well as with Cu and V (co-)doping ($x = 0.004$, 0.003, 0.002, 0.001; $y = 0.005-x$) were synthesized. All ceramics were produced by conventional solid state synthesis (*cf.* Figure 3.2.1.1 for an overview), using Bi_2O_3 (99.975%), Na_2CO_3 (99.5%), K_2CO_3 (99.0%), CuO (99.7%), V_2O_5 (99.2%) and TiO_2 (99.6%) all from Alfa Aesar (Karlsruhe, Germany).

In order to avoid water uptake of starting powders, hygroscopic K_2CO_3 was weighed (BP61s, Sartorius AG, Göttingen, Germany, ± 0.1 mg accuracy) in a glove-box in argon atmosphere (< 10 ppm O_2, < 5 ppm H_2O). Na_2CO_3 was kept at 110°C in a drying oven and transferred to a desiccator to cool down to RT for subsequent weighing. All powders were weighed with ± 0.1 mg accuracy according to their stoichiometric formula and wet milled in ethanol, in custom-made polyamide containers; utilizing 300 g 3.0 mm yttria toughened ZrO_2 milling balls for 30 g powder and milling for 12 hours at 250 RPM (Pulverisette 5, Fritsch, Idar-Oberstein, Germany).

Following drying took place for more than 24 hours in a ventilated oven at 90 °C. The dried powder was then mortared manually in an agate mortar and transferred to alumina crucibles. The compositions were calcined in ambient atmosphere at 800 °C, 850°C or 900 °C with a heating rate of 5 K/min and a dwell time of 5 hours (L9/KM, Nabertherm GmbH, Lilienthal, Germany). Obtained, calcined powders were transferred to a polyamide container and milled as described above.

Subsequent to drying the slurries at 90 °C for more than 24 hours, the dry powders were mortared and the particles were separated manually with a polyamide mesh sieve, having 160 μm sieve openings (LINKER Industrie-Technik GmbH, Kassel, Germany). The fine grains were further pressed uniaxially with 5 kN into disks of 10-15 mm diameter, or bar-shaped pellets of 5 mm times 5 mm times 35 mm for neutron diffraction samples. Then they were placed in a latex sheath, evacuated and closed, followed by cold isostatic pressing at 350 MPa in oil (KIP 100E, Paul-Otto Weber GmbH, Remshalden, Germany). Sintering took place at temperatures between 1080 °C and 1150 °C (L16/14 Nabertherm GmbH, Lilienthal, Germany) in closed alumina crucibles, while the samples were placed in a powder bed of the respective calcined sample composition in order to reduce the evaporation of volatile species.

Powder Processing
- milling mixed oxides/carbonates, 250 RPM, 12 hours in ethanol
- drying at 90 °C >24 hours and mortaring
- calcining, 800 - 900 °C, 5 K/min, 5 h
- milling calcined powder, 250 RPM, 12 hours in ethanol
- drying at 90 °C >24 hours, mortaring and manual sieving

Greenbody Forming
- uniaxial pressing (hand press)
- sealing of pellets
- cold isostatic pressing at 350 mPa

Sintering
- 1080 -1150 °C, 5 K/min, 2-3 h
- ambient atmosphere
- furnace cooling

Finishing
- grinding samples close to final shape
- polishing samples
- application of silver electrode for electrical measurements

Figure 3.2.1.1 Schematic of the ceramic processing route from raw starting powders to the final, sintered and shaped sample.

Sintered ceramics were ground and polished to a thickness less than 1/10 of their diameter in the case of round samples (WEILER Werkzeugmaschinen GmbH,

Emskirchen/Mausdorf, Germany). In all cases at least 150 μm of the surface layer was removed to minimize surface effects. For scanning electron microscope (SEM) investigations the samples were fine polished with diamond pastes (DP Paste on polishing cloth DP-DUR, STRUERS GmbH, Willich, Germany) starting from 15 μm down to a final diamond particle size of 0.25 μm. In addition prior to SEM investigation, they were thermally etched at 1000 °C for 10 minutes, with a heating ramp of 5 K/min in air (L16/14 Nabertherm GmbH, Lilienthal, Germany) to allow for the observation of individual grains. For electrical characterization, silver paste (C60704D8, Gwent, Pontypool, United Kingdom) was fired onto both top and bottom sides of the cylindrical disc samples and on opposing sides of the bars in air at 400 °C for 2 h.

3.2.2. X-Ray Diffraction

XRD (D8 Advance, Bruker, Karlsruhe, Germany with Bragg–Brentano Θ/2Θ geometry) was carried out on both calcined powders and sintered, ground samples. For each unique calcined and sintered composition, one XRD pattern was acquired for every employed sintering temperature. An energy dispersive Si(Li) detector was used in combination with Cu- Kα radiation as source of λ = 1.5406 Å X-rays. Diffractograms were measured from 10° up to 90° 2Θ with a step size of 0.03° 2Θ using a rotating sample holder. Resulting unit cell parameters were calculated from the lattice parameters, determined from peak positions from the pattern. They were further used to determine the theoretical density as described in following section 3.2.3 *via* the respective cell volume. X-ray diffraction patterns were acquired by Jean-Christophe Jaud at the Technische Universität Darmstadt, Darmstadt, Germany.

3.2.3. Density of Sintered Ceramics

The ceramic density and open porosity of ground samples was determined according to the Archimedes method. Before the measurement, samples were submerged in a vial filled with deionized water and exposed to a vacuum of < 50 mbar (Vacuubrand RD8, Vacuubrand GmbH & Co. KG, Wertheim, Germany) for at least 15 minutes to remove enclosed air from open pores, while a subsequent waiting period of 20 minutes ensured a RT water temperature of the vials. Deionized water was taken as immersion liquid and the sample weight of the wet samples in water ($\boldsymbol{m_{wet,H_2O}}$) as well as the weight of the wet samples in air after careful removal of water on the surface without removing water in open pores ($\boldsymbol{m_{wet,air}}$) was determined (BA110s, Sartorius AG, Göttingen, Germany, ± 0.1 mg accuracy). The water temperature during immersion was determined with an accuracy of 0.1 K to obtain the density of water from literature. The samples were then dried over night at 90 °C to then determine

the weight of the dry samples in air ($m_{dry,air}$). Next, the density was calculated according to:

$$\rho_{Archimedes} = \frac{m_{dry,air} \cdot \rho_{H_2O}}{m_{wet,air} - m_{wet,H_2O}} \quad .$$ (3.2.3.1)

The precision of the method is estimated as ± 0.2 %.

The theoretical density of the sintered ceramics can be calculated with following equation:

$$\rho_{theo} = \frac{Z_u \cdot m_a}{V_{unit}} \quad ,$$ (3.2.3.2)

where Z_u is the number (respectively fraction) of formula units per unit cell for the sample composition, m_a the atomic mass of the respective atoms and (V_{unit}) is the volume of the unit cell as determined from lattice constants, calculated from XRD patterns. The resulting relative theoretical density (ρ_{rel}) can then be expressed by

$$\rho_{rel} = \frac{\rho_{Archimedes}}{\rho_{theo}} \quad ,$$ (3.2.3.3)

utilizing results from equations 3.2.3.1 and 3.2.3.2.

3.2.4. SEM Measurements and Grain Size Determination

The sintered, fine polished and thermally etched (*cf.* section 3.2.1) SEM samples were fixed on conductive carbon tape (G3348, Plano GmbH, Wetzlar, Germany), sputtered with gold/palladium (Sputter Coater SCD 050, Balzers; now Oerlikon Leybold Vacuum, Köln, Germany) applying 40 mA for 40 seconds and later connected to the carbon tape with conductive silver glue (G3691, Plano GmbH, Wetzlar, Germany) in order to avoid charging of the samples by primary electrons. At least five secondary electron (SE) and one backscattered electron (BSE) SEM images were taken (Philips XL30FEG, Philips, Amsterdam, Netherlands) for individual compositions.

For further grain size distribution analysis, the SE images were digitally processed, using the software *ImageJ* 1.48v, identifying grains with aspect ratios from 0.23 to 0.77 and grain areas of 0.1 μm² to 100 μm². The total area analyzed was about 2×10^{-3} mm² and consisted of a combination of at least five images of different sample locations, selected from different regions. For plotting the histograms of the grain diameter, the number of grains in a diameter range of 250 nm (n_{range}) was counted from 0 to 7 μm. This was compared to the total number of grains, identified for all analyzed ranges (n_{total}).

3.2.5. Electrical Large Signal Measurements
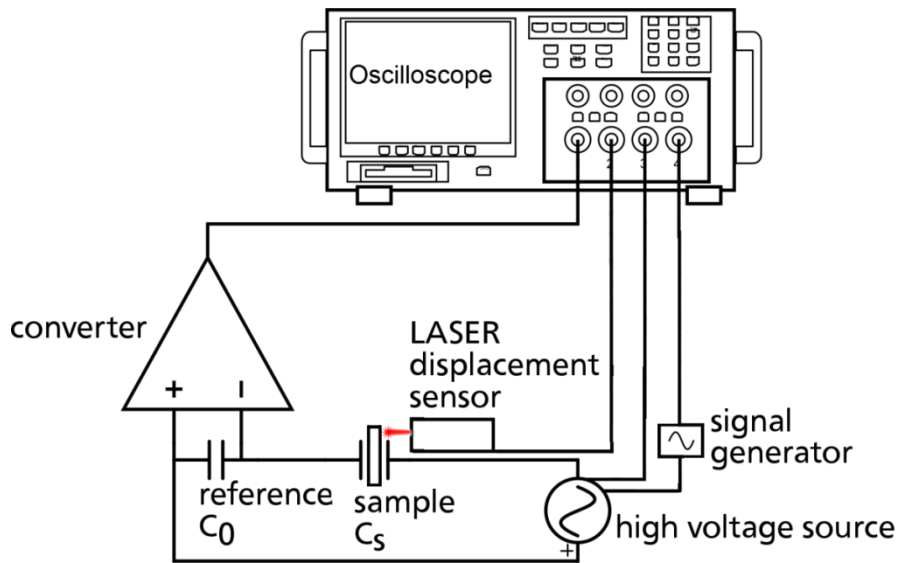
Figure 3.2.5.1   Schematic of a modified Sawyer-Tower circuit with LASER and light sensor for strain determination.

In order to determine the crucial parameters strain and polarization under applied electric field and thereby obtain the characteristic FE hystereses, a modified Sawyer-Tower setup was employed, as sketched in Fig. 3.2.5.1. All samples were measured by using an equilateral triangular wave function with a frequency of one Hz (Agilent 33220A arbitrary waveform generator, Agilent Technologies, Inc., Santa Clara, CA, USA) with further amplification of output voltage to the respective maximum field between 1 and 8 kV/mm (TREK 20/20C High Voltage Power Amplifier, TREK, INC., Lockport, NY, USA). For measuring bipolar properties, the samples were exposed to at least two cycles, each consisting of a negative and a positive triangular wave; unipolar measurements comprised the use of at least two triangular waves in one field direction only (either positive or negative electric field). The strain of the material was determined by optical means (Philtec, Inc., Model D63-A1+H+LNPQ, Annapolis, USA). Samples were immersed in silicone oil (AK 35 or AK 200 Silicone Fluid, WACKER CHEMIE AG, München, Germany) to prevent the electric breakdown occurring in air. If not otherwise stated, all samples were measured with a reference capacitance (C_0) of 10 μF. All signals (displacement sensor, converted capacitance, generated triangular signal and amplified signal) were analyzed with an oscilloscope (Agilent Infiniti Vision MSO7014B, Agilent Technologies, Inc., Santa Clara, CA, USA). The polarization of the sample (P_S) was calculated by

$$P_S = \frac{C_0 \cdot V_0}{A_s} \quad ,$$

<div align="right">(3.2.5.1)</div>

where V_0 is the applied (amplified) electric voltage and A_s is the top/bottom electrode area of the cylindrical ceramic samples. The measurements were carried out, testing at least two samples per unique composition.

3.2.6. Electrical Small Signal Measurements

The temperature dependence of the lossless part of the dielectric permittivity (ε') and $\tan\delta$ were determined for all samples from 20 °C to 400 °C with measuring frequencies being 100 Hz, 1 kHz, 10 kHz, 100 kHz and 1 MHz (HP 4284A Impedance Analyzer, Palo Alto, USA) that were acquired at each integer temperature. The furnace (LE 4/11/R6, Nabertherm, Lilienthal, Germany) was equipped with a custom-made alumina specimen holder with platinum wire contacts and a platinum disk (thickness < 0.1 mm) was used on both faces of the disk-shaped samples to ensure proper electrical contact between sample and platinum wire. A heating rate of 2 K/min was maintained throughout both heating and cooling cycles of poled as well as unpoled samples. $T_{f\text{-}r}$ was determined by the inflection point of the obtained permittivity at 1 kHz; the maximum of $\tan\delta$ at 1 kHz was taken as further qualitative indication, however, was not used for calculating $T_{f\text{-}r}$. The measurements were carried out, testing one to two samples per unique composition.

Room temperature measurement of the small signal piezoelectric coefficient (d_{33}) of poled (6 kV/mm at RT for 60 min) samples was carried out using a Berlincourt meter (YE2730, Sinocera, Yangzhou, PRC) to ensure successful poling. The d_{33} values were recorded in both positive and negative poling direction of each sample and those values were further averaged to obtain a d_{33} less affected from a possible zero offset of the Berlincourt meter.

3.2.7. Dielectric Spectroscopy Under Resonance Conditions

In order to elucidate the energy storage and dissipation behavior of the ceramics, dielectric spectroscopy, also called impedance spectroscopy, was employed in a frequency range of $10^2 - 10^7$ Hz (Alpha-A high measurement system with HVB300 extension test interface / ZG4 4-point impedance interface, all from Novocontrol Technologies, Montabaur, Germany). In this range, ionic and dipolar interactions can be characterized. In particular k_p and the coupling factor in thickness direction (k_t) of ceramic disk samples, lying at about 500 kHz and 3 MHz, respectively, were assessed. Approx. 50 mm of gold wire with 25 μm diameter (99.95% purity, annealed, Alfa Aesar, Karlsruhe, Germany) was attached (as sketched in Figure 3.2.7.1 (a)) to the middle of each silver electrode face of the sample disks

with the help of a silver-containing, conductive glue (G3691, Plano GmbH, Wetzlar, Germany). Samples were then connected by placing the gold wires in a fixture (Test Fixture 16047A, Agilent Technologies, Inc., Santa Clara, CA, USA) with the disks being in a free-floating condition. For each composition **two** samples were measured. In a preliminary experiment, BNKT10:0.1Cu,0.4V was measured with two different diameters (~7 mm and ~ 10 mm), showing comparable coupling. In this work the values of the samples with ~10 mm in diameter are reported, because both PIC151 and PIC181 (by PI Ceramic GmbH, Lederhose, Germany) standard samples have a diameter of ~10 mm.
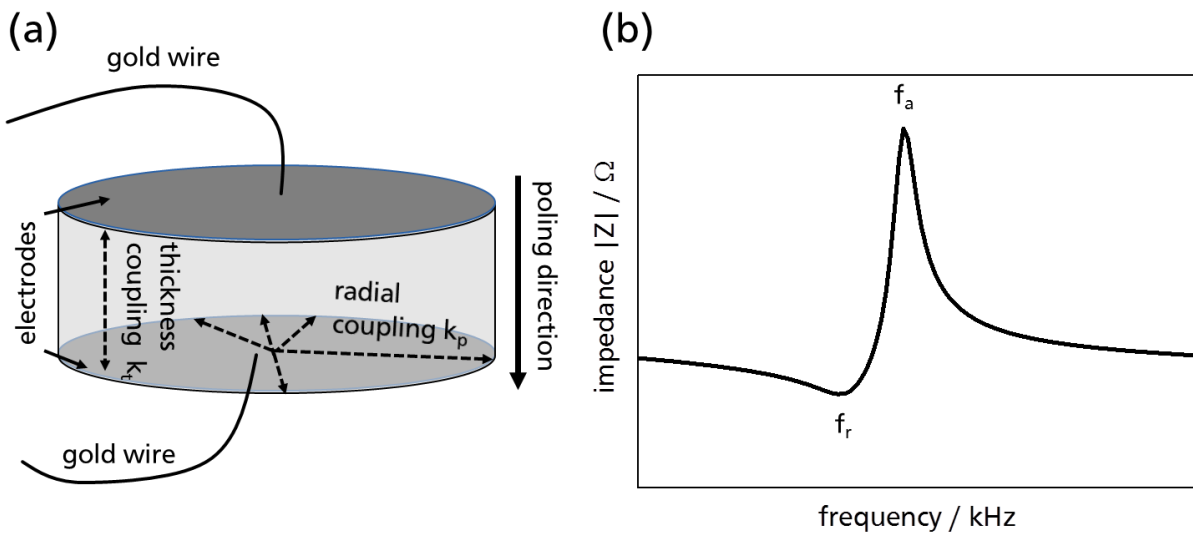
Figure 3.2.7.1   Schematic of a poled sample (a) prepared for impedance measurement with indication of thickness and planar coupling mode directions. (b) is a characteristic impedance spectrum representing the electric impedance as function of frequency. The resonance frequency (f_r) and the antiresonance frequency (f_a) are indicated.

The characteristic impedance at resonance (represented in Figure3.2.7.1 (b)) consists of a minimum at about f_r and a maximum in impedance at about f_a.
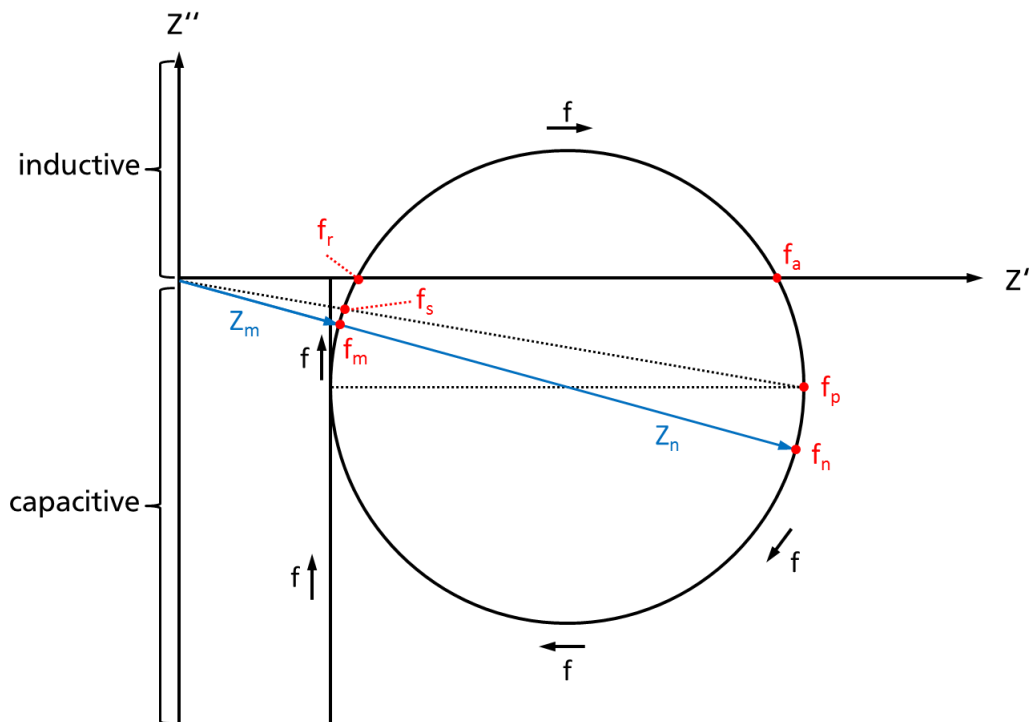
Figure 3.2.7.2 Simplified vector impedance diagram, characteristic for a piezoceramic transducer. Characteristic frequencies of the resonance behavior are highlighted in red. Blue arrows represent the impedance vectors of the maximum (Z_m) and minimum (Z_n) impedance

However, as evident from Figure 3.2.7.2, though equal in first approximation, the resonance frequency f_r does not exactly coincide with the motional resonance frequency at maximum conductance (f_s) or the frequency of maximal impedance (f_m). Likewise f_a does not exactly coincide with the parallel resonance frequency at maximum resistance (f_p) or the frequency of minimal impedance (f_n).

In case of lead-based piezoceramics, it is common to determine the coupling factors and electromechanical quality factors by approximating $f_r \sim f_s \sim f_m$ and $f_a \sim f_p \sim f_n$. This may not be accurate for lead-free materials. Thus, to assess f_r and f_a, an equivalent circuit, featuring inductive, resistive, CPEs and capacitive elements as exemplified in Figure 3.2.7.3 was used to determine f_r and f_a more accurately by means of simulation (RelaxIS version 2.4.1.10 rhd instruments GmbH & Co. KG, Marburg, Germany).
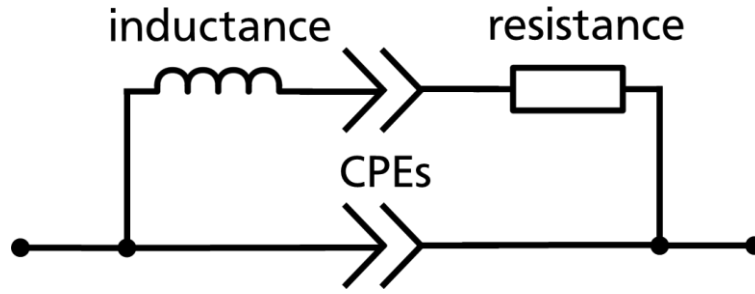
Figure 3.2.7.3 Schematic of an equivalent circuit used to fit the resonance-antiresonance-behavior of the piezoelectric ceramics, having inductance, CPE and resistance in series, parallel to another CPE.

With thereby obtained f_r and f_a, the coupling factors, which are a measure of the effectiveness of the conversion from mechanical to electrical energy and *vice versa* were calculated by the following equation:

$$k^2 \approx \frac{f_a^2 - f_r^2}{f_r^2} \quad . \tag{3.2.7.1}$$

One has to distinguish two different occurring resonance events in piezoelectric disk samples: coupling in thickness direction and coupling in planar direction, which occur in different frequency regions. In detail, the resonance frequency depends on both material properties and sample geometry, however, in case of the sample geometry with ten times larger diameter than thickness, k_p occurs at frequencies lower than k_t. For given sample geometries and material, k_p can roughly be found around 450 kHz and k_t roughly around 3 MHz.

The mechanical quality factor, describing the amplification of the mechanical vibration amplitude compared to off-resonance was calculated using

$$Q_M = \frac{1}{2\pi f_r Z_m C_\mathbf{0}} \cdot \frac{f_a^2}{f_a^2 - f_r^2} \quad , \tag{3.2.7.2}$$

where Z_m is the maximum impedance at resonance and C_0 is the shunt capacitance of the equivalent circuit. Since both occurring resonances described earlier (Section 2.2.2), have distinct frequencies and differ in f_a, f_r and Z_m, both also feature distinct corresponding mechanical quality factors, which are indicated as $Q_{M,p}$ and $Q_{M,t}$ for planar and thickness mechanical quality factors, respectively. Z_m was determined from the equivalent circuit used for fitting the resonance.

3.2.8. Dielectric Spectroscopy in Atmospheres with Different Oxygen Partial Pressure

With dielectric spectroscopy at elevated temperature and in different atmospheres it is possible to evaluate the contribution of multiple conduction processes to the overall conductivity (or inversely, the proportional resistivity) of the ceramics. Thus, grain boundary contributions may be distinguished from bulk contributions and furthermore, the influence of the contacts can likewise be determined. Furthermore, the determination of the activation energy E_A of the conduction processes is possible.
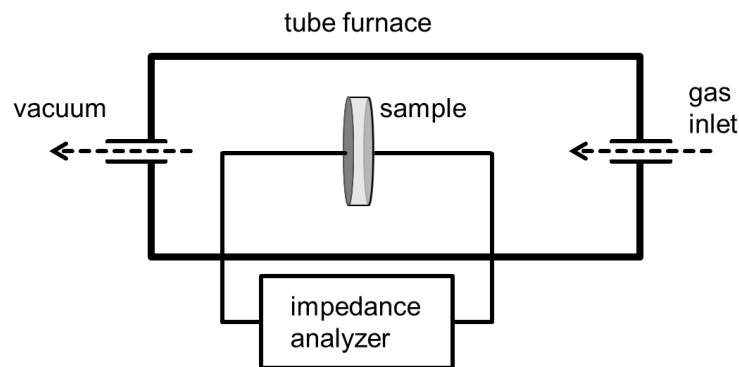
Figure 3.2.8.1   Schematic of the high temperature impedance tube furnace for purging samples with different gases.

Electroded ceramic samples were fixed with platinum wires (*cf*. Figure 3.2.8.1) in-between two thin (< 150 μm) platinum disks in a sealed tube furnace (LOBA/I 1400-45-400-1, HTM Reetz GmbH, Berlin, Germany) and exposed to ambient air, 99.999 vol.% N_2, 99.998 vol.% O_2 or a mixture of Ar gas and two vol.% H_2. Measuring temperatures ranged from 300 °C to 500 °C with measurements being performed at every increment of 25 °C. For atmospheres other than ambient air, a vacuum pump (Duo 5 M, Pfeiffer Vacuum GmbH, Asslar, Germany) was used to evacuate the furnace. Then with the vacuum valve closed, the respective gas was introduced into the furnace and stabilized at the maximum target temperature of 500°C. The furnace was evacuated again, followed by a subsequent gas introduction. This procedure was repeated until the impedance spectrum of the sample in the respective gas atmosphere was stable. The impedance was measured at all temperature steps with frequencies ranging from 0.01 Hz to 5 MHz (Alpha-A high measurement system with HVB300 extension test interface / ZG4 4-point impedance interface, all from Novocontrol Technologies, Montabaur, Germany). One sample per investigated composition was measured.
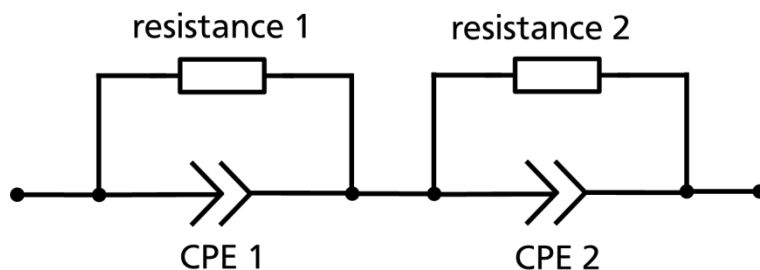
Figure 3.2.8.2 Schematic of an equivalent circuit to fit two independent electric processes, for instance grain boundary and bulk contribution to the overall conductivity.

The obtained impedance semicircles were fitted (RelaxIS version 2.4.1.10, rhd instruments GmbH & Co. KG, Marburg, Germany) by means of up to a series of four equivalent circuits, each comprising a resistance and CPE in parallel (Figure 3.2.8.2 sketches an example of two consecutive circuit units of CPE in parallel with a resistance) in addition to a resistor. This resistor was used to take the contribution of the contacts into account by adding it to the equivalent circuit.
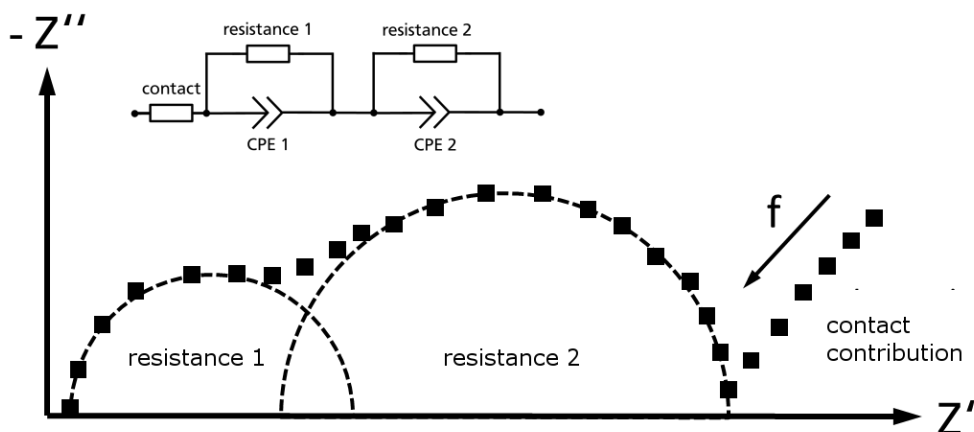
Figure 3.2.8.3 Schematic of Nyquist plot at one temperature with two identifiable semicircles and additional contact contribution. The inset figure details the corresponding equivalent circuit to obtain the simulated individual resistances.

3.2.9. Electron Paramagnetic Resonance Spectroscopy

In order to further elucidate the defect chemistry of doped and co-doped BNKT, EPR was chosen as a method that enables crucial insight. Beyond that, it allows for the detection of minute amounts of employed dopants. In EPR spectrometry, unpaired electrons are aligned by a defined magnetic field (*cf*. Figure 3.2.9.1). The absorption of microwave radiation (X-band EPR with a frequency of 9.41 GHz was employed) by the sample is detected in a Bruker EMX EPR spectrometer (Bruker, Karlsruhe, Germany) and correlates with a spin direction change of unpaired electrons parallel to the external magnetic field into the reverse direction antiparallel to the magnetic field, the latter one being higher in energy. Polycrystalline 2,2-diphenyl-1-picrylhydrazyl with **g** = 2.0036 was taken as a reference material in order to accurately determine the resonance magnetic field values and the **g**-factor and the magnetic field was detected by a Gauss-meter (ER 035M, Bruker, Karlsruhe, Germany). The EPR spectra were acquired under the guidance of Dr. Emre Erdem at the Unversität Freiburg, Freiburg, Germany. One sample of calcined powder and one sintered disk sample were measured for each composition.
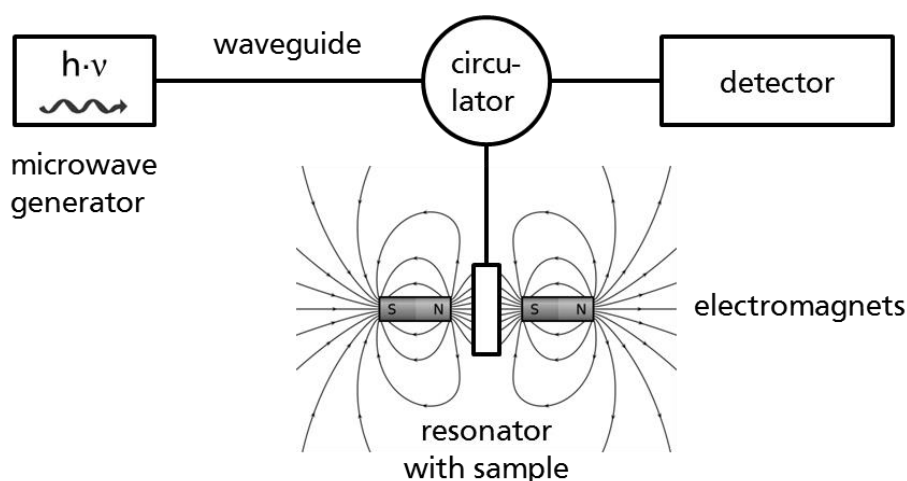
Figure 3.2.9.1   Schematic of an EPR spectrometer.

3.2.10. X-Ray Photoelectron Spectroscopy

X-ray photoelectron spectroscopy (XPS) spectra were obtained using a PHI VersaProbe 5000 spectrometer (Physical Electronics, Inc, Chanhassen, USA), which is hosted in the Darmstadt Integrated System for Battery Research (DAISY-BAT).[260] The samples were excited with monochromatic Al Kα radiation (hv = 1.4866 keV) and binding energies are compared to the Fermi level of an Ag foil. The pass energy, E_{pass} = 23.5 eV, during the collection of photoelectrons took place at a take-off angle of Θ = 45° with respect to the surface normal. Due to low electronic conductivity, the build-up of charge on the surface was compensated by a dual beam charge neutralization system, consisting of both ion beam (low energy argon ions) and electron beam. No further shift of spectra was performed. The XPS samples were measured by Dr. Shunyi Li and evaluated in collaboration with Dr. Shunyi Li and Prof. Dr. Andreas Klein at the Technische Universität Darmstadt, Darmstadt, Germany. One sample for each investigated composition was measured.
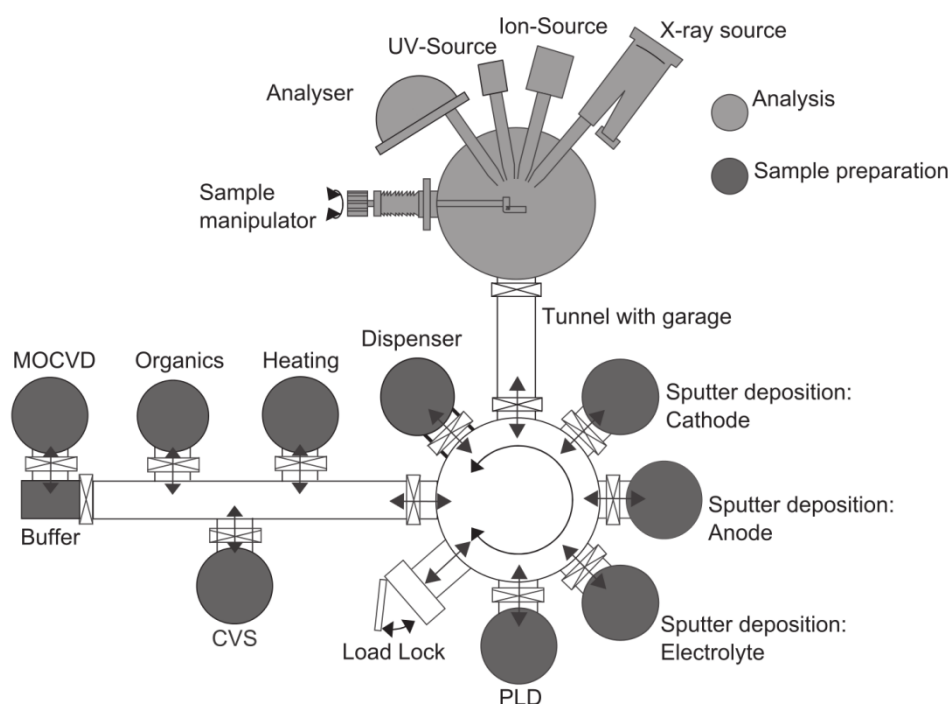
Figure 3.2.9.2   Schematic of the DAISY-BAT facility Integrated System for Battery research, adapted from Schwöbel *et al.*[260] and reprinted with permission, copyright © 2014 Elsevier B.V. All rights reserved.).

4. Results and Discussion

4.1. Microstructure and Phases

One aspect that is influenced by doping of ceramics is the microstructure of the final ceramic material. It is furthermore possible to introduce foreign phases in the host material BNKT. Thus, in particular it is important to know the density of the produced ceramics, determine which phases exist in the ceramics and in addition assess how grains are sized, shaped and distributed. Characterizing changes in microstructure upon Cu and V doping of the ceramics allows for the correlation of microstructure and phases in context with results of the following sections 4.2 - 4.6.

Table 4.1.1 | Densities of Undoped and Cu Doped BNKT10 Ceramic Samples

dopant	none	none	0.01Cu	0.05Cu	0.5Cu
T_{sint} / °C	1130	1080	1130	1130	1080
ρ_{rel} / %	98.7	94.0	95.2	96.0	96.7

The undoped and doped BNKT ceramics, produced in this work, mostly displayed high densities >90 % after sintering. The density tables (Table 4.1.1 - 4.1.3) list the highest obtained density for each composition, sintered at the indicated temperature T_{sint}. Three BNKT30 compositions (BNKT30:0.5V, BNKT30:0.4Cu,0.4V and BNKT30:0.5Cu) exhibit maximum densities < 90 % albeit different investigated sintering ramps (3 K/min and 5 K/min) and investigated T_{sint} (1080 °C, 1110 °C, 1130 °C and 1150°C).

Table 4.1.2 | Relative Densities of Cu and V Doped BNKT10 Ceramic Samples

dopants	1V	0.5V	0.1Cu,0.4V	0.2Cu,0.3V	0.25Cu,0.25V	0.3Cu,0.2V	0.4Cu,0.1V
T_{sint} / °C	1130	1080	1080	1080	1080	1080	1080
ρ_{rel} / %	98.5	93.9	94.0	95.8	96.0	96.0	96.3

To elucidate the influence of the Cu content on the density, ρ_{rel} at different Cu doping levels was compared for BNKT10 ceramics, sintered with the same T_{sint} (1080 °C). A trend towards higher ceramic densities with increasing Cu content can be observed (*cf*. Figure 4.1.1). Thus, at the same sintering temperature, Cu improves the densification process. This yields relative densities of up to 96.7 % in the case of BNKT10:0.5Cu, which exceeds ρ_{rel} of the undoped BNKT10 ceramics, sintered at

1080 °C, by 2.7 %. Nevertheless ρ_{rel} of undoped BNKT ceramics, sintered at 1130 °C, is 1.8 % lower. In order to achieve maximum densification, sintering undoped BNKT10 at 50 °C higher temperatures appears to be superior *vs.* doping BNKT10 with 0.5 at.% Cu, while sintering at 1080 °C.

Table 4.1.3 | Overview of the Relative Densities of Doped BNKT Ceramics

dopant(s)	none	0.5V	0.1Cu,0.4V	0.2Cu,0.3V	0.3Cu,0.2V	0.4Cu,0.1V	0.5Cu
BNKT20							
T_{sint} / °C	1130	1130	1130	1130	1150	1130	1080
ρ_{rel} / %	97.7	95.3	95.5	95.9	95.8	97.1	95.3
BNKT30							
T_{sint} / °C	1150	1130	1130	1130	1130	1130	1110
ρ_{rel} / %	97.0	88.0	94.4	92.5	96.2	88.7	86.4

For BNKT20 and BNKT30 ceramics, the maximum ρ_{rel} is nearly exclusively found at sintering temperatures higher than 1080 °C. The low (1080 °C) T_{sint} of BNKT20:0.5Cu may be explained by the improvement of the densification process by Cu doping at lower temperatures. As this effect was found to be strongest at a Cu content of 0.5 at.%, the optimum T_{sint} is also lowest. However, with the exception of BNK10:1V, all doped ceramics display a lower maximum ρ_{rel} compared to undoped ceramics, sintered at higher temperatures. It is not uncommon for BNKT ceramics of comparably lower density to exhibit higher piezoelectric properties, as for instance described by Zhang *et al.*[110] for BNKT22 compositions, which display a maximum density at a T_{sint} of 1130 °C, while displaying maximum polarization at a T_{sint} of 1150 °C.
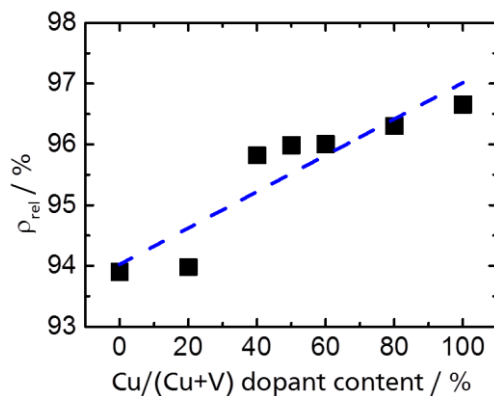
Figure 4.1.1   Changes in ρ_{rel} upon increasing Cu dopant content of BNKT10 ceramics, all sintered at 1080 °C. The dashed line is a linear fit to guide the eye. *C.f.* Blömker *et al.*[261].

Multiple studies[76,211,262,263] on the addition (note: this means excess doping instead of substitutional doping, which was employed in this work) of Cu to BNKT-based

materials, revealed the same trend of densification at lower T_{sint} upon Cu addition. Those authors attributed this behavior to liquid phase sintering, enabled by Cu.

To elucidate the microstructure, both representative SEM images, as well as grain diameter histograms, serve to highlight the changes in microstructure upon doping.
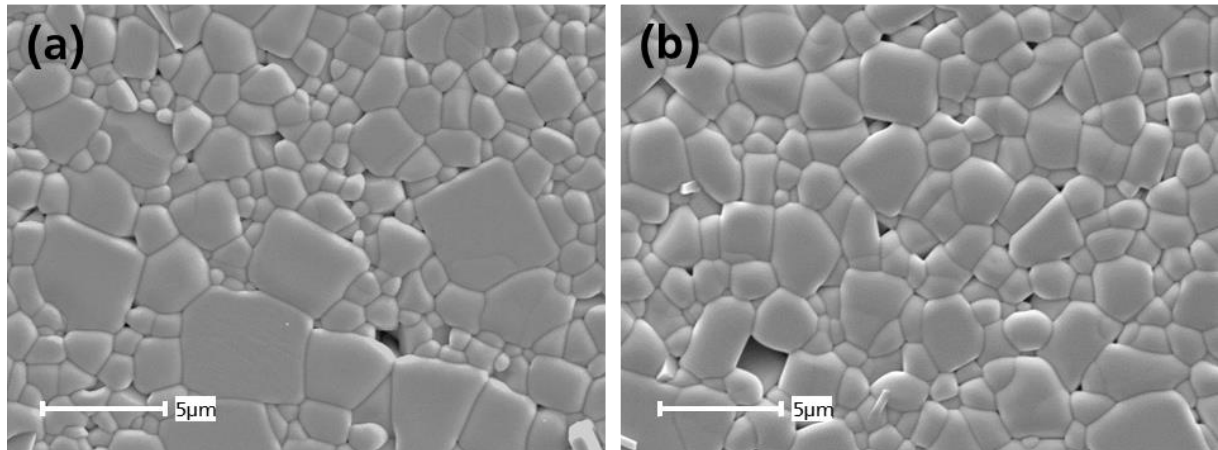
Figure 4.1.2   Representative SE image of the microstructure of (a) undoped BNKT10 and (b) BNKT10:0.2Cu,0.3V ceramics. Please note that the image location was chosen to best represent the grain size distribution and is neither representative of the pore size nor the pore fraction.

The quality of the thermal etching is fairly good, as individual grains and grain boundaries are clearly distinguishable by eye and by the employed analysis software in *ImageJ*. BNKT10:0.5V, BNKT10:0.1Cu,0.4V and BNKT10:0.3Cu,0.2V (*cf*. Figure 4.1.3 (a), (b) and (c), respectively) compositions display different thermal etching behavior under the same etching conditions. This slight over etching, compared to undoped ceramics or ceramics with lower V content, is correlated with faster grain growth for BNKT10:0.5V, BNKT10:0.1Cu,0.4V and BNKT10:0.3Cu,0.2V. This is likely related to their higher V content, compared to the other compositions investigated in this work. It is also in conformity with the low temperature sintering of piezoceramics upon the addition of V_2O_5, observed by Wittmer *et al.*[264].

However, an enlargement of grains as for instance reported by Kim *et al.*[265], could not be observed. Two possible explanations for this phenomenon are: (I) though the necessary sintering temperature to obtain dense ceramics is lowered, as discussed previously in this section, the substitution doping undertaken in this work differs from the excess doping, carried out by Kim *et al.* or Wittmer *et al.* and therefore the enhanced grain growth through liquid sintering is not prevalent; and (II) the enhanced grain growth upon V addition in PZT-based materials requires Pb within the composition and is therefore limited to Pb-containing compositions. A combination of the two explanations is considered possible.
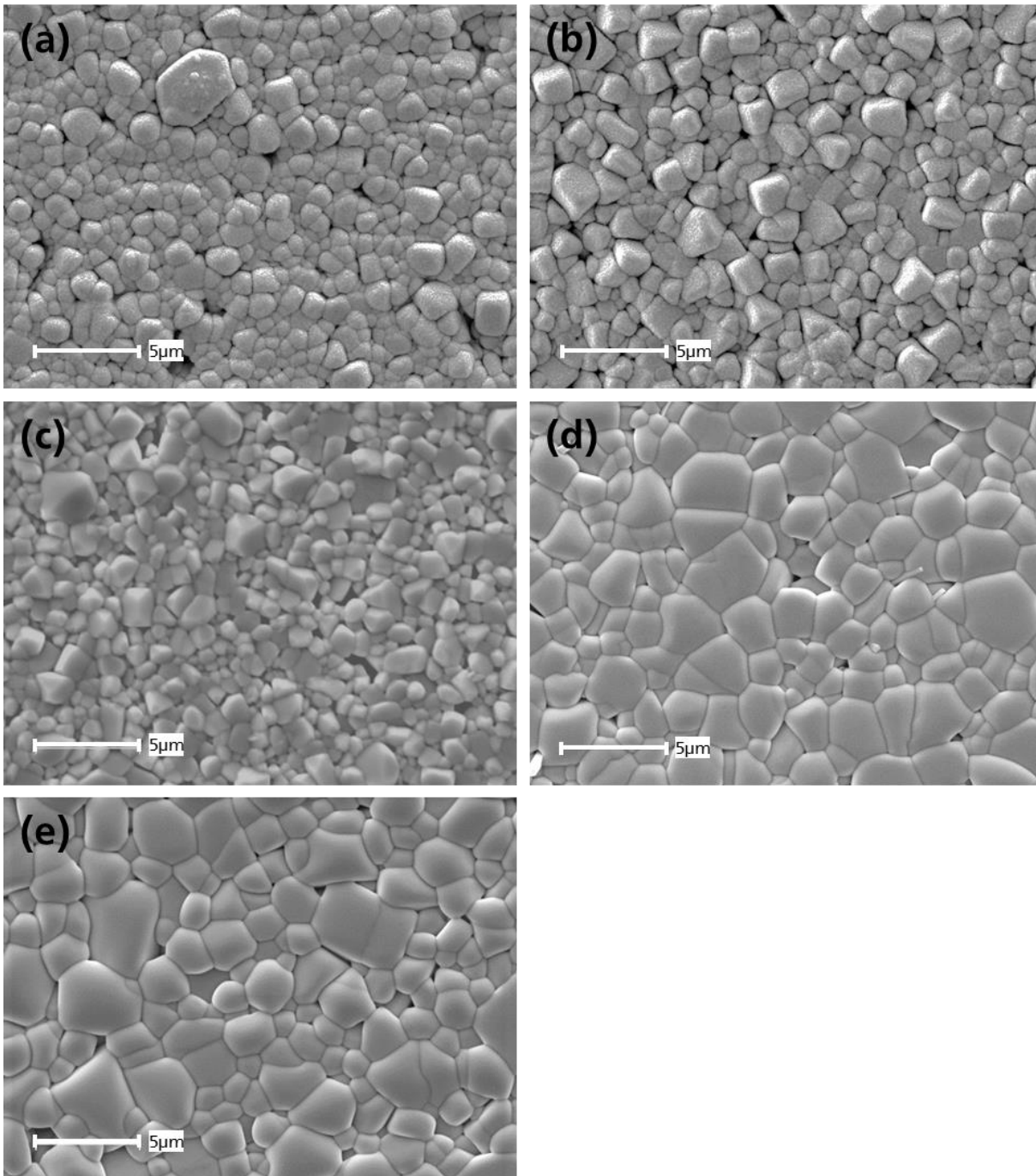
Figure 4.1.3 Representative SE images of (a) BNKT10:0.5V, (b) BNKT10:0.1Cu,0.4V, (c) BNKT10:0.3Cu,0.2V, (d) BNKT10:0.4Cu,0.1V and (e) BNKT10:0.5Cu ceramics. For BNKT10:0.5V and BNKT10:0.1Cu,0.4V and BNKT10:0.3Cu,0.2V the thermal etching temperature was 1020 °C. Please note that the image location was chosen to best represent the grain size distribution and is neither representative of the pore size nor the pore fraction.

In general, all grains of all investigated ceramics are characterized by a shape with an aspect ratio close to unity (*cf*. Figure 4.1.2 and Figure 4.1.3). For the determination of the grain size distributions (*cf*. Figure 4.1.4), it was possible to identify all analyzed grains, while restricting the allowed aspect ratios, used for grain identification, from 0.23 to 0.77. Undoped BNKT ceramics display a higher amount of grains with larger

diameters > 4 μm, which is qualitatively reflected in the corresponding representative SEM image (*cf.* Figure 4.1.2 (a)). The average grain diameter of undoped BNKT10 is 1.3 μm. All doped compositions, however, exhibit a more homogeneous grain size distribution with average grain diameters ranging from 0.7 μm (BNKT10:0.3Cu,0.2V) to 1.3 μm (BNKT10:0.5Cu) (*cf.* Table 4.1.4 for details).

Table 4.1.4 | Average Grain Size Diameters of BNKT10 Ceramics

dopants	none	0.5V	0.1Cu,0.4V	0.2Cu,0.3V	0.3Cu,0.2V	0.4Cu,0.1V	0.5Cu
mean grain diameter /µm	1.3	0.8	1.0	1.2	0.7	1.3	1.3
standard derivation	0.8	0.3	0.4	0.7	0.2	0.8	0.7

The deviation of the average grain diameters of the BNKT10 ceramics with different dopants is not very strong (0.6 μm maximum deviation). Thus, the detailed analysis of the distribution of the grain diameters (*cf.* Figure 4.1.4) sheds further light on the microstructure and highlights the presence of a higher number of larger (>4 μm) grains in undoped BNKT10 as compared to doped BNKT10.

Especially BNKT10:0.5V, BNKT10:0.1Cu,0.4V and BNKT10:0.3Cu,0.2V (*cf.* Figure 4.1.4 (b), (c) and (e), respectively) display very homogenous grain diameter distributions with no indication of larger grains with a diameter > 4 μm.
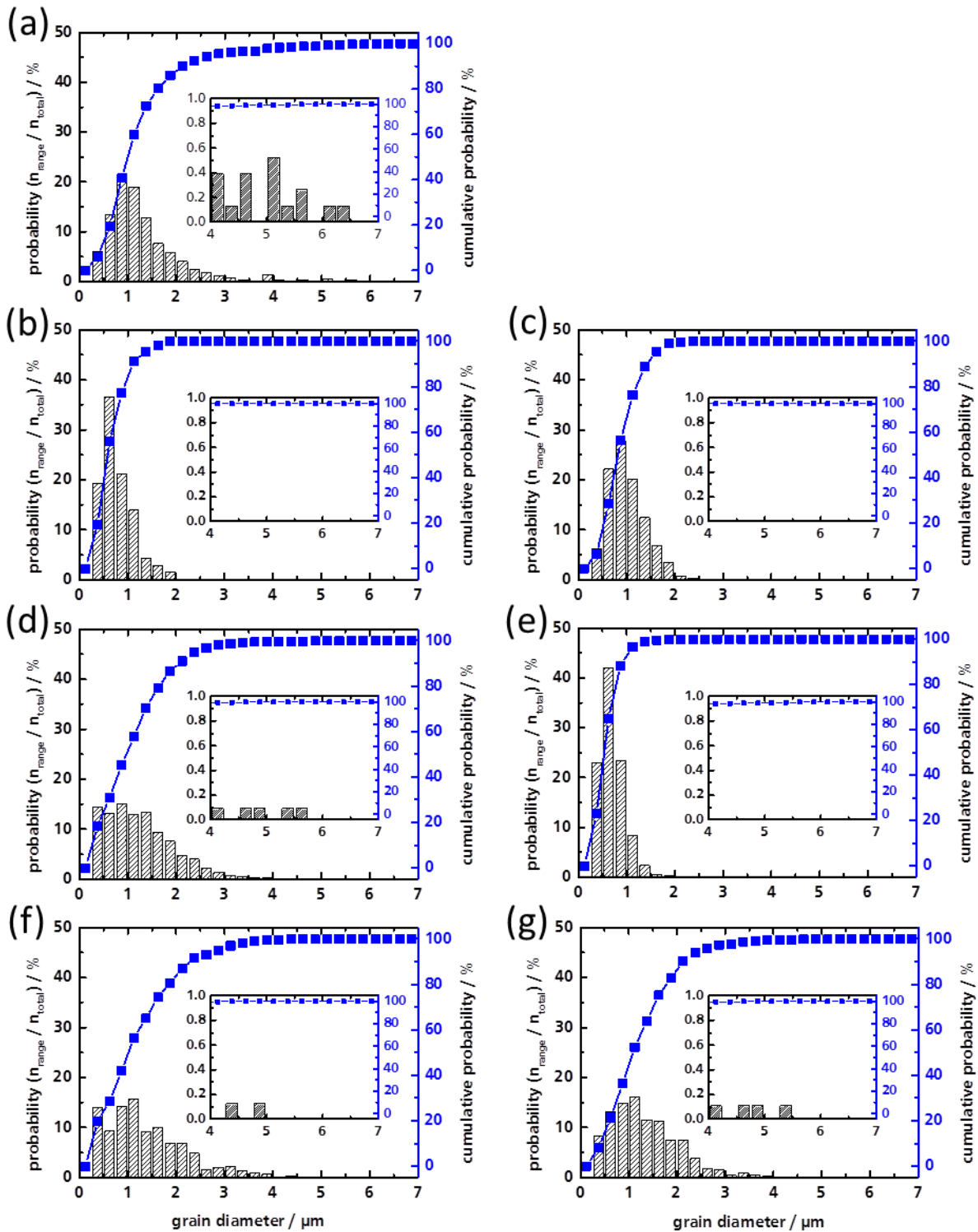
Figure 4.1.4 Grain size histograms of undoped BNKT10 (a) and BNKT10 ceramics doped with (b) 0.5V, (c) 0.1Cu,0.4V, (d) 0.2Cu,0.3V, (e) 0.3Cu,0.2V, (f) 0.4Cu,0.1V, (g) 0.5Cu. Grain occurrence probabilities are plotted by taking the number of the particles *vs*. the total number of grains into account. The respective inset figures show the grain size probabilities for four to seven micrometers in detail.
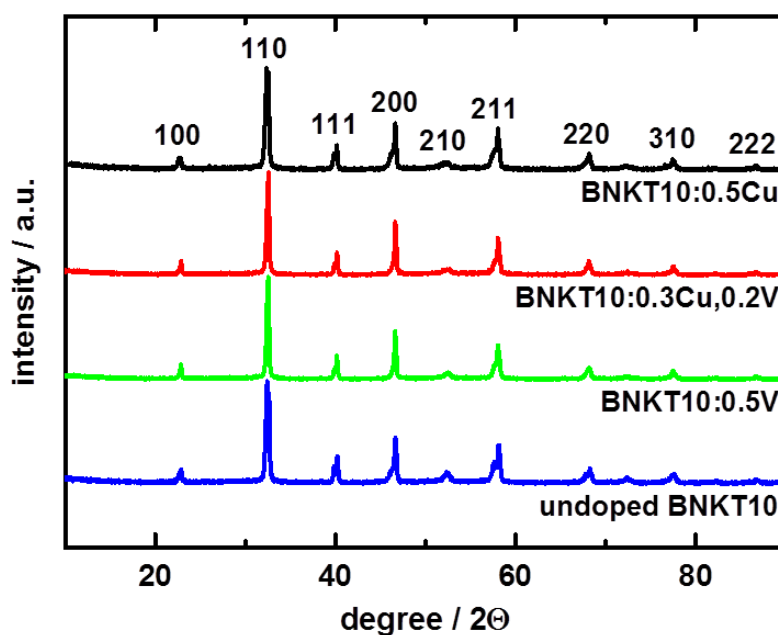
Figure 4.1.5   Representative XRD patterns of Cu doped, V doped, Cu-V doped and undoped BNKT10.

The investigation of samples *via* XRD allows for the observation of major (> 3 at.%) crystalline phases and thereby, in addition, for the detection of larger secondary impurity phases. All XRD peaks of the synthesized, sintered ceramics could be identified as belonging to a perovskite phase. There was no indication of crystalline secondary phases, observed within the limits of detection.

All peaks match a perovskite phase. Unit cell parameters were further extracted for the density calculation. Figure 4.1.5 emphasizes the major reflections, which sintered BNKT10 ceramics exhibit and representatively compares undoped with doped ceramics. Upon doping with Cu and V, only BNTK10-based compositions displayed noticeable peak splitting (*cf*. Figure 4.1.6), while BNKT20 and BNKT30 compositions did not. The splitting can indicate lower elongation or shortening of the unit cell (*c/a* ratio closer to unity). For BNKT10 ceramics, this is in accordance with the XRD peak splitting trends in BNKT systems with respect to potassium content. This is described in literature (*e.g.* Otoničar *et al.*[23]) and attributed to the rhombohedral *R3c* (undoped BNT or K content < ~20 at.%) phase symmetry.
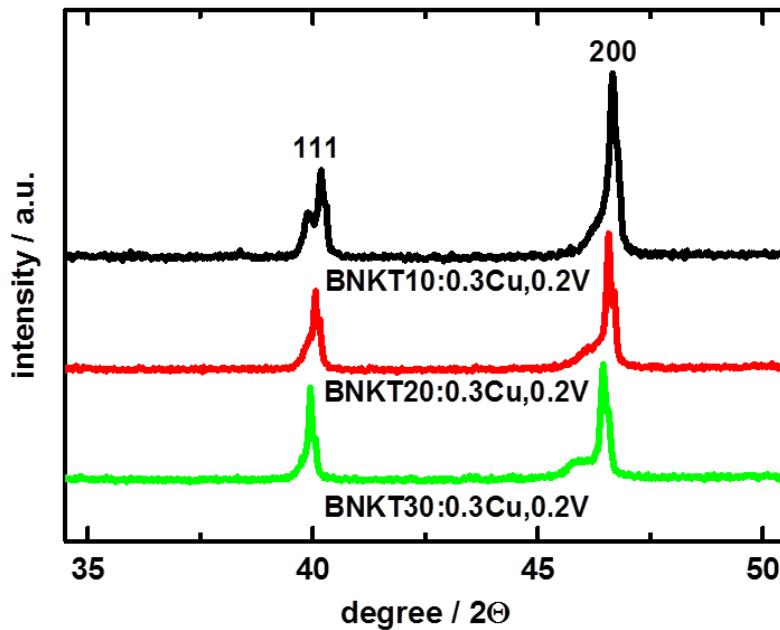
Figure 4.1.6 Representative XRD patterns of the same amount of Cu and V dopants for different potassium contents of the base composition (BNKT10, BNKT20 and BNKT30).

For BNKT10 ceramics, which are on the rhombohedral side of the MPB, minute differences could be observed, as for instance the {111} and {211} reflections display a variance in the degree of splitting of the peaks (*cf*. Figure 4.1.7). Undoped BNKT10 most clearly displays peak splitting, BNKT10:0.5Cu exhibits clear speak splitting, however, to a lesser degree and the other doped BNKT10 ceramics possess side shoulders instead of individually distinguishable peaks. This can be attributed to the rhombohedral phase symmetry of BNKT10-based ceramics.

For doped BNKT20 and BNKT30 compositions, the tetragonal *P4mm* (undoped BKT or K content > ~20 at.%) peak splitting of the {200} reflection is not very pronounced (*cf*. Figure 4.1.6 and Figure 4.1.7) and it is arguable, whether or not there is any indication of splitting at all. Nevertheless, a discernible side shoulder of the {200} reflection is present. The respective undoped ceramics, however, display stronger peak splitting or side shoulder of for instance the {200} reflection. This indicates that BNTK30 ceramics lose their tetragonal character (reflected in a lower *c/a* ratio) to a certain degree. The doped BNKT30 ceramics are therefore, from a XRD standpoint, closer to a cubic or pseudocubic material than undoped BNKT30 ceramics.
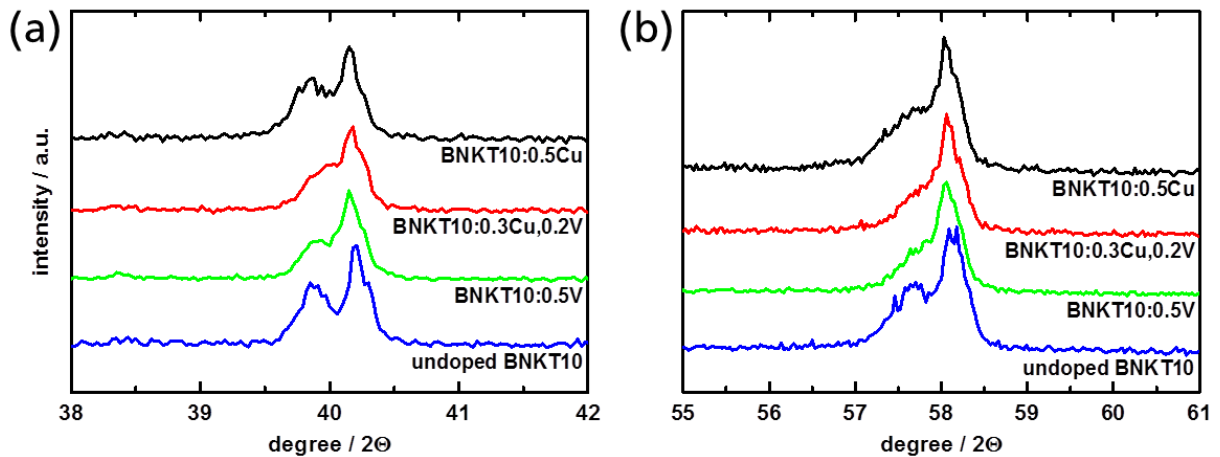
Figure 4.1.7 Details of representative XRD patterns of Cu doped, V doped, Cu-V doped and undoped BNKT10 ceramics. The {111} (a) and {211} (b) reflections are presented.

4.2. Piezoelectric Large- and Small Signal Measurements

Key figures for piezoelectric materials are divided in large- and small signal parameters. This categorization refers to the applied electric field during the respective measurement. Large signal measurements to determine parameters like S_{max}, P_{sat}, P_{max} and P_{rem}, are typically performed in a range of > 1 kV/mm, depending on which piezoelectric material is measured. Small signal measurements are performed in an electric field range, which is far below the coercive field strength and allows for an essentially linear response of the material. The European Standard EN 50324-2:2002, for instance, specifies a maximum field of 1 V/mm for permittivity measurements to ensure mentioned linear response.[266]

Dielectric spectroscopy, which is sometimes referred to as impedance spectroscopy, is as well considered a small signal measurement. Dielectric spectroscopy, however, is discussed separately in the subsequent sections 4.3 and 4.4.

Polarization *vs*. electric field (P-E) loops and strain *vs*. electric field (S-E) loops, of all synthesized ceramics with BNKT10, BNKT20 and BNKT30 base composition were measured at 6 kV/mm and are presented in Figures 4.2.1 and 4.2.3 - 4.2.6. Below, the effect of Cu and V doping will be discussed in detail for each base composition. Detailed characteristic large signal measurement values of all synthesized and discussed ceramics are provided in the appendix (*cf*. Table 8.3).

BNKT10 based piezoceramics display a butterfly-like S-E loop, which is characteristic for ferroelectric materials. They are able to provide a strain of about 1 ‰, which

correlates with a large signal d_{33} (d_{33}^*) of 120 pm/V (at 6 kV/mm) for undoped BNKT10. Doping BNKT10 in general increased the strain and a d_{33}^* of up to 177 pm/V could be obtained in case of BNKT10:0.5Cu. All compositions display a high negative strain S_{neg} of at least -0.58 ‰. Upon doping, the negative strain is in all cases of larger magnitude.
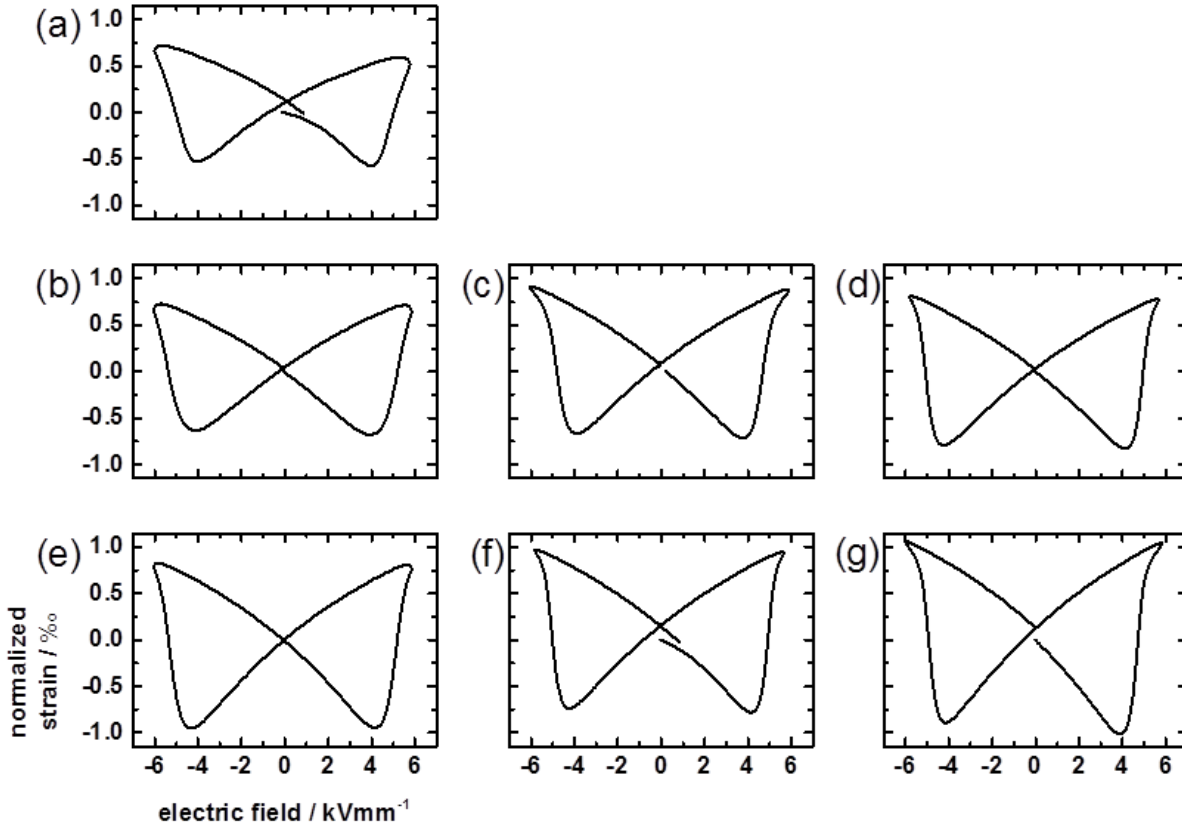
Figure 4.2.1 Strain *vs*. electric field at a maximum electric field of 6 kV/mm for (a) undoped BNKT10, (b) BNKT10:0.5V, (c) BNKT10:0.1Cu,0.4V, (d) BNKT10:0.2Cu,0.3V, (e) BNKT10:0.3Cu,0.2V, (f) BNKT10:0.4Cu,0.1V and (g) BNKT10:0.5Cu ceramics.

Most S-E loops display saturated strain loops, which are characterized by a pointed shape at maximum strain, corresponding with decreased hysteresis behavior (*cf*. Figure 4.2.1). Exceptions are undoped BNKT10 and BNKT10:0.5V, which exhibit a more round shape at maximum strain. This finding is also in conformity with the features of the P-E loops at maximum field (*cf*. Figure 4.2.3). The maximum polarization (P_{max}) of doped BNKT10 is consistently higher than of undoped BNKT10 (25.0 μC/m²). This can amount to up to 31.8 μC/m² in case of BNKT10:0.3Cu,0.2V.
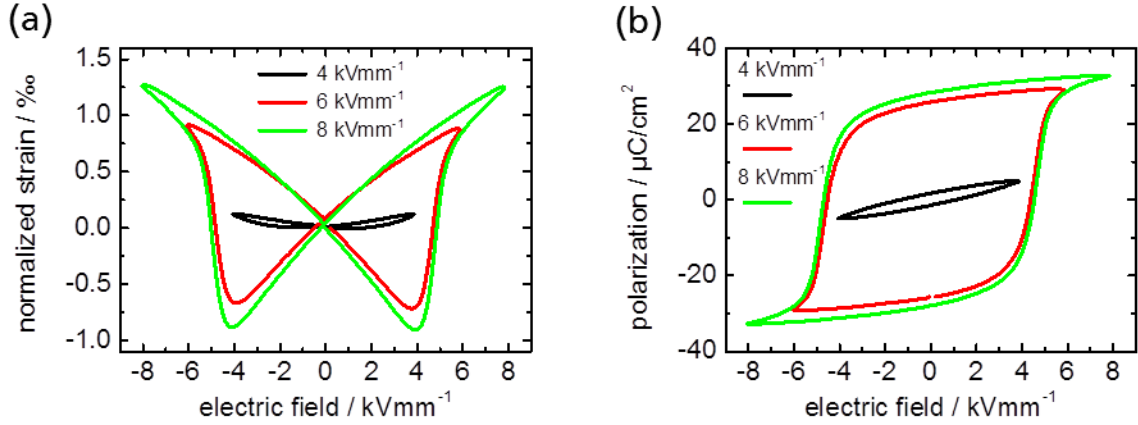
Figure 4.2.2 Strain (a) and polarization (b) *vs.* electric field at different maximum applied electric fields, representatively detailed for the composition BNKT10:0.1Cu,0.4V.

A different switching behavior above the coercive field is additionally reflected in the evolution of the S-E loop with increasing electric field. Figure 4.2.2 representatively details the behavior of BNKT10:0.1Cu0.4V for 4, 6 and 8 kV/mm. While for an electric field of 4 kV/mm (slightly below the E_c of 4.5 kV/mm, determined for BNKT10:0.1Cu0.4V) no significant P_{max} (5.0 μC/m²) and S_{max} (0.12 ‰) can be observed, a field of 6 kV/mm suffices to significantly increase the mentioned parameters (P_{max} = 29.2 μC/m²; S_{max} = 0.91 ‰). For higher fields of 8 kV/mm, S_{max} increases notably (to 1.27 ‰), while P_{max}, increases marginally (to 32.8 μC/m²). The corresponding d_{33}^* of BNKT10:0.1Cu0.4V increases from 60 pm/V to 152 pm/V and eventually to 158 pm/V at 4 kV/mm, 6 kV/mm and 8 kV/mm, respectively. It is evident, that the minor (6 pm/V) increase of the d_{33}^* is due to the fact, that the piezoceramic already reached the saturation at an electric field at or close to 6 kV/mm. This can be rationalized by the movement of domain walls, causing the non-linear response at about E_c, which was for instance described in detail by Damjanovic *et al.*[154].

Samples with BNKT10 base composition are in general characterized by a high coercive field (E_c), which is in all cases ≥ 4.5 kV/mm. In addition, all loops feature a sharp increase of the polarization about E_c. Doping only slightly influences E_c, leading to a maximum E_c of 4.8 kV/mm in case of BNKT10:0.5V and BNKT10:0.2Cu,0.3V. This change of 0.3 kV/mm is a rather low change in E_c. In contrast, $BaTiO_3$ materials were for instance reported to display a strong dependence of E_c on dopant concentrations, as described by *e.g.* Karaki *et al.* [167]. They observed an increase of E_c by a factor of 5 (from approximately 0.1 kV/mm to 0.5 kV/mm) upon the addition of Bi_2O_3 and Li_2O to $BaTiO_3$.
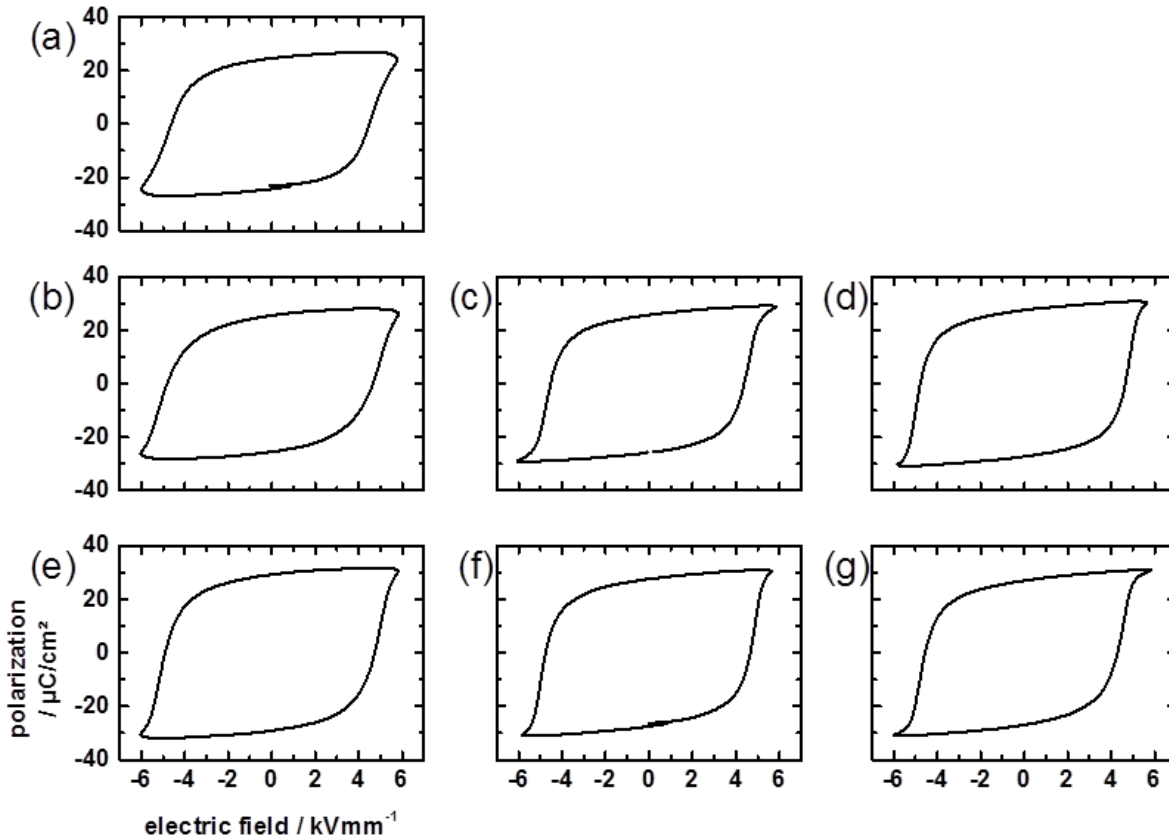
Figure 4.2.3   Polarization *vs*. electric field at a maximum electric field of 6 kV/mm for (a) undoped BNKT10, (b) BNKT10:0.5V, (c) BNKT10:0.1Cu,0.4V, (d) BNKT10:0.2Cu,0.3V, (e) BNKT10:0.3Cu,0.2V, (f) BNKT10:0.4Cu,0.1V and (g) BNKT10:0.5Cu ceramics.

The higher P_{max} and P_{sat} upon doping is in contrast to the consistent lower density of doped *vs*. undoped BNKT10 ceramics (as discussed in section 4.1). When observing the same material with different porosity, P_{max} and P_{sat} are expected to decline with decreasing density, which is ascribed to a higher pore concentration and a resulting less homogeneous electric field, as discussed by Dunn *et al.*[267] or Kar-Gupta *et al.*[268]. Pores can in this respect be treated as a second phase, consisting of air, which possesses a significantly lower permittivity, compared to the bulk FE material. Like P_{max} and P_{sat}, the remanent polarization (P_{rem}) of ceramics produced in this work is consistently higher upon doping and reaches a maximum value of 29.2 μC/m² in case of BNKT10:0.3Cu,0.2V.
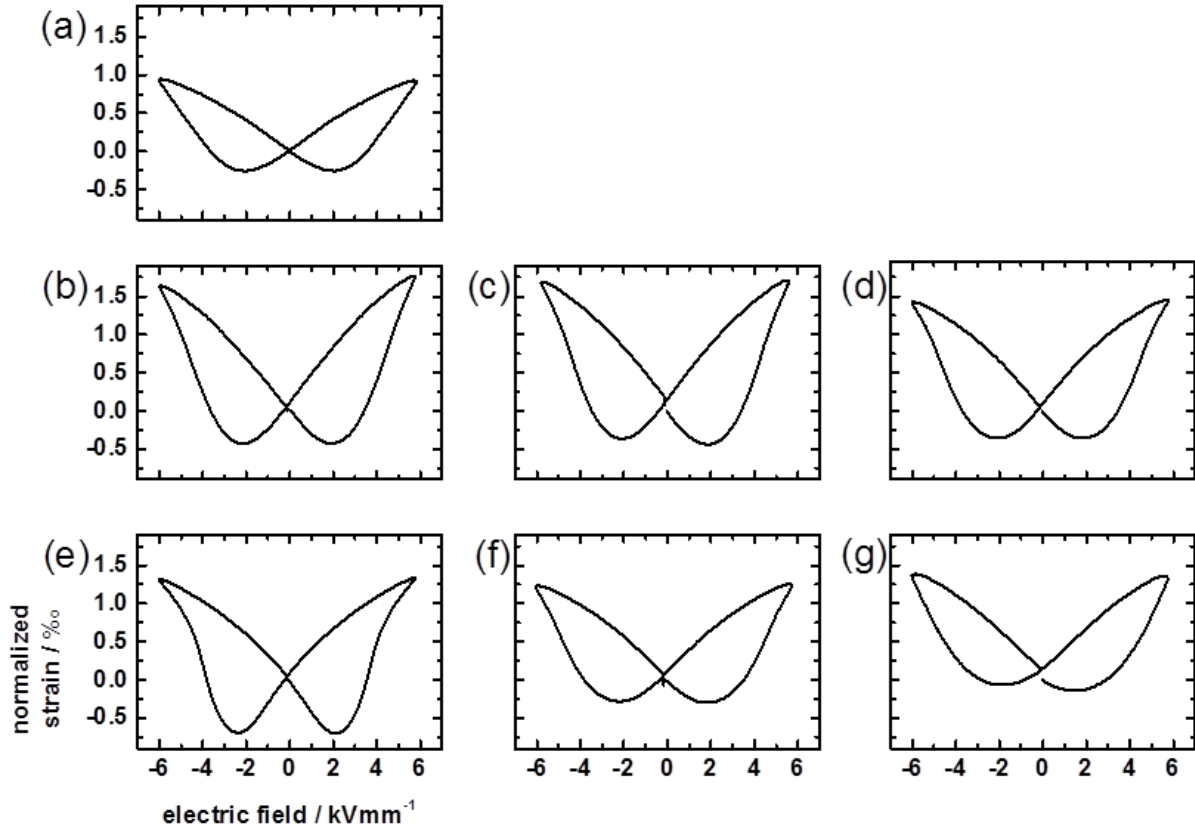
Figure 4.2.4 Strain *vs*. electric field at a maximum electric field of 6 kV/mm for (a) undoped BNKT20, (b) BNKT20:0.5V, (c) BNKT20:0.1Cu,0.4V, (d) BNKT20:0.2Cu,0.3V, (e) BNKT20:0.3Cu,0.2V, (f) BNKT20:0.4Cu,0.1V and (g) BNKT20:0.5Cu ceramics.

BNKT20 based materials, however, exhibit slightly different S-E behavior compared to BNKT10 based ceramics (*cf*. Figure 4.2.4 and 4.2.5). Namely S_{neg} of the material has a magnitude lower than 0.44 ‰ with the exception of BNKT20:0.3Cu,0.2V, being -0.70 ‰. The highest obtainable d_{33}^* for doped BNKT20 was 293 pm/V at an electric field of 6 kV/mm. In contrast to the findings for BNKT10 based ceramics, E_c of doped BNKT20 ceramics was consistently lower (< 2.4 kV/mm), compared to undoped ceramics (2.9 kV/mm). This is reflected in the rather slim P-E loops of BNKT20 materials. In addition, P_{max} and P_{sat} were found to be consistently lower in doped BNKT20 ceramics (*cf*. Figure 4.2.5). This finding is more in line with the consistently lower density of doped BNKT20 *vs.* undoped BNKT20 ceramics, discussed in section 4.1, following previously discussed trend of lowered polarization with decreasing density.
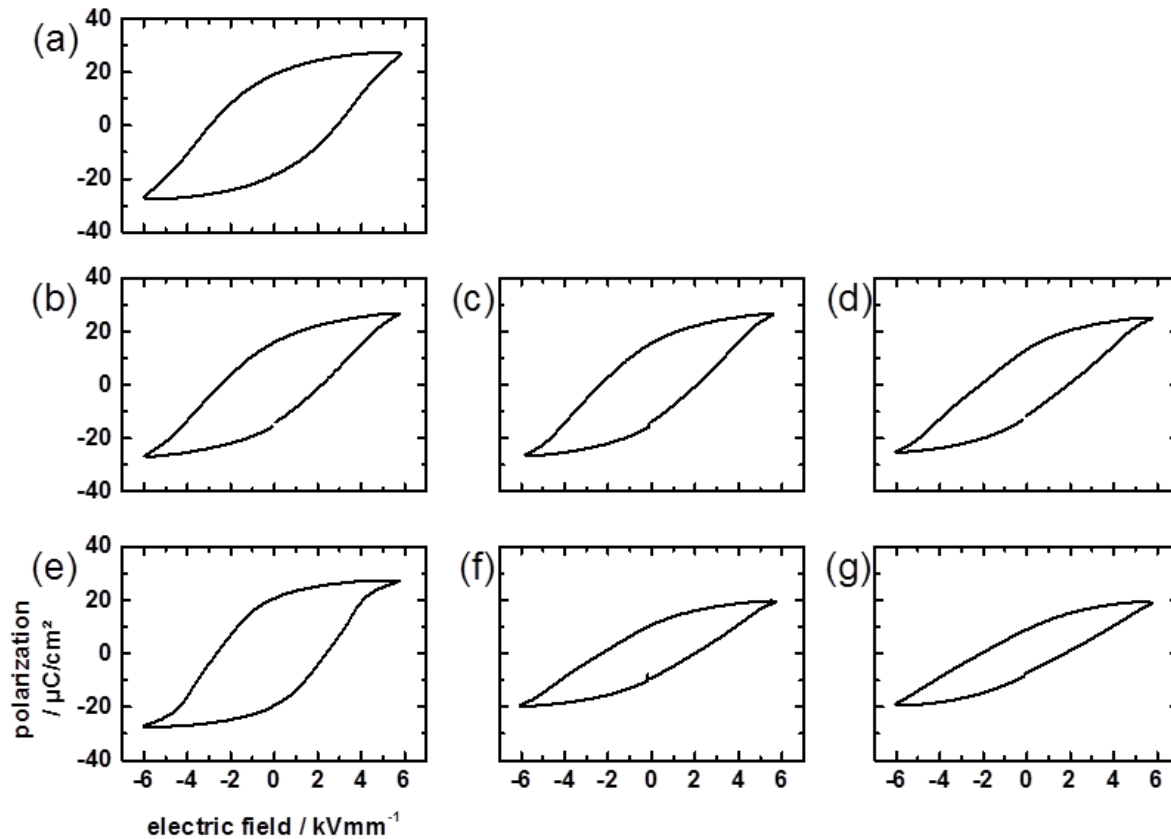
Figure 4.2.5 Polarization *vs*. electric field at a maximum electric field of 6 kV/mm for (a) undoped BNKT20, (b) BNKT20:0.5V, (c) BNKT20:0.1Cu,0.4V, (d) BNKT20:0.2Cu,0.3V, (e) BNKT20:0.3Cu,0.2V, (f) BNKT20:0.4Cu,0.1V and (g) BNKT20:0.5Cu ceramics.

BNKT30 based ceramics display both lower S_{neg} (*cf*. Figure 4.2.6) as well as slimmer P-E loops (*cf*. Figure 4.2.7). The P-E loop shapes are more sprout-like compared to the butterfly type loops for especially BNKT10 based ceramics.

Ceramics of the compositions BNKT30:0.5V and BNKT30:0.5Cu could not be synthesized with a desired high density, high homogeneity and reasonable piezoelectric properties. Though ceramics of these compositions could be sintered with densities > 85 % during the course of this work, they displayed highly leaky electric behavior. This was reflected in a far greater P_{max} ($70 - 200 \, \mu C/m^2$), measured at 6 kV/mm, than the polarization at maximum electric field. Thus the compositions BNKT30:0.5V and BNKT30:0.5Cu are excluded from further consideration and discussion.

The d_{33}^* of doped BNKT30 varies greatly with different dopant combinations. While the d_{33}^* was identified to be 150 pm/V for undoped BNKT30, lower values of 75 pm/V, as well as higher values up to 228 pm/V were measured for doped BNTK30 ceramics. This is clearly reflected in the shape of the S-E loops and the magnitude of the normalized strain (*cf*. Figure 4.2.6).
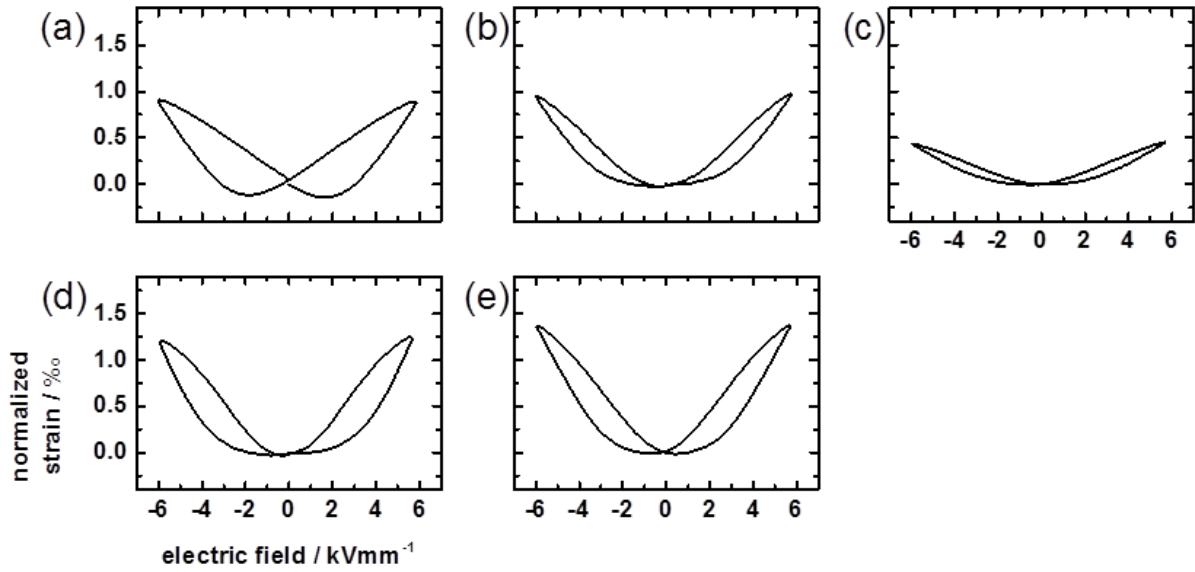
Figure 4.2.6   Polarization *vs*. electric field at a maximum electric field of 6 kV/mm for (a) undoped BNKT30, (b) BNKT30:0.1Cu,0.4V, (c) BNKT30:0.2Cu,0.3V, (d) BNKT30:0.3Cu,0.2V and (e) BNKT30:0.4Cu,0.1 ceramics.
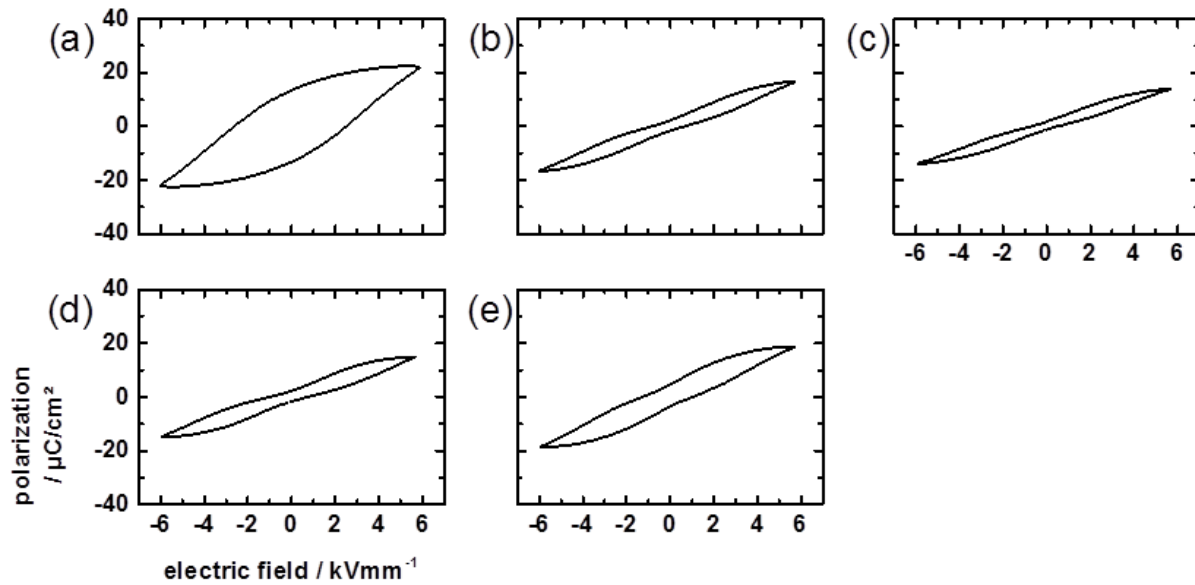
Figure 4.2.7   Polarization *vs*. electric field at a maximum electric field of 6 kV/mm for (a) undoped BNKT30, (b) BNKT30:0.1Cu,0.4V, (c) BNKT30:0.2Cu,0.3V, (d) BNKT30:0.3Cu,0.2V and (e) BNKT30:0.4Cu,0.1 ceramics.

The coercive field of doped BNKT30 ceramics is consistently lower, compared to undoped BNKT30. The decrease of E_c is significantly larger (decrease of ≤ 1.9 kV/mm) than for BNKT20 based ceramics (decrease of ≤ 1.2 kV/mm) and in contrast to the increase of E_c, observed for BNKT10 based ceramics (increase of ≤ 0.3 kV/mm). Upon

doping BNKT30, the P_{rem} nearly diminishes to 4.3 $\mu C/m^2$ or less. P_{max} is consistently lower, compared to undoped BNKT30 ceramics.

In Figure 4.2.8, d_{33}^* as a function of K content and $\frac{Cu}{Cu+V}$ dopant ratio is presented. It is apparent from the figure that a maximum d_{33}^* can be observed for doped BNKT20 compositions, close to the MPB of BNKT. That is an indication that, regardless of the aspect of doping, the K content is a critical parameter to influence the large signal strain behavior of BNKT ceramics.
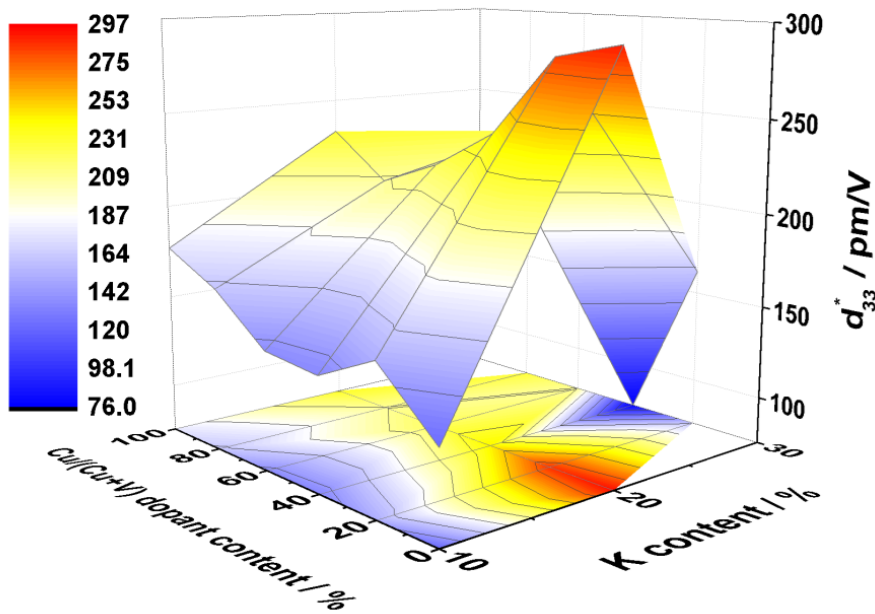
Figure 4.2.8   Piezoelectric d_{33}^* as function of K content and $\frac{Cu}{Cu+V}$ dopant content. The applied maximum electric field was 6 kV/mm.

The permittivity (ε_r) and loss tangent (tanδ) small signal parameters at temperatures from RT to 400°C of all synthesized ceramics with BNKT10, BNKT20 and BNKT30 base composition were measured at five different frequencies (100 Hz, 1kHz, 10kHz, 100kHz and 1 MHz). This allowed for the simultaneous characterization of both the temperature dependence and the frequency dependence of ε_r and tanδ.
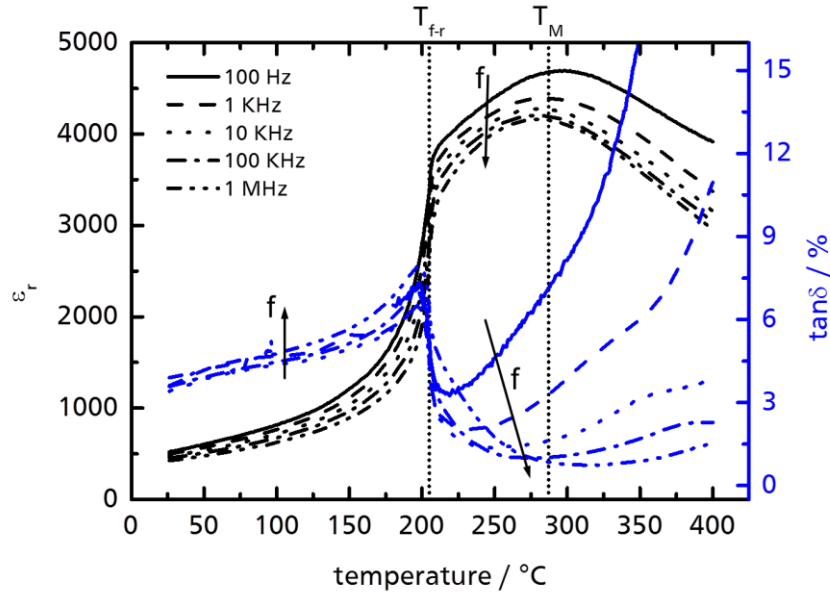
Figure 4.2.9 Permittivity and tanδ *vs.* temperature at varying frequencies of poled, undoped BNKT10 ceramics. The arrows indicate the increase of the measurement frequencies. The dotted vertical lines are highlighting T_{f-r} and T_M.

A typical permittivity *vs.* temperature plot of undoped BNKT ceramics is presented with the example of undoped BNKT10 in Figure 4.2.9. Coming from lower (ε_r is in the range of 10^2 to 10^3 at RT) permittivity at room temperature, upon heating the poled ceramics, a sharp increase in ε_r can be seen. This sharp increase is correlated with the transition temperature from ferroelectric to relaxor (T_{f-r}) behavior of the piezoelectric ceramic. Eventually at temperatures larger than T_{f-r}, a maximum in permittivity could be found for all investigated ceramics. The temperature, at which this maximum in ε_r occurs (T_M), was > 280 °C for all ceramics. Slight frequency dispersion could be observed within the temperature range. The permittivity was decreasing with increasing frequency within the whole temperature range.

Contrary to that, in a typical tanδ *vs.* temperature curve of undoped BNKT ceramics (*cf*. Figure 4.2.9), the loss at T < T_{f-r} is increasing with increasing frequency. At about T_{f-r}, the tanδ curve exhibited a maximum for all frequencies. The temperature associated with the maximum in tanδ is slightly depending on the measurement frequency. At T < T_{f-r}, the loss at lower frequencies was larger than at higher frequencies. In undoped BNKT compositions, it is evident (*cf*. Figure 4.2.9) to the eye that the maxima of tanδ and the maximum slope of the permittivity curve, both associated with the transition temperature T_{f-r}, coincide in a range of no more than ± 5 °C. The loss tangent was found to be < 10 % at and below T_{f-r}.

Detailed characteristic small signal values of all synthesized and discussed ceramics are provided in the appendix (*cf*. Table 8.4). These are T_{f-r}, T_M and the maximum ε_r.

To illustrate the changes of the permittivity *vs*. temperature and tanδ *vs*. temperature plots upon doping the BNKT ceramics, two samples were chosen to exemplify the range of possible deviations in temperature and frequency dependence of ε_r and tanδ. One plot is characteristic for ceramics, that exhibit a lesser deviation from the undoped behavior (*cf*. Figure 4.2.10), while the other plot exhibits a larger deviation from the undoped behavior (*cf*. Figure 4.2.13).
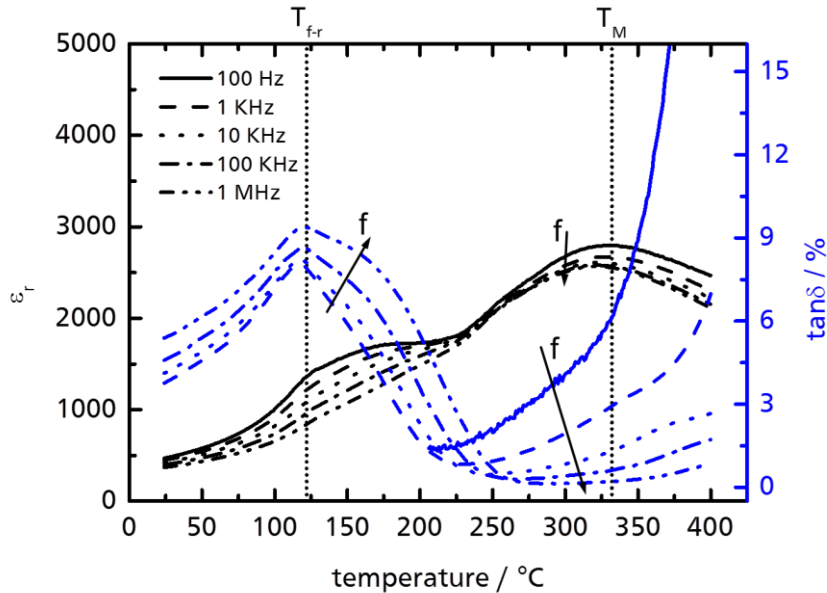
Figure 4.2.10   Representative plot (BNKT10:0.2Cu,0.3V) of relative permittivity and tanδ *vs*. temperature at varying frequencies with slightly decreased T_{f-r} (as characteristic for the BNKT10 doping series). The arrows indicate the increase of the measurement frequencies. The dotted vertical lines are highlighting T_{f-r} and T_M.

Doped BNKT10 ceramics are characterized by a consistently lower T_{f-r}, which was determined to be 122 °C – 157 °C in the doped case *vs*. 205 °C in the undoped case (*cf*. Figure 4.2.10). In all doped ceramics, the respective T_M is shifted to higher temperatures. The maximum ε_r, however, does not follow a trend. Compared to undoped BNKT10 (ε_r of 3905), slightly higher (ε_r of 3993 in case of BNKT10:0.4Cu,0.1V) as well as significantly lower (ε_r of 2062 in case of BNKT10:0.2Cu,0.3V) could be observed upon doping (*cf*. Figure 4.2.10).

Doped BNKT10 ceramics could in addition be characterized as having a lesser deviation of the doped from the undoped behavior of ε_r and tanδ, as exemplified in Figure 4.2.10. In proximity of the shifted increase in ε_r at about T_{f-r}, a broad, increased frequency dispersion can be noted. For tanδ, this dispersion in frequency is far more pronounced throughout the whole temperature range and in addition, the peak of tanδ is slightly broadened in comparison to the undoped BNKT ceramics. The slope of the increase in ε_r of the doped BNKT10 ceramics is in addition less steep, compared to the undoped BNKT10 ceramics.
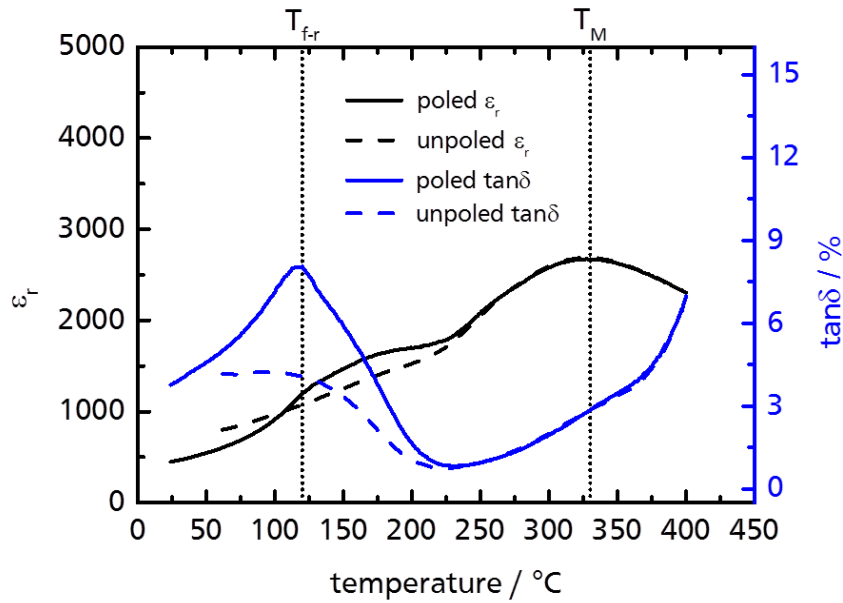
Figure 4.2.11 Representative plot of BNKT10:0.2Cu,0.3V ceramics, indicating the relative permittivity and tanδ *vs.* temperature of poled and unpoled (depoled at 400 °C) samples at 1 kHz. The dotted vertical lines are highlighting T_{f-r} and T_M of the poled samples.

From the comparison of poled with unpoled samples (*cf.* Figure 4.2.11), it is apparent, that a FE to relaxor transition occurs upon heating poled doped BNKT10, while the unpoled samples are characterized by a significantly reduced tanδ around T_{f-r}. The relative permittivity of the poled samples as well deviates from the unpoled samples: slightly below T_{f-r}, it is higher than of poled samples and above T_{f-r} it is lower than of poled samples.

T_M of doped ceramics is in all cases higher than of undoped BNKT20 and BNKT30. T_M of up to 351 °C (BNKT20:0.5V) were obtained upon doping. Furthermore the maximum ε_r increased consistently upon doping BNKT20 and BNKT30. For BNTK20 ceramics, a 1.6- to 3.0-fold increase in maximum permittivity from an ε_r of 1750 of undoped BNKT20 (to 2844 – 5281) could be observed. Doped BNKT30 ceramics exhibit a 1.7- to 2.0-fold increase in maximum permittivity (ε_r of 2561 – 3077), compared to an ε_r of 1524 of undoped ceramics (*cf.* Figure 4.2.12).
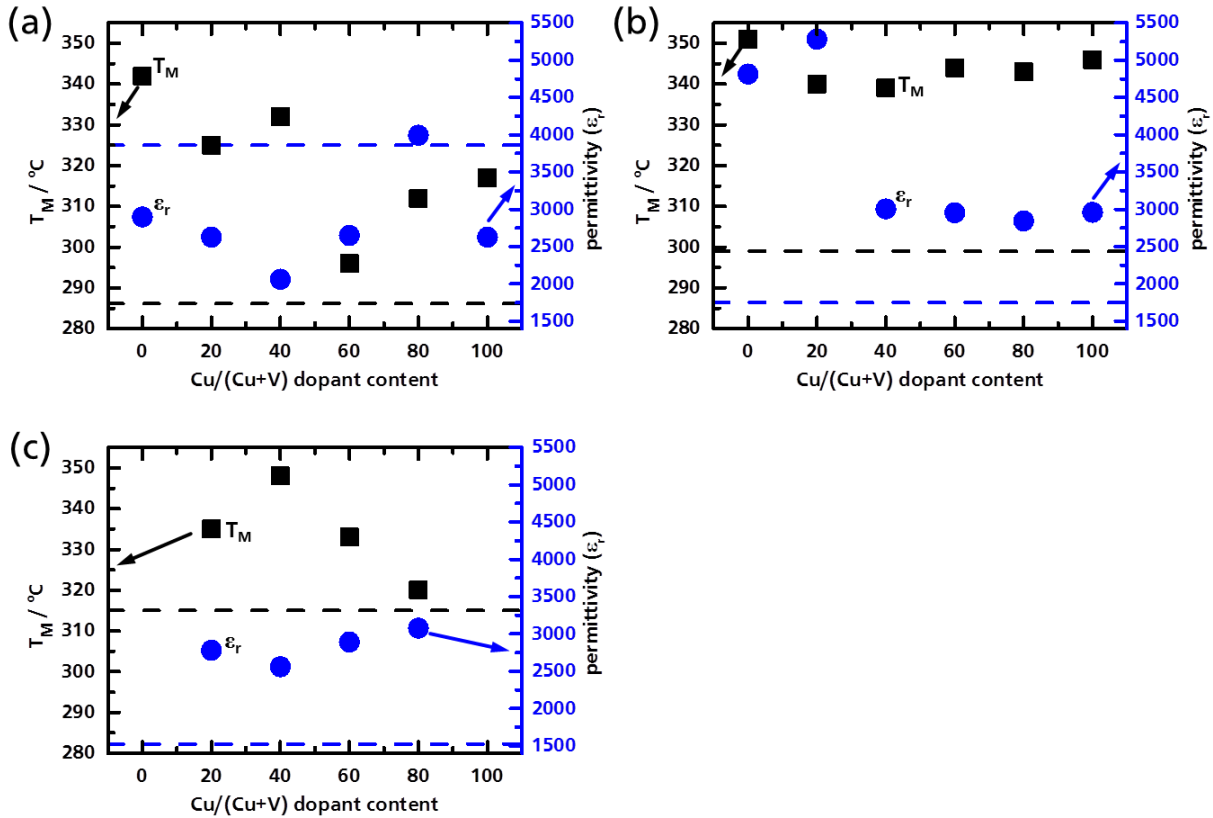
Figure 4.2.12 Piezoelectric maximum small signal ε_r RT and T_M of doped (a) BNKT10, (b) BNKT20 and (c) BNKT30 ceramics. The dashed horizontal lines each represent the value of T_M and ε_r of the respective undoped ceramics.

Analogously to doped BNKT10 ceramics, doped BNKT20 and BNKT30 ceramics are characterized by a consistently lower T_{f-r}, however, with a shift to T_{f-r} being as low as 85 °C. This is especially drastic for BNKT30 based compositions, where all doped ceramics possess a low T_{f-r} close to RT ($< 61°C$), while undoped BNKT30 ceramics possess a high T_{f-r} of 200 °C (*cf.* Figure 4.2.15). Doped BNKT20 and BNKT30 ceramics could be characterized as having a larger deviation of the doped from the undoped behavior of ε_r and tanδ, as exemplified in Figure 4.2.13. The frequency dispersion of tanδ was, compared to doped BNKT10 ceramics, broader and additionally, the peak of tanδ itself was significantly broadened.
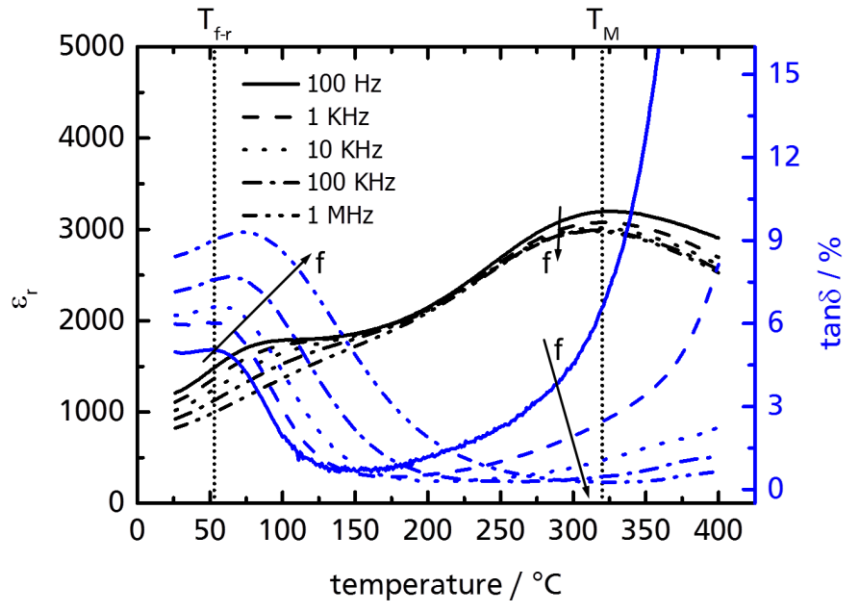
Figure 4.2.13 Representative plot (BNKT30:0.4Cu,0.1V) of relative permittivity and tanδ *vs*. temperature at varying frequencies with significantly decreased T_{f-r} (as characteristic for the BNKT20 and BNKT30 doping series). The arrows indicate the increase of the measurement frequencies. The dashed lines each represent the value of T_M and ε_r of the respective undoped ceramics.

The drop in T_{f-r} can be explained by the existence of more defects in the ceramics: As aliovalent elements (Cu and V) are introduced to the system, they introduce internal random fields in the material in addition to the already existing internal fields, explained by for instance Wu *et al.*[269]. Schütz *et al.*[270] attribute T_{f-r} to the transition from ferroelectric long range order behavior to disordered short range order relaxor behavior to the disruption of the Bi-O hybridization in the material, which they observed at about T_{f-r} (by Schütz *et al.* referred to as T_d). Cu and V therefore likely have an influence on the Bi-O hybridization.

The deviation of ε_r and tanδ of poled from unpoled samples is not very pronounced for doped BNKT20 and BNKT30 ceramics (*cf*. Figure 4.2.15). This correlates with the fact that these ceramics do not display a strong FE behavior, which is in accordance with for instance their low P_r. Above T_{f-r}, a higher ε_r and tanδ can be observed. In case of ε_r, the deviation persists up to temperatures as high as T_M. This indicates the presence of polar entities up to temperatures higher than T_{f-r}.
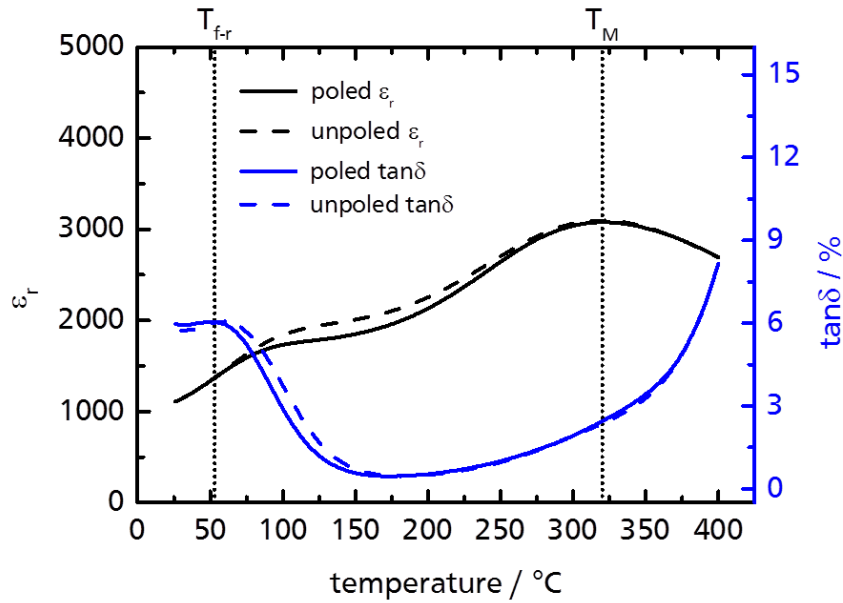
Figure 4.2.14 Representative plot of BNKT30:0.4Cu,0.1V ceramics, indicating the relative permittivity and tanδ *vs.* temperature of poled and unpoled (depoled at 400 °C) samples at 1 kHz. The dotted vertical lines are highlighting T_{f-r} and T_M of the poled samples.

The maximization of strain at the MPB was more pronounced in case of doped BNKT ceramics, which can be easily grasped, comparing Figure 4.2.15 (a) and (b). This implies, that the increase in strain, from which an increased d_{33}^* results, was not exclusively caused by the lowering of the transition temperature T_{f-r}.
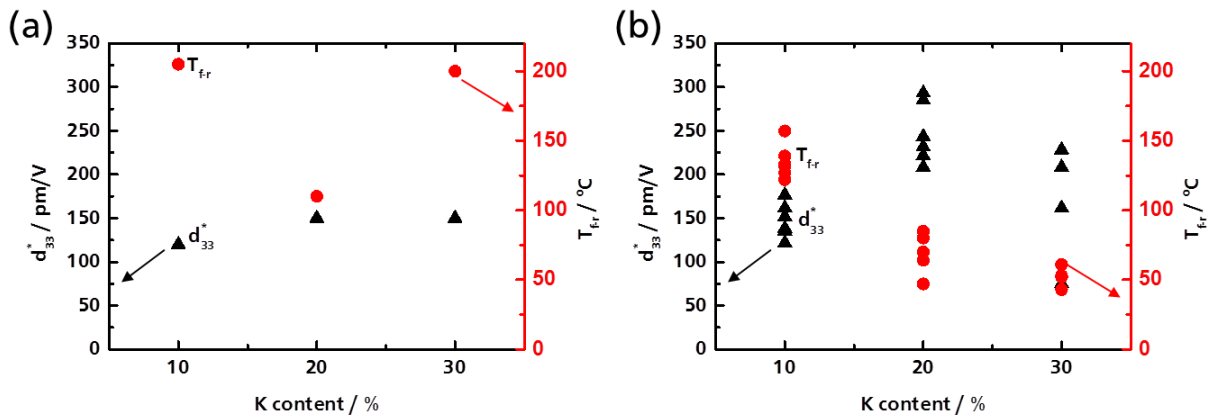
Figure 4.2.15 Piezoelectric d_{33}^* and T_{f-r} of (a) undoped and (b) doped BNKT ceramics with different potassium content, emphasizing global trends upon doping. The applied maximum electric field was 6 kV/mm.

The maximum polarization of undoped BNKT ceramics follows the general trend of the maximum d_{33}^* of BNKT ceramics: at the MPB, d_{33}^* as well as P_{max} are highest (*cf.* Figure 4.2.15(a)). This is not true for doped ceramics. Upon increasing K content of doped BNKT ceramics, P_{max} displayed a noticeable decreasing trend (*cf.* Figure 4.2.15(b)).

With respect to P_{rem} and E_c, undoped and doped ceramics display the same global trend: higher K content lead to a trend towards lower E_c as well as a lower P_{rem}. However, the decrease in E_c upon increasing K content was found to be stronger for doped ceramics, compared to undoped BNKT ceramics (*cf*. Figure 4.2.16). This trend of undoped BNKT ceramics is also reported in the literature by for instance Otoničar *et al.*[23], however, their E_c for BNKT30 was reported higher (3.7 kV/mm *vs*. 2.5 kV/mm in this study). This is most probably rooted in the significantly different T_{sint} of 1090 °C (*vs*. 1150 °C in this study). Yoshii *et al.*[25] also report, that the coercive field of BNKT10 ceramics is the largest, followed by BNKT20 and BNKT30, with their measured E_c of BNKT30 being at about 3.5 kV/mm. However, they do not specify the sintering temperature. Thus the difference may be rooted in a difference in T_{sint}.
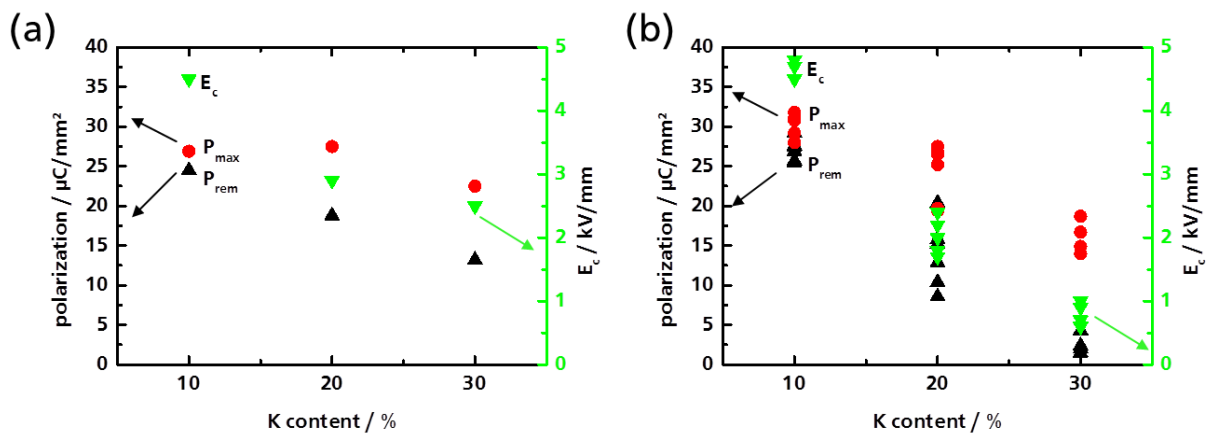
Figure 4.2.16 E_c, P_{rem} and P_{max} of (a) undoped and (b) doped BNKT ceramics with different potassium content, emphasizing global trends upon doping. The applied maximum electric field was 6 kV/mm.

The variation of piezoelectric key figures within one set of doped ceramics of a single BNKT base composition was in general not very high, compared to the variation in-between BNKT10, BNKT20 and BNKT30 based, doped ceramics (the only major exception being the considerably lower d_{33}^* of BNKT30:0.2Cu,0.3V). Exemplarily, the variation of piezoelectric key figures of BNKT10 ceramics is depicted in Figure 4.2.17. Within compositions of a set with fixed K content, the values fluctuate, but no clear trend with respect to the Cu/(Cu+V) ratio is evident.
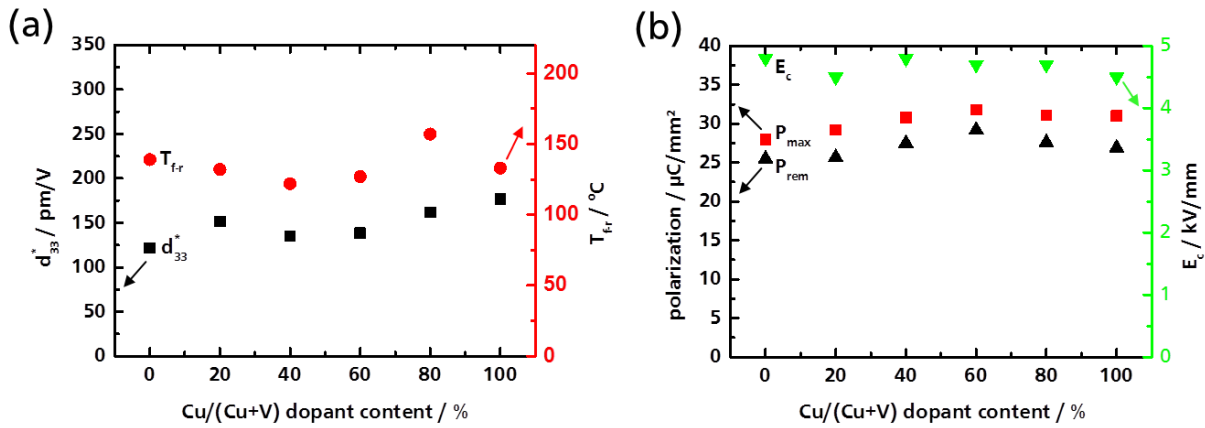
Figure 4.2.17 Piezoelectric d_{33}^* and $T_{f\text{-}r}$ (a) as well as E_c, P_{rem} and P_{max} (b) of BNKT10 ceramics, doped with different amounts of Cu and V. The applied maximum electric field was 6 kV/mm.

4.3. Dielectric Spectroscopy Under Resonance

Doped BNKT10 displays promising piezoelectric characteristics for instance for application as sensor, such as a comparably high $T_{f\text{-}r}$, high P_{max} and high P_{rem}. To focus on this aspect, selected doped BNKT10 compositions were characterized in greater detail and depth with advanced methods. Dielectric spectroscopy was employed to evaluate the resistances at varying frequencies and determine E_A at different temperatures under different P_{O_2}. EPR and XPS were used to assess local environment and oxidation states. From here on, in the following sections 4.3- 4.6, exclusively results for undoped and doped BNKT10 ceramics are presented and discussed in greater depth.

In order to assess characteristics, important for sensing applications, the resonance behavior of BNKT10 ceramic samples was investigated by means of dielectric spectroscopy. One is able to obtain detailed information on the electro-mechanic processes occurring in the ceramics, by using electrical models to describe (simulate) the data obtained *via* dielectric spectroscopy.
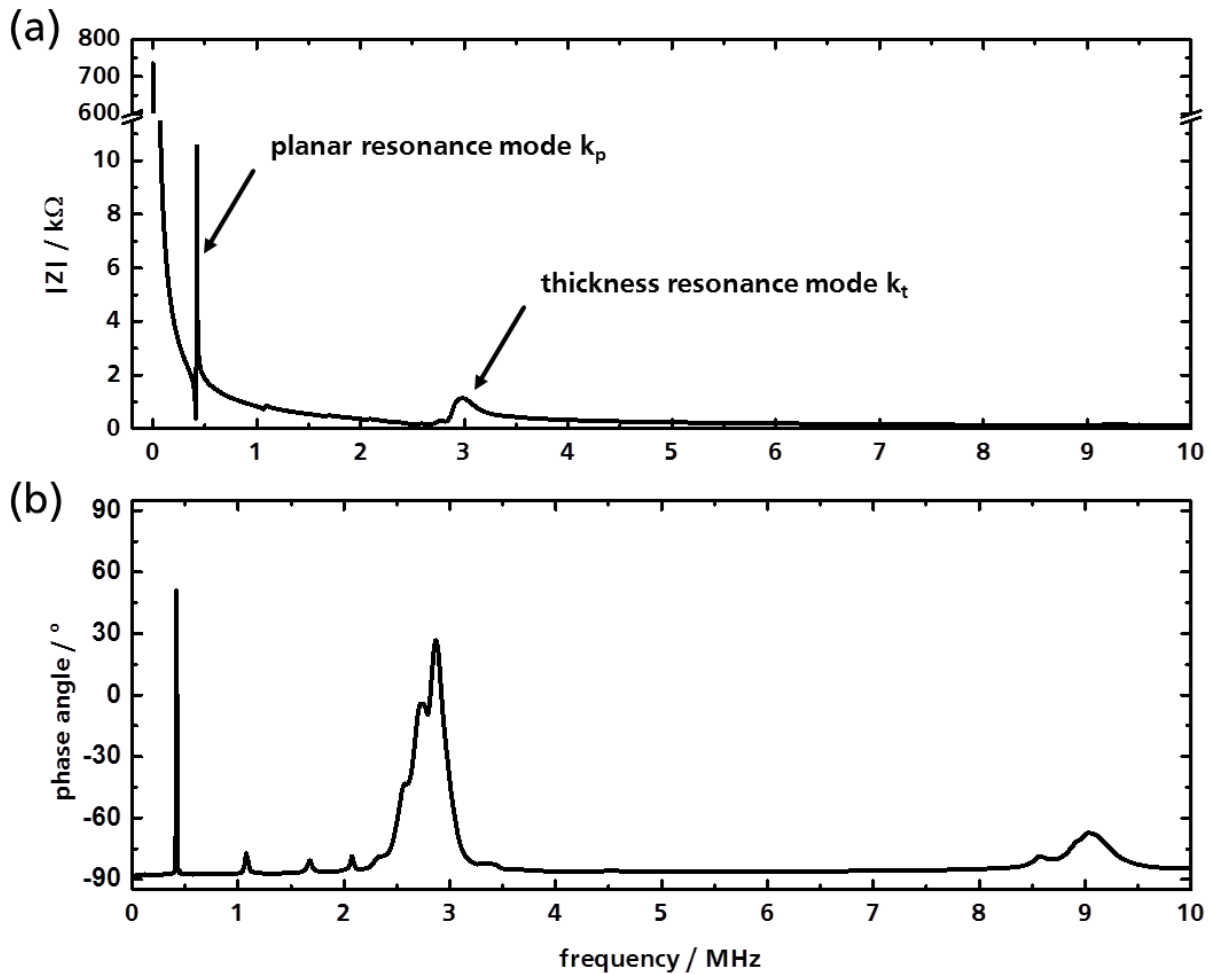
Figure 4.3.1 Impedance |Z| (a) and phase angle (b) survey spectrum of undoped BNKT10 from 1 kHz to 10 MHz with indicated resonance modes. Please note that due to identification of the modes the impedance axis (ordinate) features a break with different scaling afterward.

All BNKT10 ceramics possess a distinct dielectric spectrum, which is characterized by two major resonances (*cf*. Figure 4.3.1) in case of the disk-shaped samples, employed in this work. One resonance, roughly observed at a frequency of 400 kHz, was associated with the coupling in plane of the disk (k_p) and the other at a frequency of about 3 MHz, was associated with the coupling in thickness of the ceramic disks (k_t). They are characterized by a peak in the phase angle at frequencies lower than at the respective resonance. PZT-based materials are characterized by a reported peak in-phase angle of close to 90°, when poled sufficiently (according to Manabu *et al*.).[271] However, in undoped and doped BNKT10 based ceramics, synthesized in this work, the maximum phase angle did not exceed 65.7° (BNKT10:0.3Cu,0.2V). The planar mode is characterized by a narrow (approximately 15 kHz wide) resonance event, while the thickness mode exhibits a broader (approximately 0.7 MHz wide) resonance event. Both thickness, as well as planar resonance spectra may exhibit minor resonances, which exist as side shoulders on the major resonances or can be observed independently.
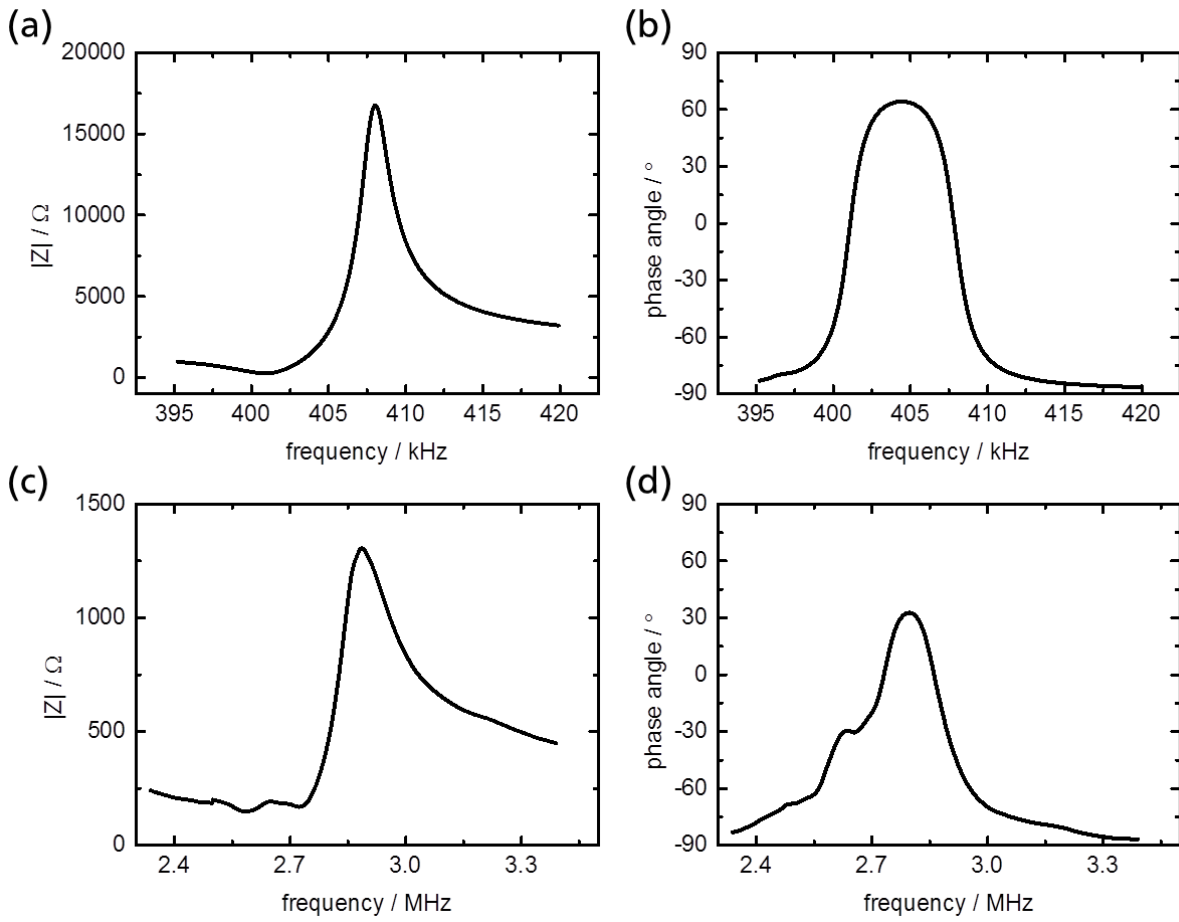
Figure 4.3.2 Impedance spectra at resonance of undoped BNKT10 with (a) and (b) detailing the resonance in the sample plane, associated with k_p and (c) and (d) indicating the resonance in sample thickness direction, associated with k_t.

In order to more accurately evaluate the measured data and correctly assess k_p and k_t, the impedance resonance spectra were fitted, by using equivalent circuits to model the electric behavior of the samples at the respective resonance (*cf.* Figure 4.3.3). The Nyquist plot, depicting the real part *vs.* the imaginary part of the impedance (*cf.* Figure 4.3.3 (a)) served as a means to evaluate the resonance response of the BNKT10 ceramics. For all samples, characteristic elliptically shaped circles were obtained. Those extend to both, the negative, as well as the positive imaginary impedance quadrant, while having positive real impedance. For one major resonance with no minor resonances, one equivalent circuit as detailed in Figure 4.3.3 (b) was used. This equivalent circuit with two CPE, allowed fitting the data more accurately, however, one has to bear in mind that this combination may not be physically meaningful. As discussed in Section 2.2.2, a simpler model should be used, which accounts exclusively for the resonance behavior. The here employed equivalent circuit takes additional contributions, which do not result from the resonance, in account, too.
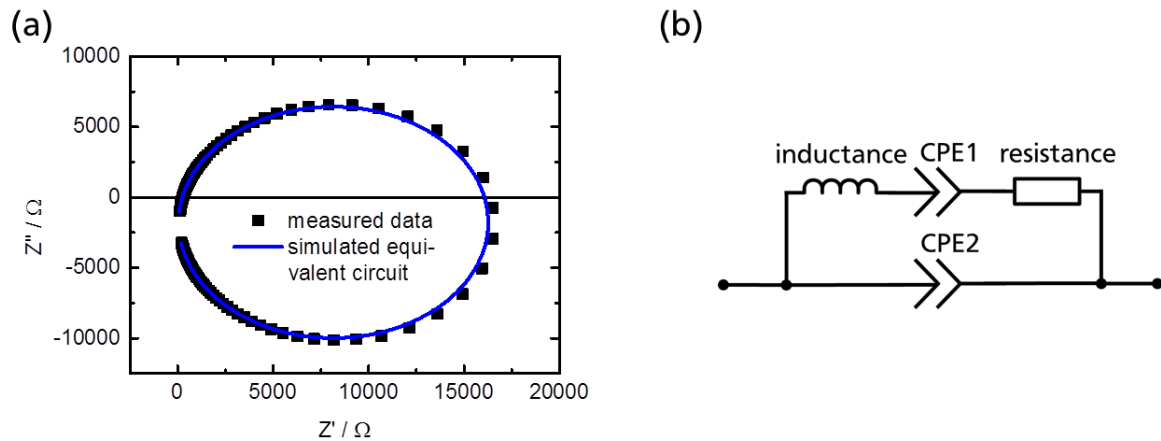
Figure 4.3.3   Exemplary Nyquist plot (a) of the in plane resonance of undoped BNKT10 with the corresponding equivalent circuit (b) for the simulation of the experimental data.

While the planar coupling of doped samples was mostly unchanged compared to undoped BNKT10 (*cf.* Figure 4.3.4 (a)+(b)), doped samples displayed minor secondary resonances in the thickness resonance mode, compared to undoped samples (*cf.* Figure 4.3.4 (c)+(d)).

When plotted as a Nyquist plot, these minor resonances occur in the form of minor loops within the major loop (*cf.* Figure 4.3.5 (a)). These minor resonances could be fitted, employing two or more combined equivalent circuits (of the circuit detailed in Figure 4.3.3 (b)) in order to fit the data obtained through experiments (*cf.* Figure 4.3.5 (b)). Every additional equivalent circuit, like the one described in Figure 4.3.3 (b), enables the fitting of an additional resonance loop. Thus it is possible to fit any given number of minor resonances in addition to the major resonance; however, only significant minor resonances were fitted.
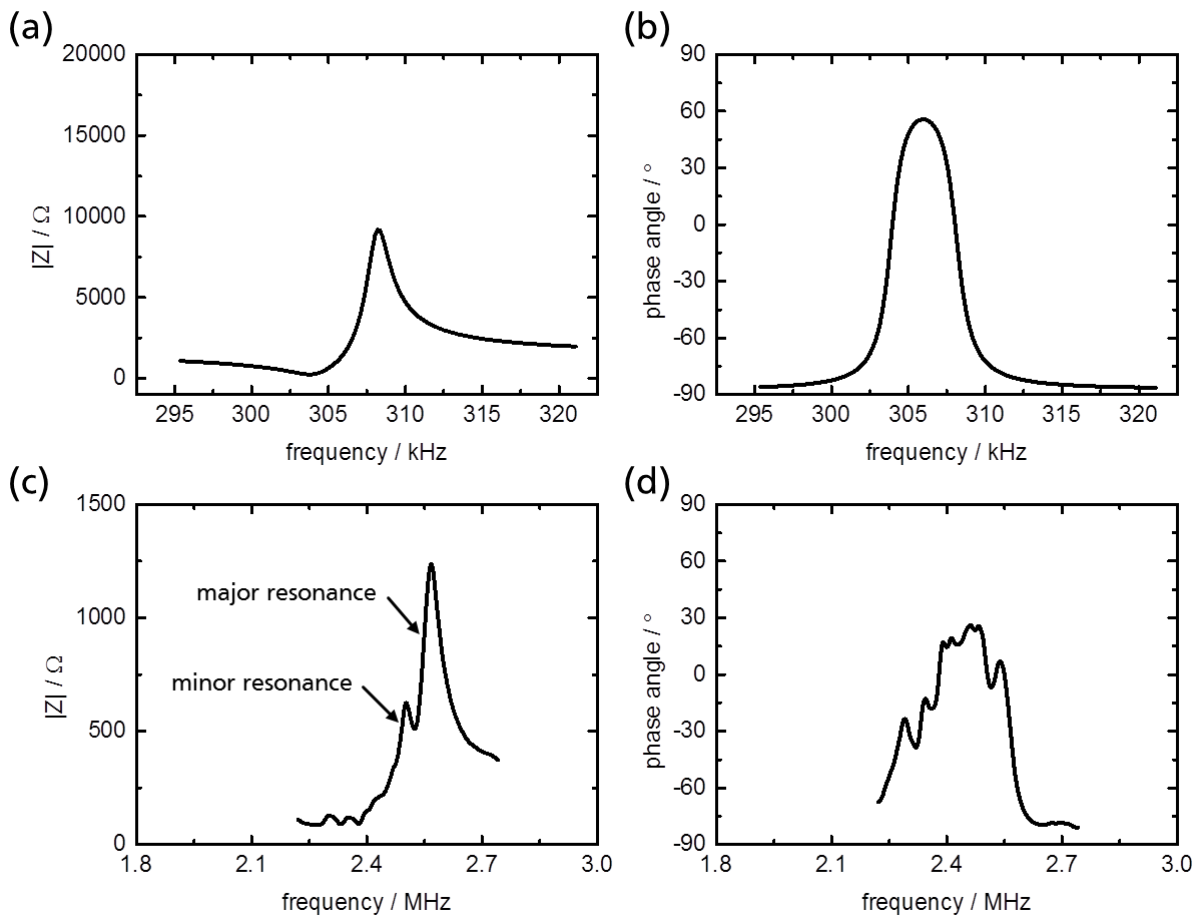
Figure 4.3.4   Representative resonance impedance spectra of doped BNKT10:0.1Cu,0.4V with (a) and (b) detailing the resonance in the sample plane, associated with k_p and (c) and (d) indicating the resonance in thickness direction, associated with k_t.

As apparent from Figure 4.3.4 (c), very weak, minor resonances exist (in-between 2.2 and 2.4 MHz in this example), however, were neglected in the fit. Despite this fact, as evident from Figure 4.3.5 (a), a fairly good fit of the major and stronger minor resonance could be obtained to describe the behavior of the material at thickness resonance. These minor resonances occur due to an inhomogeneous response of the material, which manifests itself in the additional resonance(s).

From this fitted data, the coupling factors k_p and k_t, as well as the mechanical quality factors ($Q_{M,p}$ in planar and $Q_{M,t}$ in thickness direction) of all synthesized BNKT10 ceramics, were determined (*cf.* Table 4.3.1). The planar coupling factor of undoped and doped BNKT10 is not significantly influenced by doping and varies between 0.19 and 0.23. There is, however, a strong influence of doping on k_t. It varies from as large as 0.56 to as small as 0.31. The resonance behavior of $Q_{M,p}$ and k_p is decoupled from the resonance behavior in thickness direction. $Q_{M,p}$ shows a largely decreasing trend with increasing Cu dopant content, with the only exception being BNKT10:0.5V, exhibiting a slightly lower $Q_{M,p}$ than BNKT10:0.4V,0.1Cu (191 *vs.* 195, respectively). The decreasing trend can be rationalized by Cu segregation at the grain boundary, likely resulting in secondary phases below XRD detection limit.
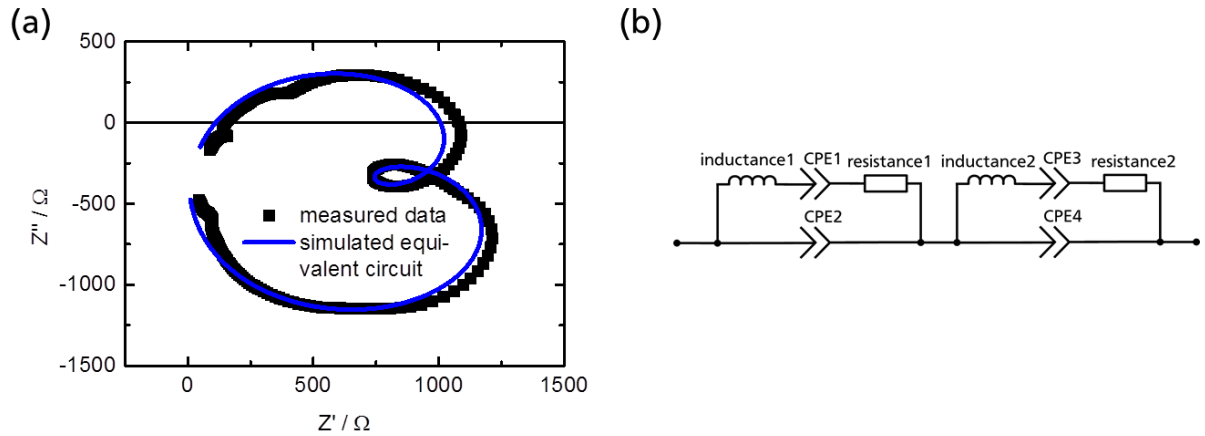
Figure 4.3.5   Exemplary Nyquist plot (a) of two overlapping thickness mode resonances of BNKT10:0.2Cu,0.3V with the corresponding equivalent circuit (b) for the simulation of the experimental data.

In case of k_t, there is no clear trend evident. One can observe, that the k_t may be inversely related to $Q_{M,t}$, as k_t is consistently higher, when $Q_{M,t}$ is lower (*cf.* Figure 4.3.6). As described by Kamel *et al.*[272], the coupling factors depend on the domain wall motion and thus on pinning of the domain walls due to immobile defects. Consequently a different defect distribution or concentration is to be expected for samples with different k_t.

Table 4.3.1 | Coupling Factors and Mechanical Quality Factors of BNKT10 Ceramics (partially adapted from Blömker *et al.*[261] and reprinted with permission, © 2015 The American Ceramic Society).

composition	planar resonance				thickness resonance			
	F_a / kHz	F_r / kHz	k_p	$Q_{M,p}$	F_a / MHz	F_r / MHz	k_t	$Q_{M,t}$
undoped BNKT10	400.95	407.99	0.21	207	2.58	2.89	0.50	10
BNKT10:0.5V	423.05	429.44	0.19	191	2.46	2.65	0.41	17
BNKT10:0.1Cu,0.4V	303.75	308.34	0.19	195	2.23	2.57	0.56	9
BNKT10:0.2Cu,0.3V	445.96	453.38	0.20	161	2.55	2.82	0.48	12
BNKT10:0.3Cu,0.2V	451.32	460.81	0.23	111	2.70	2.84	0.31	22
BNKT10:0.4Cu,0.1V	447.64	456.041	0.21	75	3.67	3.96	0.42	22
BNKT10:0.5Cu	445.83	453.91	0.21	50	2.44	2.66	0.45	6

$Q_{M,t}$ is very low (≤ 22), indicating a high dampening at the resonance. This is actually desirable for sensor applications, especially in combination with high k_t.[21,273] It

additionally allows for a broad usable resonance bandwidth. Especially BNKT10:0.1Cu,0.4V stands out with a high k_t of 0.56 in combination with a low $Q_{M,t}$ of 9.
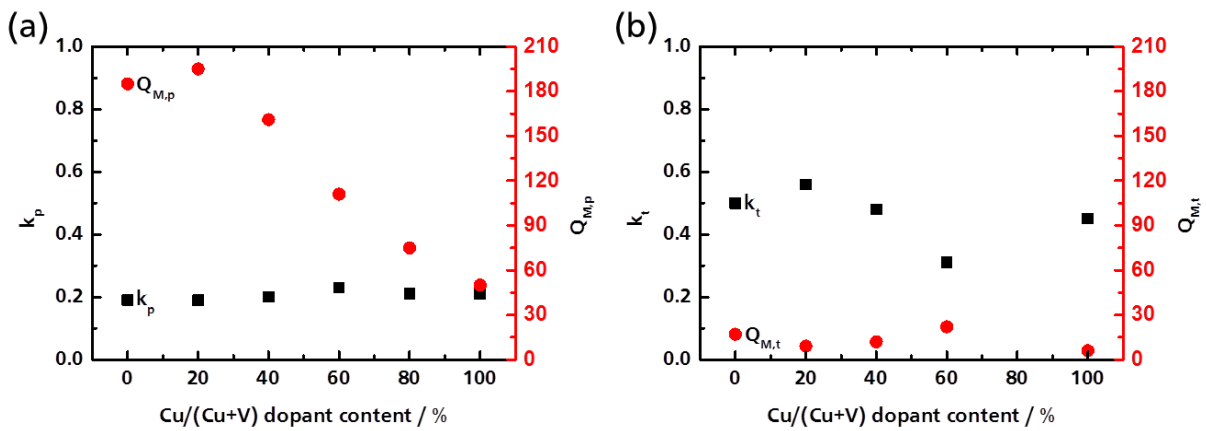
Figure 4.3.6 Planar (a) and thickness (b) resonance coupling factors and mechanical quality factors of BNKT10 ceramics, doped with different amounts of Cu and V.

4.4. Dielectric Spectroscopy in Atmospheres with Different Oxygen Partial Pressure

Dielectric spectroscopy at elevated temperatures and in different atmospheres allows for the assessment of the conduction processes, exhibited by the investigated BNKT10 ceramics.

The Cole-Cole plots of the BNKT10 ceramics are characterized by one or more independent or overlapping semicircles (*cf*. Figure 4.4.1). The measured data could be fitted, using equivalent circuits, comprising a contact resistance in series with one or more units, consisting of a resistance and a constant phase element (CPE), in parallel. This is detailed in Figure 4.4.2 for the example of four units of resistance parallel to CPE, each unit representing one individual conduction process. In general the fit by a simulated equivalent circuit was in very good agreement with the measured data.
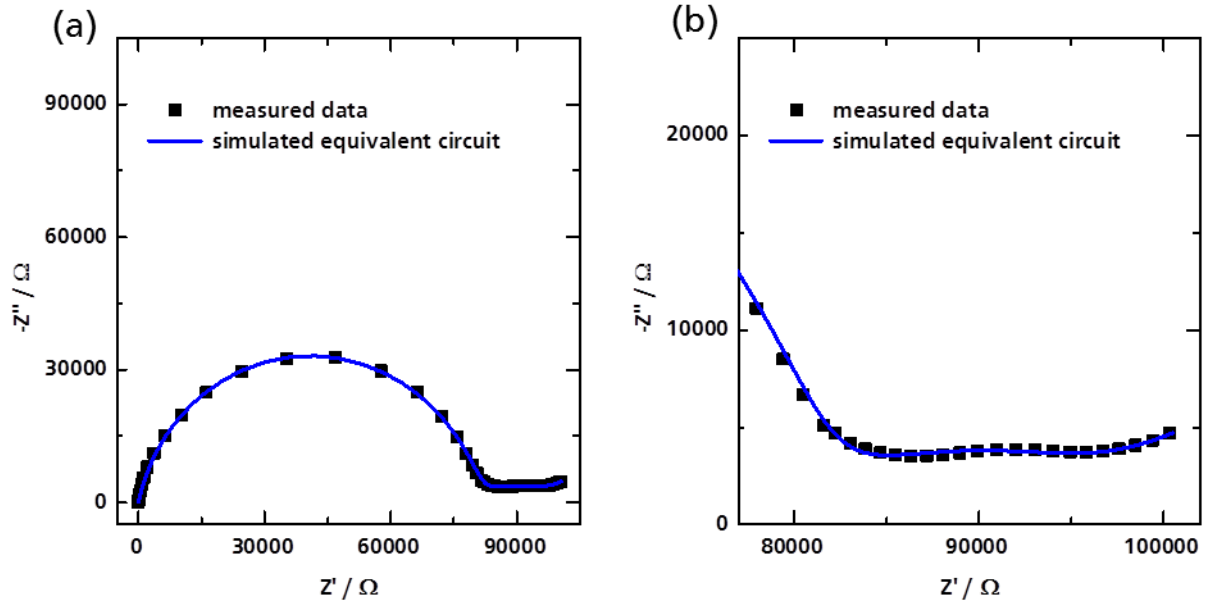
Figure 4.4.1 Exemplary Cole-Cole plot of impedance spectroscopic measurement of BNKT10:0.5V at 500°C and the respective fit by an equivalent circuit, detailed in Figure 4.4.2. Overview (a) of the whole Cole-Cole plot and detail (b) of the high Z' region, to illustrate the additional semi-circle and the final increase at high Z' due to contact contributions.

The measurement of dielectric properties at different elevated temperatures was in addition used to calculate the resistivity of the bulk material at the respective temperatures. All measured data points of the bulk resistivity, plotted in an Arrhenius-type of graph (*cf.* Figure 4.4.3), could be fit fairly well, assuming linear dependence, with the adjusted R^2 being > 99.4 % in all cases. Thus the investigated BNTK10 ceramics follow Arrhenius behavior within the investigated temperature range.
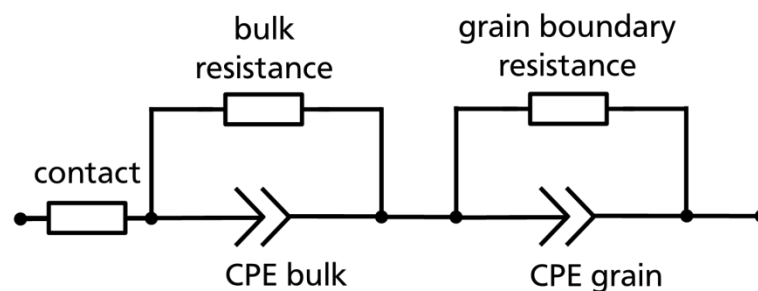
Figure 4.4.2 Exemplary equivalent circuit to simulate impedance spectroscopic data (as presented in Figure 4.4.1) at elevated temperature, taking contact, bulk and grain boundary contributions into account.

Undoped BNKT10 ceramics display the largest bulk resistivity of the investigated BNKT10 ceramics in the investigated temperature range (1.6×10^5 Ωm to 2.0×10^8 Ωm). Regardless of whether the samples were doped with Cu only, V only or both Cu and V, the resistivity in the observed temperature range decreased in all cases, compared to undoped BNKT10. BNKT10:0.1Cu,0.4V displays the highest

resistivity (1.8×10^4 Ωm to 1.3×10^7 Ωm) of the doped samples and the determined resistivity was in close proximity to BNKT10:0.5Cu (~1.0×10^4 Ωm to 7.3×10^6 Ωm). BNKT10:0.5V exhibits still significantly lower (3.3×10^3 Ωm to 1.8×10^6 Ωm) resistivity compared to undoped BNKT10, but also, compared to the other investigated doped BNTK10 ceramic.

This observed maximum in resistivity implies that the undoped BNKT10 will most likely (I) contain the lowest amount of charge carriers of the investigated ceramics or (II) contain a relatively lower amount charge carriers with fast transport processes. Any addition of Cu, V or a combination thereof, displayed increased conductivity, which can be correlated with (I) a higher charge carrier concentration and (II) charge carrier mobility.
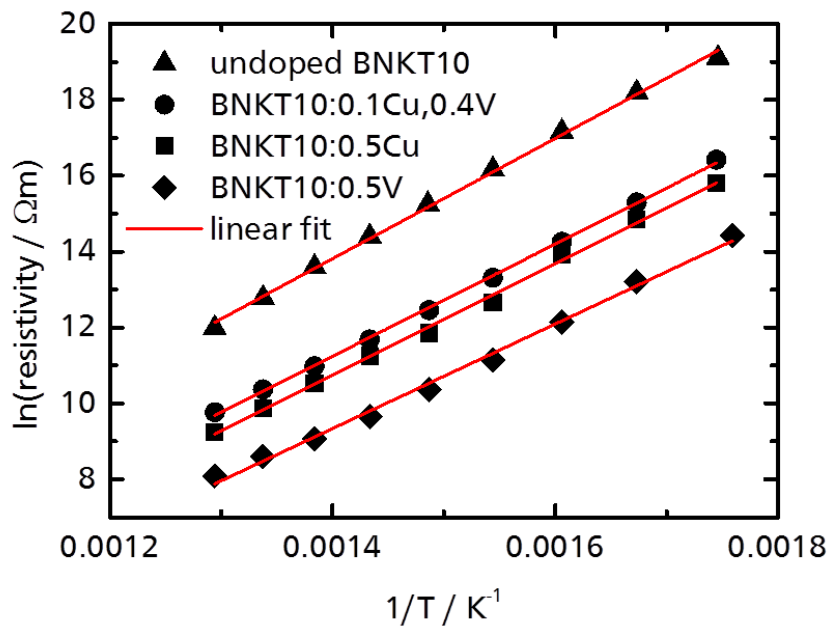
Figure 4.4.3   Arrhenius plot of different BNKT10 compositions measured in ambient air with their respective linear fit indicated by red lines.

The activation energies (E_A) of the bulk of BNKT10 ceramics, measured in ambient air (as extracted from the Arrhenius plot in Figure 4.4.3), were all in the range of 1.25 eV to 1.37 eV, which is no significant deviation (*cf.* Table 4.4.1). This could allow for the conclusion, that the major conduction process in BNKT10 ceramics is unchanged upon doping.

Table 4.4.1 | Arrhenius Plot Fitting Parameters and E_A of BNKT10 Ceramics in Air

sample	atmosphere	intercept of fit /Ωm	slope of fit /ΩmK	bulk E_A /eV
undoped BNKT10	air	-8.4	15849	1.37
BNKT10:0.5Cu	air	-9.8	14694	1.27
BNKT10:0.1Cu,0.4V	air	-9.1	14570	1.26
BNKT10:0.5V	air	-9.4	14770	1.25

In general the E_A, determined in this work, are comparable to energies reported in literature (*cf*. Table 4.4.1). BNKT10 ceramics prepared by Rao *et al.*[245] exhibit E_A of 1.06 eV for the bulk, which is slightly lower. In addition, the resistivity is $< 5\times10^2$ Ωm. This likely indicates a higher leakage current, which is further corroborated be the fact that their reported P_{max} and P_{rem} are also lower than in this work.

Table 4.4.2 | E_A of Other BNKT and BNKT-Based Ceramics in Air

sample	bulk E_A /eV	grain boundary E_A /eV	reference
BNKT10	1.06	1.07	[245]
BNKT12	2.14	-	[274]
BNKT15	0.95	1.05	[245]
BNKT16	2.21	-	[274]
BNKT18	1.73	2.09	[275]
BNKT18	1.26	1.23	[123]
BNKT18 with 0.1Li substituted *vs*. Na	0.87	0.93	[123]
BNKT20	0.85	0.83	[245]
BNKT20	2.18	-	[274]
BNKT20 with 0.1 Li substituted *vs*. Na	0.45	0.52	[276]
$0.97Bi_{0.5}(Na_{0.78}K_{0.22})_{0.5}TiO_3$-0.03KNN	1.08	1.08	[277]
BNKT30	1.13	0.83	[245]
BNKT45	1.28	0.81	[245]
BNKT50	0.46	0.45	[278]

Some of the reported E_A deviate significantly from each other. This is especially evident in case of BNKT18 and BNKT20, where E_A with large differences of 0.53 eV and 1.33 eV, respectively, are reported by different authors. The results of Li *et al.*[274] have to be seen critical in this context, as firstly, they determine the E_A by using the relaxation times as an indicator instead of the specific resistivities (used in this work and the other works presented in Table 4.4.1). Secondly, they use 2 to 4 temperature steps to determine E_A, compared to no less than nine steps used in this work. Considering this heterogeneous picture, further studies on BNKT-based ceramics seem necessary to clarify the E_A of the different compositions.

In order to assess the conduction processes under different oxygen partial pressures (P_{O_2}), different gases and pressures were used at the elevated temperatures during the dielectric measurements. The respective P_{O_2} of the saturated, sufficiently purged atmosphere in O_2 was one bar, in air was 0.21 bar, in vacuum was $2.1 \cdot 10^{-6}$ bar and in Ar with 1 vol.% H_2 was $< 10^{-18}$ bar [279].
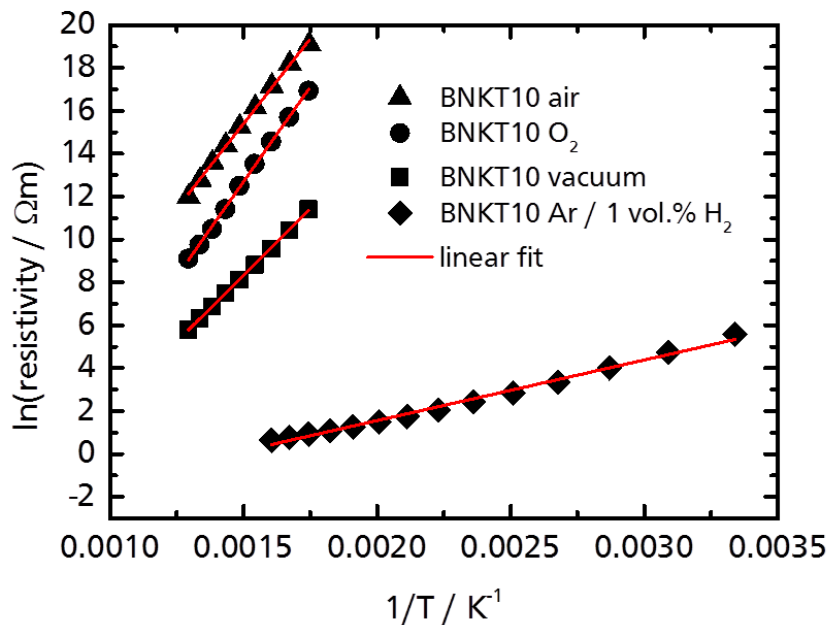
Figure 4.4.4 Arrhenius plot of undoped BNKT10 measured in different atmospheres, with the respective linear fit indicated by red lines. Samples in Ar/H$_2$ atmosphere were measured in a different temperature range (25 °C – 350 °C).

Varying P_{O_2} resulted in a distinct decrease in resistivity (*cf.* Figure 4.4.4). This is true for exposing ceramics at elevated temperatures to higher P_{O_2} (one bar), as well as for exposing ceramics to lower P_{O_2} (as low as $< 10^{-18}$ bar). Of all investigated P_{O_2}, the resistivity of undoped BNKT10 in air was the highest (1.6×10^5 Ωm to 2.0×10^8 Ωm). Next lowest, the resistivity of BNKT10 in pure oxygen was in the range of 9.0×10^3 Ωm to 2.3×10^8 Ωm. Despite the lower resistivity in the observed temperature

range, E_A of undoped BNKT10 in O_2 was higher than that in air (1.52 eV *vs.* 1.37 eV, respectively). In vacuum, the resistivity was reduced to 3.3×10^2 Ωm to 8.9×10^4 Ωm and E_A decreased to 1.07 eV.

In Ar/H$_2$ atmosphere with the lowest P_{O_2}, a significantly lowered E_A of 0.23 eV was found. This is accompanied by a considerably lower observed resistivity (1.9×10^0 Ωm to ~2.7×10^3 Ωm) of undoped BNKT10 in Ar/H$_2$ atmosphere. The samples were black and displayed metallic luster after treatment in Ar/H$_2$ atmosphere.

In the investigated temperature range, oxygen diffusion into and out of the BNKT10 ceramics according to

$$2O_O^X \leftrightarrow O_2 + 2V_O^{\bullet\bullet} + 4e' \tag{4.4.1}$$

can occur. As the P_{O_2} is influenced, this will also influence the concentration of $v_O^{\bullet\bullet}$ - *i.e.*: an increase of P_{O_2}, will result in a decrease of $v_O^{\bullet\bullet}$ and *vice versa*. The overall conductivity (σ_{total}) of the ceramics can be described by

$$\sigma_{total} = \sigma_n + \sigma_p + \sigma_i \quad , \tag{4.4.2}$$

with σ_n being the electronic conduction, σ_p being the hole conduction and σ_i being the ionic conduction.[280]
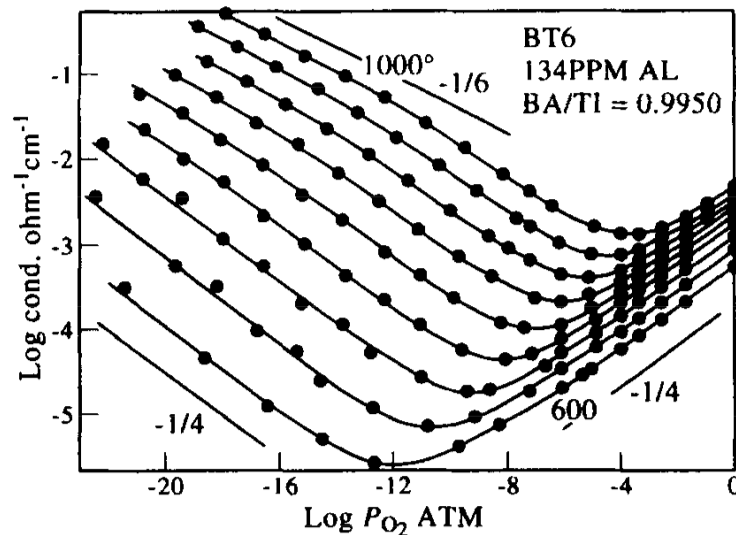
Figure 4.4.5 The equilibrium electrical conductivity of undoped BaTiO$_3$ as a function of P_{O_2}. The lines highlight isotherms at 50 °C intervals from 600 °C to 1000 °C. Adapted from Raymond *et al.*[281] and reprinted with permission, copyright © 1996 Published by Elsevier Ltd.).

However, the valence band of BNT lies at a rather deep level due to the fact that very high energies are required to oxidize O^{2-}. Therefore electron holes seem to be not likely present in large amounts. This is comparable to PZT and BaTiO$_3$ systems.

The fact, that BNKT10 in air has the highest resistivity is in qualitative agreement with the general trend in resistivity *vs.* oxygen partial pressure that is to be expected in acceptor doped ceramics like BaTiO$_3$. This is presented in both Figure 4.4.5 (BaTiO$_3$) with a clearly visible trend and in Figure 4.4.6 with the indicated rough guide to the eye indicating the same trend (please note: for BT the conductivity is plotted, while for BNKT10 the resistivity is plotted). The indicated trend of BNKT10 should be considered as very approximate due to (I) the limited number of data points and (II) the initial approximation of P_{O_2}.
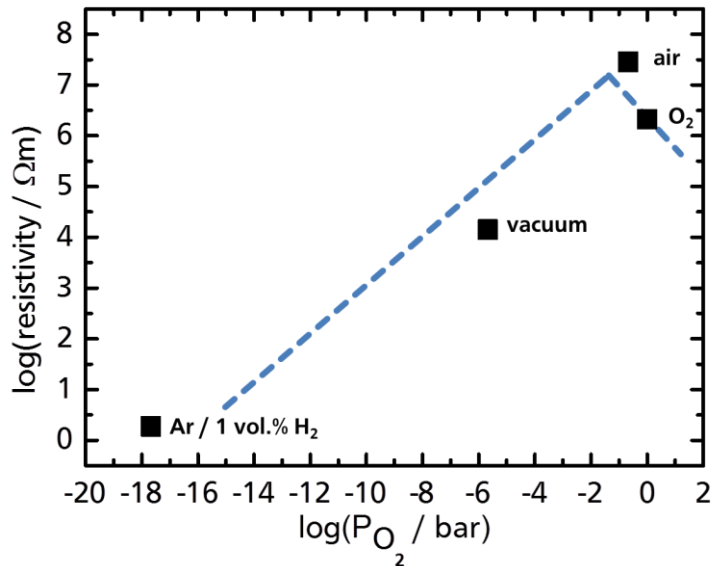
Figure 4.4.6 The equilibrium resistivity of undoped BNKT10 ceramics at 350 °C as a function of P_{O_2}. The dashed line is a guide to the eye to approximate the trends in resistivity.

In case of PZT, σ_{total} is reported to consist only of σ_n and σ_i, for instance by Boukamp *et al.*[282].

Oxygen vacancies contribute to the ionic conductivity and their E$_A$ is known to be in the range of 1 eV according to Smyth [283], which is slightly lower than the E$_A$ found for undoped BNKT10 in air, O$_2$ and vacuum (*cf.* Tables 4.4.1 and 4.4.3) and also for doped BNKT10 in air. A trapping of $v_O^{\bullet\bullet}$ by acceptor defects, in the ceramics is furthermore possible. Trapped defects, *e.g.* $(Cu_{Ti}'' - v_O^{\bullet\bullet})^X$, are usually (depending on their dissociation energy) not mobile, thus do not contribute to the overall conductivity. In addition, detrapping these states requires further activation energy.

In addition, the grain boundary $v_O^{\bullet\bullet}$ ion diffusion in Nb doped PZT was found to be significantly higher, compared to the bulk $v_O^{\bullet\bullet}$ ion diffusion, as reported by

Frömling *et al.*[284], who performed ^{18}O tracer experiments to characterize the diffusion of oxygen.

Like in the case of Nb doped PZT, in a dielectric study at elevated temperature on BNKT18, Chen *et al.*[275] noted a higher grain boundary conductivity, compared to bulk conductivity, and attributed this to conduction paths induced by Bi evaporation of the ceramics. Their argument was supported by observed transgranular fractures in BNKT ceramics, opposed to intergranular fractures, which they found in lead-based PZN. This is likely occurring in all BNT-based materials, as well in the investigated BNKT10 ceramics.

Table 4.4.3 | Arrhenius Plot Fitting Parameters and E$_A$ of BNKT10 Ceramics at Different P_{O_2}

sample	atmosphere	intercept of fit /Ωm	slope of fit /ΩmK	bulk E$_A$ /eV
undoped BNKT10	air	-8.4	15849	1.37
undoped BNTK10	O$_2$	-13.8	17692	1.52
undoped BNKT10	vacuum	-10.3	12391	1.07
undoped BNKT10	Ar / H$_2$	4.1	2825	0.23

4.5. Electron Paramagnetic Resonance Spectroscopy

Electron paramagnetic resonance (EPR) spectroscopy is able to provide information on unpaired electrons in a system. Thus it is possible to detect Cu and V in certain oxidation states (2+ and 4+, respectively) in very low concentrations. Information on the local electronic environment, in particular the symmetry and the oxidation state can be extracted from the EPR spectra.

Cu^{2+} could be detected in the Cu doped BNKT10 ceramics (*cf*. Figure 4.5.1). A broad Cu^{2+} signal was observed for higher concentrations of Cu (BNKT10:0.5Cu) of the respective calcined powder and sintered ceramics. Cu^{2+} displayed multiple individual resonances in the ceramics. The Cu^{2+} resonances could be simulated, using the software *EasySpin*[285], assuming a rhombic local environment. They can be attributed to two distinctive Cu^{2+} defect centers (*cf*. Table 4.5.1) in calcined powders and sintered ceramics (designated as center1 and center2).
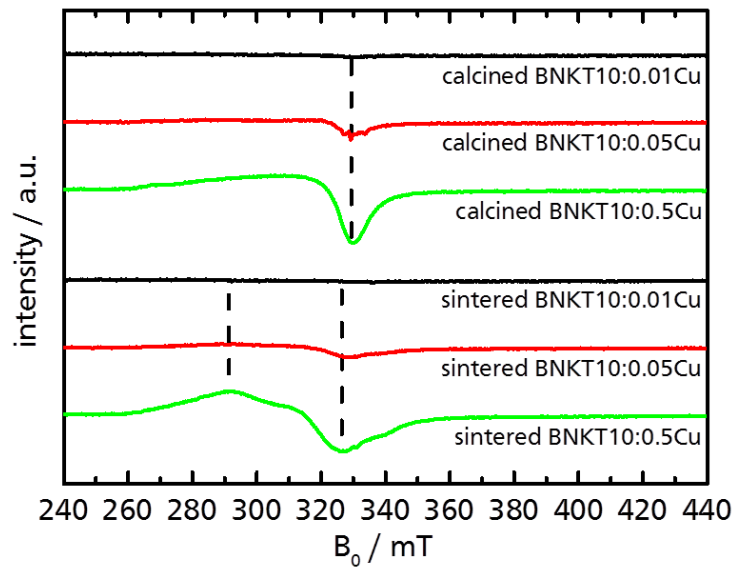
Figure 4.5.1 EPR spectra of calcined and sintered samples with varying Cu content. The dashed lines are a guide to the eye to identify the individual resonances. Partially adapted from Blömker *et al.*[261].

Both center1 (at about 290 mT) and center2 (at about 330 mT) are altered upon sintering. In general both centers (indicated by the dashed lines in Figure 4.5.1) broaden noticeably upon sintering. While center1 was additionally slightly shifted towards lower magnetic fields upon sintering, center2 was shifted significantly to lower magnetic fields. This is an indication that at least defect center2 of Cu^{2+} is segregating, likely to the grain boundaries: The calcined BNKT10 powders already consist of a perovskite phase, which is not altered notably upon sintering. Sintering mainly affects the grain size, grain boundaries and the defect chemistry, while the perovskite lattice of the bulk is not subject to major changes.

As evident from Figure 4.5.1, the Cu^{2+} peaks were generally very broad (additionally *cf*. Figure 4.5.2). This broadening of the EPR resonance peak of Cu^{2+} in BNKT10 can be attributed to (I) spin-spin interaction of multiple Cu^{2+} defect centers in close vicinity to each other or (II) an inhomogeneous local environment of the host lattice due to more than one crystal phase or a significant amount of internal stresses. Case (II) was for instance described by Eichel *et al.*[286] for PZT at the MPB. Spin-spin interactions appear at very high concentrations of Cu^{2+} throughout the ceramic or when Cu^{2+} is not homogeneously distributed across the ceramic, which results in local spin-spin interactions in regions with high Cu^{2+} concentration.

Neither calcined, nor sintered BNKT10:0.01Cu, exhibited an EPR signal; BNKT10:0.05Cu ceramics, however, did. This indicates a limit of detection for Cu^{2+} in BNKT10 between 0.05 at.% Cu and 0.01 at.% Cu. Furthermore it is evident from the absence of other resonance signals in the EPR spectra of BNKT10:0.01Cu, that no unintended paramagnetic impurities (*e.g.* Fe^{3+} or Mn^{3+}, described by Eichel *et al.* [287])

or reduced titanium (Ti^{3+}, described by Warren *et al.*[288]) defects were present in undoped BNKT10 powders and bulk.
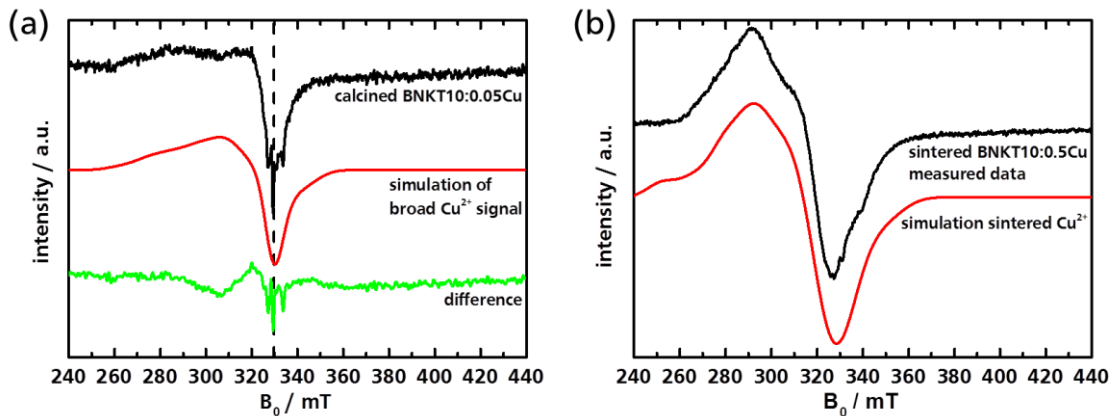
Figure 4.5.2 EPR spectra of calcined and sintered BNKT10 ceramics and their respective simulations. The broad Cu peak of calcined BNKT10:0.05Cu (a) on the top was simulated as illustrated in the middle. On the bottom the difference between the measured data and the simulation of the broad Cu^{2+} is plotted. The dashed line is a guide to the eye to indicate the Cu^{2+} resonance. The measured spectrum of BNKT10:0.5Cu (b) on top was fitted by simulating the bottom Cu^{2+} spectrum. Partially adapted from Blömker *et al.*[261].

A significant contribution of the crystal phase or stresses to the dipolar broadening, as described by Eichel *et al.* will occur at any given concentration, as no other Cu^{2+} defect is required in close proximity. However, for very low (0.05 at.% Cu) concentration, the characteristic fingerprint spectrum of Cu^{2+} (*cf.* Figure 4.5.2(a)), sitting on top of the broad dipolar signal, was observed in this work. A spectrum, in which the simulated broadened Cu^{2+} signal is subtracted from the experimentally obtained spectrum, is presented to emphasize the remaining fingerprint signal. This is in contradiction with dipolar broadening at any given Cu^{2+} concentration. Thus a dipolar broadening due to multiple crystal phases or internal stresses can be excluded from consideration. Since the investigated Cu concentrations are very low (< 0.5 at.%), a segregation of Cu^{2+} to the grain boundaries is a viable explanation for the dipolar broadening. This argument is further supported by the increasing trend in density upon increasing Cu concentration of BNKT10 ceramics, sintered at 1080 °C (*cf.* discussion in section 4.1)

For Cu^{2+} (d^9 system) a strong Jahn-Teller (JT) effect is to be expected, causing elongation of the octahedral environment and resulting in splitting of the e$_g$ orbitals. This is reflected in the ratio of A_{zz} to A_{xx} and A_{yy} in case of center1. A_{zz} is up to 40 times larger than A_{yy}. The comparably small, however, noticeable deviation of A_{xx} from A_{yy} is indicative of small rhombic distortions of the local electronic environment.
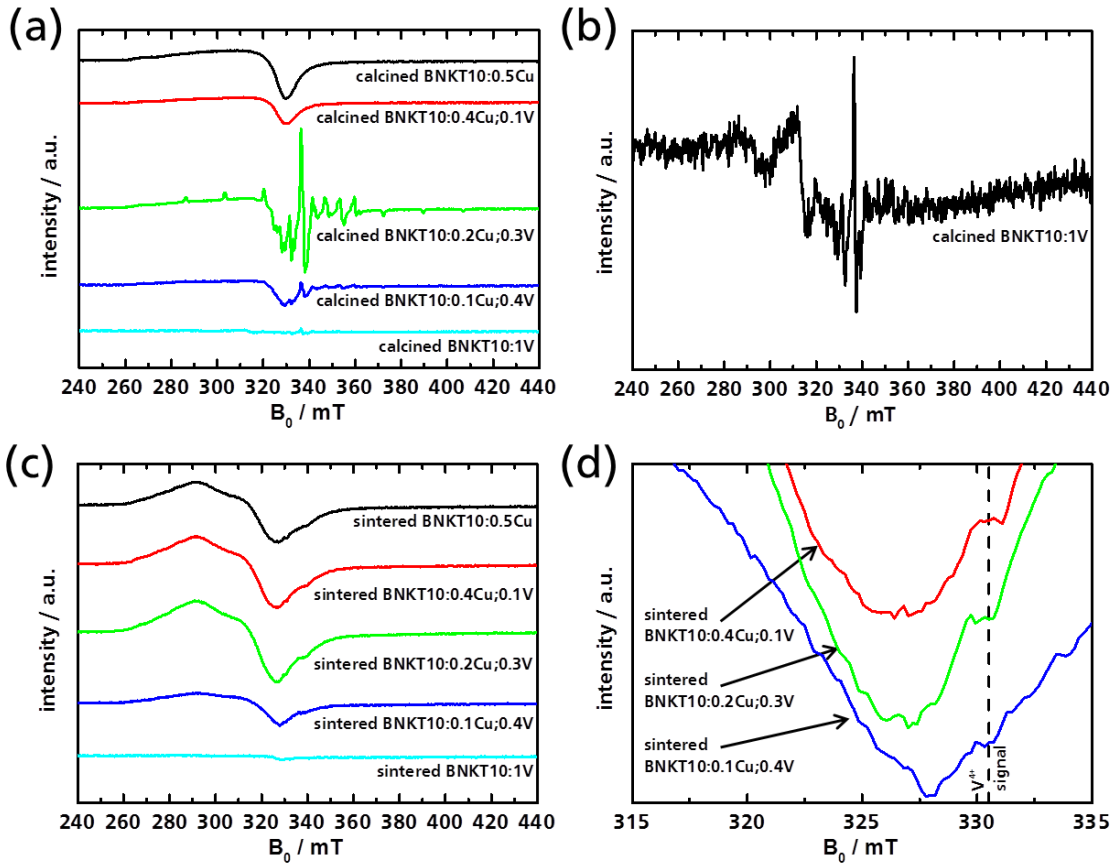
Figure 4.5.3 EPR spectra of Cu and V doped BNKT10 ceramics. Doped and calcined samples are compared in (a), while (b) is a magnification of the spectrum of calcined BNKT10:1V to emphasize the V^{4+} fingerprint signal. In (c), sintered samples are compared and (d) illustrates the V^{4+} signal in addition to the broad Cu^{2+} EPR signal of sintered Cu doped ceramics. *C.f.* Blömker *et al.*[261].

In PZT[158,289] and in KNN[290], Cu^{2+} behaves differently. It is predominantly incorporated into the lattice, residing on a B lattice site. This is different from this work, as Cu^{2+} segregates, most probably at the grain boundaries.

Calcined and sintered BNTK10 with Cu and V doping display different characteristic EPR spectra. As discussed earlier (*cf.* Figure 4.5.3 and Table 4.5.1), Cu yields an EPR signal in BNKT10, which is characterized by two centers. These centers are also apparent in calcined powders and sintered ceramics with both Cu and V dopants (*cf.* Figure 4.5.3 (a) and (c)).

Table 4.5.1. | Spin Hamiltonian Parameters of Cu^{2+} and V^{4+} in BNKT10 Ceramics, adapted from Blömker _et al._[261] and reprinted with permission, © 2015 The American Ceramic Society.

	g$_{xx}$	g$_{yy}$	g$_{zz}$	A$_{xx}$ (MHz)	A$_{yy}$ (MHz)	A$_{zz}$ (MHz)
calcined Cu^{2+} (center1)^A	2.053	2.067	2.393	17	10	404
calcined Cu^{2+} (center2)^A	2.147	1.995	2.385	71	101	306
sintered Cu^{2+} (center1)^A	2.117	2.056	2.468	120	117	451
sintered Cu^{2+} (center2)^A	2.190	2.345	1.949	201	202	152
calcined V^{4+} ^{B}	1.972	1.952	1.939	118	129	468

^{A} A and g are displayed for ^{63}Cu. A ratio of 1.588 to 1.484 for ^{65}Cu to ^{63}Cu was used for calculations.

^{B} For V^{4+} in sintered ceramics the same parameters were used.

In addition, a fingerprint V^{4+} signal is easily visible in the case of calcined BNKT10:0.2Cu,0.3V and 0.1Cu,0.4V as well as in BNKT10:1V (_cf_. Figure 4.5.3 (b)). Upon sintering, the V^{4+} signal is weaker and only visible as a side shoulder of the Cu^{2+} signal (_cf_. Figure 4.5.3 (d)). At all investigated concentration levels of V, the characteristic signal is narrow and well defined, not indicating any peak broadening. In contrast to the Cu^{2+} ions, this points at bulk introduction of V^{4+}.
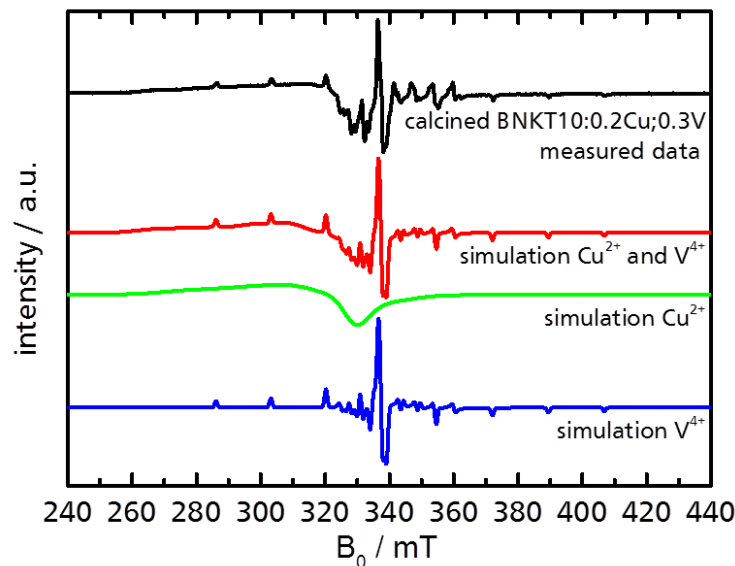
Figure 4.5.4 Measured (top) and simulated EPR spectra of BNKT10:0.2Cu;0.3V (below) with the corresponding simulation of Cu^{2+} and V^{4+} signal combined as well as the individual simulations of the broad Cu^{2+} signal and the narrow fingerprint V^{4+} resonance signal. _C.f._ Blömker et al.[261].

The **g**-factors of the simulated V^{4+} signal are in good agreement with comparable studies[291-293]. The hyperfine splitting parameters (_A_) compared to these studies are

significantly higher. As an example Davidson et al.[292] reported $A_{xx} = 31$ MHz, $A_{yy} = 45$ MHz and $A_{zz} = 156$ MHz for V^{4+} in TiO_2, while $A_{xx} = 118$ MHz, $A_{yy} = 129$ MHz and $A_{zz} = 468$ MHz in this work. This is possibly due to the elongation of the oxygen octahedron and resulting JT-splitting. Slight JT effects are expected for V^{4+} (d^1 system). In addition it is to be noted, that the samples exhibited no V^{2+} signal, which would occur at a lower applied magnetic field (B_0).[294]

Figure 4.5.4 illustrates in detail, how the simulated EPR spectra were matched to the obtained experimental data. For samples with one dopant only, as BNKT10:0.5Cu or BNKT10:1V, a simulation of the individual signal was sufficient. As apparent from Figure 4.5.4 , ceramics with simultaneous Cu and V doping required the combination of the simulation of a broad Cu^{2+} signal and a narrow V^{4+} signal to obtain a good fit.
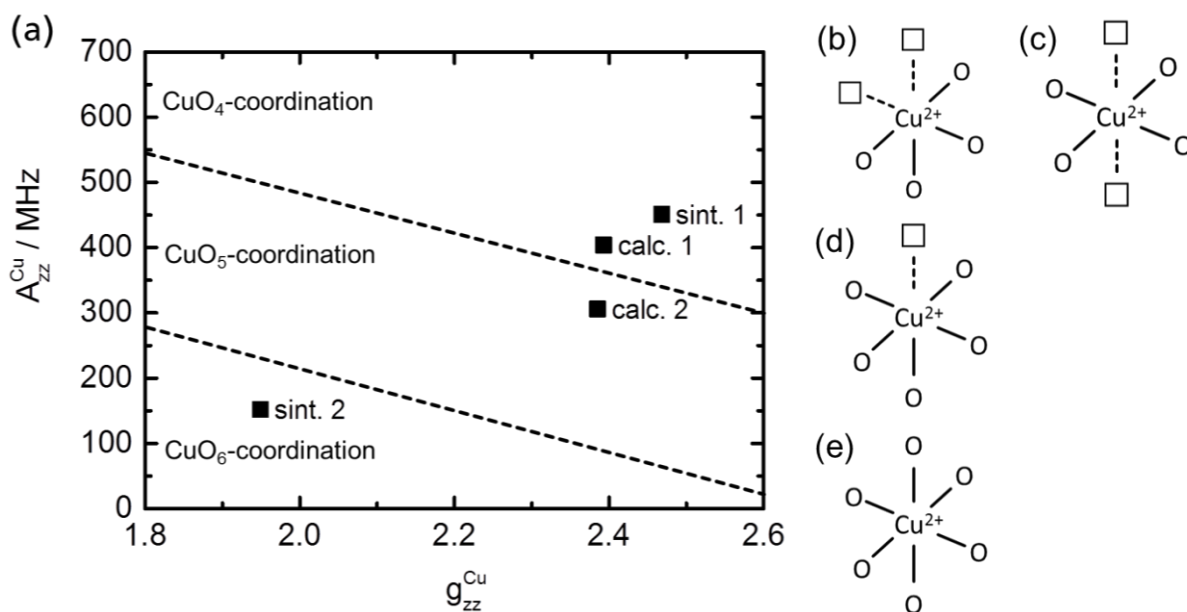
Figure 4.5.5 Dependencies of g_{zz}^{Cu} versus $^{63}A_{zz}^{Cu}$ (a) with different regions of coordination: CuO_4 coordination ($v_O^{\bullet\bullet} - Cu^{2+} - v_O^{\bullet\bullet})^{\bullet\bullet}$ defect complexes ((b) and (c)) on top, CuO_5 coordination ($v_O^{\bullet\bullet} - Cu^{2+}$) (d) in the middle and CuO_6 octahedra (e) at the bottom. The dashed lines represent a qualitative separation of the regions, calculated from experimentally obtained coordination parameters for Cu^{2+}, as approximated by Eichel et al..[286] Empty squares in (c) - (d) represent oxygen vacancies.

With the obtained Spin Hamiltonian parameters, it is possible to roughly evaluate the oxygen coordination of the different Cu^{2+} centers by means of **A** vs. **g** *Peisach-Blumberg*[295] plots. *Peisach-Blumberg* plots correlate the hyperfine splitting with the g-factor of metal-ligand complexes and allow drawing conclusions on the number of ligands. While the original *Peisach-Blumberg* diagram was used for Cu^{2+} in organic, biological specimens, Eichel et al.[286] transferred this to Cu^{2+} in various titanates and organic substances. This allows for a distinction of the number of neighboring oxygen of Cu in octahedral environment in for instance PT, PZT and BT. This distinction is possible, since electron spin density is transferred to bonding oxygen ions, which

results in less hyperfine splitting for *e.g.* CuO_5 coordination than for CuO_4 coordination (as Cu in the second case is surrounded by one oxygen less). This is why the CuO_4 coordination is associated with the highest $^{63}A_{zz}^{Cu}$, followed by CuO_5 coordination with intermediate hyperfine splitting, while CuO_6 coordination is associated with the lowest $^{63}A_{zz}^{Cu}$. The simulated Spin Hamiltonian parameters $\boldsymbol{g}$ and $\boldsymbol{A}$ of this work are displayed in a *Peisach-Blumberg* diagram with coordination regions that were adapted from Eichel *et al.* (*cf.* Figure 4.5.5).

While Cu^{2+} in calcined BNKT10 is located in a region of CuO_4 octahedral coordination and as well in a region of CuO_5 coordination, this is changed upon sintering (*cf.* Figure 4.5.5). Here a CuO_6 coordination of Cu^{2+} can be evidenced in combination with a CuO_4 coordination. For Cu^{2+} in the bulk this correlates with the amount of oxygen vacancies coordinated to the defect. However, as discussed earlier and evidenced by dipolar broadening, a segregation of Cu^{2+} to the grain boundary is expected. This implies that the observed oxygen coordination should correlate with phenomena observed at grain boundaries, *e.g.* dangling bonds. Cu^{2+} in CuO_4 coordination can in this context be rationalized by Cu^{2+} residing in the vicinity of a grain boundary defect. This can be, for instance as discussed, a one dimensional defect (vacancy), but also a two-dimensional defect (Cu^{2+} close to a dislocation) or a three-dimensional defect (Cu^{2+} at the interface of a pore).

4.6. X-Ray Photoelectron Spectroscopy

X-ray photoelectron spectroscopy (XPS) is a surface sensitive quantitative method, allowing for the assessment of the first few up to ten nanometers of the sample. Selected, doped BNKT10 ceramics were investigated by means of XPS in their polished, annealed state in order to obtain information about the oxidation states of all BNKT10 elements including oxygen and attain an estimation of the Fermi level trends upon doping.

V could be detected at the investigated (0.3 at.% - 1 at.%) doping levels, however, Cu (≤ 0.5 at.%) could not be detected, despite long measurement times over night. Presumably, since (I) the relative sensitivity factor (RSF) of Cu is lower than the RSF of for instance V, described by Powell *et al.* [296], (II) the background in the region around 930 eV, where the peak would be expected, is high and (III) the attenuation of the adsorbate layer weakens the signal. This attenuation is higher at higher binding energy (BE), resulting from the lower inelastic mean free path, as reported by Seah *et al.* [297].
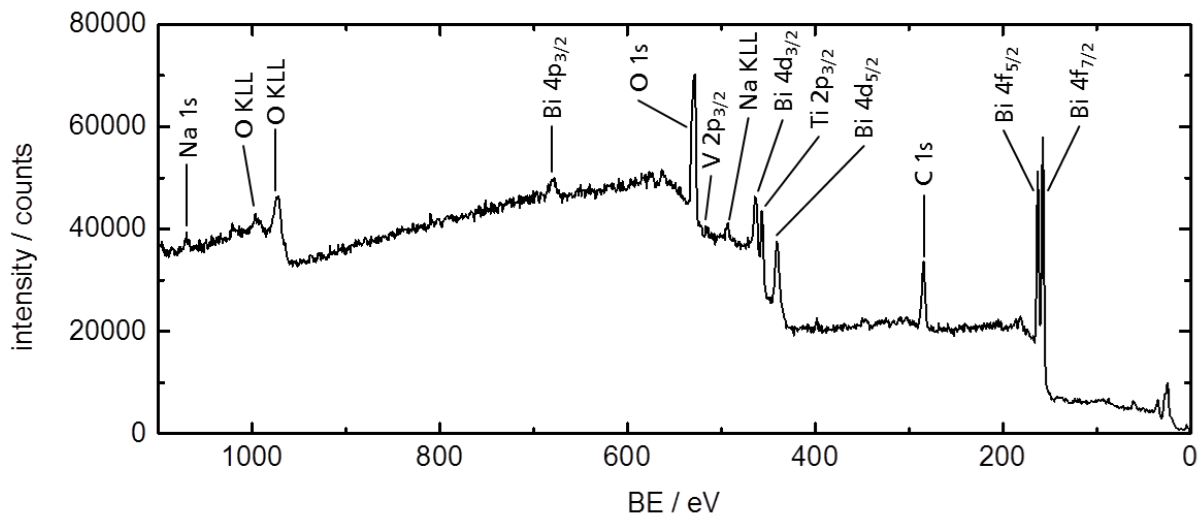
Figure 4.6.1   Exemplary survey XPS spectrum of BNKT10:1V with line identifications.

As evident from the survey spectrum (*cf*. Figure 4.6.1), all other elements, present in BNKT10 ceramics could be identified by their characteristic XPS signal. In addition, a carbon peak could be identified and can be attributed to the surface adsorbates and likely additional surface contamination. Commonly employed sputtering of the surface to remove surface contamination, was not performed in this work, as the oxidation states of the material were of interest and ion sputtering would likely change those. The binding energies are consistently shifted by approximately 2 eV. This can be attributed to charge compensation by the neutralizing beams.
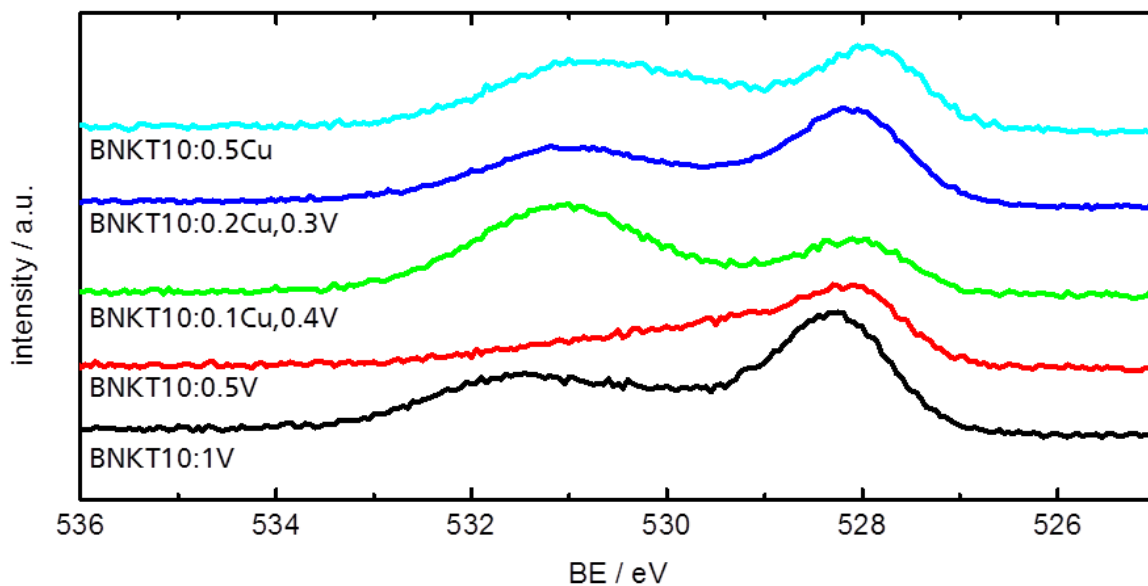
Figure 4.6.2   O 1s XPS spectra of doped BNKT10 ceramics. The peak at lower BE corresponds to BNKT. The peaks at higher BE result from adsorbates, *e.g.* water or hydroxides.

The presence of adsorbates on the sample surfaces is additionally reflected in the O 1s peak of the XPS spectra of doped BNKT10 ceramics (*cf*. Figure 4.6.2). At lower binding energy (~528 eV), a peak, corresponding with oxygen in the BNKT10 lattice environment, was observed. A peak at higher binding energy (~531 eV) indicates the discussed presence of adsorbates. In case of oxygen this is likely predominantly due to the presence of hydroxides or water on the surfaces, but could additionally be caused by small organic molecules.
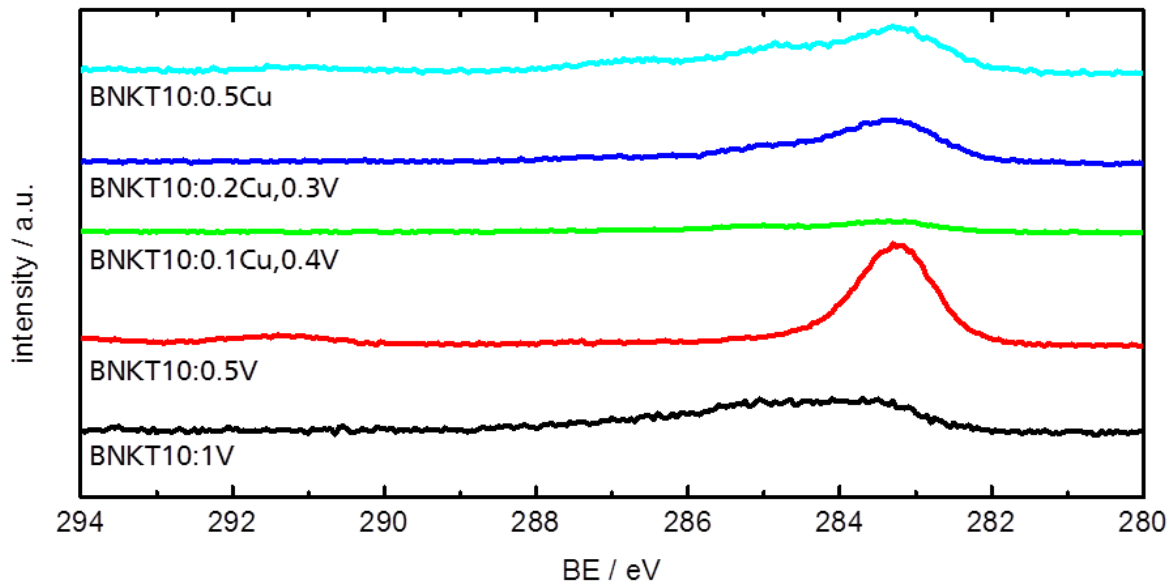
Figure 4.6.3   C 1s XPS spectra of doped BNKT10 ceramics.

The binding energy of the C 1s main peak is approximately unchanged for all employed dopants and dopant combinations (*cf*. Figure 4.6.3). Though BNKT10:1V displays a slightly higher binding energy, the deviation is minimal (< 1 eV). This corroborates the assumption of a minimal influence of the ionic and electronic charge neutralization on the surface energies of the investigated ceramics.

Figure 4.6.4 provides the XPS spectra of Bi 4f, Na 1s and Ti $2p_{3/2}$. The Na 1s spectrum (*cf*. Figure 4.6.4 (b)) clearly exhibits the discussed higher noise at high binding energies. The low signal to noise ratio is prevalent for all investigated ceramics. There is no significant change in Na 1s binding energy apparent. The low intensity of the Na 1s peak is (analogous to the not observable Cu signal) caused by the low ionization cross section and additionally by the attenuation of the peak due to the adsorbates.
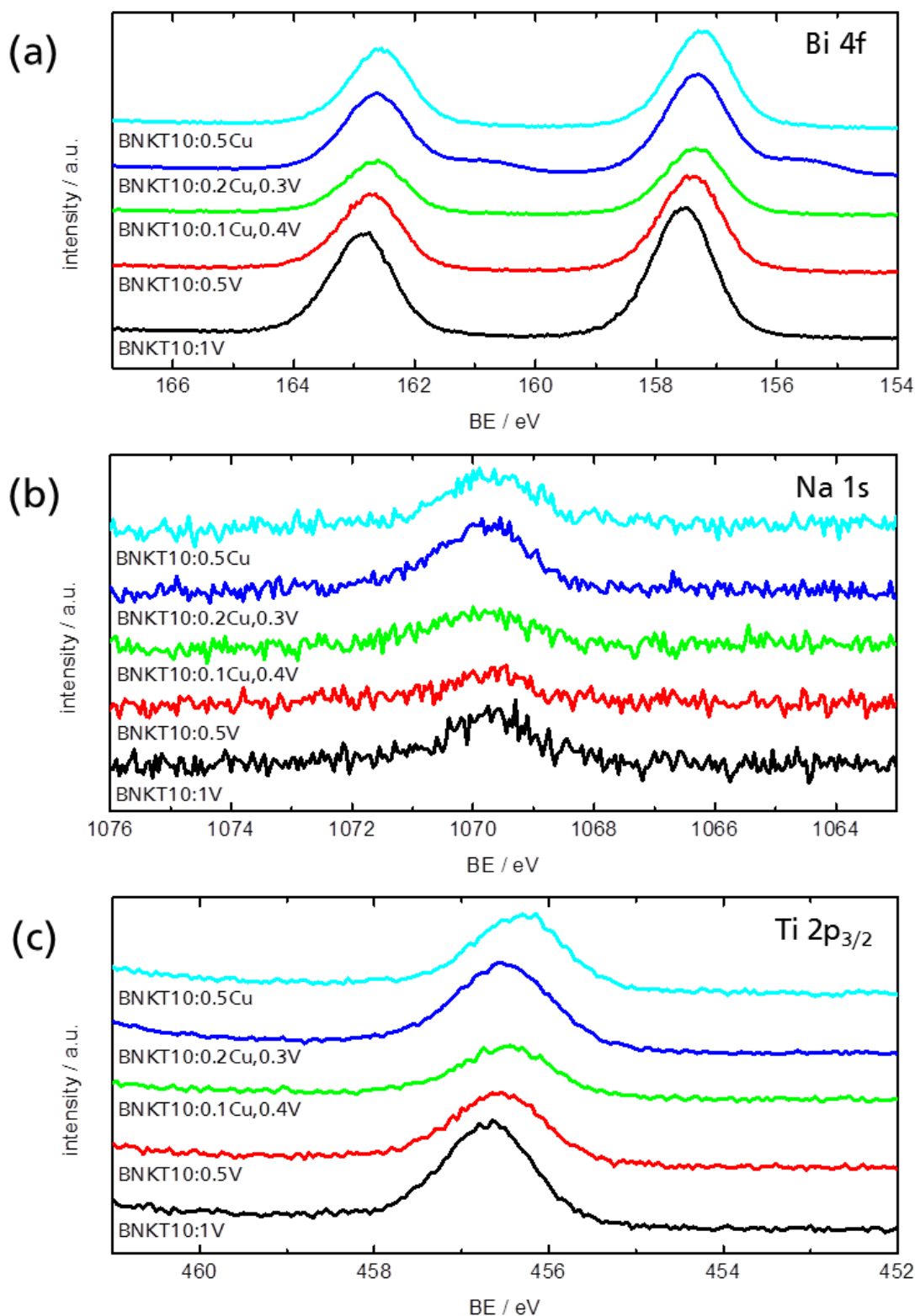
Figure 4.6.4 XPS spectra of doped BNKT10 ceramics. (a) Bi 4f spectra, (b) Na 1s spectra and (c) Ti $2p_{3/2}$ spectra. The Ti $2p_{1/2}$ peak, commonly used for quantification, is indistinguishable due to a more intense Bi emission.

The Bi 4f spectrum (*cf.* Figure 4.6.4 (a)) are all similar, despite BNKT10:0.2Cu0.3V, which exhibits an additional narrow peak, ~1 eV lower in binding energy, than the main peaks. If this peak would originate from Bi, this would indicate metallic Bi^0. This should not be the case, as Bi^0 would oxidize in air and additionally the energy of the Ar ions, used for charge compensation is very low (< 10 eV). This would typically not cause a sputtering effect, resulting in Bi^0. Thus the origin of this minor peak remains to debate.

In case of titanium, the Ti $2p_{1/2}$ peak, commonly used for quantification is indistinguishable as it is covered by a much stronger Bi emission. Therefore the Ti $p_{3/2}$ peak (*cf.* Figure 4.6.4 (c)) was used to quantify the Ti content of the ceramics.
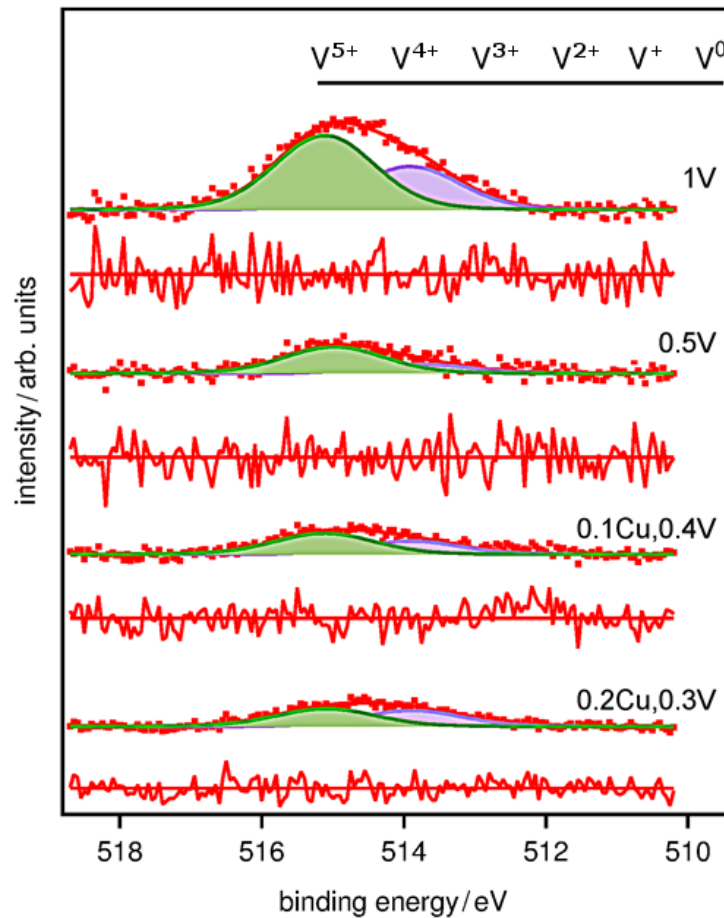
Figure 4.6.5   XPS V $2p_{3/2}$ spectra data points and fit, as well as deviation from the fit of doped BNKT10 ceramics. Additionally represented by colored peak areas, are the deconvolution of V^{5+} and V^{4+} peaks with a BE difference of 1.2 eV and identical shape. The spectra were not shifted. At the top, all V oxidation states with a BE difference of about 1.2 eV are indicated as a guide to the eye. Adapted from Blömker *et al.*[261] and reprinted with permission, © 2015 The American Ceramic Society..

The V 2p$_{3/2}$ peak is asymmetric in shape, which implies the presence of more than one oxidation state of V (V^{4+} and V^{5+}). A fitting of the V $2p_{3/2}$ signal revealed two separate V peaks with a BE difference determined as 1.2 eV. An identical shape of

both peaks was assumed to fit the experimental data. Due to the high noise level, the fitting is not very unique.

Nevertheless, this finding is in agreement with binding energies of V reported in the literature. For instance Wu et al.[298,299] observed a binding energy difference of about 1 eV, while Silversmit et al. reported 1.4 eV binding energy difference between V^{4+} and V^{5+} and Demeter et al.[300] reported a difference of 1.2 eV in binding energy. In this context the assumed oxidation states appear reasonable.
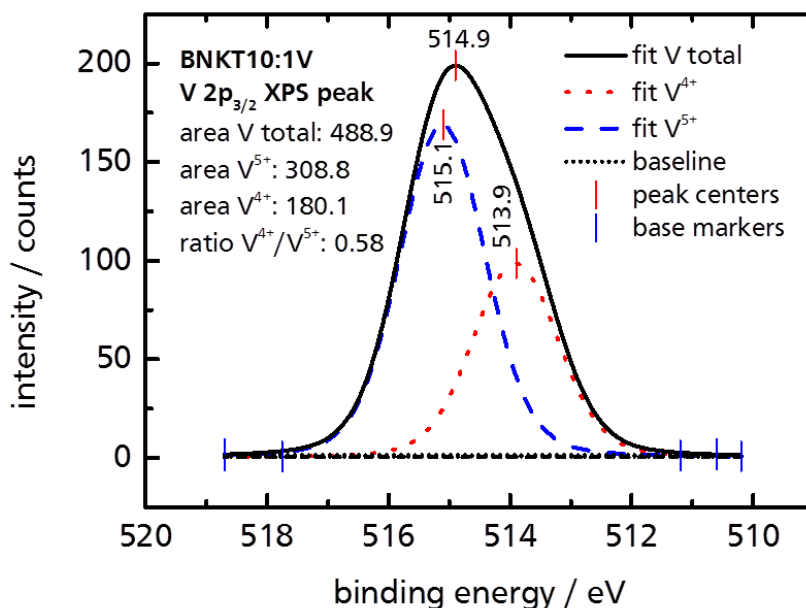
Figure 4.6.6   Exemplarily detailed peak analysis of the fitted XPS V $2p_{3/2}$ spectrum and the distinguished V^{5+} and V^{4+} peaks of BNKT10:0.1 V ceramics.

From the fitted peaks, the intensity of the V $p_{3/2}$ peak and from the individually fitted V^{4+} and V^{5+} peaks, their ratio was calculated (cf. Table 4.6.1). As to be expected, BNKT10:1V has by far the highest intensity (489), while BNKT10:0.5Cu with no V, expectedly exhibits an intensity of 0. A detailed example of a fitted V $2p_{3/2}$ peak is presented in Figure 4.6.6.

The intermediate (BNKT10 with 0.5 at.% V, 0.4 at.% V and 0.3 at.% V) display intensities very close to each other and do not follow the global trend of increasing V $2p_{3/2}$ intensity with increasing V concentration. BNKT10:0.1Cu,0.4V displayed a higher intensity (152) than BNKT10:0.5V. This emphasizes the fact, that the XPS analysis should be interpreted semi-quantitatively, as it cannot be ultimately excluded that minor (0.2 at.%) changes in nominal V content are indistinguishable with respect to their intensity. Besides fitting artefacts, a segregation of V within the ceramics to or from the surface can influence the measured and calculated V signal intensity. For above mentioned reasons, the oxidation state ratio of V, determined at < 1 at.%, appears not definite and is therefore neglected in further discussion.

Table 4.6.1. | V p$_{3/2}$ Signal Intensity and V^{4+} to V^{5+} Ratio of BNKT10 Ceramics From XPS.

	intensity V 2p$_{3/2}$	V^{4+} / V^{5+}
BNKT10:1V	489	0.6
BNKT10:0.5V	147	0.3
BNKT10:0.1Cu,0.4V	152	0.6
BNKT10:0.2Cu,0.3V	143	0.9
BNKT10:0.5Cu	0	-

When investigating the relative changes in binding energy *vs*. the nominal V concentration in detail (*cf*. Figure 4.6.7), a systematic trend of increasing relative binding energy with increasing nominal V concentration was evident, however, minor in increase (< 400 meV change). The trend is emphasized with a linear fit (*cf*. Figure 4.6.7 (a)). This is not to exclusively claim linear behavior, but to guide the eye. Though a linear dependence is likely possible, the magnitude of the increase, as well as the limited amount of data and its inherent scattering does not allow for an unequivocal conclusion (the adjusted R^2 of the linear fit is 87.2 %).
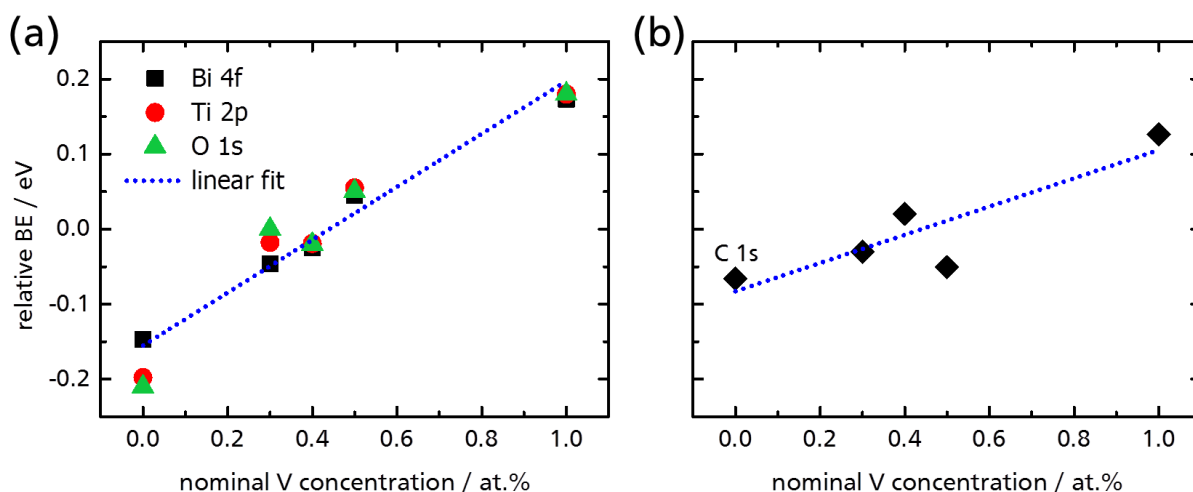
Figure 4.6.7　　　Relative change in BEs, obtained by XPS, with respect to the mean BE for each atom-specific investigated characteristic peak. (a) for Bi 4f, Ti 2p and O 1s and (b) for the C 1s peak. The linear fit in (a) was obtained, using the concatenated changes in BE for the investigated atoms (Bi, Ti and O). Both dotted linear fits serve as a guide to the eye.

This is, however, only accurate if the investigated samples are free of charging. Due to charging, the binding energies are consistently shifted by about + 2 eV (*e.g.* the peak

of Ti 2p in $SrTiO_3$ is located at 458.5 eV, while in this work it was at 456.5 eV). Commonly, the C emission is used as a reference for the Fermi level.[301] Here, as evident from Figure 4.6.7(b), the C peak of the adsorbates changes (albeit very little, with < 200 meV), depending on the nominal V concentration. Thus it is more likely that the Fermi level position is relative to the band edges or vacuum level. Nevertheless, the global consistent trend is towards higher binding energies with increasing nominal V concentration. This increase in binding energy can be attributed to a minor, however, qualitatively traceable donor effect of V in BNKT10.

4.7. Defect Chemistry of Cu and V Doped BNKT10

Summarizing and further evaluating the results of the prior sections 4.1 - 4.6, the defect chemistry of doped BNKT10 ceramics is discussed in this section in greater detail and furthermore in context with the piezoelectric response of the doped ceramics.

As evidenced by EPR (*cf.* section 4.5), V^{4+} ions can be observed in V doped BNKT10 ceramics, while V^{2+} and V^{3+} could not be detected. Complimentary to that, the analysis of the V $2p_{3/2}$ XPS peak (*cf.* section 4.6) indicates the presence of two oxidation states of V (V^{4+} and V^{5+}). This is in accordance with investigations of V doping in the literature, where lower oxidation states of V^{3+}, V^{2+} or V^+ were exclusively observed under severely (6 vol.% H_2 at ≥ 800 °C [294] or 10 vol.% H_2 at 500 °C [302]) reducing conditions. For instance Müller *et al.*[302] reported on those lower oxidation states in V doped $SrTiO_3$ and Abi-Aad *et al.*[294] reported on V based Ce catalysts. Therefore the assumption, that in V doped BNKT10 ceramics only V^{5+} and V^{4+} predominate, appears justified by complimentary EPR and XPS results, as well as mentioned relevant literature.

Thus in the further discussion of the defect chemistry, only V^{4+} and V^{5+} is taken into account.

V is incorporated into the BNKT10 lattice according to

$$V_2O_5 \xrightarrow{BNKT10} 2V_{Ti}^X + 4O_O^X + \frac{1}{2}O_2 \quad , \tag{4.7.1}$$
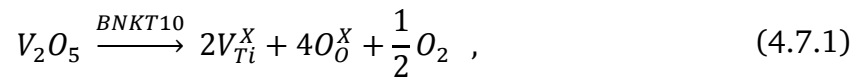
yielding V^{4+} on a Ti (B-) site, which is charge neutral with respect to the lattice. V^{5+} in the lattice is created according to

$$V_2O_5 \xrightarrow{BNKT10} 2V_{Ti}^{\bullet} + 5O_O^X + 2v_{Na,K}' \; or \; 2e' \tag{4.7.2}$$

in BNTK10 ceramics, additionally resulting in A-site vacancies (or $2e'$) upon the incorporation. On the one hand, the incorporation of V can lead to A-site vacancies of Na or K ($v'_{Na,K}$), which leads to vacancies with a single charge, as described in Equation 4.7.2. On the other hand, V doping may result in Bi A-site vacancies, according to

$$3V_2O_5 \xrightarrow{BNKT10} 6V^{\bullet}_{Ti} + 15O^X_O + 2v'''_{Bi} \; or \; 6e' \quad , \tag{4.7.3}$$
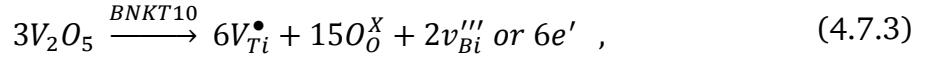
which results in triply charged Bi vacancies (or the corresponding number of e'). Once incorporated into the lattice it is possible for V to undergo a reduction or oxidation, which can be described by

$$V^X_{Ti} \Leftrightarrow V^{\bullet}_{Ti} + \; v'_{Na,K} \; or \; e' \quad . \tag{4.7.4}$$

The occupied oxidation state, strongly depends on the position of the Fermi level of the respective doped BNKT10. At or very close to 0 K, all V atoms would be in a thermodynamically defined state (only V^{4+} at higher Fermi level or only V^{5+} at lower Fermi level would be present). This is not the case, observed at RT or higher. There, V^{4+} and V^{5+} were both evidenced in the ceramics.

Ti^{3+}, a theoretically possible defect in perovskites, is not taken into consideration in this defect chemistry discussion. This is because Ti^{3+} possesses an unpaired electron and therefore would exhibit a detectable EPR signal, which was not observed in the investigated BNKT10 ceramics (*cf.* to the discussion in section 4.5).

Cu is introduced into BNKT10 and may act as an acceptor dopant in the following manner

$$CuO \xrightarrow{BNKT10} Cu''_{Ti} + \; v^{\bullet\bullet}_O \; or \; 2h^{\bullet} + O^X_O \quad , \tag{4.7.5}$$
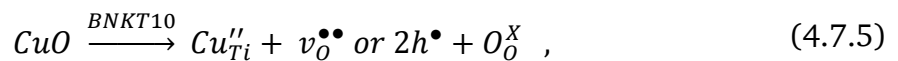
which implies the creation of $v^{\bullet\bullet}_O$ or $h^{\bullet}$ for Cu on a Ti lattice site. However, as discussed in section 4.5, a predominant fraction of Cu is not residing in the lattice, but should segregate, most likely at the grain boundary. This implies (I), Cu will thus rather influence the grain boundary defect chemistry *vs.* the bulk defect chemistry and (II) Cu will not have a dominant effect on the concentration of $v^{\bullet\bullet}_O$ in the bulk; however (III) $h^{\bullet}$, may be created at grain boundaries and migrate to the bulk, which is, nevertheless, not likely due to the deep valence band.

In general, oxygen vacancies can react to form electron holes or *vice versa*:

$$2v^{\bullet\bullet}_O + O_2 \leftrightarrow 2O^X_O + 4h^{\bullet} \quad . \tag{4.7.6}$$

It is to be noted: as presented in equation 4.7.6, both oxygen vacancies or electron holes can be present in BNKT10, accounted for on the donor side of the equation of charge neutrality. Theoretically (I) only $h^\bullet$, (II) both $h^\bullet$ and $v_O^{\bullet\bullet}$ or (III) only $v_O^{\bullet\bullet}$ can exist as defects in BNKT. Taking the defect chemistry of PZT as a reference, it is highly likely that $v_O^{\bullet\bullet}$ exists in BNKT, and $h^\bullet$ may be present, but, if at all, $h^\bullet \ll [v_O^{\bullet\bullet}]$ according to Boukamp $et\ al.$[282] or Raymond $et\ al.$[281]. Despite the fact, that the concentration of $v_O^{\bullet\bullet}$ was said to be expected higher, the major contribution to charge transport was attributed to the comparably way more mobile $h^\bullet$ by both authors. However, in contrast to this argument, the easy reducibility of BNKT10 ($cf.$ Figure 4.4.6 for details), evident from the resistivity of BNKT10 under reducing conditions contradicts notable concentrations of $h^\bullet$. Thus electron holes will not play a major role in the defect chemistry of BNKT10.

In addition to the discussed introduced defects by doping, BNT-based materials are known to be prone to the evaporation of Bi (Pb-based materials analogously loose Pb during sintering) at high temperatures during sintering according to

$$2Bi_{Bi}^X + 3O_O^X \rightarrow 2v_{Bi}''' + 3v_O^{\bullet\bullet} + Bi_2O_3\uparrow \ . \tag{4.7.7}$$
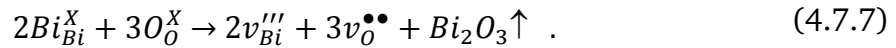
This high temperature evaporation mechanism was detailed in literature by Lamoreaux $et\ al.$[303] and is additionally described for BNKT by $e.g.$ Zhang $et\ al.$[247].

Due to the triple charge of v_{Bi}''', it is highly likely that trapping of $v_O^{\bullet\bullet}$ in the form of a defect associate occurs according to

$$v_{Bi}''' + v_O^{\bullet\bullet} \leftrightarrow (v_{Bi}''' + v_O^{\bullet\bullet})' \ . \tag{4.7.8}$$

This is more likely than the creation of $(v_{Na,K}' + v_O^{\bullet\bullet})^\bullet$ defect associates, as per defect associate, more involved charge is compensated, leading to higher BE between v_{Bi}''' and $v_O^{\bullet\bullet}$. Since additionally potassium is a volatile element at elevated temperatures, K evaporation is possible and will result in v_K' and $v_O^{\bullet\bullet}$:

$$2v_{Na,K}^X + 2O_O^X \rightarrow 2v_K' + v_O^{\bullet\bullet} + K_2O\uparrow \ . \tag{4.7.9}$$
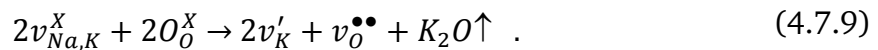
This was described in literature by Veera $et\ al.$[304] and Naderer $et\ al.$[225]. It is very likely, that in BNKT10, both Bi and K evaporation mechanisms are relevant and may be active at the same time, both resulting in A-site deficiency. The distinct difference between the two types of A-site ion loss due to evaporation is: Bi acts as triply charged acceptor ($cf.$ Equation 4.7.7) with respect to the lattice, while K acts as a singly charged acceptor ($cf.$ Equation 4.7.9) with respect to the lattice.

Taking into account Equations 4.7.5, 4.7.7 and 4.7.9, the overall state of charge neutrality of Cu doped BNTK can be described by

$$3[v_{Bi}'''] + [v_{Na,K}'] + 2[Cu_{Ti}''] \approx 7[v_O^{\bullet\bullet}] \quad . \tag{4.7.10}$$

In V doped BNKT10 ceramics, in addition to $v_O^{\bullet\bullet}$ (and theoretically $h^\bullet$, which is neglected), vanadium on the Ti-site can act as a further dopant and the overall charge neutrality is suggested to be

$$3[v_{Bi}'''] + [v_{Na,K}'] \approx 2[V_{Ti}^\bullet] + 4[v_O^{\bullet\bullet}] \quad . \tag{4.7.11}$$

Thus in the case of combined Cu and V doping of BNKT10 ceramics, from the large number of theoretically possible defects, six likely present or definitely present defects remain to be accounted for:

$$3[v_{Bi}'''] + [v_{Na,K}'] + 2[Cu_{Ti}''] + [e'] \approx 2[V_{Ti}^\bullet] + 4[v_O^{\bullet\bullet}] \quad . \tag{4.7.12}$$

These defects were either (I) directly confirmed by means of XPS ($V_{Ti}^\bullet$) and EPR (Cu_{Ti}'') and are therefore definitely present in BNTK or (II) could not be excluded by the employed measurements and appear highly likely from a thermodynamic point of view ($h^\bullet$ were excluded as discussed at the example of Equation 4.7.6) and were reported relevant according to literature elsewhere (v_{Bi}''', v_K' and $v_O^{\bullet\bullet}$).

As indicated by EPR spectroscopy (*cf.* section 4.5), Cu_{Ti}'' is present, however, in very low concentration in the bulk, while Cu dominantly segregates at the grain boundary. Despite the low amount of Cu anticipated to be present in the bulk, the T_{f-r} of Cu doped BNKT ceramics is evidently reduced, which can be attributed to the introduction of random fields, even at low Cu concentrations. Those findings are consistent with the absence of a clear trend in T_{f-r} upon changing the Cu concentration, as the solubility limit is expected to not be affected by the amount of Cu dopant. Thus it appears justified to exclude Cu_{Ti}'' from the defects, which significantly contribute to the bulk defect chemistry of BNKT10.

5. Conclusions

This work has demonstrated that Cu and V doping significantly influenced the defect chemistry and thereby the electric and piezoelectric properties of BNKT ceramics on several levels.

A more homogenous microstructure of doped BNKT10 ceramics, had mean grain sizes of 0.7 to 1.3 μm and lacked the abnormally large grains ($> 4\mu$m) that were present in the undoped samples as determined through SEM images. This was accompanied by liquid phase sintering, enabled by Cu at the grain boundary. This finding is supported by a trend towards higher relative densities upon increased Cu concentration in BNKT10 ceramics, all sintered at 1080 °C.

The synthesized BNKT ceramics are free of major impurity phases; XRD indicates the formation of a pseudocubic perovskite phase with minor peak splitting or side shoulders due to rhombohedral (BNKT10), tetragonal (BNKT30) or both distortions (BNKT20). The rhombohedral character of BNKT10 ceramics is reduced upon doping, indicated by less pronounced peak splitting of the {111} reflection. The same trend was observed for the tetragonal phase, which is reduced, as was apparent from less pronounced peak splitting of for instance the {211} reflection. Cu and V doping and co-doping of BNKT drives the phases closer to a (pseudo-) cubic structure, regardless of which side of the MPB the composition is located.

Doped BNKT10 ceramics are in general characterized by strong FE behavior, indicated by characteristic butterfly type S-E loops and display high E_C (up to 4.8 kV/mm), intermediate strain (d_{33}^* up to 177 pm/V), high P_{max} (up to 31.8 μC/m²) and high P_{rem} (up to 29.2 μC/m²). The T_{f-r} is slightly, but noticeably, reduced to as low as 122 °C from the undoped value of 205 °C. Doping the MPB-region BNKT20 leads to higher strain (d_{33}^* up to 293 pm/V), reduced E_C in the range of 1.7 kV/mm to 2.9 kV/mm, slightly reduced P_{max} and notably reduced P_{rem}. In comparison to other lead-based and lead-free materials, however, d_{33}^* is inferior. For these doped BNKT20 samples, however, the T_{f-r} is significantly reduced down to about RT compared to the undoped case with T_{f-r} of 110 °C. BNKT30 exhibits an even more drastically reduced E_c with values as low as 0.6 kV/mm, while maintaining a relatively high d_{33}^* of up to 228 pm/V and T_{f-r} close to RT. The lowering in T_{f-r} observed in all BNKT compositions upon doping can be rationalized by the introduced defects and the subsequently enhanced distribution of random fields in the bulk. Most likely $v'_{Na,K}$ and v'''_{Bi} play a major role by disrupting the Bi-O hybridization and thereby the FE long range order.

The K content has a significant effect on the strain of doped and undoped BNKT, which is also reflected in a stronger doping effect with increased amounts of K that results in predominantly higher S_{max} and d_{33}^*. The values of E_c as well as P_{rem} are lowered with higher K content; however, the decrease in E_c was determined to be even stronger for all doped BNKT ceramics. With respect to T_{f-r}, E_c, and P_{rem}, out of

the three phases investigated, the tetragonal phase was shown to be the most affected by doping with Cu and V.

The resonance behavior of $Q_{M,p}$ and k_p in BNKT10 ceramics was evidenced to be decoupled from the resonance behavior in thickness direction ($Q_{M,t}$ and k_t). $Q_{M,p}$ is, with one exception, characterized by a largely decreasing trend with increasing Cu dopant content, which was attributed to Cu segregation at the grain boundary. BNKT10:0.1Cu,0.4V stands out in terms of piezoelectric resonance properties with a high k_t of 0.56 in combination with a low $Q_{M,t}$ of 9, which are both beneficial properties for sensing applications, e.g. as flow meter.

EPR measurements proved an absence of significant amounts of paramagnetic impurities (*e.g.* Fe or Mn), as well as the absence of reduced Ti (Ti^{3+}) in undoped BNTK10. Furthermore the V lattice position in doped BNKT10 ceramics was observed to be confined to the B-site, where a rhombic environment was evident. The apparent confinement of the B-site octahedral distortion in one direction correlates well with an expected Jahn-Teller effect of V. Lower oxidation states of V (V^{3+}, V^{2+}, V^+ and V^0) were excluded by evidence from XPS as well as EPR spectroscopy.

When doping with Cu, it was indicated to enter the B-site of the bulk lattice at very low concentrations of < 0.05 at.%. While this was shown to be sufficient to decrease the T_{f-r}, the majority of the Cu could be demonstrated, by observed EPR peak broadening to segregate from the bulk, forming a liquid phase at the grain boundaries during sintering. This is supported by the densification trend of the BNKT10 ceramics with increasing Cu content. Furthermore the lower resistivity (1.0×10^4 Ωm to 7.3×10^6 Ωm) of Cu doped samples translates to increased conduction of the material, likely due to changes in the grain boundary. The local electronic environment of Cu in BNKT10 ceramics as determined by EPR is rhombic and the Cu is present in two different electronic environments: CuO_6 and CuO_4 which was manifested by *Peisach-Blumberg* plots assessing the correlation of hyperfine splitting *A* and the g-factor.

An increasing, however, small (< 400 meV) tendency of an increase in binding energies of doped BNKT10 ceramics with increasing V content was observed in the evaluated dopant concentration range from 0 to 1 at.% V. This implies a slight increase in Fermi level upon V doping, which additionally correlates with the lower resistivity and E_A of V doped BNKT10 determined *via* impedance spectroscopy. The oxidation states V^{4+} and V^{5+} were unequivocally confirmed; nevertheless the exact ratio of the two oxidation states for V concentrations $\leq$ 0.5 at.% remains debatable due to the nature of quantification technique.

Regardless of the employed dopant or the change in P_{O_2} in this work, E_A and the resistivity were in all cases lowered, as determined by impedance spectroscopy. The values of E_A and resistivity dropped from 1.37 eV and and 1.6×10^5 Ωm to

$2.0 \times 10^8\,\Omega$m for undoped BNKT10 in air, to as low as 0.23 eV and $1.9 \times 10^0\,\Omega$m to $2.7 \times 10^3\,\Omega$m for the case of undoped BNKT10 in Ar / H_2 atmosphere. Doping BNKT10 with Cu and V resulted in slightly lower E_A (110 ± 10 meV), accompanied by lower resistivities ($1.8 \times 10^4\,\Omega$m to $1.3 \times 10^7\,\Omega$m) compared to the undoped sample.

The contribution of $h^{\bullet}$ to the conductivity can be neglected, as BNKT10 was easily reduced. Doped BNKT10 ceramics were demonstrated to be predominantly influenced by (I) v_{Bi}''' and $v_{Na,K}'$ A-site acceptor vacancies, resulting from the host material, (II) very likely also e', (III) few bulk B-site Cu_{Ti}'' acceptor centers, resulting from Cu doping, as well as (IV) bulk B-site $V_{Ti}^{\bullet}$ donor states, introduced through V doping and generally (V) $v_O^{\bullet\bullet}$.

6. Outlook

In order to further investigate the effect of doping on the defect chemistry and piezoelectric properties of BNKT ceramics, several approaches appear sensible and likely to create further insight.

As apparent from the discussion in context of the resonance behavior of piezoelectric BNKT10 ceramics, the poling of the ceramics plays a crucial role in obtaining high coupling factors. As in this study no extensive poling studies were performed beyond the investigation of a limited number of applied electric fields, temperatures and poling times, it would be highly interesting to investigate the poling in detail. Besides varying mentioned parameters independent of each other to extract trends and optimum poling conditions, the effect of quenching, annealing and ageing samples should be investigated. A good indicator that there is still leeway for improvement of the already promising coupling factors is the low phase angle of the thickness resonance, which is still far from 90°.

In order to assess the applicability of the high electromechanical coupling in thickness direction, building an actual sensor or transducer (*e.g.* a surface acoustic wave sensor with an interdigitated transducer) and determining the behavior of the ceramics under working conditions could be highly insightful with respect to possible applications.

The strain mechanism in BNKT systems is not clearly understood yet, thus *in-situ* neutron diffraction under applied electric field may clarify the underlying mechanisms of BNKT compositions in the rhombohedral, tetragonal and MPB-region of the system. In addition it may be possible to explain the difference in strain response of rhombohedral vs. tetragonal Cu or V doped BNKT10.

To fully address the location of the Cu dopant, scanning tunneling electron microscope with energy dispersive X-ray spectroscopy could be used to investigate grain boundaries and bulk of the ceramics. However, one has to bear in mind that the technique is rather time consuming in terms of sample preparation and measurement.

Using more measuring points to assess the resistivity of samples as a function of oxygen partial pressure and having a more defined oxygen partial pressure would highly benefit the understanding of the defect chemistry. In this work four points with different oxygen partial pressure were investigated and lead to a rough qualitative understanding of the involved defect species. A detailed description will allow for a more precise assessment of the involved species with a greater level of confidence.

In this context it would additionally be interesting to also investigate the high temperature conduction behavior of Cu and V doped BNKT10 ceramics to elucidate the differences in the defect chemistry due to doping.

This work dealt with B-site dopants in detail. It should be beneficial to the understanding of the defect chemistry of BNKT to furthermore investigate the conduction behavior of A-site acceptor (or donor) dopants on the defect chemistry.

To evaluate the influence of oxygen vacancies on the conductivity and have a direct, complimentary assessment of the contributions to the overall conductivity, electromotive force measurements represent a viable method to assess this.

Though probably restricted due to availability and complexity, positron annihilation spectroscopy can provide insight into the vacancies present in undoped and doped BNKT.

The simulation of doping of BNKT or other FE materials in general is highly interesting; however, this involves on the one hand atomistic aspects, which need to be considered, but on the other hand at the same time deals with the continuum scale (*i.e.* domain and grain size). In addition the high degree of disorder (and the number of possible involved defects) in the system is prohibitive of using very simple approaches, applicable to single crystals or more homogeneous FE materials.

7. Literature

1   Tressler, J., Alkoy, S. & Newnham, R. Piezoelectric sensors and sensor materials. *J. Electrocer.* **2**, 257-272 (1998).
2   Newnham, R. E. & Ruschau, G. R. Smart electroceramics. *J. Am. Ceram. Soc.* **74**, 463-480 (1991).
3   Saito, Y. *et al.* Lead-free piezoceramics. *Nature* **432**, 84-87 (2004).
4   Steven, R. A. & Henry, A. S. A review of power harvesting using piezoelectric materials (2003–2006). *Smart Mater. Struct.* **16**, R1 (2007).
5   Rödel, J. *et al.* Transferring lead-free piezoelectric ceramics into application. *J. Eur. Ceram. Soc.* (2015).
6   Haertling, G. H. Ferroelectric ceramics: history and technology. *J. Am. Ceram. Soc.* **82**, 797-818 (1999).
7   Stohs, S. J. & Bagchi, D. Oxidative mechanisms in the toxicity of metal ions. *Free Radical Biol. Med.* **18**, 321-336 (1995).
8   Tanaka, D. *et al. Proc. 28th FMA*, 49-50 (2011).
9   United States Environmental Protection Agency. Prohibition on gasoline containing lead or lead additives for highway use. *Fed. Regist.* **61:3832–8** (1996).
10   EU-Directive 2000/53/EC of the European Parliament and of the Council of 18 September 2000 on end-of life vehicles. *Off. J. Eur. Union* **L269**, 34–42 (2000).
11   EU-Directive 2011/65/EC: Restriction of the use of certain hazardous substances in electrical and electronic equipment (RoHS). *Off. J. Eur. Union* **54**, 88–110 (2011).
12   Panda, P. K. & Sahoo, B. PZT to lead free piezo ceramics: A review. *Ferroelectrics* **474**, 128-143 (2015).
13   Coondoo, I., Panwar, N. & Kholkin, A. Lead-free piezoelectrics: Current status and perspectives. *J. Adv. Dielectr.* **03**, 1330002 (2013).
14   Lee, H. J., Ural, S. O., Chen, L., Uchino, K. & Zhang, S. High power characteristics of lead-free piezoelectric ceramics. *J. Am. Ceram. Soc.* **95**, 3383-3386 (2012).
15   Rödel, J. *et al.* Perspective on the development of lead-free piezoceramics. *J. Am. Ceram. Soc.* **92**, 1153-1177 (2009).
16   Shvartsman, V. V. & Lupascu, D. C. Lead-free relaxor ferroelectrics. *J. Am. Ceram. Soc.* **95**, 1-26 (2012).
17   Shrout, T. & Zhang, S. Lead-free piezoelectric ceramics: Alternatives for PZT? *J. Electroceram.* **19**, 113-126 (2007).
18   Zhang, S., Xia, R. & Shrout, T. Lead-free piezoelectric ceramics *vs.* PZT? *J. Electroceram.* **19**, 251-257 (2007).
19   Takenaka, T. & Nagata, H. Current status and prospects of lead-free piezoelectric ceramics. *J. Eur. Ceram. Soc.* **25**, 2693-2700 (2005).
20   Panda, P. K. Review: environmental friendly lead-free piezoelectric materials. *J. Mater. Sci.* **44**, 5049-5062 (2009).
21   Aksel, E. & Jones, J. L. Advances in lead-free piezoelectric materials for sensors and actuators. *Sensors* **10**, 1935-1954 (2010).
22   Takenaka, T., Nagata, H. & Hiruma, Y. Phase transition temperatures and piezoelectric properties of $Bi_{1/2}Na_{1/2}TiO_3$- and $Bi_{1/2}K_{1/2}TiO_3$-based bismuth

perovskite lead-free ferroelectric ceramics. *IEEE Trans. Ultrason. Ferroelectr. Freq. Control* **56**, 1595-1612 (2009).

23   Otonicar, M., Skapin, S. D., Spreitzer, M. & Suvorov, D. Compositional range and electrical properties of the morphotropic phase boundary in the $Na_{0.5}Bi_{0.5}TiO_3$-$K_{0.5}Bi_{0.5}TiO_3$ system. *J. Eur. Ceram. Soc.* **30**, 971-979 (2010).

24   Zhao, S., Li, G., Ding, A., Wang, T. & Yin, Q. Ferroelectric and piezoelectric properties of $(Na,K)_{0.5}Bi_{0.5}TiO_3$ lead free ceramics. *J. Phys. D: Appl. Phys.* **39**, 2277-2281 (2006).

25   Yoshii, K., Hiruma, Y., Nagata, H. & Takenaka, T. Electrical properties and depolarization temperature of $(Bi_{1/2}Na_{1/2})TiO_3$-$(Bi_{1/2}K_{1/2})TiO_3$ lead-free piezoelectric ceramics. *Jpn. J. Appl. Phys., Part 1* **45**, 4493-4496 (2006).

26   Levin, I. *et al.* Local structure, pseudosymmetry, and phase transitions in $Na_{1/2}Bi_{1/2}TiO_3$-$K_{1/2}Bi_{1/2}TiO_3$ ceramics. *Phys. Rev. B: Condens. Matter Mater. Phys.* **87**, 024113/024111-024113/024111 (2013).

27   Elkechal, O., Manier, M. & Mercurio, J. P. $Na_{0.5}Bi_{0.5}TiO_3$-$K_{0.5}Bi_{0.5}TiO_3$ (NBT-KBT) system. A structural and electrical study. *Phys. Status Solidi A* **157**, 499-506 (1996).

28   Hiruma, Y., Yoshii, K., Aoyagi, R., Nagata, H. & Takenaka, T. Piezoelectric properties and depolarization temperatures of $(Bi_{1/2}Na_{1/2})TiO_3$-$(Bi_{1/2}K_{1/2})TiO_3$-$BaTiO_3$ lead-free piezoelectric ceramics. *Key Eng. Mater.* **320**, 23-26 (2006).

29   Hiruma, Y., Yoshii, K., Nagata, H. & Takenaka, T. Investigation of phase transition temperatures on $(Bi_{1/2}Na_{1/2})TiO_3$-$(Bi_{1/2}K_{1/2})TiO_3$ and $(Bi_{1/2}Na_{1/2})TiO_3$-$BaTiO_3$ lead-free piezoelectric ceramics by electrical measurements. *Ferroelectrics* **346**, 114-119 (2007).

30   Wang, X. X., Choy, S. H., Tang, X. G. & Chan, H. L. W. Dielectric behavior and microstructure of $Bi_{1/2}Na_{1/2}TiO_3$-$Bi_{1/2}K_{1/2}TiO_3$-$BaTiO_3$ lead-free piezoelectric ceramics. *J. Appl. Phys.* **97**, 104101/104101-104101/104104 (2005).

31   Takenaka, T., Nagata, H., Hiruma, Y., Yoshii, Y. & Matumoto, K. Lead-free piezoelectric ceramics based on perovskite structures. *J. Electroceram.* **19**, 259-265 (2008).

32   Nagata, H., Yoshida, M., Makiuchi, Y. & Takenaka, T. Large piezoelectric constant and high Curie temperature of lead-free piezoelectric ceramic ternary system based on bismuth sodium titanate-bismuth potassium titanate-barium titanate near the morphotropic phase boundary. *Jpn. J. Appl. Phys., Part 1* **42**, 7401-7403 (2003).

33   Fan, G., Lu, W., Wang, X. & Liang, F. Morphotropic phase boundary and piezoelectric properties of $(Bi_{1/2}Na_{1/2})TiO_3$-$(Bi_{1/2}K_{1/2})TiO_3$- $KNbO_3$ lead-free piezoelectric ceramics. *Appl. Phys. Lett.* **91**, 202908/202901-202908/202903 (2007).

34   Hussain, A., Ahn, C. W., Ullah, A., Lee, J. S. & Kim, I. W. Dielectric, ferroelectric and field-induced strain behavior of $K_{0.5}Na_{0.5}NbO_3$-modified $Bi_{0.5}(Na_{0.78}K_{0.22})_{0.5}TiO_3$ lead-free ceramics. *Ceram. Int.* **38**, 4143-4149 (2012).

35   Seifert, K. T. P., Jo, W. & Rödel, J. Temperature-insensitive large strain of $(Bi_{1/2}Na_{1/2})TiO_3$-$(Bi_{1/2}K_{1/2})TiO_3$- $(K_{0.5}Na_{0.5})NbO_3$ lead-free piezoceramics. *J. Am. Ceram. Soc.* **93**, 1392-1396 (2010).

36   Anton, E.-M., Jo, W., Trodahl, J., Damjanovic, D. & Rödel, J. Effect of $K_{0.5}Na_{0.5}NbO_3$ on properties at and off the morphotropic phase boundary in

Bi$_{0.5}$Na$_{0.5}$TiO$_3$-Bi$_{0.5}$K$_{0.5}$TiO$_3$ ceramics. *Jpn. J. Appl. Phys.* **50**, 055802/055801-055802/055807 (2011).

37   Hiruma, Y., Nagata, H. & Takenaka, T. Depolarization temperature and piezoelectric properties of (Bi$_{1/2}$Na$_{1/2}$)TiO$_3$-(Bi$_{1/2}$Li$_{1/2}$)TiO$_3$-(Bi$_{1/2}$K$_{1/2}$)TiO$_3$ lead-free piezoelectric ceramics. *Ceram. Int.* **35**, 117-120 (2009).

38   Nagata, H., Hiruma, Y. & Takenaka, T. High power piezoelectric characteristics for perovskite-type lead-free ferroelectric ceramics. *Integr. Ferroelectr.* **115**, 63-70 (2010).

39   Zhang, H., Jiang, S., Xiao, J. & Kajiyoshi, K. Low temperature preparation and electrical properties of sodium-potassium bismuth titanate lead-free piezoelectric thick films by screen printing. *J. Eur. Ceram. Soc.* **30**, 3157-3165 (2010).

40   Yuan, Y., Zhang, S., Zhou, X. & Liu, J. Phase transition and temperature dependences of electrical properties of [Bi$_{0.5}$(Na$_{1-x-y}$K$_x$Li$_y$)$_{0.5}$]TiO$_3$ ceramics. *Jpn. J. Appl. Phys., Part 1* **45**, 831-834 (2006).

41   Wu, Y., Wang, X., Zhong, C. & Li, L. Effect of Mn doping on microstructure and electrical properties of the (Na$_{0.85}$K$_{0.15}$)$_{0.5}$Bi$_{0.5}$TiO$_3$ thin films prepared by sol-gel method. *J. Am. Ceram. Soc.* **94**, 3877-3882 (2011).

42   Xu, M. *et al.* Phase diagram and electric properties of the (Mn, K)-modified Bi$_{0.5}$Na$_{0.5}$TiO$_3$-BaTiO$_3$ lead-free ceramics. *J. Mater. Sci.* **46**, 4675-4682 (2011).

43   Taghaddos, E., Hejazi, M. & Safari, A. Electromechanical properties of acceptor-doped lead-free piezoelectric ceramics. *J. Am. Ceram. Soc.*, n/a-n/a (2014).

44   Bierer, D. W. Bismuth subsalicylate: history, chemistry, and safety. *Rev. Infect. Dis.* **12**, S3-S8 (1990).

45   Tillman, L. A., Drake, F. M., Dixon, J. S. & Wood, J. R. Safety of bismuth in the treatment of gastrointestinal diseases. *Alimentary Pharmacology & Therapeutics* **10**, 459-467 (1996).

46   Pramanick, A., Prewitt, A. D., Forrester, J. S. & Jones, J. L. Domains, domain walls and defects in perovskite ferroelectric oxides: A review of present understanding and recent contributions. *Crc. Cr. Rev. Sol. State* **37**, 243-275 (2012).

47   Smyth, D. M., Harmer, M. P. & Peng, P. Defect chemistry of relaxor ferroelectrics and the implications for dielectric degradation. *J. Am. Ceram. Soc.* **72**, 2276-2278 (1989).

48   Cao, W. in *Disorder and strain-induced complexity in functional materials* Vol. 148 *Springer Series in Materials Science* (eds Tomoyuki Kakeshita, Takashi Fukuda, Avadh Saxena, & Antoni Planes) Ch. 7, 113-134 (Springer Berlin Heidelberg, 2012).

49   Kröger, F. A. & Vink, H. J. in *Solid State Phys.* Vol. Volume 3 (eds Seitz Frederick & Turnbull David) 307-435 (Academic Press, 1956).

50   Noheda, B. *et al.* A monoclinic ferroelectric phase in the Pb(Zr$_{1-x}$Ti$_x$)O$_3$ solid solution. *Appl. Phys. Lett.* **74**, 2059-2061 (1999).

51   Groth, P. Über Beziehungen zwischen Krystallform und chemische Constitution bei einigen organischen Verbindungen. *Ann. d. Phys.* **217**, 31-43 (1870).

52   West, A., Sinclair, D. & Hirose, N. Characterization of electrical materials, especially ferroelectrics, by impedance spectroscopy. *J. Electroceram.* **1**, 65-71 (1997).

53   Irvine, J. T. S., Sinclair, D. C. & West, A. R. Electroceramics: characterization by impedance spectroscopy. *Adv. Mater.* **2**, 132-138 (1990).

54   Barsoukov, E. & MacDonald, R. *Impedance Spectroscopy: Theory, Experiment, and Applications, 2nd Edition*. (John Wiley & Sons, 2005).

55   Zhao, T.-L., Guo, Z.-L. & Wang, C.-M. The effects of Na/K ratio on the electrical properties of sodium-potassium bismuth titanate $Na_{0.5}Bi_{4.5}Ti_4O_{15}$–$K_{0.5}Bi_{4.5}Ti_4O_{15}$. *J. Am. Ceram. Soc.* **95**, 1062-1067 (2012).

56   Caballero Cuesta, A., Jardiel, T. & Villegas, M. Aurivillius ceramics: $Bi_4Ti_3O_{12}$-based piezoelectrics. *J. Ceram. Soc. Jpn.* **116**, 511-518 (2008).

57   Wang, C.-M. & Wang, J.-F. High performance Aurivillius phase sodium-potassium bismuth titanate lead-free piezoelectric ceramics with lithium and cerium modification. *Appl. Phys. Lett.* **89**, 202905/202901-202905/202903 (2006).

58   Yan, H. *et al.* A lead-free high-Curie-point ferroelectric ceramic, $CaBi_2Nb_2O_9$. *Adv. Mater.* **17**, 1261-1265 (2005).

59   Jaffe, B., Cook, W. R., Jr. & Jaffe, H. *Piezoelectric ceramics (nonmetallic solids, no. 3)*. (Academic, 1971).

60   Cross, L. E. & Pohanka, R. C. Ferroelectricity in bismuth oxide type layer structure compounds. *Mater. Res. Bull.* **6**, 939-949 (1971).

61   Gao, X., Zhou, Z., Xue, J. & Wang, J. Effects of excess Bi_2O_3 on the ferroelectric behavior of Nd-doped $Bi_4Ti_3O_{12}$ thin films. *J. Am. Ceram. Soc.* **88**, 1037-1040 (2005).

62   Ringgaard, E. & Wurlitzer, T. Lead-free piezoceramics based on alkali niobates. *J. Eur. Ceram. Soc.* **25**, 2701-2706 (2005).

63   Hayashi, J. *et al.* Piezoelectric material. WO2013005702A1 (2013).

64   Nagai, N. & Watanabe, K. Barium calcium titanate zirconate ceramic composition and capacitor. JP08012427A (1996).

65   Priya, S. & Nahm, S. *Lead-Free Piezoelectrics*. (Springer Science+Business Media, LLC, 2012).

66   Zhang, S. *et al.* Dielectric and piezoelectric properties of niobium-modified $BiInO_3$–$PbTiO_3$ perovskite ceramics with high Curie temperatures. *J. Mater. Res.* **20**, 2067-2071 (2005).

67   Yan, H., Ning, H., Kan, Y., Wang, P. & Reece, M. J. Piezoelectric ceramics with super-high Curie points. *J. Am. Ceram. Soc.* **92**, 2270-2275 (2009).

68   Tsuguto, T., Toshihiko, T. & Yasuyoshi, S. Piezoelectric properties of bismuth layer-structured ferroelectric ceramics with a preferred orientation processed by the reactive templated grain growth method. *Jpn. J. Appl. Phys.* **38**, 5553 (1999).

69   Enzhu, L., Hirofumi, K., Takuya, H. & Takaaki, T. A shear-mode ultrasonic motor using potassium sodium niobate-based ceramics with high mechanical quality factor. *Jpn. J. Appl. Phys.* **47**, 7702 (2008).

70   Matsubara, M. *et al.* Processing and piezoelectric properties of lead-free $(K,Na)(Nb,Ta)O_3$ ceramics. *J. Am. Ceram. Soc.* **88**, 1190-1196 (2005).

71   Daisuke, T., Takeo, T., Masahito, F., Satoshi, W. & Yoshihiro, K. Thermal reliability of alkaline niobate-based lead-free piezoelectric ceramics. *Jpn. J. Appl. Phys.* **48**, 09KD08 (2009).

72   Choy, S. H. *et al.* 0.90(Bi$_{1/2}$Na$_{1/2}$)TiO$_3$-0.05(Bi$_{1/2}$K$_{1/2}$)TiO$_3$- 0.05BaTiO$_3$ transducer for ultrasonic wirebonding applications. *Appl. Phys. A: Mater. Sci. Process.* **84**, 313-316 (2006).

73   Li, F. & Zuo, R. Bismuth sodium titanate based lead-free ceramic/epoxy 1–3 composites: fabrication and electromechanical properties. *J. Mater. Sci.: Mater. Electron.* **25**, 2730-2736 (2014).

74   Dittmer, R., Aulbach, E., Jo, W., Webber, K. G. & Rödel, J. Large blocking force in Bi$_{1/2}$Na$_{1/2}$TiO$_3$-based lead-free piezoceramics. *Scr. Mater.* **67**, 100-103 (2012).

75   Zhang, S.-T., Kounga, A. B., Aulbach, E., Ehrenberg, H. & Rödel, J. Giant strain in lead-free piezoceramics Bi$_{0.5}$Na$_{0.5}$TiO$_3$-BaTiO$_3$-K$_{0.5}$Na$_{0.5}$NbO$_3$ system. *Appl. Phys. Lett.* **91**, 112906 (2007).

76   Ahn, C. W. *et al.* Low-temperature sintering of Bi$_{0.5}$(Na,K)$_{0.5}$TiO$_3$ for multilayer ceramic actuators. *J. Am. Ceram. Soc.* **98**, 1877-1883 (2015).

77   Liu, W. & Ren, X. Large piezoelectric effect in Pb-free ceramics. *Phys. Rev. Lett.* **103**, 257602/257601-257602/257604 (2009).

78   Xue, D. *et al.* Elastic, piezoelectric, and dielectric properties of Ba(Zr$_{0.2}$Ti$_{0.8}$)O$_3$-50(Ba$_{0.7}$Ca$_{0.3}$)TiO$_3$ Pb-free ceramic at the morphotropic phase boundary. *J. Appl. Phys.* **109**, 054110 (2011).

79   Ando, A. & Hisaki, T. Piezoelectric ceramic composition. EP780350A1 (1997).

80   Shirane, G., Newnham, R. & Pepinsky, R. Dielectric properties and phase transitions of NaNbO$_3$ and (Na,K)NbO$_3$. *Phys. Rev.* **96**, 581-588 (1954).

81   Shirane, G., Danner, H., Pavlovic, A. & Pepinsky, R. Phase transitions in ferroelectric KNbO$_3$. *Phys. Rev.* **93**, 672-673 (1954).

82   Zhen, Y. & Li, J.-F. Normal sintering of (K,Na)NbO$_3$-based ceramics: Influence of sintering temperature on densification, microstructure, and electrical properties. *J. Am. Ceram. Soc.* **89**, 3669-3675 (2006).

83   Zhang, S., Xia, R., Shrout, T. R., Zang, G. & Wang, J. Characterization of lead free K$_{0.5}$Na$_{0.5}$NbO$_3$-LiSbO$_3$ piezoceramic. *Solid State Commun.* **141**, 675-679 (2007).

84   Saito, T., Wada, T., Adachi, H. & Kanno, I. Pulsed laser deposition of high-quality (K,Na)NbO$_3$ thin films on SrTiO$_3$ substrate using high-density ceramic targets. *Jpn. J. Appl. Phys., Part 1* **43**, 6627-6631 (2004).

85   Li, J.-F., Wang, K., Zhang, B.-P. & Zhang, L.-M. Ferroelectric and piezoelectric properties of fine-grained Na$_{0.5}$K$_{0.5}$NbO$_3$ lead-free piezoelectric ceramics prepared by spark plasma sintering. *J. Am. Ceram. Soc.* **89**, 706-709 (2006).

86   Wang, R., Xie, R., Sekiya, T. & Shimojo, Y. Fabrication and characterization of potassium-sodium niobate piezoelectric ceramics by spark-plasma-sintering method. *Mater. Res. Bull.* **39**, 1709-1715 (2004).

87   Zhang, B.-P., Li, J.-F., Wang, K. & Zhang, H. Compositional dependence of piezoelectric properties in Na$_x$K$_{1-x}$NbO$_3$ lead-free ceramics prepared by spark plasma sintering. *J. Am. Ceram. Soc.* **89**, 1605-1609 (2006).

88   Egerton, L. & Bieling, C. A. Isostatically hot-pressed sodium-potassium niobate transducer material for ultrasonic devices. *Amer. Ceram. Soc., Bull.* **47**, 1151-1156 (1968).

89   Li, E., Kakemoto, H., Wada, S. & Tsurumi, T. Influence of CuO on the structure and piezoelectric properties of the alkaline niobate-based lead-free ceramics. *J. Am. Ceram. Soc.* **90**, 1787-1791 (2007).

90   Ahn, C.-W. *et al.* Low temperature sintering and piezoelectric properties of CuO-doped $(K_{0.5}Na_{0.5})NbO_3$ ceramics. *Ferroelectr., Lett. Sect.* **35**, 66-72 (2008).

91   Park, H.-Y. *et al.* Low-temperature sintering and piezoelectric properties of CuO-added $0.95(Na_{0.5}K_{0.5})NbO_3$-$0.05BaTiO_3$ ceramics. *J. Am. Ceram. Soc.* **90**, 4066-4069 (2007).

92   Park, H.-Y., Seo, I.-T., Choi, J.-H. & Nahm, S. Low-temperature sintering and piezoelectric properties of $(Na_{0.5}K_{0.5})NbO_3$ lead-free piezoelectric ceramics. *J. Am. Ceram. Soc.* **93**, 36-39 (2010).

93   Wang, C.-H. Effect of Bi_2O_3 addition and sintering time on the physical and electrical properties of lead-free $(Na_{0.5}Bi_{0.5})TiO_3$-$Ba(Zr_{0.04}Ti_{0.96})O_3$ ceramics. *J. Ceram. Soc. Jpn.* **117**, 693-697 (2009).

94   Matsubara, M., Yamaguchi, T., Kikuta, K. & Hirano, S.-I. Sinterability and piezoelectric properties of $(K,Na)NbO_3$ ceramics with novel sintering aid. *Jpn. J. Appl. Phys., Part 1* **43**, 7159-7163 (2004).

95   Ahtee, M. & Hewat, A. W. Structural phase transitions in sodium-potassium niobate solid solutions by neutron powder diffraction. *Acta Crystallogr., Sect. A* **A34**, 309-317 (1978).

96   Zhang, S., Xia, R., Hao, H., Liu, H. & Shrout, T. R. Mitigation of thermal and fatigue behavior in $K_{0.5}Na_{0.5}NbO_3$-based lead free piezoceramics. *Appl. Phys. Lett.* **92**, 152904/152901-152904/152903 (2008).

97   Mgbemere, H. E., Herber, R.-P. & Schneider, G. A. Investigation of the dielectric and piezoelectric properties of potassium sodium niobate ceramics close to the phase boundary at $(K_{0.35}Na_{0.65})NbO_3$ and partial substitutions with lithium and antimony. *J. Eur. Ceram. Soc.* **29**, 3273-3278 (2009).

98   Yilmaz, E. D., Mgbemere, H. E., Oezcoban, H., Fernandes, R. P. & Schneider, G. A. Investigation of fracture toughness of modified $(K_xNa_{1-x})NbO_3$ lead-free piezoelectric ceramics. *J. Eur. Ceram. Soc.* **32**, 3339-3344 (2012).

99   Smolenskii, G. A., Isupov, V. A., Agranovskaya, A. I. & Krainik, N. N. New ferroelectrics with complex compounds. IV. *Fiz. Tverd. Tela (S.-Peterburg)* **2**, 2982-2985 (1960).

100   Hiruma, Y., Nagata, H. & Takenaka, T. Thermal depoling process and piezoelectric properties of bismuth sodium titanate ceramics. *J. Appl. Phys.* **105**, - (2009).

101   Hiruma, Y., Watanabe, Y., Nagata, H. & Takenaka, T. Phase transition temperatures of divalent and trivalent ions substituted $Bi_{1/2}Na_{1/2}TiO_3$ ceramics. *Key Eng. Mater.* **350**, 93-96 (2007).

102   Ma, C., Guo, H., Beckman, S. P. & Tan, X. Creation and destruction of morphotropic phase boundaries through electrical poling: a case study of lead-free $(Bi_{1/2}Na_{1/2})TiO_3$-$BaTiO_3$ piezoelectrics. *Phys. Rev. Lett.* **109**, 107602/107601-107602/107605 (2012).

103   Ogino, M. *et al.* Polarization rotation and monoclinic distortion in ferroelectric $(Bi_{0.5}Na_{0.5})TiO_3$-$BaTiO_3$ single crystals under electric fields. *Crystals* **4**, 273-295, 223 pp. (2014).

104   Takenaka, T., Maruyama, K.-J. & Sakata, K. $Bi_{1/2}Na_{1/2}TiO_3$-$BaTiO_3$ system for lead-free piezoelectric ceramics. *Jpn. J. Appl. Phys.* **30**, 2236 (1991).

105   Hiruma, Y., Aoyagi, R., Nagata, H. & Takenaka, T. Piezoelectric properties of $BaTiO_3$-$Bi_{1/2}K_{1/2}TiO_3$ ferroelectric ceramics. *Jpn. J. Appl. Phys.* **43 Part1**, 7556-7559 (2004).

106   Sakata, K. & Masuda, Y. Ferroelectric and antiferroelectric properties of $(Na_{0.5}Bi_{0.5})TiO_3$-$SrTiO_3$ solid solution ceramics. *Ferroelectrics* **7**, 347-349 (1974).

107   Xie, H., Jin, L., Shen, D., Wang, X. & Shen, G. Morphotropic phase boundary, segregation effect and crystal growth in the NBT-KBT system. *J. Cryst. Growth* **311**, 3626-3630 (2009).

108   Zhao, W., Zhou, H., Yan, Y. & Liu, D. Morphotropic phase boundary study of the BNT-BKT lead-free piezoelectric ceramics. *Key Eng. Mater.* **368-372**, 1908-1910 (2008).

109   Sasaki, A., Chiba, T., Mamiya, Y. & Otsuki, E. Dielectric and piezoelectric properties of $Bi_{0.5}Na_{0.5}TiO_3$-$Bi_{0.5}K_{0.5}$-TiO_3 systems. *Jpn. J. Appl. Phys.* **38**, 5564 (2008).

110   Zhang, Y.-R., Li, J.-F. & Zhang, B.-P. Enhancing electrical properties in NBT-KBT lead-free piezoelectric ceramics by optimizing sintering temperature. *J. Am. Ceram. Soc.* **91**, 2716-2719 (2008).

111   Izumi, M., Yamamoto, K., Suzuki, M., Noguchi, Y. & Miyayama, M. Large electric-field-induced strain in $Bi_{0.5}Na_{0.5}TiO_3$-$Bi_{0.5}K_{0.5}TiO_3$ solid solution single crystals. *Appl. Phys. Lett.* **93**, 242903/242901-242903/242903 (2008).

112   Morishita, A., Kitanaka, Y., Izumi, M., Noguchi, Y. & Miyayama, M. Crystal growth and ferroelectric properties in $Bi_{0.5}K_{0.5}TiO_3$-$Bi_{0.5}Na_{0.5}TiO_3$ crystals. *Key Eng. Mater.* **445**, 7-10 (2010).

113   Morishita, A., Kitanaka, Y., Izumi, M., Noguchi, Y. & Miyayama, M. Enhanced piezoelectric properties in $(Bi_{0.5}K_{0.5})TiO_3$-$(Bi_{0.5}Na_{0.5})TiO_3$ ferroelectric single crystals. *J. Adv. Dielectr.* **1**, 63-69 (2011).

114   Teranishi, S. *et al.* Giant strain in lead-free $(Bi_{0.5}Na_{0.5})TiO_3$-based single crystals. *Appl. Phys. Lett.* **92**, 182905/182901-182905/182903 (2008).

115   Sun, R. *et al.* Growth and electrical properties of $0.95Na_{0.5}Bi_{0.5}TiO_3$–$0.05K_{0.5}Bi_{0.5}TiO_3$ lead-free piezoelectric crystal by the TSSG method. *J. Cryst. Growth* **341**, 34-37 (2012).

116   Sun, R. *et al.* Growth and characterization of $Na_{0.5}Bi_{0.5}TiO_3$-$K_{0.5}Bi_{0.5}TiO_3$ lead-free piezoelectric crystal by the TSSG method. *J. Adv. Dielectr.* **1**, 237-242 (2011).

117   Sun, R. *et al.* Growth and orientation dependence of electrical properties of $0.92Na_{0.5}Bi_{0.5}TiO_3$-$0.08K_{0.5}Bi_{0.5}TiO_3$ lead-free piezoelectric single crystal. *J. Appl. Phys.* **109**, 124113/124111-124113/124118 (2011).

118   Stokes, H. T., Kisi, E. H., Hatch, D. M. & Howard, C. J. Group-theoretical analysis of octahedral tilting in ferroelectric perovskites. *Acta Crystallogr., Sect. B: Struct. Sci.* **B58**, 934-938 (2002).

119   Dittmer, R., Jo, W., Daniels, J., Schaab, S. & Rödel, J. Relaxor characteristics of morphotropic phase boundary $(Bi_{1/2}Na_{1/2})TiO_3$-$(Bi_{1/2}K_{1/2})TiO_3$ modified with $Bi(Zn_{1/2}Ti_{1/2})O_3$. *J. Am. Ceram. Soc.* **94**, 4283-4290 (2011).

120   Patterson, E. A., Cann, D. P., Pokorny, J. & Reaney, I. M. Electromechanical strain in $BiZn_{1/2}Ti_{1/2}O_3$-$Bi_{1/2}Na_{1/2}TiO_3$-$Bi_{1/2}K_{1/2}TiO_3$ solid solutions. *J. Appl. Phys.* **111** (2012).

121   Hao, J. *et al.* Switching of morphotropic phase boundary and large strain response in lead-free ternary $Bi_{0.5}Na_{0.5}TiO_3$-$K_{0.5}Bi_{0.5}TiO_3$-$K_{0.5}Na_{0.5}NbO_3$ system. *J. Appl. Phys.* **113**, 114106-114113 (2013).

122   Gao, F. *et al.* Texture development and dielectric relaxor behavior of 0.80Na$_{0.5}$Bi$_{0.5}$TiO$_3$-0.20K$_{0.5}$Bi$_{0.5}$TiO$_3$ ceramics templated by plate-like NaNbO$_3$ particles. *J. Eur. Ceram. Soc.* **31**, 2987-2996 (2011).

123   Chen, P.-Y., Chou, C.-C., Tseng, T.-Y. & Chen, H. H. D. Impedance spectroscopic study on Li-doped BNKT piezoelectric ceramics. *Ferroelectrics* **381**, 100-104, 104 plates (2009).

124   Lei, N., Zhu, M., Wang, L., Yang, P. & Hou, Y. Microstructure and phase transition of lead-free (Bi$_{1/2}$Na$_{1/2}$)TiO$_3$-based ferroelectrics via different Li$^+$ introduction sources. *Phys. Status Solidi A* **208**, 186-190 (2011).

125   Lei, N. *et al.* Depolarization behavior of lead-free (Bi$_{1/2}$Na$_{1/2}$)TiO$_3$-based ferroelectric with different Li$^+$ introduction sources. *Adv. Mater. Res.* **177**, 215-218 (2011).

126   Jiang, X. P., Li, L. Z., Zeng, M. & Chan, H. L. W. Dielectric properties of Mn-doped (Na$_{0.8}$K$_{0.2}$)$_{0.5}$Bi$_{0.5}$TiO$_3$ ceramics. *Mater. Lett.* **60**, 1786-1790 (2006).

127   Jiang, X., Li, L., Jiang, F., Zheng, Y. & Liu, L. Effects of Mn-doping on the piezoelectric and ferroelectric properties of (Na$_{0.8}$K$_{0.2}$)$_{0.5}$Bi$_{0.5}$TiO$_3$ ceramics. *Key Eng. Mater.* **368-372**, 69-71 (2008).

128   Wu, Y., Wang, X., Zhong, C. & Li, L. Effect of anneal conditions on electrical properties of Mn-doped (Na$_{0.85}$K$_{0.15}$)$_{0.5}$Bi$_{0.5}$TiO$_3$ thin films prepared by sol-gel method. *J. Am. Ceram. Soc.* **94**, 1843-1849 (2011).

129   Wang, B. *et al.* Piezoelectric and ferroelectric properties of (Bi$_{1-x}$Na$_{0.8}$K$_{0.2}$La$_x$)$_{0.5}$TiO$_3$ lead-free ceramics. *J. Alloys Compd.* **526**, 79-84 (2012).

130   Zhang, H., Jiang, S., Kajiyoshi, K. & Xiao, J. Dielectric, ferroelectric, pyroelectric, and piezoelectric properties of La-modified lead-free sodium-potassium bismuth titanate thick films. *J. Am. Ceram. Soc.* **93**, 750-757 (2010).

131   Yoo, J. *et al.* Piezoelectric and dielectric properties of La$_2$O$_3$ added Bi(Na, K)TiO$_3$-SrTiO$_3$ ceramics for pressure sensor application. *Sens. Actuators, A* **A126**, 41-47 (2006).

132   Yoshii, K., Hiruma, Y., Suzuki, M., Nagata, H. & Takenaka, T. The piezoelectric properties of La$_2$O$_3$ doped (Bi$_{1/2}$Na$_{1/2}$)TiO$_3$-(Bi$_{1/2}$K$_{1/2}$)TiO$_3$ ceramics. *Ferroelectrics* **358**, 134-138 (2007).

133   Ullah, A., Ahn, C. W., Hussain, A., Lee, S. Y. & Kim, I. W. Phase transition, electrical properties, and temperature-insensitive large strain in BiAlO$_3$-modified Bi$_{0.5}$(Na$_{0.75}$K$_{0.25}$)$_{0.5}$TiO$_3$ lead-free piezoelectric ceramics. *J. Am. Ceram. Soc.* **94**, 3915-3921 (2011).

134   Ullah, A. *et al.* Effect of potassium concentration on the structure and electrical properties of lead-free Bi$_{0.5}$(Na,K)$_{0.5}$TiO$_3$-BiAlO$_3$ piezoelectric ceramics. *J. Alloys Compd.* **509**, 3148-3154 (2011).

135   Ullah, A., Ahn, C. W. & Kim, I. W. Phase transition, microstructure and electric-field-induced large strain in Bi$_{0.5}$(Na$_{0.85}$K$_{0.15}$)$_{0.5}$TiO$_3$-BiAlO$_3$ lead-free piezoelectric ceramics. *Phys. Status Solidi A* **207**, 2578-2584 (2010).

136   Ullah, A. *et al.* Structural transition and large electric field-induced strain in BiAlO$_3$-modified Bi$_{0.5}$(Na$_{0.8}$K$_{0.2}$)$_{0.5}$TiO$_3$ lead-free piezoelectric ceramics. *Solid State Commun.* **150**, 1145-1149 (2010).

137   Ullah, A. *et al.* Phase transition, microstructures and electromechanical properties of BiAlO$_3$-modified Bi$_{0.5}$(Na,K)$_{0.5}$TiO$_3$ lead-free piezoelectric ceramics. *J. Korean Phys. Soc.* **57**, 1102-1105 (2010).

138   Lee, D. S., Lim, D. H., Kim, M. S., Kim, K. H. & Jeong, S. J. Electric field-induced deformation behavior in mixed $Bi_{0.5}Na_{0.5}TiO_3$ and $Bi_{0.5}(Na_{0.75}K_{0.25})_{0.5}TiO_3$-BiAlO$_3$. *Appl. Phys. Lett.* **99**, 062906/062901-062906/062903 (2011).

139   Fu, P. *et al.* Structure and electrical properties of (1-x)($Bi_{0.5}(Na_{0.82}K_{0.18})_{0.5}$)TiO$_3$-xBiAlO$_3$ lead-free piezoelectric ceramics. *J. Alloys Compd.* **535**, 5-9 (2012).

140   Su, L. D., Jong, J. S., Soo, K. M. & Hyuk, K. J. Electric field induced polarization and strain of Bi-based ceramic composites. *J. Appl. Phys.* **112**, 124109/124101-124109/124111 (2012).

141   Kawada, S. *et al.* in *International Symposium on Applications of Ferroelectrics and International Symposium on Piezoresponse Force Microscopy and Nanoscale Phenomena in Polar Materials.* 20-23 (Institute of Electrical and Electronics Engineers).

142   Hayashi, H. *et al.* Reliability of nickel inner electrode lead-free multilayer piezoelectric ceramics. *Jpn. J. Appl. Phys.* **51**, 09LD01/01-09LD01/04 (2012).

143   Eichel, R. A., Kungl, H. & Jakes, P. Defect structure of non-stoichiometric and aliovalently doped perovskite oxides. *Mater. Technol.* **28**, 241-246 (2013).

144   Elissalde, C., Simon, A. & Ravez, J. A new perovskite oxyfluoride relaxor ferroelectric. *Ferroelectrics* **199**, 217-221 (1997).

145   Ohtaka, O., Von Der Mühll, R. & Ravez, J. Dielectric, piezoelectric and pyroelectric properties of Pb(Zr, Ti)O$_3$ ceramics elaborated by low temperature sintering with the aid of oxyfluoride additives. *Ferroelectrics Letters Section* **19**, 13-18 (1995).

146   Aliouane, K., Hamadène, M., Guehria-Laïdoudi, A., Simon, A. & Ravez, J. New oxyfluoride lead-free ferroelectric relaxors in the $BaTiO_3$–$BaZrO_3$–$CaLiF_3$ system. *J. Fluorine Chem.* **105**, 71-76 (2000).

147   Hinuma, Y. *et al.* First-principles study on relaxor-type ferroelectric behavior without chemical inhomogeneity in $BaTaO_2N$ and $SrTaO_2N$. *Chem. Mater.* (2012).

148   Kim, Y.-I. *et al.* Epitaxial thin-film deposition and dielectric properties of the perovskite oxynitride $BaTaO_2N$. *Chem. Mater.* **19**, 618-623 (2007).

149   Kim, Y.-I., Woodward, P. M., Baba-Kishi, K. Z. & Tai, C. W. Characterization of the structural, optical, and dielectric properties of oxynitride perovskites AMO_2N (A = Ba, Sr, Ca; M = Ta, Nb). *Chem. Mater.* **16**, 1267-1276 (2004).

150   Zhang, Y.-R., Motohashi, T., Masubuchi, Y. & Kikkawa, S. Sintering and dielectric properties of perovskite SrTaO2N ceramics. *J. Eur. Ceram. Soc.* **32**, 1269-1274 (2012).

151   Fuertes, A. Chemistry and applications of oxynitride perovskites. *J. Mater. Chem.* **22**, 3293-3299 (2012).

152   Nitesh, K. *et al.* Effect of co-substitution of nitrogen and fluorine in BaTiO$_3$ on ferroelectricity and other properties. *J. Phys: Condens. Mat.* **25**, 345901 (2013).

153   Da Wang, Y. & Umeya, K. Electrical properties of PTCR barium titanate. *J. Am. Ceram. Soc.* **73**, 669-677 (1990).

154   Dragan, D. Ferroelectric, dielectric and piezoelectric properties of ferroelectric thin films and ceramics. *Rep. Prog. Phys.* **61**, 1267 (1998).

155   Kholkin, A. L., Colla, E. L., Tagantsev, A. K., Taylor, D. V. & Setter, N. Fatigue of piezoelectric properties in Pb(Zr,Ti)O$_3$ films. *Appl. Phys. Lett.* **68**, 2577-2579 (1996).

156   Carl, K. & Härdtl, K. H. Electrical after-effects in Pb(Ti, Zr)O$_3$ ceramics. *Ferroelectrics* **17**, 473-486 (1977).

157   Erdem, E. *et al.* Characterization of (Fe'$_{Zr,Ti}$ - V$_O^{\bullet\bullet}$). defect dipoles in (La,Fe)-codoped PZT 52.5/47.5 piezoelectric ceramics by multifrequency electron paramagnetic resonance spectroscopy. *IEEE Trans. Ultrason. Ferroelectr. Freq. Control* **55**, 1061-1068 (2008).

158   Eichel, R.-A. *et al.* High-field/high-frequency EPR of paramagnetic functional centers in Cu^{2+}- and Fe^{3+}-modified polycrystalline PbZr$_x$Ti$_{(1-x)}$O$_3$ ferroelectrics. *Magn. Reson. Chem.* **43**, S166-S173 (2005).

159   Erdem, E., Böttcher, R., Semmelhack, H.-C., Gläsel, H.-J. & Hartmann, E. Multi-frequency EPR study of Cr^{3+} doped lead titanate (PbTiO$_3$) nanopowders. *Phys. Status Solidi B* **239**, R7-R9 (2003).

160   Keeble, D. J., Li, Z. & Harmatz, M. Electron paramagnetic resonance of Cu^{2+} in PbTiO$_3$. *J. Phys. Chem. Solids* **57**, 1513-1515 (1996).

161   Erdem, E. *et al.* Defect structure in "soft" (Gd,Fe)-codoped PZT 52.5/47.5 piezoelectric ceramics. *Funct. Mater. Lett.* **1**, 7-11 (2008).

162   Yang, W.-C., Hu, C.-T. & Lin, I. N. Effect of Y$_2$O$_3$/MgO Co-doping on the electrical properties of base-metal-electroded BaTiO$_3$ materials. *J. Eur. Ceram. Soc.* **24**, 1479-1483 (2004).

163   Heywang, W. Resistivity anomaly in doped barium titanate. *J. Am. Ceram. Soc.* **47**, 484-490 (1964).

164   Ting, C.-J., Peng, C.-J., Lu, H.-Y. & Wu, S.-T. Lanthanum-magnesium and lanthanum-manganese donor-acceptor-codoped semiconducting barium titanate. *J. Am. Ceram. Soc.* **73**, 329-334 (1990).

165   Lewis, G. V. & Catlow, C. R. A. Defect studies of doped and undoped barium titanate using computer simulation techniques. *J. Phys. Chem. Solids* **47**, 89-97 (1986).

166   Wu, D., Fang, B., Du, Q. & Ding, J. Preparation and properties of La and K co-doped BaTiO$_3$ lead-free piezoelectric ceramics. *Ferroelectrics* **432**, 81-91 (2012).

167   Karaki, T., Maruyama, S., Chikazawa, R. & Adachi, M. Modified BaTiO$_3$ piezoelectric ceramics with Bi$_2$O$_3$-Li$_2$O additive. *Ferroelectrics* **439**, 83-87 (2012).

168   Yan, M. F., Cannon, R. M. & Bowen, H. K. Space charge, elastic field, and dipole contributions to equilibrium solute segregation at interfaces. *J. Appl. Phys.* **54**, 764-778 (1983).

169   Chiang, Y.-M. & Takagi, T. Grain-boundary chemistry of barium titanate and strontium titanate: I, high-temperature equilibrium space charge. *J. Am. Ceram. Soc.* **73**, 3278-3285 (1990).

170   Shihua, D., Ping, Z., Tianxiu, S. & Xiaojing, Y. The dielectric behavior of BaTiO$_3$ based ceramics doped with La/Mn. *Ferroelectrics* **426**, 66-71 (2012).

171   Lu, D.-Y., Toda, M. & Sugano, M. High-permittivity double rare-earth-doped barium titanate ceramics with diffuse phase transition. *J. Am. Ceram. Soc.* **89**, 3112-3123 (2006).

172 Lee, C.-E., Kang, S.-H., Sinn, D.-S. & Yoo, H.-I. Co-doping effect of Mn and Y on charge and mass transport properties of $BaTiO_3$. *J. Electroceram.* **13**, 785-791 (2004).

173 Lee, E. J., Jeong, J. & Han, Y. H. Defects and degradation of $BaTiO_3$ codoped with Dy and Mn. *Jpn. J. Appl. Phys.* **45**, 822 (2006).

174 Hwang, J. H., Choi, S. K. & Han, Y. H. Dielectric Properties of $BaTiO_3$ Codoped with Er_2O_3 and MgO. *Jpn. J. Appl. Phys.* **40**, 4952 (2001).

175 Hsiang, H.-I., Mei, L.-T. & Chun, Y.-J. Dielectric properties and microstructure of Nb-Co codoped $BaTiO_3$–$(Bi_{0.5}Na_{0.5})TiO_3$ ceramics. *J. Am. Ceram. Soc.* **92**, 2768-2771 (2009).

176 Lambeck, P. V. & Jonker, G. H. The nature of domain stabilization in ferroelectric perovskites. *J. Phys. Chem. Solids* **47**, 453-461 (1986).

177 Zhu, W., Fujii, I., Ren, W. & Trolier-McKinstry, S. Domain wall motion in A and B site donor-doped $Pb(Zr_{0.52}Ti_{0.48})O_3$ films. *J. Am. Ceram. Soc.* **95**, 2906-2913 (2012).

178 Zhang, Q. M., Zhao, J., Uchino, K. & Zheng, J. Change of the weak-field properties of $Pb(Zr,Ti)O_3$ piezoceramics with compressive uniaxial stresses and its links to the effect of dopants on the stability of the polarizations in the materials. *J. Mater. Res.* **12**, 226-234 (1997).

179 Haertling, G. H. & Land, C. E. Hot-pressed $(Pb,La)(Zr,Ti)O_3$ ferroelectric ceramics for electrooptic applications. *J. Am. Ceram. Soc.* **54**, 1-11 (1971).

180 Majumder, S. B., Roy, B., Katiyar, R. S. & Krupanidhi, S. B. Effect of acceptor and donor dopants on polarization components of lead zirconate titanate thin films. *Appl. Phys. Lett.* **79**, 239-241 (2001).

181 Ramam, K. & Lopez, M. Effect of acceptor and donor dopants on ferroelectric and piezoelectric properties of lead zirconate titanate ceramics. *Phys. Status Solidi A* **203**, 3852-3860 (2006).

182 Guiffard, B., Boucher, E., Lebrun, L., Guyomar, D. & Pleska, E. Influence of fluorine co-doping on the properties of cationic doped PZT ceramics. Effect on the valency state of acceptor and donor dopants. *Ferroelectrics* **313**, 135-144 (2004).

183 Zhang, S., Lebrun, L., Randall, C. A. & Shrout, T. R. Growth and electrical properties of (Mn,F) co-doped $0.92Pb(Zn_{1/3}Nb_{2/3})O_3$–$0.08PbTiO_3$ single crystal. *J. Cryst. Growth* **267**, 204-212 (2004).

184 Guiffard, B., Boucher, E., Eyraud, L., Lebrun, L. & Guyomar, D. Influence of donor co-doping by niobium or fluorine on the conductivity of Mn doped and Mg doped PZT ceramics. *J. Eur. Ceram. Soc.* **25**, 2487-2490 (2005).

185 Detalle, M., Remiens, D., Lebrun, L. & Guyomar, D. Electrical property evaluation of manganese-fluorine codoping of lead zirconate titanate thin films. Compatibility between hard material and piezoelectric activity. *J. Appl. Phys.* **100**, 094102/094101-094102/094105 (2006).

186 Nguyen, T. T., Detalle, M., Remiens, D., Lebrun, L. & Guyomar, D. Studies of some dopants: effect of Mn, Mg, F on (Ba, Sr)PZT films piezoelectric response for specific MEMS applications. *Integr. Ferroelectr.* **96**, 40-50 (2008).

187 Boucher, E., Guiffard, B., Lebrun, L. & Guyomar, D. Effects of Zr/Ti ratio on structural and electrical properties of (Mn,F) co-doped PBSZT ceramics. *Adv. Sci. Technol.* **33**, 695-702 (2003).

188   Park, J.-H., Kim, B.-K., Song, K.-H. & Park, S. Piezoelectric properties of Nb_2O_5 doped and MnO_2—Nb_2O_5 co-doped $Pb(Zr_{0.53}Ti_{0.47})O_3$ ceramics. *J. Mater. Sci.: Mater. Electron.* **6**, 97-101 (1995).

189   Cheon, C. & Lee, H. The piezoelectric properties and the stability of the resonant frequency in Mn–Cr Co-doped PSZT ceramics. *J. Mater. Sci.: Mater. Electron.* **10**, 81-84 (1999).

190   Gao, F., Hong, R., Liu, J., Li, Z. & Tian, C.-S. Effects of ZnO/Li_2O codoping on microstructure and piezoelectric properties of low-temperature sintered PMN-PNN-PZT ceramics. *Ceram. Int.* **35**, 1863-1869 (2009).

191   Bourim, E. M. *et al.* Creep behavior of undoped and La-Nb codoped PZT based micro-piezoactuators for micro-optical modulator applications. *Sens. Actuators, A* **A155**, 290-298 (2009).

192   Shi, G., Wang, D., Bu, S., Jin, D. & Cheng, J. Piezoelectric properties of low loss and high Curie temperature $(Bi, La)FeO_3$-$Pb(Ti, Mn)O_3$ ceramics with Mn doping. *Rare Met.* **31**, 595-598 (2012).

193   Zhang, R. F., Zhang, H. P., Ma, J., Chen, Y. Z. & Zhang, T. S. Effect of Y and Nb codoping on the microstructure and electrical properties of lead zirconate titanate ceramics. *Solid State Ionics* **166**, 219-223 (2004).

194   Davies, M., Aksel, E. & Jones, J. L. Enhanced high-temperature piezoelectric coefficients and thermal stability of Fe- and Mn-substituted $Na_{0.5}Bi_{0.5}TiO_3$ ceramics. *J. Am. Ceram. Soc.* **94**, 1314-1316 (2011).

195   Eichel, R.-A. Structural and dynamic properties of oxygen vacancies in perovskite oxides-analysis of defect chemistry by modern multi-frequency and pulsed EPR techniques. *Phys. Chem. Chem. Phys.* **13**, 368-384 (2011).

196   Han, H.-S., Ahn, C.-W., Kim, I. W., Hussain, A. & Lee, J.-S. Destabilization of ferroelectric order in bismuth perovskite ceramics by A-site vacancies. *Mater. Lett.* **70**, 98-100 (2012).

197   Sung, Y. S. & Kim, M. H. *Effects of B-site donor and acceptor doping in Pb-free $(Bi_{0.5}Na_{0.5})TiO_3$ ceramics*. (InTech, 2010).

198   Yeo, H.-G. *et al.* Donor doping effects on the ferroelectric and the piezoelectric properties of Pb-free $(Bi_{0.5}Na_{0.5})TiO_3$ ceramics. *J. Korean Phys. Soc.* **54**, 896-900 (2009).

199   Li, M. *et al.* A family of oxide ion conductors based on the ferroelectric perovskite $Na_{0.5}Bi_{0.5}TiO_3$. *Nat. Mater.* **13**, 31-35 (2014).

200   Chen, T. *et al.* Effect of $Li_{0.12}Na_{0.88}NbO_3$ content on the electrical properties of $Bi_{0.5}Na_{0.5}TiO_3$ lead-free piezoelectric ceramics. *J. Alloys Compd.* **520**, 7-10 (2012).

201   Kim, J. S., Chung, C. H., Lee, H. S. & Chung, S. T. Dielectric and ferroelectric properties of $LiNbO_3$ doped lead-free $Bi_{0.5}Na_{0.5}TiO_3$ (BNT) ceramics. *J. Korean Phys. Soc.* **58**, 659-662 (2011).

202   Jo, W. *et al.* On the phase identity and its thermal evolution of lead free $(Bi_{1/2}Na_{1/2})TiO_3$-6 mol.% $BaTiO_3$. *J. Appl. Phys.* **110**, 074106/074101-074106/074109 (2011).

203   Simons, H. *et al.* Electric-field-induced strain mechanisms in lead-free 94%$(Bi_{1/2}Na_{1/2})TiO_3$-6%$BaTiO_3$. *Appl. Phys. Lett.* **98**, 082901 (2011).

204   Ehmke, M., Glaum, J., Jo, W., Granzow, T. & Rödel, J. Stabilization of the Fatigue-Resistant Phase by CuO Addition in $(Bi_{1/2}Na_{1/2})TiO_3$–$BaTiO_3$. *J. Am. Ceram. Soc.* **94**, 2473-2478 (2011).

205 Jo, W. *et al.* Evolving morphotropic phase boundary in lead-free $(Bi_{1/2}Na_{1/2})TiO_3$-$BaTiO_3$ piezoceramics. *J. Appl. Phys.* **109**, 014110/014111-014110/014117 (2011).

206 Schmitt, L. A. *et al.* Structural investigations on lead-free $Bi_{1/2}Na_{1/2}TiO_3$-based piezoceramics. *J. Mater. Sci.* **46**, 4368-4376 (2011).

207 Jo, W., Granzow, T., Aulbach, E., Rödel, J. & Damjanovic, D. Origin of the large strain response in $K_{0.5}Na_{0.5}NbO_3$-modified $Bi_{0.5}Na_{0.5}TiO_3$-$BaTiO_3$ lead-free piezoceramics. *J. Appl. Phys.* **105**, 094102 (2009).

208 Jo, W. *et al.* Effect of Nb-donor and Fe-acceptor dopants in $(Bi_{1/2}Na_{1/2})TiO_3$-$BaTiO_3$-$(K_{0.5}Na_{0.5})NbO_3$ lead-free piezoceramics. *J. Appl. Phys.* **108**, 014110 (2010).

209 Daniels, J. E., Jo, W., Rödel, J., Honkimäki, V. & Jones, J. L. Electric-field-induced phase-change behavior in $(Bi_{0.5}Na_{0.5})TiO_3$–$BaTiO_3$–$(K_{0.5}Na_{0.5})NbO_3$: A combinatorial investigation. *Acta Mater.* **58**, 2103-2111 (2010).

210 Dittmer, R., Jo, W., Rödel, J., Kalinin, S. & Balke, N. Nanoscale insight into lead-free BNT-BT-xKNN. *Adv. Funct. Mater.*, n/a-n/a (2012).

211 Jo, W. *et al.* CuO as a sintering additive for $(Bi_{1/2}Na_{1/2})TiO_3$–$BaTiO_3$–$(K_{0.5}Na_{0.5})NbO_3$ lead-free piezoceramics. *J. Eur. Ceram. Soc.* **31**, 2107-2117 (2011).

212 Zhou, C. R. & Liu, X. Y. Effect of B-site substitution by $(Ni_{1/3}Nb_{2/3})^{4+}$ for Ti^{4+} on microstructure and piezoelectric properties in $(Bi_{1/2}Na_{1/2})TiO_3$ piezoelectric ceramics. *J. Alloys Compd.* **466**, 563-567 (2008).

213 Wang, F., Xu, M., Wang, T., Tang, Y. & Shi, W. Phase transition and electrical properties in the Li-modified $Bi_{0.5}Na_{0.5}TiO_3$-based lead-free ceramics. *J. Mater. Sci.* **47**, 2352-2358 (2012).

214 Ullah, A., Ahn, C. W., Jang, K. B., Hussain, A. & Kim, I. W. Phase transition and electrical properties of $BiAlO_3$-modified $(Bi_{0.5}Na_{0.5})TiO_3$ piezoelectric ceramics. *Ferroelectrics* **404**, 167-172 (2010).

215 Hiruma, Y., Nagata, H. & Takenaka, T. Detection of morphotropic phase boundary of $(Bi_{1/2}Na_{1/2})TiO_3$-$Ba(Al_{1/2}Sb_{1/2})O_3$ solid-solution ceramics. *Appl. Phys. Lett.* **95**, 052903/052901-052903/052903 (2009).

216 Bai, W., Bian, Y., Hao, J., Shen, B. & Zhai, J. The composition and temperature-dependent structure evolution and large strain response in $(1-x)(Bi_{0.5}Na_{0.5})TiO_3$-$xBa(Al_{0.5}Ta_{0.5})O_3$ ceramics. *J. Am. Ceram. Soc.* **96**, 246-252 (2013).

217 Hiruma, Y., Nagata, H. & Takenaka, T. Formation of morphotropic phase boundary and electrical properties of $(Bi_{1/2}Na_{1/2})TiO_3$-$Ba(Al_{1/2}Nb_{1/2})O_3$ solid solution ceramics. *Jpn. J. Appl. Phys.* **48**, 09KC08/01-09KC08/06 (2009).

218 Kobune, M., Teraoka, K., Nishioka, H., Yamaguchi, H. & Honda, K. Fabrication and characterization of binary piezoelectric $(Bi_{1/2}Na_{1/2})TiO_3$-$Ba(Cu_{1/3}Nb_{2/3})O_3$ solid solutions. *Jpn. J. Appl. Phys.* **50**, 09ND08/01-09ND08/05 (2011).

219 Tou, T. *et al.* Properties of $(Bi_{0.5}Na_{0.5})TiO_3$-$BaTiO_3$-$(Bi_{0.5}Na_{0.5})(Mn_{1/3}Nb_{2/3})O_3$ lead-free piezoelectric ceramics and its application to ultrasonic cleaner. *Jpn. J. Appl. Phys.* **48**, 07GM03/01-07GM03/04 (2009).

220 Wang, L., Zhang, C., Ji, W.-J., Zhang, S.-T. & Chen, Y.-F. Morphotropic phase boundary in $(1-x)Bi_{0.5}Na_{0.5}TiO_3$-$x(Bi_{0.8}La_{0.2})FeO_3$ with improved depolarization temperature. *Phys. Status Solidi RRL* **3**, 245-247 (2009).

221 Danwittayakul, S., Vaneesorn, N., Jinawath, S. & Thanaboonsombut, A. Influence of isovalent and aliovalent substitutions at Ti site on bismuth sodium titanate-based compositions on piezoelectric properties. *Ceram. Int.* **34**, 765-768 (2008).

222 Mahboob, S., Prasad, G. & Kumar, G. S. Impedance spectroscopy and conductivity studies on B site modified $(Na_{0.5}Bi_{0.5})(Nd_xTi_{1-2x}Nb_x)O_3$ ceramics. *J. Mater. Sci.* **42**, 10275-10283 (2007).

223 Singh, A. & Chatterjee, R. 0.40% Bipolar Strain in Lead Free BNT–KNN System Modified with Li, Ta and Sb. *J. Am. Ceram. Soc.* **96**, 509-512 (2013).

224 Chen, P.-Y., Chou, C.-C., Tseng, T.-Y. & Chen, H. Second phase and defect formation in $Bi_{0.5}Na_{0.5-x}K_xTiO_3$ ceramics. *Jpn. J. Appl. Phys.* **49**, 061506/061501-061506/061507 (2010).

225 Naderer, M., Schütz, D., Kainz, T., Reichmann, K. & Mittermayr, F. The formation of secondary phases in $Bi_{0.5}Na_{0.375}K_{0.125}TiO_3$ ceramics. *J. Eur. Ceram. Soc.* **32**, 2399-2404 (2012).

226 Fukuchi, E., Kimura, T., Tani, T. & Takeuchi, T. Oriented $Bi_{0.5}(Na,K)_{0.5}TiO_3$ ceramics. *Ceram. Trans.* **104**, 227-233 (2000).

227 Ahn, C. W. *et al.* The effect of $Bi_4Ti_3O_{12}$ particles addition in lead-free $Bi_{0.5}(Na_{0.75}K_{0.25})_{0.5}TiO_3$ ceramics. *J. Electroceram.* **23**, 402-405 (2009).

228 Chen, Y. Q., Zheng, X. J. & Li, W. Size effect of mechanical behavior for lead-free $(Na_{0.82}K_{0.18})_{0.5}Bi_{0.5}TiO_3$ nanofibers by nanoindentation. *Mater. Sci. Eng., A* **A527**, 5462-5466 (2010).

229 Fukuchi, E., Kimura, T., Tani, T., Takeuch, T. & Saito, Y. Effect of potassium concentration on grain orientation in bismuth sodium potassium titanate. *J. Am. Ceram. Soc.* **85**, 1461-1466 (2002).

230 Fuse, K. & Kimura, T. Effect of particle sizes of starting materials on microstructure development in textured $Bi_{0.5}(Na_{0.5}K_{0.5})_{0.5}TiO_3$. *J. Am. Ceram. Soc.* **89**, 1957-1964 (2006).

231 Gao, F., Liu, X.-C., Zhang, C.-S., Cheng, L.-H. & Tian, C.-S. Fabrication and electrical properties of textured $(Na,K)_{0.5}Bi_{0.5}TiO_3$ ceramics by reactive-templated grain growth. *Ceram. Int.* **34**, 403-408 (2008).

232 Ji, W.-J. *et al.* Microstructure and electric properties of lead-free $0.8Bi_{1/2}Na_{1/2}TiO_3$-$0.2Bi_{1/2}K_{1/2}TiO_3$ ceramics. *Ceram. Int.* **38**, 1683-1686 (2012).

233 Jing, X., Li, Y., Yang, Q., Zeng, J. & Yin, Q. Influence of different templates on the textured $Bi_{0.5}(Na_{1-x}K_x)_{0.5}TiO_3$ piezoelectric ceramics by the reactive templated grain growth process. *Ceram. Int.* **30**, 1889-1893 (2004).

234 Shoji, T., Yoshida, Y. & Kimura, T. Mechanism of texture development in $Bi_{0.5}(Na,K)_{0.5}TiO_3$ templated by platelike Al_2O_3 particles. *J. Am. Ceram. Soc.* **91**, 3883-3888 (2008).

235 Shoji, T., Fuse, K. & Kimura, T. Mechanism of texture development in $Bi_{0.5}(Na,K)_{0.5}TiO_3$ prepared by the templated grain growth process. *J. Am. Ceram. Soc.* **92**, S140-S145 (2008).

236 West, D. L. & Payne, D. A. Reactive-templated grain growth of $Bi_{1/2}(Na,K)_{1/2}TiO_3$: Effects of formulation on texture development. *J. Am. Ceram. Soc.* **86**, 1132-1137 (2003).

237 Zhao, W., Zhou, H. & Yan, Y. Preparation and characterization of textured $Bi_{0.5}(Na_{0.8}K_{0.2})_{0.5}TiO_3$ ceramics by reactive templated grain growth. *Mater. Lett.* **62**, 1219-1222 (2008).

238   Otonicar, M., Skapin, S. D. & Jancar, B. TEM analyses of the local crystal and domain structures in $(Na_{1-x}K_x)_{0.5}Bi_{0.5}TiO_3$ perovskite ceramics. *IEEE Trans. Ultrason. Ferroelectr. Freq. Control* **58**, 1928-1938 (2011).

239   Kreisel, J. *et al.* An x-ray diffraction and Raman spectroscopy investigation of A-site substituted perovskite compounds: the $(Na_{1-x}K_x)_{0.5}Bi_{0.5}TiO_3$ $(0 \leq x \leq 1)$ solid solution. *J. Phys.: Condens. Matter* **12**, 3267-3280 (2000).

240   Seno, Y. & Tani, T. TEM observation of a reactive template for textured $Bi_{0.5}(Na_{0.87}K_{0.13})_{0.5}TiO_3$ polycrystals. *Ferroelectrics* **224**, 793-800 (1999).

241   Gong, Y. *et al.* Large piezoelectric response of $Bi_{0.5}(Na_{1-x}K_x)_{0.5}TiO_3$ thin films near morphotropic phase boundary identified by multi-peak fitting. *J. Phys. D: Appl. Phys.* **45**, 305301 (2012).

242   Gong, Y. *et al.* Large piezoelectric response of $Bi_{0.5}(Na_{1-x}K_x)_{0.5}TiO_3$ thin films near morphotropic phase boundary identified by multi-peak fitting. *J. Phys. D: Appl. Phys.* **45**, 305301/305301-305301/305309 (2012).

243   Lim, D. H. *et al.* Electric properties of a textured $BiNaKTiO_3$ ceramic for energy harvesting system. *J. Korean Phys. Soc.* **60**, 240-243 (2012).

244   Ni, F., Luo, L., Li, W. & Chen, H. A-site vacancy-induced giant strain and the electrical properties in non-stoichiometric ceramics $Bi_{0.5+x}(Na_{1-y}K_y)_{0.5-3x}TiO_3$. *J. Phys. D: Appl. Phys.* **45**, 415103/415101-415103/415106 (2012).

245   Rao, P. V. B. & Sankaram, T. B. Electrical and Piezoelectric Studies of $(Na_{1-x}K_x)_{1/2}Bi_{1/2}TiO_3$. *Integr. Ferroelectr.* **120**, 64-74 (2010).

246   Suchanicz, J., Mercurio, J. P., Konieczny, K. & Kruzina, T. V. Influence of compressive stress on electric properties of $Na_{0.5-x}K_xBi_{0.5}TiO_3$ solid solutions (x $\leq$ 0.1). *Ferroelectrics* **290**, 161-167 (2003).

247   Zhang, Y.-R., Li, J.-F., Zhang, B.-P. & Peng, C.-E. Piezoelectric and ferroelectric properties of Bi-compensated $Bi_{1/2}Na_{1/2}TiO_3$-$Bi_{1/2}K_{1/2}TiO_3$ lead-free piezoelectric ceramics. *J. Appl. Phys.* **103**, 074109/074101-074109/074106 (2008).

248   Zhang, Y., Zheng, X. & Zhang, T. Characterization and humidity sensing properties of $Bi_{0.5}Na_{0.5}TiO_3$-$Bi_{0.5}K_{0.5}TiO_3$ powder synthesized by metal-organic decomposition. *Sens. Actuators, B* **B156**, 887-892 (2011).

249   Zhao, S., Zhang, L., Li, G., Li, B. & Ding, A. Dielectric and ferroelectric properties of $Na_{0.42}K_{0.08}TiO_3$ and $Na_{0.25}K_{0.25}Bi_{0.5}TiO_3$ relaxor ceramics. *Integr. Ferroelectr.* **78**, 119-126 (2006).

250   Thongtha, A. & Bongkarn, T. Optimum sintering temperature for fabrication of $0.8Bi_{0.5}Na_{0.5}TiO_3$-$0.2Bi_{0.5}K_{0.5}TiO_3$ lead-free ceramics by combustion technique. *Key Eng. Mater.* **474-476**, 1754-1759 (2011).

251   Won, S. S., Ahn, C. W. & Kim, I. W. The effect of annealing temperature on the piezoelectric and dielectric properties of lead-free $Bi_{0.5}(Na_{0.85}K_{0.15})_{0.5}TiO_3$ thin films. *J. Korean Phys. Soc.* **61**, 928-932 (2012).

252   Chen, P.-Y., Chou, C.-C., Tseng, T.-Y. & Chen, H. H. D. Comparative study between conventional and microwave sintered lead-free BNKT ceramics. *Ferroelectrics* **381**, 196-200, 192 plates (2009).

253   Li, W., Xu, Z., Chu, R., Fu, P. & Zhang, Y. Synthesis and characterization of $(Na_{0.85}K_{0.15})_{0.5}Bi_{0.5}TiO_3$ ceramics by different methods. *Mater. Res. Bull.* **46**, 871-874 (2011).

254 Nguyen, V.-Q. *et al.* Strain enhancement in $Bi_{1/2}(Na_{0.82}K_{0.18})_{1/2}TiO_3$ lead-free electromechanical ceramics by co-doping with Li and Ta. *J. Alloys Compd.* **511**, 237-241 (2012).

255 Zaman, A. *et al.* Influence of zirconium substitution on dielectric, ferroelectric and field-induced strain behaviors of lead-free $0.99[Bi_{1/2}(Na_{0.82}K_{0.18})_{1/2}(Ti_{1-x}Zr_x)O_3]$-0.01LiSbO_3 ceramics. *J. Korean Phys. Soc.* **61**, 773-778 (2012).

256 Zhou, C., Liu, X., Li, W. & Yuan, C. Microstructure and electrical properties of $Bi_{0.5}Na_{0.5}TiO_3$-$Bi_{0.5}K_{0.5}TiO_3$-LiNbO_3 lead-free piezoelectric ceramics. *J. Phys. Chem. Solids* **70**, 541-545 (2009).

257 Do, N. B. *et al.* Low temperature sintering of lead-free $Bi_{0.5}(Na_{0.82}K_{0.18})_{0.5}TiO_3$ piezoelectric ceramics by co-doping with CuO and Nb_2O_5. *Ceram. Int.* **38**, S359-S362 (2012).

258 Ullah, A., Ahn, C. W., Lee, S. Y., Kim, J. S. & Kim, I. W. Structure, ferroelectric properties, and electric field-induced large strain in lead-free $Bi_{0.5}(Na,K)_{0.5}TiO_3$-$(Bi_{0.5}La_{0.5})AlO_3$ piezoelectric ceramics. *Ceram. Int.* **38**, S363-S368 (2012).

259 Ahart, M. *et al.* Origin of morphotropic phase boundaries in ferroelectrics. *Nature* **451**, 545-548 (2008).

260 Schwöbel, A., Hausbrand, R. & Jaegermann, W. Interface reactions between LiPON and lithium studied by in-situ X-ray photoemission. *Solid State Ionics* (2014).

261 Blömker, M. *et al.* Defect structure of doped lead-free $0.9(Bi_{0.5}Na_{0.5})TiO_3$-$0.1(Bi_{0.5}K_{0.5})TiO_3$ piezoceramics. *J. Am. Ceram. Soc.* **99**, 543-550 (2016).

262 Han, H.-S. *et al.* Sintering behaviour and piezoelectric properties of CuO-added lead-free $Bi(Na,K)TiO_3$ ceramics. *Ferroelectrics* **421**, 88-91 (2011).

263 Lim, J. B., Suvorov, D. & Jeon, J.-H. Ferroelectric $Bi(Na,K)TiO_3$-based materials for lead-free piezoelectrics. *Ceram. Int.* **38**, S355-S358 (2012).

264 Wittmer, D. E. & Buchanan, R. C. Low-temperature densification of lead zirconate-zitanate with vanadium pentoxide additive. *J. Am. Ceram. Soc.* **64**, 485-490 (1981).

265 Kim, G. B., Jung, J. M., Park, Y. H. & Choi, S. W. Effect of vanadium doping on dielectric, pyroelectric and piezoelectric properties of $0.66Pb(Mg_{1/3}Ta_{2/3})O_3$-$0.34PbTiO_3$ ceramics. *Ferroelectrics* **230**, 121-126 (1999).

266 CENELEC. in *Piezoelectric properties of ceramics materials and components, Part 2: Methods of measurement - low power, European Standard EN 50324-2* (European Committee for Electrotechnical Standardization, Brussels, 2002).

267 Dunn, M. L. & Taya, M. Electromechanical properties of porous piezoelectric ceramics. *J. Am. Ceram. Soc.* **76**, 1697-1706 (1993).

268 Kar-Gupta, R. & Venkatesh, T. A. Electromechanical response of porous piezoelectric materials. *Acta Mater.* **54**, 4063-4078 (2006).

269 Wu, Z., Duan, W., Wang, Y., Gu, B.-L. & Zhang, X.-W. Effect of defect-induced internal field on the aging of relaxors. *Phys. Rev. B: Condens. Matter Mater. Phys.* **67**, 052101/052101-052101/052104 (2003).

270 Schuetz, D. *et al.* Lone-pair-induced covalency as the cause of temperature- and field-induced instabilities in bismuth sodium titanate. *Adv. Funct. Mater.* **22**, 2285-2294 (2012).

271 Manabu, H., Takuya, H., Hiroaki, T. & Takaaki, T. Identicalness between piezoelectric loss and dielectric loss in converse effect of piezoelectric ceramic resonators. *Jpn. J. Appl. Phys.* **51**, 09LD10 (2012).

272 Kamel, T. M. & de With, G. Poling of hard ferroelectric PZT ceramics. *J. Eur. Ceram. Soc.* **28**, 1827-1838 (2008).

273 Benes, E., Gröschl, M., Burger, W. & Schmid, M. Sensors based on piezoelectric resonators. *Sensor. Actuat. A: Phys.* **48**, 1-21 (1995).

274 Li, Y.-M., Liao, R.-H., Jiang, X.-P. & Zhang, Y.-P. Impedance spectroscopy and dielectric properties of $Na_{0.5}Bi_{0.5}TiO_3$–$K_{0.5}Bi_{0.5}TiO_3$ ceramics. *J. Alloys Compd.* **484**, 961-965 (2009).

275 Chen, P.-Y., Chou, C.-C., Tseng, T.-Y. & Chen, H. Correlation of microstructures and conductivities of ferroelectric ceramics using complex impedance spectroscopy. *Jpn. J. Appl. Phys.* **49**, 061505/061501-061505/061506 (2010).

276 Rajulu, K. C. V., Tilak, B. & Rao, K. S. Impedance spectroscopy study of BNKLT polycrystalline ceramic. *Appl. Phys. A: Mater. Sci. Process.* **106**, 533-543 (2012).

277 Hussain, A. *et al.* Impedance spectroscopy of lead-free $Bi_{0.5}(Na_{0.78}K_{0.22})_{0.5}TiO_3$-$(Na_{0.5}K_{0.5})NbO_3$ piezoelectric ceramics. *J. Korean Phys. Soc.* **57**, 1106-1110 (2010).

278 Kumar, K. & Kumar, B. Effect of Nb-doping on dielectric, ferroelectric and conduction behavior of lead free $Bi_{0.5}(Na_{0.5}K_{0.5})_{0.5}TiO_3$ ceramic. *Ceram. Int.* **38**, 1157-1165 (2012).

279 Schulz, M., Brillo, J., Stenzel, C. & Fritze, H. Oxygen partial pressure control for microgravity experiments. *Solid State Ionics* **225**, 332-336 (2012).

280 Chang, E. K., Mehta, A. & Smyth, D. M. Ionic transport numbers from equilibrium conductivities. *Proc. - Electrochem. Soc.* **88-3**, 35-45 (1988).

281 Raymond, M. V. & Smyth, D. M. Defects and charge transport in perovskite ferroelectrics. *J. Phys. Chem. Solids* **57**, 1507-1511 (1996).

282 Boukamp, B. A., Pham, M. T. N., Blank, D. H. A. & Bouwmeester, H. J. M. Ionic and electronic conductivity in lead–zirconate–titanate (PZT). *Solid State Ionics* **170**, 239-254 (2004).

283 Smyth, D. M. *The defect chemistry of metal oxides*. (Oxford University Press, 2000).

284 Frömling, T., Schintlmeister, A., Hutter, H. & Fleig, J. Oxide ion transport in donor-doped $Pb(Zr_xTi_{1-x})O_3$: The role of grain boundaries. *J. Am. Ceram. Soc.* **94**, 1173-1181 (2011).

285 Stoll, S. *Spectral simulations in solid-state electron paramagnetic resonance*, (2003).

286 Eichel, R.-A. *et al.* Defect structure and formation of defect complexes in Cu^{2+}-modified metal oxides derived from a spin-Hamiltonian parameter analysis. *Mol. Phys.* **107**, 1981-1986 (2009).

287 Eichel, R.-A. Characterization of defect structure in acceptor-modified piezoelectric ceramics by multifrequency and multipulse electron paramagnetic resonance spectroscopy. *J. Am. Ceram. Soc.* **91**, 691-701 (2008).

288 Warren, W. L., Seager, C. H., Dimos, D. & Friebele, E. J. Optically induced absorption and paramagnetism in lead lanthanum zirconate titanate ceramics. *Appl. Phys. Lett.* **61**, 2530-2532 (1992).

289 Warren, W. L., Tuttle, B. A., Rong, E. C., Gerardi, G. J. & Poindexter, E. H. Electron paramagnetic resonance investigation of acceptor centers in $Pb(Zr,Ti)O_3$ ceramics. *J. Am. Ceram. Soc.* **80**, 680-684 (1997).

290 Jakes, P., Kungl, H., Schierholz, R. & Eichel, R.-A. Analyzing the defect structure of CuO-Doped PZT and KNN piezoelectrics from electron

paramagnetic resonance. *IEEE Trans. Ultrason. Ferroelectr. Freq. Control.* **61**, 1447-1455 (2014).

291 Bogomolova, L. D., Stefanovsky, S. V., Troole, A. Y. & Vance, E. R. EPR spectra of V(IV) in zirconolite-rich ceramics. *J. Mater. Sci.* **36**, 1213-1217 (2001).

292 Davidson, A. & Che, M. Temperature-induced diffusion of probe vanadium(IV) ions into the matrix of titanium dioxide as investigated by ESR techniques. *J. Phys. Chem. US* **96**, 9909-9915 (1992).

293 Vassilikou-Dova, A. B. & Lehmann, G. EPR of V^{4+} and Fe^{3+} in titanites. *Phys. Chem. Minerals* **15**, 559-563 (1988).

294 Abi-Aad, E., Matta, J., Courcot, D. & Aboukaïs, A. EPR and TPR investigation of the redox properties of vanadia based ceria catalysts. *J. Mater. Sci.* **41**, 1827-1833 (2006).

295 Peisach, J. & Blumberg, W. E. Structural implications derived from the analysis of EPR spectra of natural and artificial copper proteins. *Arch. Biochem. Biophys.* **165**, 691-708 (1974).

296 Powell, C. J. & Jablonski, A. Progress in quantitative surface analysis by X-ray photoelectron spectroscopy: Current status and perspectives. *J. Electron. Spectrosc.* **178–179**, 331-346 (2010).

297 Seah, M. P. & Gilmore, I. S. Simplified equations for correction parameters for elastic scattering effects in AES and XPS for Q, β and attenuation lengths. *Surf. Interface Anal.* **31**, 835-846 (2001).

298 Wu, Q.-H., Thissen, A. & Jaegermann, W. Photoelectron spectroscopic study of Li intercalation into V_2O_5 thin films. *Surf. Sci.* **578**, 203-212 (2005).

299 Silversmit, G., Depla, D., Poelman, H., Marin, G. B. & De Gryse, R. Determination of the V 2p XPS binding energies for different vanadium oxidation states (V^{5+} to V^{0+}). *J. Electr. Spectrosc.* **135**, 167-175 (2004).

300 Demeter, M., Neumann, M. & Reichelt, W. Mixed-valence vanadium oxides studied by XPS. *Surf. Sci.* **454–456**, 41-44 (2000).

301 Kurasawa, M. & Mclntyre, P. C. Surface passivation and electronic structure characterization of $PbTiO_3$ thin films and $Pt/PbTiO_3$ interfaces. *J. Appl. Phys.* **97**, 104110 (2005).

302 Müller, K. A., Aguilar, M., Berlinger, W. & Blazey, K. W. V^{2+} in $SrTiO_3$: an extreme double acceptor. *J. Phys. - Condens. Mat.* **2**, 2735 (1990).

303 Lamoreaux, R. H. & Hildenbrand, D. L. High-temperature vaporization behavior of oxides. I. Alkali metal binary oxides. *J. Phys. Chem. Ref. Data* **13**, 151-173 (1984).

304 Veera Gajendra Babu, M. *et al.* Enhanced piezoelectric constant and remnant polarisation in K-compensated sodium potassium bismuth titanate. *Mater. Lett.,* Ahead of Print (2015).

305 Chen, X. *et al.* Microstructure and piezoelectric properties of Li-doped $Bi_{0.5}(Na_{0.825}K_{0.75})_{0.5}TiO_3$ piezoelectric ceramics. *Phys. Status Solidi A* **206**, 1616-1619 (2009).

306 Jarupoom, P. *et al.* Lead-free ternary perovskite compounds with large electromechanical strains. *Appl. Phys. Lett.* **99**, 152901-152903 (2011).

307 Qiao, S. *et al.* Effect of $Ba_{0.85}Ca_{0.15}Ti_{0.90}Zr_{0.10}O_3$ content on the microstructure and electrical properties of $Bi_{0.51}(Na_{0.82}K_{0.18})_{0.50}TiO_3$ ceramics. *Ceram. Int.* **38**, 4845-4851 (2012).

308   Ni, F., Luo, L., Pan, X., Zhang, Y. & Chen, H. Piezoelectric and dielectric properties of $Bi_{0.5}Na_{0.5}TiO_3$-$Bi_{0.5}K_{0.5}TiO_3$-$Ba_{0.77}Ca_{0.23}TiO_3$ lead-free piezoelectric ceramics. *J. Mater. Sci.* **47**, 3354-3360 (2012).

309   Wu, B. *et al.* Investigation of a new lead-free (0.89 - x)$(Bi_{0.5}Na_{0.5})TiO_3$-$0.11(Bi_{0.5}K_{0.5})TiO_3$-$xBa_{0.85}Ca_{0.15}Ti_{0.90}Zr_{0.10}O_3$ ceramics. *Mater. Res. Bull.* **47**, 3937-3940 (2012).

310   Wu, Y., Wang, X. & Li, L. Effect of Sc doping on the structure and electrical properties of $(Na_{0.85}K_{0.15})_{0.5}Bi_{0.5}TiO_3$ thin films prepared by sol-gel processing. *J. Am. Ceram. Soc.* **94**, 2518-2522 (2011).

311   Zhang, H., Jiang, S. & Kajiyoshi, K. Pyroelectric and dielectric properties of Mn modified $0.82Bi_{0.5}Na_{0.5}TiO_3$-$0.18Bi_{0.5}K_{0.5}TiO_3$ lead-free thick films. *J. Am. Ceram. Soc.* **92**, 2147-2150 (2009).

312   Zou, M., Fan, H., Chen, L. & Yang, W. Microstructure and electrical properties of (1- x)$[0.82Bi_{0.5}Na_{0.5}TiO_3$-$0.18Bi_{0.5}K_{0.5}TiO_3]$-$xBiFeO_3$ lead-free piezoelectric ceramics. *J. Alloys Compd.* **495**, 280-283 (2010).

313   Yamada, Y. *et al.* Effect of B-ions substitution in $(K_{1/2}Bi_{1/2})$-$(Na_{1/2}Bi_{1/2})(Ti-B)O_3$ system with B = Zr, $Fe_{1/2}Nb_{1/2}$, $Zn_{1/3}Nb_{2/3}$ or $Mg_{1/3}Nb_{2/3}$. *Jpn. J. Appl. Phys., Part 1* **34**, 5462-5466 (1995).

314   Wang, K., Hussain, A., Jo, W. & Rödel, J. Temperature-dependent properties of $(Bi_{1/2}Na_{1/2})TiO_3$–$(Bi_{1/2}K_{1/2})TiO_3$–$SrTiO_3$ lead-free piezoceramics. *J. Am. Ceram. Soc.* **95**, 2241-2247 (2012).

315   Hussain, A., Ahn, C. W., Lee, J. S., Ullah, A. & Kim, I. W. Large electric-field-induced strain in Zr-modified lead-free $Bi_{0.5}(Na_{0.78}K_{0.22})_{0.5}TiO_3$ piezoelectric ceramics. *Sens. Actuators, A* **A158**, 84-89 (2010).

316   Hao, J., Wang, J., Bai, W., Shen, B. & Zhai, J. Switching of morphotropic phase boundary and large electrostrictive effect in lead-free BNT-BKT-KNN ceramics. *Phys. Status Solidi RRL*, Ahead of Print.

317   Pham, K.-N. *et al.* Dielectric, ferroelectric, and piezoelectric properties of Nb-substituted $Bi_{1/2}(Na_{0.82}K_{0.18})_{1/2}TiO_3$ lead-free ceramics. *J. Korean Phys. Soc.* **60**, 207-211 (2012).

318   Wang, C.-H. Electrical and physical properties of lead-free $(Na_{0.5}K_{0.5})NbO_3$-$Bi_{0.5}(Na_{0.93}K_{0.07})_{0.5}TiO_3$ ceramics. *Key Eng. Mater.* **512-515**, 1351-1354 (2012).

319   Wang, C. H. Piezoelectric and electrical properties of lead-free $(Na_{0.5}K_{0.5})NbO_3$-$Bi_{0.5}(Na_{0.80}K_{0.20})_{0.5}TiO_3$ ceramics. *Adv. Mater. Res.* **230-232**, 12-15 (2011).

320   Wang, C. H. Dielectric and piezoelectric properties of lead-free $(Na_{0.5}K_{0.5})NbO_3$-$Bi_{0.5}(Na_{0.85}K_{0.15})_{0.5}TiO_3$ ceramics. *Adv. Mater. Res.* **211-212**, 152-155 (2011).

321   Chen, Z., Hu, J. & He, X. Piezoelectric and dielectric properties of $(Na_{0.5}K_{0.5})NbO_3$-$Bi_{0.5}(Na_{0.8}K_{0.2})_{0.5}TiO_3$ lead-free ceramics. *J. Ceram. Soc. Jpn.* **116**, 661-663 (2008).

322   Pham, K.-N. *et al.* Giant strain in Nb-doped $Bi_{0.5}(Na_{0.82}K_{0.18})_{0.5}TiO_3$ lead-free electromechanical ceramics. *Mater. Lett.* **64**, 2219-2222 (2010).

323   Singh, A. & Chatterjee, R. Structural, electrical, and strain properties of stoichiometric 1-x-y$(Bi_{0.5}Na_{0.5})TiO_3$-$x(Bi_{0.5}K_{0.5}TiO_3)$-$y(Na_{0.5}K_{0.5})NbO_3$ solid solutions. *J. Appl. Phys.* **109**, 024105/024101-024105/024105 (2011).

324   Kumar, K., Singh, B. K., Gupta, M. K., Sinha, N. & Kumar, B. Enhancement in dielectric and ferroelectric properties of lead free $Bi_{0.5}(Na_{0.5}K_{0.5})_{0.5}TiO_3$ ceramics by Sb-doping. *Ceram. Int.* **37**, 2997-3004 (2011).

325   Kumar, K. & Kumar, B. Synthesis and Characterization of Sb-Doped $Bi_{0.5}(Na_{0.5}K_{0.5})_{0.5}TiO_3$ Ceramics. *Integr. Ferroelectr.* **121**, 99-105 (2010).

326   Cheng, S.-Y., Shieh, J., Ho, N.-J. & Lu, H.-Y. Phase-transformation-induced microstructure in lead-free ferroelectric ceramics based on $(Bi_{0.5}Na_{0.5})TiO_3$-$BaTiO_3$-$(Bi_{0.5}K_{0.5})TiO_3$. *Philos. Mag.* **91**, 4013-4032 (2011).

327   Choy, S. H. *Study of BNT-BKT-BT lead-free piezoelectric ceramics and their application in piezoelectric devices,* PhD thesis, Hong Kong Polytechnic University, (2007).

328   Hiruma, Y., Makiuchi, Y., Aoyagi, R., Nagata, H. & Takenaka, T. Lead-free piezoelectric ceramic based on $(Bi_{1/2}Na_{1/2})TiO_3$-$(Bi_{1/2}K_{1/2})TiO_3$-$BaTiO_3$ solid solution. *Ceram. Trans.* **174**, 139-146 (2006).

329   Li, Y. *et al.* Electromechanical and dielectric properties of $Na_{0.5}Bi_{0.5}TiO_3$-$K_{0.5}Bi_{0.5}TiO_3$-$BaTiO_3$ lead-free ceramics. *Mater. Chem. Phys.* **94**, 328-332 (2005).

330   Trelcat, J.-F. *et al.* Morphotropic phase boundary in the BNT–BT–BKT system. *Ceram. Int.* **38**, 2823-2827 (2012).

331   Abe, Y. & Kimura, T. Preparation of grain oriented BNKT-based perovskite solid solutions. *Key Eng. Mater.* **228-229**, 21-26 (2002).

332   Chen, W., Li, Y., Xu, Q. & Zhou, J. Electromechanical properties and morphotropic phase boundary of $Na_{0.5}Bi_{0.5}TiO_3$-$K_{0.5}Bi_{0.5}TiO_3$-$BaTiO_3$ lead-free piezoelectric ceramics. *J. Electroceram.* **15**, 229-235 (2005).

333   Chen, Z. & Lu, Z. Piezoelectric and dielectric properties of $(Bi_{0.5}Na_{0.5})TiO_3(Bi_{0.5}K_{0.5})TiO_3$- $BaTiO_3$ lead-free piezoelectric ceramics. *Key Eng. Mater.* **336-338**, 54-57 (2007).

334   Choy, S. H., Wang, X. X., Chan, H. L. W. & Choy, C. L. Study of compressive type accelerometer based on lead-free BNKBT piezoceramics. *Appl. Phys. A: Mater. Sci. Process.* **82**, 715-718 (2006).

335   Choy, S. H., Wang, X. X., Chan, H. L. W. & Choy, C. L. Electromechanical and ferroelectric properties of $(Bi_{1/2}Na_{1/2})TiO_3$-$(Bi_{1/2}K_{1/2})TiO_3$- $(Bi_{1/2}Li_{1/2})TiO_3$-$BaTiO_3$ lead-free piezoelectric ceramics for accelerometer application. *Appl. Phys. A: Mater. Sci. Process.* **89**, 775-781 (2007).

336   Lam, K. H., Wang, X. X. & Chan, H. L. W. Lead-free piezoceramic cymbal actuator. *Sens. Actuators, A* **A125**, 393-397 (2006).

337   Wang, X. X., Tang, X. G. & Chan, H. L. W. Electromechanical and ferroelectric properties of $(Bi_{1/2}Na_{1/2})TiO_3$ - $(Bi_{1/2}K_{1/2})TiO_3$ -$BaTiO_3$ lead-free piezoelectric ceramics. *Appl. Phys. Lett.* **85**, 91-93 (2004).

338   Zeng, J. T. *et al.* Plate-like $Na_{0.5}Bi_{0.5}TiO_3$ template synthesized by a topochemical method. *J. Am. Ceram. Soc.* **89**, 3850-3853 (2006).

339   Zhang, S.-T., Yang, B. & Cao, W. The temperature-dependent electrical properties of $Bi_{0.5}Na_{0.5}TiO_3$-$BaTiO_3$-$Bi_{0.5}K_{0.5}TiO_3$ near the morphotropic phase boundary. *Acta Mater.* **60**, 469-475 (2012).

340   Fu, P. *et al.* Gd2O3 doped 0.82Bi0.5Na0.5TiO3-0.18Bi0.5K0.5TiO3 lead-free piezoelectric ceramics. *Mater. Des.* **35**, 276-280 (2012).

341   Fu, P. *et al.* Structure and electrical properties of Er_2O_3 doped $0.82Bi_{0.5}Na_{0.5}TiO_3$-$0.18Bi_{0.5}K_{0.5}TiO_3$ lead-free piezoelectric ceramics. *Mater. Des.* **40**, 373-377 (2012).

342   Li, Y. *et al.* Piezoelectric and dielectric properties of CeO_2-doped $Bi_{0.5}Na_{0.44}K_{0.06}TiO_3$ lead-free ceramics. *Ceram. Int.* **33**, 95-99 (2006).

343   Supriya, S., Kalainathan, S. & Swaroop, S. Synthesis and characterization of CeO_2 doped bismuth sodium potassium titanate ceramics. *Int. J. ChemTech Res.* **3**, 488-494 (2011).

344   Yang, Z., Hou, Y., Liu, B. & Wei, L. Structure and electrical properties of Nd_2O_3-doped $0.82Bi_{0.5}Na_{0.5}TiO_3$-$0.18Bi_{0.5}K_{0.5}TiO_3$ ceramics. *Ceram. Int.* **35**, 1423-1427 (2009).

345   Chen, Z.-H., Ding, J.-N., Lin, M., Yuan, N.-Y. & Zhang, W.-W. Piezoelectric and Dielectric Properties of Dy_2O_3-Doped $Bi_{0.5}(Na_{0.82}K_{0.18})_{0.5}TiO_3$ Lead-Free Ceramics. *Ferroelectrics* **425**, 63-71 (2011).

346   Zhang, Y. *et al.* Piezoelectric and dielectric properties of Sm_2O_3-doped $0.82Bi_{0.5}Na_{0.5}TiO_3$-$0.18Bi_{0.5}K_{0.5}TiO_3$ ceramics. *J. Alloys Compd.* **502**, 341-345 (2010).

347   Hussain, A., Ahn, C. W., Ullah, A., Lee, J. S. & Kim, I. W. Effects of hafnium substitution on dielectric and electromechanical properties of lead-free $Bi_{0.5}(Na_{0.78}K_{0.22})_{0.5}(Ti_{1-x}Hf_x)O_3$ ceramics. *Jpn. J. Appl. Phys.* **49**, 041504/041501-041504/041505 (2010).

348   Tran, V. D. N. *et al.* Comparison of ferroelectric and strain properties between $BaTiO_3$- and $BaZrO_3$-modified $Bi_{1/2}(Na_{0.82}K_{0.18})_{1/2}TiO_3$ ceramics. *Jpn. J. Appl. Phys.* **51**, 09MD02/01-09MD02/04 (2012).

349   Tran, V. D. N., Dinh, T. H., Han, H.-S., Jo, W. & Lee, J.-S. Lead-free $Bi_{1/2}(Na_{0.82}K_{0.18})_{1/2}TiO_3$ relaxor ferroelectrics with temperature insensitive electrostrictive coefficient. *Ceram. Int.* (2012).

350   Sun, T., Dai, Y.-J. & Wang, H.-Q. Sol-gel derived Li_2O doped BNT-BKT-BT ceramics: microstructure and piezoelectric properties. *Key Eng. Mater.* **512-515**, 1355-1358 (2012).

351   Pham, K. N., Dinh, T. H., Lee, H.-Y., Kong, Y.-M. & Lee, J.-S. Effects of $Bi(Mg_{1/2}Sn_{1/2})O_3$ modification on the dielectric and piezoelectric properties of $Bi_{1/2}(Na_{0.8}K_{0.2})_{1/2}TiO_3$ ceramics. *J. Korean Ceram. Soc.* **49**, 266-271 (2012).

352   Lee, H.-B. *et al.* Lead-free $Bi_{1/2}(Na_{0.82}K_{0.18})_{1/2}TiO_3$ ceramics exhibiting large strain with small hysteresis. *Ceram. Int.*, Ahead of Print (2012).

353   Jaita, P., Watcharapasorn, A. & Jiansirisomboon, S. Investigation of a new lead-free $Bi_{0.5}(Na_{0.40}K_{0.10})TiO_3$-$(Ba_{0.7}Sr_{0.3})TiO_3$ piezoelectric ceramic. *Nanoscale Res. Lett.* **7** (2012).

354   Tran, V. D. N. *et al.* Lead-free electrostrictive bismuth perovskite ceramics with thermally stable field-induced strains. *Mater. Lett.* **65**, 2607-2609 (2011).

355   Huang, X.-y., Gao, C.-h., Wei, M.-x. & Chen, Z.-g. Influence of La_2O_3 doping amount on properties of NBT-KBT-BT lead-free piezoelectric ceramics. *Appl. Mech. Mater.* **43**, 614-618 (2011).

356   Huang, X., Gao, C., Wei, M., Chen, Z. & Cui, Y. Influence of Sb_2O_3 doping on the properties of KBT-NBT-BT lead-free piezoelectric ceramics. *Rare Met.* **30**, 72-75 (2011).

357   Hu, H. *et al.* Effect of Co_2O_3 additive on structure and electrical properties of $85(Bi_{1/2}Na_{1/2})TiO_3$-$12(Bi_{1/2}K_{1/2}) TiO_3$-$3BaTiO_3$ lead-free piezoceramics. *J. Am. Ceram. Soc.* **92**, 2039-2045 (2009).

358   Hu, H., Zhu, M., Hou, Y. & Yan, H. Dielectric, piezoelectric, and ferroelectric properties of $MnCO_3$-added $74Bi_{1/2}Na_{1/2}TiO_3$-$20.8Bi_{1/2}K_{1/2}TiO_3$-$5.2BaTiO_3$ lead-free piezoelectric ceramics. *IEEE Trans. Ultrason. Ferroelectr. Freq. Control* **56**, 897-905 (2009).

359   Chen, Z. W. & Hu, J. Q. Piezoelectric and dielectric properties of $Bi_{0.5}(Na_{0.84}K_{0.16})_{0.5}$-$TiO_3$-$Ba(Zr_{0.04}Ti_{0.96})O_3$ lead free piezoelectric ceramics. *Adv. Appl. Ceram.* **107**, 222-226 (2008).

360   Choy, S. H., Wang, X. X., Chan, H. L. W. & Choy, C. L. $0.75(Bi_{1/2}Na_{1/2})TiO_3$-$0.20(Bi_{1/2}K_{1/2})TiO_3$-$0.05BaTiO_3$ lead-free ceramics with addition of CeO_2. *Ferroelectrics* **336**, 69-79, 63 plates (2006).

8. Appendix

Table 8.1 | Effects of the Addition of Single Elements to BNKT

ele-ment	lattice site / type[A]	doping range[A]	effect(s)	literature sources
Li	A / Ac	< 1 wt% BLT	T_d slightly higher, d_{33} up to 180 pCN^{-1}	39,40,123-125,305
Mg	B / Ac	< 10 at% BiMgT	T_d slightly lower, d_{33}^* up to 570 pmV^{-1}	306
Al	B / Ac	< 1 wt% BiAlO$_3$	T_d similar, temperature insensitive d_{33}^* of 450-500 pmV^{-1}	133-139
Ca	A / Is	see co-doping	see co-doping, not used as single additive	307-309
Sc	B / Ac	<0.5%	d_{33} of 67pmV^{-1}, T_c of 384	310
Mn	A / Ac	< 0.5 wt.% MnO	T_d at MPB lower, at higher contents increasing, d_{33}^* of about 150 pmV^{-1} at 4kV/mm	41,126-128,311
Fe	B / Ac	0-10 mole%	d_{33} of 122 pCN^{-1}	312
Cu	B / Ac	0.01 mole	decreases T_{sinter} by 200 K, slightly decreased electromechanical properties	262,263
Zn	B / Ac	< 20 mole%	d_{33} of about 120 pCN^{-1}	119,120,313
Sr	A / Is	< 5 mole%	T_d decreases significantly until 14°C, d_{33}^* of 600 pmV^{-1}	314
Zr	B / Is	< 5 mole%	T_d decreases, d_{33}^* of up to 614 pmV^{-1}	313,315
Nb	B / Do	< 3 wt. %	T_d decreases (MPB), temperature insensitive d_{33}^* of 300 pmV^{-1} (Na/K=1/1)	33-36,277,278,316-323
Sn	B / Is	< 5 mole% SnO$_2$	T_d below RT, d_{33}^* of about 600 pmV^{-1}	196
Sb	B / Ac	<1 wt.% SbO$_3$	T_d of 350°C (Na/K=1/1), higher d_{33} of 129 pCN^{-1}	324,325
Ba	A / Is	around MPB	d_{33} of up to 170 pCN^{-1}	28-31,72,326-339
La	A / Do	< 4 mole%	T_d decreases, d_{33} of 155 pCN^{-1}	129-132
Other Rare earth	A / Do	< 1mole% Rare Earth oxide	T_d increase to 190°C for erbium, otherwise slight decrease, d_{33} of up to 145 pCN^{-1}	340-346
Hf	B / Is	< 5 mole%	d_{33}^* of 475 pmV^{-1} at 8 kV/mm	347
Ta	B / Do	< 5 mole % Ta$_2$O$_5$	ferroelectric order lost, strain about 0.4%	196

[A] considering $A^{2+}B^{4+}O_3$ as basic formula unit; substituents are indicated as : Ac = acceptor, Is = isovalent, Do = donor

Table 8.2 | Effects of the Addition of Multiple Elements to BNKT

added elements			lattice site[A]	type[A]	remarks	d_{33}^{*}	d_{33}	k_p	
at.%	at.%	at.%				pm/V	pCN^{-1}		
Li: 0.2	Sb: 0.2	Zr: 0 - 0.8	A A B	A D I	only Zr content varied	500	-	-	255
Ba: 0.68 - 1.36	Ca: 0.12 - 0.24	Zr: 0.08 - 0.16	A A B	I I I	only BNT replaced, not BKT	-	198	-	309
La: 0 - 0.3	Al: 0 - 0.6	-	A B	D A	BNKT replaced by $(Bi,La)_{0.5}AlO_3$	579	-	-	258
Ba: 0 - 1.0	Zr: 0 - 1.0	-	A B	I I	$BaZrO_3$ added to BNKT	-	-	-	348
Ba: 0 - 1.0	Zr: 0 - 1.0	-	A B	I I	$BaZrO_3$ added to BNKT	500	-	-	349
Li: 0 - 1.278	Ba: 0.76	-	A A	A I	Na replaced with Li; K and Ba constant	-	184	0.3	350
Ba: 0 - 2.55	Ca: 0 - 0.45	Zr: 0 - 0.3	A A B	I I I	BNKT replaced by $Ba_{0.85}Ca_{0.15}(Ti_{0.9}Zr_{0.1})O_3$	-	205	-	307
Mg: 0 - 0.6	Sn: 0 - 0.6	-	B B	A I	$Bi(Mg_{0.5}Sn_{0.5})O_3$	633	-	-	351
Ba: 0 - 0.616	Ca: 0 - 0.184	-	A A	I I	Na replaced with Li; K constant	-	175	-	308
Li: 0 - 1.5	Ta: 0.5	-	A B	A D	Na replaced with Li, K constant	727	-	-	254
Ba: 0 - 0.8	Ca: 0 - 0.3	Zr: 0 - 1.0	A A	I I	$Ba_{0.8}Ca_{0.2}ZrO_3$ added to BNKT	549	-	-	352
Ba: 0 - 2.8	Sr: 0 - 1.2	-	A A	I I	BNKT replaced by $Ba_{0.7}Sr_{0.3}TiO_3$	-	214	-	353
Cu: 0 - 1.0	Nb: 0 - 1.6	-	B B	A D	excess doping with CuO and Nb_2O_5	427	>140	0.35	257
Sr: 0 - 1.0	Nb: 0 - 0.75	-	A B	I D	BNKT replaced by $SrK_{0.25}Nb_{0.75}O_3$	709	-	-	354
Ba: 0.12	La: excess	-	A A	I D	BNKT:BT + La_2O_3	-	151	-	355

[A] considering $A^{2+}B^{4+}O_3$ as basic formula unit; substituents are indicated as : A = acceptor, I = isovalent, D = donor

Table 8.2 continued | Effects of the Addition of Multiple Elements to BNKT

added elements at.%	lattice site at.%	type at.%	remarks			d_{33}^* pm/V	d_{33} pCN^{-1}	k_p	
Li: 0 - 0.4	Nb: 0 - 0.4	-	A B	A D	Na/K ratio varied, BNKT replaced by LiNbO$_3$	-	195	0.336	256
Ba: 0.6	Co: 0 - 0.8	-	A B	I D	Ba constant, Co$_2$O$_3$ added	-	142	0.25	357
Ba: 0.52	Mn: 0.008	-	A B	I I	Ba constant, MnCO$_3$ added	-	140	0.18	358
Ba: 0 - 2.0	Zr: 0 - 0.8	-	A B	I I	-	-	190	0.35	359
Ba: 0.1	Li: 0 - 0.5	-	A A	I A	Ba constant, Li$_{0.5}$Bi$_{0.5}$TiO$_3$ added	-	160	0.35	335
Ba: 0.1	Ce: 0 - 0.49	-	A A	I D	-	-	129	0.165	360

Table 8.3 | Large Signal Characteristics of BNKT10 Ceramics at 6 kV/mm

dopant(s)	none	0.5V	0.1Cu,0.4V	0.2Cu,0.3V	0.3Cu,0.2V	0.4Cu,0.1V	0.5Cu
BNKT10							
d_{33}^* / pm/V	120	122	152	135	138	162	177
S_{neg} / ‰	-0.58	-0.68	-0.72	-0.83	-0.95	-0.78	-1.02
E_c / kV/mm	4.5	4.8	4.5	4.8	4.7	4.7	4.5
P_{max} / µC/cm²	27.0	28.0	29.2	30.8	31.8	31.1	31.0
P_{rem} / µC/cm²	25.0	25.5	25.7	27.5	29.2	27.6	26.9
BNKT20							
d_{33}^* / pm/V	150	293	285	243	222	208	232
S_{neg} / ‰	-0.30	-0.43	-0.44	-0.36	-0.70	-0.30	-0.14
E_c / kV/mm	2.9	2.2	2.4	1.8	2.4	2.0	1.7
P_{max} / µC/cm²	28.0	26.8	26.5	25.2	27.5	19.7	19.4
P_{rem} / µC/cm²	19.0	15.8	15.2	12.9	20.4	10.4	8.6
BNKT30							
d_{33}^* / pm/V	150	-	162	75	208	228	-
S_{neg} / ‰	-0.14	-	-0.04	-0.01	-0.04	-0.01	-
E_c / kV/mm	2.5	-	0.9	0.6	0.7	1	-
P_{max} / µC/cm²	23.0	-	16.7	14.0	14.9	18.7	-
P_{rem} / µC/cm²	13.0	-	2.0	1.5	2.4	4.3	-

Table 8.4 | Overview of Small Signal Measurement Data

dopant(s)	none	0.5V	0.1Cu,0.4V	0.2Cu,0.3V	0.3Cu,0.2V	0.4Cu,0.1V	0.5Cu
BNKT10							
$T_{f\text{-}r}$ / °C	205	139	132	122	127	157	133
T_M / °C	287	342	325	332	296	312	317
maximum permittivity	3905	2897	2627	2062	2649	3993	2626
BNKT20							
$T_{f\text{-}r}$ / °C	110	70	64	47	80	85	70
T_M / °C	299	351	340	339	344	343	346
maximum permittivity	1750	4813	5281	3005	2954	2844	2960
BNKT30							
$T_{f\text{-}r}$ / °C	200	-	52	43	61	53	-
T_M / °C	315	-	335	348	333	320	-
maximum permittivity	1524	-	2781	2561	2891	3077	-

Erklärung

Ich versichere, dass ich die vorliegende Dissertation selbstständig und nur mit den angegebenen Quellen und Hilfsmitteln angefertigt habe. Die Arbeit hat in gleicher oder ähnlicher Form noch keiner Prüfungsbehörde vorgelegen.

Darmstadt, 09. November 2015   Martin Manfred Blömker

Curriculum Vitae

Personal Information

Martin Manfred Blömker

Martinstraße 91,

64285 Darmstadt, Germany

Born on the 14th of May 1984 in Münster, North Rhine-Westphalia, Germany

Education

August 1994 – July 2003	"Städtisches Gymnasium Borghorst", 48565 Steinfurt, Germany
	Qualification: general higher education entrance (allgemeines Abitur)
August 2004 – September 2008	Department of Chemical Engineering, Münster University of Applied Sciences, 48565 Steinfurt, Germany
	Degree: *"Diplom-Chemieingenieur (FH)"* (specialization: "Angewandte Materialwissenschaft")
August 2010 – April 2012	Department of Chemical Engineering, Münster University of Applied Sciences, 48565 Steinfurt, Germany
	Degree: *"Master of Science"* in chemical engineering (specialization: "Applied Chemistry")
Since July 2012	Department "Material- und Geowissenschaften", Technische Universität Darmstadt, 64287 Darmstadt, Germany
	Anticipated degree: D*octor rerum naturalium*

Work Experience

October 2007 – August 2008	Laboratory for High Performance Ceramics, Swiss Federal Laboratories for Materials Testing and Research, 8600 Dübendorf, Switzerland
	University internship and diploma thesis work on synthesis and thermo-electrical characterization of $MoSi_2$-Al_2O_3 composite ceramics
October 2008 – December 2008	Materials and Failure Analysis Group, Sulzer Innotec AG, 8400 Winterthur, Switzerland
	Materials and failure analysis as well as customer consulting
February 2010 – August 2010	Testing Laboratory, Quadrant AG, 5600 Lenzburg, Switzerland
	Materials testing of high performance plastics and fiber reinforced plastics, quality control and REACH safety data sheets
March 2011 – August 2011	Research group Prof. Ulrich Kynast, Department of Chemical Engineering, Münster University of Applied Sciences, 48565 Steinfurt, Germany
	Research assistant for wet chemical syntheses of nano-materials and ceramics
October 2011 – April 2012	Materials and Surface Science Institute, University of Limerick, Limerick, Ireland
	Master studies with research work on novel syntheses of 3-dimensionally ordered nanocrystalline SnO_2
Since July 2012	Research group "Nichtmetallisch-Anorganische Werkstoffe" of Prof. Jürgen Rödel, department „Material- und Geowissenschaften", Technische Universität Darmstadt, Darmstadt.
	Research assistant and doctoral candidate, working on the effects of doping on $Bi_{1/2}Na_{1/2}TiO_3$ - $Bi_{1/2}K_{1/2}TiO_3$ -based piezoceramics

Peer Reviewed Publications

Collins G., Blömker, M., Osiak, M., Holmes, J. D., Bredol, M., and O'Dwyer, C. (2013). "Three-Dimensionally Ordered Hierarchically Porous Tin Dioxide Inverse Opals and Immobilization of Palladium Nanoparticles for Catalytic Applications." *Chemistry of Materials* **25** (21), pp. 4312–4320. *doi: 10.1021/cm402458v*

(This publication was a designated research highlight in the 2013 November issue [12] of *Nature Materials*, p. 1080, doi: 10.1038/nmat3833.)

Armstrong, E., Khunsin, W., Osiak, M., Bloemker, M., Torres, C. M. S, and O'Dwyer., C. (2014). "Ordered 2D Colloidal Photonic Crystals on Gold Substrates by Surfactant-Assisted Fast-Rate Dip Coating." *Small*, **10**, pp. 1895-1901. *doi: 10.1002/smll.201303616*

Blömker, M., Erdem, E. Li, S., Weber, S., Klein, A., Rödel, J. Frömling, T. (2016). "Defect Structure of Doped Lead-Free $0.9(Bi_{0.5}Na_{0.5})TiO_3$-$0.1(Bi_{0.5}K_{0.5})TiO_3$ Piezoceramics." *Journal of the American Ceramic Society* **99** (2), pp. 543-550. *doi: 10.1111/jace.13999*

Oral Presentations at Conferences

Blömker, M., Erdem, E., Wollstadt, S. and Rödel, J., "Co-doping of Lead-free $Bi_{1/2}Na_{1/2}TiO_3$ (BNT) - $Bi_{1/2}K_{1/2}TiO_3$ (BKT) -based Piezoceramics", European Conference on Application of Polar Dielectrics, Vilnius, Lithuania 7th-11th of July 2014

Blömker, M., Erdem, E., Wollstadt, S. and Rödel, J., "(Co-)doping of Lead-free $Bi_{0.5}(Na_{0.9}K_{0.1})_{0.5}Ti_{(1-x-y)}Cu_xV_yO_3$ Piezoceramics", International Symposium on Electrical Fatigue in Functional Materials, Sellin, Germany, 15th-18th of September 2014

Proffered Communications at Conferences

Blömker, M. and O'Dwyer, C, "Precursor Influence on the Structure of 3-Dimensionally Ordered Tin Oxide Materials for Photonic Crystal Lithium-ion Batteries", NUI Galway Energy Night, Galway, Ireland, 6th of March 2012

Dittmer, R., Blömker, M., Aulbach, E., Webber, K. G., Jo, W. and Rödel, J., "Large Blocking Force in $Bi_{1/2}Na_{1/2}TiO_3$-Based Lead-Free Piezoceramics", Materials Science and Engineering, Darmstadt, 25th-27th of September 2012

Zhang S-T., Kounga A. B., Seifert, K. T. P., Dittmer, R., Blömker, M., Jo, W. and Rödel, J., "Manufacturing of Ceramic, Textured Actuators with High Strain", International Symposium on Electrical Fatigue in Functional Materials, Sellin, Germany, 15th-18th of September 2014